



Ph.D. dissertation

Jesper Baldtzer Liisberg

Abrupt climate change and the nitrogen cycle

Supervisor:

Prof. Thomas Blunier

Submitted: 25/05-2020

Name of department: Niels Bohr institute, Physics of ice climate and earth

Title and subtitle: Abrupt climate change and the nitrogen cycle

Topic description: Applying isotopic gas measurements for the analysis of paleo climate change.

Supervisor: Prof. Thomas Blunier
Niels Bohr institute, Physics of ice, climate and earth, Copenhagen Denmark

Committee: Prof. Barth F. Smets
DTU ENVIRONMENT, Department of Environmental Engineering, Lynby Denmark
Dr. Thomas Keith Bauska
British Antarctic Survey, High Cross, Madingley Road, Cambridge

Submitted on: 25/5-2020

Acknowledgments

The work presented here, whether you will find it satisfying or not, could not have been done alone, and so a few, not too token, words of appreciation are certainly warranted.

I might as well start with the greatest appreciation that goes to my supervisor Thomas Blunier. I have learned a great deal from my work in your group, and feel that I have grown significantly as a scientist thanks to you. Your good attitude in letting me try my hands at things first, but always having an open door for questions helped develop what I consider a fairly independent attitude to lab-work. Something I greatly appreciate. With the many points of frustration that has dotted my work here, between broken instruments and moving you have always been there to share in my frustration and tried to work it out as best as possible. So, for those occasions I am happy that there was someone with a head cooler than mine to help get through the situations.

My work has been a continuation of a line of fellow Ph.D. students starting with David Morten Balslev-Clausen who in collaboration with Picarro helped develop the Picarro G5131-I and Malte Winter that followed him and tried to apply the unit to ice measurements. I owe special thanks to Malte for introducing me to the instrument and the lab in your last days of your Ph.D. at the beginning of mine. A huge thank you to the both of you, and in that line my thoughts also go out to the eventual fourth instalment of this line of N₂O-focused Ph.D. students. The stage is set!

The gas-lab has harboured many good people during my time here, with everyone adding to the joy of working in the lab. From the old guard of Sindhu, Gabriella, Diana and Malte to the newest members, David, Janani, Maureen, Rebeka and Micheal (and Micheal) who will carry this group forward. Thank you all!

To the team at EMPA Switzerland, I can only extend my greatest appreciation for the great work we did together. Joachim Mohn, your supervision during my stay in your lab was a pleasure and I am very happy to have worked with you. Similar words go out to Stephen Harris for sharing those warm evenings awaiting the liberating sound of the alarm. Best of luck to you "mate".

Matthew Johnson also deserves my appreciation, both as my former supervisor for both my master and bachelor, but also for the collaboration done between the two atmosphere groups. It was a pleasure working with you and Merve. And to Merve, thank you for your great work and diligence in and out of the lab.

The CFA-team prior, during and following the campaign was a thrill to work with. Special thanks must of course go to the two poor master students David and Janani, who had to navigate the ill temper brought on by the frailty of glass capillaries (and in my defence poor ventilation). I wish you all the best!

Special thanks to Todd Sowers for sharing the measurements of the discretely sampled air measurements aiding in the analysis of the Dye-3 isotope data. And to Bo Vinther for sharing data on dating and data from NGRIP.

My old colleagues from the chemistry department are also deserving of praise, even if they won't see this due to it being a ph.d. in physics. A sell-out I know... I appreciate the good comradery enjoyed during those five years together, my studying time not just an enrichment of the mind but also of the heart. And I would be amiss, if I forgot to give additional attention to the best of the bunch, Anders and Benjamin. It has been both a pleasure and inspiration to take this journey alongside you both. With equal measure silly and serious mindset, I believe we must have touched on every topic during our study together. I can't wait to do it again. Special thanks to Anders for a reading and correcting this work.

My parents also get a well-deserved word of gratitude as the extensive proof-reading was needed. (and for being all around good sport throughout my life. Good job! ;))

A final and well deserved thank you to my wonderful girlfriend Cathryn, who has supported me through these past three and a half years. And though you had the dubious pleasure of being locked-in with me in the midst of my writing period during the early covid-19 period, you did so with a stiff upper lip and understanding. Greatly appreciated.

Abstract

For studying the climate of the past hundred thousand years, the long-lived ice-sheets located in Greenland and Antarctica offer one of the most versatile types of climatic archives. Especially of interest is the air captured in the ice, allowing for measurement of paleo atmosphere.

The analysis of gaseous isotopes is a powerful method for determining the changes taking place during past climatic transitions. Whether it be physical changes like the firn column depth as can be determined from measuring the enrichment of ^{15}N in N_2 , or the changes in biological output as can be determined by the position of ^{15}N in N_2O , isotope analysis is offering a way to assess this. Isotope analysis has conventionally been done by isotopic ratio mass spectrometry, but thanks to the advances in laser and detection technology, analysis by laser spectroscopy is becoming possible.

The first part of this thesis outlines the development of an experimental setup allowing for improved measurement of gaseous isotopes in ice cores. This was accomplished by combining the existing methods of continuous flow analysis giving high temporal resolution with the measurements of nitrogen and argon isotopes by isotope ratio mass spectrometry. The measurement of argon isotopes was made possible by a novel method for continuous oxygen removal using a perovskite membrane.

This system was put to the test on ice from the bottom of Dye 3, one of the first deep cores, collected from Greenland in the beginning of the 1980's. Due to the uncommonly shallow firn column of Dye 3 compared to other cores, the isotopic increases were bigger and more sudden compared to other cores. It was able to detect the relative changes in $\delta^{15}\text{N}$ with a 50 per meg uncertainty, and was used together with the $\delta^{40}\text{Ar}$ to quantify the driving fractionation effects in the firn during climate transitions. Additionally, the trends in total air content were detectable and related to the climatic variation. While the system and calibration scheme ultimately failed at binding the isotope ratios to an absolute scale, the concept of the system was proven and offers a powerful addition to the CFA gas measurements.

The second part of this work is a paper outlining an inter-lab collaboration undertaken at Empa in Switzerland. Here the performance and limitations of ambient measurements of N_2O and its isotopes were compared between different instruments using laser spectroscopy. Effects from trace gas and matrix composition were determined, and the non-linear relationship with N_2O abundance was described. An extensive guideline was developed for how to produce reproducible measurements of N_2O isotopes using these instruments, giving comparable precision to IRMS.

The last addition to this work details a project investigating a novel way of removing methane from a sample stream for the purpose of scrubbing gas for analysis. The motivation for this was the observed interference from methane on N_2O measurements found in the inter-lab comparison. This was done by photolyzing chlorine gas and let it speed up the oxidation path of methane, similar to the process in the atmosphere. A removal efficiency of 98% was achieved, and the effect of varying parameters was determined via a combination of experiments and modelling. Additional experiments are needed to determine if the achieved removal was sufficient to correct for the methane interference.

Dansk resumé

Hvis man vil studere klimaet igennem de sidste hundrede tusind år, udgør iskapperne, der dækker Grønland og Antarktis, en af de mest alsidige kilder til viden. Isen er et af de eneste steder, hvor fortidens atmosfære kan måles direkte. Dette kan lade sig gøre takket være de luftbobler, der gemmer sig i isen.

For at ekstrahere information ud af gassen, er målingen af isotoper en effektiv måde at måle de forandringer, der finder sted i forbindelse med klimatiske overgange. Måling af berigelsen ^{15}N i kvælstof kan redegøre for ændringer i de lokale forhold som temperatur og nedbør igennem tiden. Biologiske forandringer kan også undersøges ved for eksempel at måle på den dominerende placering af ^{15}N i N_2O , som ændrer sig i takt med produktivitet mellem forskellige bakterier. Måling af isotoper er normalt blevet udført ved brug af isotopforhold massespektrometre, men i kraft af udviklingen inden for laser- og detektionsteknologi er det nu muligt at måle isotoper ved atmosfærisk niveau med laser spektroskopi.

Det første afsnit i denne afhandling redegør for udviklingen af en eksperimentel-opstilling, der udvidede den eksisterende måling af gas fra iskerner til at inkludere måling af isotoper. Dette blev gjort ved at tilføje et isotopforhold massespektrometer, der normalt benytter diskrete prøver, til det eksisterende system for continuous flow analysis, der tillader en konstant strøm af data. En essentiel del af denne kombination var udviklingen af en ny metode for kontinuerligt at fjerne oxygen ved brug af en opvarmet perovskit membran. Dette system blev afprøvet i forbindelse med målekampagnen for is fra Dye 3, der er en af de første dybe iskerner samlet fra Grønland i begyndelsen af 1980'erne. På grund af den atypiske højtliggende lock-in zone for Dye 3 i forhold til andre kerner, er isotopsignalerne større og bevaret med mindre blanding årene imellem, hvilket gør det til en ideal kerne at undersøge gas isotoper for. Det udviklede system var i stand til at måle de relative ændringer i $\delta^{15}\text{N}$ med en usikkerhed på 50 per meg, og kunne i kombination med de samtidige målinger af $\delta^{40}\text{Ar}$ bruges til at udregne de drivende effekter bag de observerede berigelser. I forbindelse med udviklingen af opstillingen var der indført nok kontinuerlige målinger af prøvens flow og tryk, at det var muligt at følge ændringerne i det totale luftindhold i isen. Selvom system med de udviklede kalibreringer i sidste ende ikke var i stand til at producere isotop data, der kunne bindes op på en absolut skala, er det underliggende koncept blevet bekræftet og er en udvidelse til CFA gasmålinger med et stort potentiale.

Anden del af denne afhandling er en artikel, der beskriver et internationalt samarbejde mellem flere laboratorier. Samarbejdet undersøgte præstationen og begrænsningerne mellem forskellige laser spektrometre udviklet til måling af lattergas og dets isotoper. Instrumenternes præstation ved atmosfærisk niveau af lattergas og deres tilbøjelighed til at blive påvirket af varierende gas sammensætninger blev fundet. Disse effekter blev i øvrigt bekræftet til at være afhængige af lattergaskoncentrationen, og denne sammenhæng blev beskrevet. Baseret på resultaterne fra dette arbejde, blev der udarbejdet en uddybende manual, der giver vejledning til, hvordan disse instrumenter kan producere reproducerbare målinger af lattergas isotoper, der kan sammenlignes med IRMS.

Det sidste afsnit beskriver et projekt, der undersøger en innovativ måde at fjerne CH_4 fra en prøve i kontinuerligt flow. Motivationen for dette var en CH_4 effekt på lattergasmålinger, der blev beskrevet i overnævnte artikel. Dette blev opnået ved at introducere Cl_2 til en prøve danne Cl -radikaler ved brug af lys. Disse kunne dernæst initiere CH_4 oxidation, sammenligneligt med de atmosfæriske processer. Denne metode opnåede en effektivitet på 98% af metan fjernet. Systemets afhængighed af lys, Cl_2 , CH_4 og reaktionstid blev undersøgt både via forsøg og modeller.

Abbreviations

BPR: Back pressure regulator

CCAR: Copenhagen Centrum for Atmospheric Research

CFA: Continuous flow analysis

CRDS: Cavity ring-down spectroscopy

D.M.STD: Dynamically mixed standard

DO: Dansgaard-Oeschger

EX: Extraction efficiency

FPR: Forward pressure regulator

GC: Gas chromatogram

GH: Green house

GWP: Global warming potential

G%: Gas ratio in percentage of volume

IRMS: Isotope ratio mass spectrometry

MS: Mass spectrometry

m/z: Mass to charge ratio

PICE: Department for Physics of Ice, Climate and Earth

SS: Stainless steel (when discussing Swagelok tubing or fittings)

STP: Standard temperature and pressure (298K and 1 atm)

TAC: total air content ($m_{\text{gas}}/g_{\text{ice}}$)

Contributions to the work

The work detailed in the first part of this dissertation, was done in close collaboration with David Aaron Soestmeyer and Janani Venkatesh, who were both doing their masters on the CFA system. The data treatment shown reflects the continued collaboration following the end of the campaign.

In the paper “N₂O isotopocule measurements using laser spectroscopy: analyzer characterization and intercomparison” I shared first-authorship with Stephen Harris, as I was intricately involved throughout the project. Working with development and execution of the experiments, data treatment and interpretation as well as writing the paper.

For the second paper “Cl-initiated Methane oxidation” as second author I was responsible for development of experimental design, data collection and interpretation as well as writing the paper.

It should be noted that the second paper is still a work in progress, and as such might be subject to changes from the version presented here.

Contents

Acknowledgments.....	2
Abstract.....	3
Dansk resumé.....	4
Abbreviations.....	5
Contributions to the work.....	6
1. Dye 3 CFA campaign.....	9
1.1 Dye 3 firn.....	10
1.1.1 Firn densification and its effect on N ₂ and Ar.....	11
1.1.2 Dye-3.....	15
1.2 Setup development.....	17
1.2.1 Mass spectrometer.....	18
1.2.2 CFA setup.....	19
1.2.3 Gas extraction.....	20
1.2.4 Oxygen removal.....	22
1.2.5 Running the system.....	24
1.3 Data treatment.....	26
1.3.1 Calibration scheme.....	28
1.3.2 Solubility effect.....	32
1.3.3 Age assignment.....	36
1.3.2 Uncertainty.....	38
1.4 Result and discussion.....	40
1.4.1 $\delta^{15}\text{N}$ record.....	43
1.4.2 Thermal and gravitational fractionation.....	48
1.4.3 $\delta\text{Ar}/\text{N}_2$ discussion.....	51
1.4.4 Total air content reconstruction.....	54
1.6 Future work.....	57
1.7 Conclusion.....	58
References.....	59
2. Paper on N ₂ O isotopic measurements using laser spectroscopy; analyser characterization and intercomparison.....	62
3. Cl-initiated Methane oxidation.....	98
Appendix.....	117
1. CFA Dye 3.....	117
1.1 Thermal and gravitational fractionation calculation.....	117
1.2 Main matlab script.....	117

1.3 Matlab script for applying pressure imbalance and chemical slope corrections.	124
1.4 Matlab script for applying the solubility effect corrections.	126
1.6 Chemical slope assessment data	129
1.7 Dynamically mixed standard reconnected for full system effect determination.	130
1.8 Error propagation for $\delta^{29}\text{N}_2$	131
1.9 Error propagation of $\delta^{40}\text{Ar}$	131
1.10 Error propagation for $\delta\text{Ar}/\text{N}_2$	132
3. Chlorine induced methane oxidation	133

1. Dye 3 CFA campaign

Studying paleo-atmospheres is important as it gives us a view into how the global system worked with regards to temperature, greenhouse gas abundance and the emergence of life. Digging back in time often becomes a literal explanation, as the investigation into the past often relies on going deep in various media in order to find the hidden traces of what has transpired on Earth. Whether it is through oceanic or lake sediments, terrestrial layers or as shall be investigated in this work ice cores, it all requires going deep and determining the history unfolding during this travel. When studying the atmosphere of the past, most of this work will have to rely on proxies, such as interpreting the sudden appearance of oxidized minerals in terrestrial layers indicating the rising presence of oxygen (Kasting, 2001). Going forward in time to Jurassic periods, proxies for CO₂ abundance can be found by looking at the density of stomata (“breathing holes”) of fossilised leaves (Roth-Nebelsick, 2004), or determining the timing of vegetative responses from the isotopic enrichment in speleothems (KONG Xinggong, 2005).

While there is a plethora of options for piecing together the atmosphere of the past, it will have to be based on proxies, each restricted to certain time periods for which they can account for. The complete composition of the atmosphere therefore remains unresolvable with the current techniques, with the exception of the latest 2 million years, where the formation of lasting ice-sheets allows for “direct” measurement of the past atmosphere. (Stauffer et al. 1985) Firn is the denomination of the top layer of an ice-sheet where the conversion from snow to ice occurs. Due to the formation of the ice-sheet going from snow to ice through densification within this firn layer the structure is porous and as such filled with air. These pores become sealed off and form pockets as the ice densifies, thereby trapping the air within a layer as it travels further down with new layers forming above and layers thinning below (Buizert, 2013). By the use of measurements of the trapped air, it has been possible to recreate the CO₂ and CH₄ record throughout the past going as far back as 800,000 years with Antarctic cores { (Dieter Lüthi, 2008) (Laetitia Loulergue, 2008)}. In combination with temperature reconstructions based on the $\delta^{18}\text{O}$ of the ice, the behaviour of the 100,000-year glacial-interglacial cycle has been determined. A part of these findings was the observation in older glacial periods of rapid warming events similar to the Dansgaard-Oeschger events (henceforth DO) observed in the last glacial period. DO events are rapid heating events occurring during the last glacial on a decadal timescale, with temperature increases that are maintained for hundreds to thousands of years (Sune O. Rasmussen, 2014). The rapidness with which these changes occurred on a global scale is worth our interest as it offers a way to investigate the stability and sensitivity of the earth’s climatic systems. While the dominant mechanisms for glacial climate was significantly different compared to our current interglacial world, there is still value in the insight to be gained, even if the climatic changes seen cannot take place currently. As of now the exact mechanism driving the DO events is still undetermined, despite having been investigated extensively for the last decades. Some suggestions point to that the breakdown of the large northern ice-sheets covering the North Atlantic could lead to initial rapid heating (G. H. Denton, 2010), that is then reinforced by positive feedback among which increased levels of greenhouse gases are found.

In the work presented here, the desire was to perform a continuous flow analysis (CFA) investigation on the Dye 3 core from the depth of 1750-1920m with a focus on analysing the gases stored. The chosen depth contains the termination of the glacial, the Younger Dryas, Bølling-Allerød and the DO-events 4-11.

Besides the intention of generating data, the goal of the campaign was to develop a robust addition to the gas measurements of continuous flow analysis (CFA henceforth), able to measure the isotopic enrichment of $\delta^{15}\text{N}$ and $\delta^{40}\text{Ar}$ as well as the elemental ratio between Ar and N_2 . This would rely on sufficient sample preparation including the challenge of continuously removing O_2 from the sample stream. Furthermore, it would necessitate a well-established fractionation across the system to account for the effects of the sample treatment. Finally, it was intended to compare and verify the acquired results with discreet samples from the same ice and from similar Greenlandic cores by binding it to the general age-scale.

1.1 Dye 3 firn

Nitrogen and argon are respectively the most and third most abundant gas in earth's atmosphere, making up around 78% and 0.934% respectively (John H. Seinfeld, 2006). Unlike the second most abundant gas, O_2 , both of these gases are relatively inert, with argon not participating in the biochemical cycle to any degree. A consequence of this in combination with their atmospheric abundance is that their isotopic ratios are less prone to variations, resulting in $^{15}\text{N}/^{14}\text{N}$ and $^{40}\text{Ar}/^{36}\text{Ar}$ staying stable on the $>10^4$ year time scale (Bender T. S., 1989). Because of this, the measurement of $^{15}\text{N}/^{14}\text{N}$ and $^{40}\text{Ar}/^{36}\text{Ar}$ lends itself to the study of the firn column of the past, as the local fractionation is going to dominate the observed variation in both ratios. Measurements of this have already been made (Bender T. S., 1989), (Jeffrey P. Severinghaus, 1998)) and show how climatic events also leave a mark in the isotopic ratio of these inert gases. The common convention when describing isotopic ratios is by the use of the delta-nomenclature, which gives the relative difference in isotopic ratio between a measured sample and known standard is described.

$$\delta = \left(\frac{r}{r_{STD}} - 1 \right) \quad (1)$$

δ is the relative difference between two ratios and is conventionally given in ‰, r is the ratio of the sample while r_{STD} is the ratio of the standard both of which are unitless.

In the selected core-section the point of most interest is the transition from the Younger-Dryas to the Holocene. This transition from glacial to interglacial should be highlighted by a major shift in the densification, as the temperature will increase alongside accumulation. This change in the firn condition will leave a clear signal in the $\delta^{15}\text{N}$ because of the changed fractionation effects.

1.1.1 Firn densification and its effect on N₂ and Ar

In order to understand the signals of gas stored in ice-sheets it is important to have an understanding of the dynamics that trapped it within the ice. The trapping goes on in the porous interface between atmosphere and the ice-sheet that is the firn-layer. This process is initially a mechanical densification where the weight of the new layers on top densifies the layers below. Densification is dependent on temperature, snow density and yearly accumulation as described by Herron-Langway (Michael M. Herron, 1980). In their model the journey from snow to ice can be followed through the density profile of the firn column, with relatively fast densification to 0.55kg/l that can be interpreted as the denser packing of the snow as the flakes get rounded off. This densification occurs within the top 10-20 meters depending on the local conditions. After a density of 0.55kg/l is reached, the snow can no longer be packed any closer, and the remaining densification occurs via morphology of the snow towards ice as the density approaches 0.92kg/l. This process of densification can be seen in Figure 1 (a), where the density follows a near linear dependence on depth until 0.55kg/l is reached, where after the densification rate slows down.

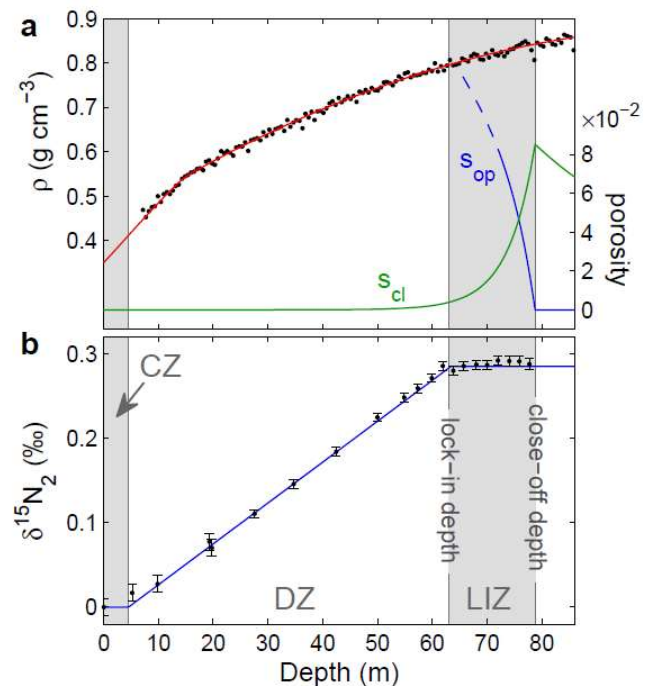


Figure 1: “(a) Firn density ρ (left axis), and the open and closed porosity S_{op} and S_{cl} , respectively (right axis). Black dots show firn density measurements in 0.55m segments. (b) Gravitational enrichment as shown by $\delta^{15}N_2$, corrected for thermal effects (Severinghaus, Grachev, & Battle, 2001)” – from (C. Buizert P. M., 2012)

In relation to the air storage, it is conventionally separated into three regions, consisting of a convective zone, diffusive zone and the lock-in zone. (C. Buizert P. M., 2012) The convective zone is the youngest region made up of the upper few meters, where the ice structure and density are still close to that of snow. In this region the air within the firn matrix is freely able to exchange with the open air above, and the air composition within this region is controlled by the convective movement of wind.

Below the convective zone is the diffusive zone that continues, through densification until the lock-in depth. As the name suggests this region is dominated by the diffusion of gas within the semi-connected pores. The gas is not able to freely exchange with the current atmosphere, but as the porosity of the firn-ice still allows for diffusion. Below the diffusive zone the lock-in-zone starts where the permeability throughout the ice matrix gets reduced to the point, where bubbles get formed as gas is enclosed in the ice structure. The gas captured is no longer prone to isotopic fractionation effects, as it is limited from diffusive movements driving the fractionations. This end to the fractionation can be observed in Figure 1 (b), where the enrichment in $\delta^{15}N$ remains constant along depth after entering the lock-in-zone. The lock-in-zone covers upwards of a few meters to 20 meters depending on local conditions, as the closing off of bubbles is a gradual process (C. Buizert P. M., 2012). The lock-in-zone ends at the close-off depth below which all the gas is stored in the ice. Below the close-off depth only one more transformation occurs to the gas stored, and that takes place when the ice-matrix has been compressed and densified to such a degree that the bubbles themselves get squeezed into the ice, dislocating the gas into clathrates within the ice-matrix itself (Miller, 1969). The region in the ice-sheet, 500-1200m, where this transformation occurs is termed the brittle-zone as the

formation of clathrates exerts a great pressure on the ice itself, rendering it brittle when removed from the high pressure stabilizing it in the ice-sheet. Below this the depth the ice is stabilized in the new configuration and will not be as brittle. With time, ice cores from this depth will relax under the reformation of bubbles. The gas measured in this campaign will therefore likely be a mix of clathrates and bubbles, though to which degree is unknown.

In the diffusive zone thermo and gravitational describes the isotopic enrichment, as the gas transport within the limited free-path is dictated by these physical effects. Both of these effects are consequences of lighter molecules requiring less energy to move around, and as such will tend to move upwards in comparison to their heavier counterparts. The thermo fractionation describes the steady state reached where thermo diffusion upwards is countered by a concentration gradient going the opposite way. In relation to isotope ratios the relationship between ratios and temperature can be described as (Jeffrey P. Severinghaus, 1998)

$$\delta = \frac{r_c}{r_h} - 1 = \left(\frac{T_h}{T_c}\right)^\alpha - 1 \quad (2)$$

δ is the relative deviation between the isotope ratio at the cold end of the temperature gradient, r_c , when compared to the isotope ratio at the hot end r_h . Both of these are the ratio between the abundance of the heavier isotope and the lighter, which in the case of N_2 , becomes $[^{15}N]/[^{14}N]$. T_h and T_c are the temperatures in kelvin at the hot and cold end of the gradient respectively. The last value, α , is the thermal diffusion coefficient and is an isotopic/molecule-pair unique constant that describes the relationship between fractionation and temperature. With a positive α the resulting response to a temperature increase at the T_o compared to T would mean an increase in the heavier isotope. An issue with applying the equation above is the dependence on absolute temperatures for both the hot and cold region. These values require a reconstruction of both temperatures, for the purpose of extracting the associated fractionation. The uncertainty for these temperatures will then be propagated through the equation above. In order to minimize this effect, the use of the alternative temperature sensitivity is common (K. Kawamura, 2013), (Severinghaus, Grachev, & Battle, 2001). It is approximately related to the thermal diffusion factor through:

$$\Omega \cong \frac{\alpha}{T_{avg}} \quad (3)$$

Where the average temperature is defined as:

$$T_{avg} \equiv \frac{T_h * T_c}{T_h - T_c} * \ln\left(\frac{T_h}{T_c}\right) \quad (4)$$

The use of thermal sensitivity allows for an easy assessment of the scaling of the expected fractionation, as it only relies on the differences between temperatures rather than the absolute value of both temperatures.

$$\delta x \equiv \Omega_x \cdot (T_h - T_c) \quad (5)$$

Where δx is the enrichment in isotope x , based on its thermal sensitivity Ω_x and the difference in temperature. This equation is not able to provide the resulting enrichment, but it is able to compare the response between isotope pairs with different thermal sensitivity. Here relative values can be used, and it has been found that the thermal sensitivity of $\Omega^{40}Ar$ is 65% of the thermal sensitivity of $\Omega^{15}N$ at $T_{avg} = 240^\circ C$ (Severinghaus, Grachev, & Battle, 2001).

Thermal fractionation is most pronounced in the top of the firn column where the seasonal variation in temperature is propagated down, leading to variation in the delta values (Severinghaus, Grachev, & Battle, 2001). As can be seen in Figure 2 the seasonal variations average out further down the firn column and below the top 25 meters a stable temperature across the firn is established and the thermal fractionation across the rest of the firn column approaches zero. In the lock-in zone where the gas is trapped, no thermal signal fractionation is expected to be stored. This holds true for stable periods of yearly averages, except in events of rapid and maintained temperature changes as seen with DO events. In these events the rapid increase in temperature shifts the otherwise steady-state temperature in the firn column and allows for a temperature gradient to develop across the firn column. This in turn gives a signal in the isotopic enrichment, documenting the temperature change. This effect is only maintained while the temperature gradient across the firn is maintained, so when a new average has been established the effect approaches zero again.

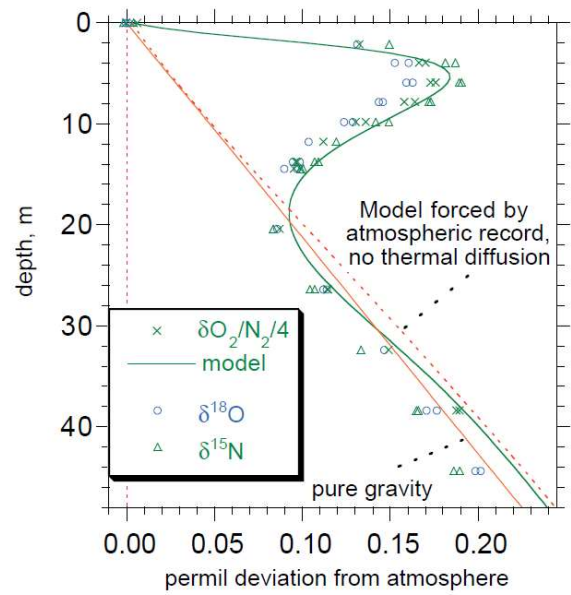


Figure 2: Observed Siple Dome $\frac{1}{4} \delta O_2/N_2$ compared with model runs forced by atmospheric $\frac{1}{4} \delta O_2/N_2$ as an upper boundary condition, in addition to temperature forcing. (Severinghaus, Grachev, & Battle, 2001)

The gravitational fractionation is assuming steady state between a concentration gradient and the density gradient of the air. Due to the slower speed for heavier molecules they are enriched with depth, as it will require more energy to move upwards in the firn. The effect is described as:

$$\delta = \frac{r}{r_o} - 1 = \exp\left(\frac{\Delta m g z}{R \cdot T}\right) - 1 \quad (6)$$

Where δ is the resulting gravitational fractionation, r is the ratio at depth z and r_o is the ratio at the surface. Δm is the difference in molecular weight between the two isotopes, in the case of $^{15}N/^{14}N$ that would be 1g/mol and for $^{40}Ar/^{36}Ar$ would be 4g/mol, g is the gravitational acceleration which at the latitude of Dye-3 is $9.823m/s^2$. R is the gas constant and T is the temperature in kelvin. z is the height difference between the depth of comparison and the top of the diffusion zone in meters. Here it is important to note that the exact height of the convective zone is uncertain, and would depend on the densifying conditions that may vary with time.

The fractionation predicted by the gravitational and thermal effect in eq. 5 and 6 is the maximum expected fractionation, and the degree to which this will be reached can be limited by upward advective flow (H. CRAIG, 1988). Greater advective flow introduces more mixing and reduces the gravitational and thermal fractionation. Advective flow has been found to depend on the inverse difference of density between the density at depth z and the close-off density $\left(\frac{1}{\rho_z} - \frac{1}{\rho_{co}}\right)$, with the effect scaling with ice-accumulation. The potential effect of this needs to be considered when interpreting the found enrichments.

As environmental changes that would result in a response in both the thermal and gravitational fractionation are often coupled, the responses are also going to be near simultaneous. It is possible to disentangle them as the thermal fractionation is molecule specific while the gravitational is a universal

fractionation. The fractionation for each of the two isotopes can be expressed as a sum of the fractionation resulting from their respective thermal and gravitational effects.

$$\delta^{15}N_{obs} = \delta T_{N_2} + \delta G_{N_2} \quad (7)$$

$$\delta^{40}Ar_{obs} = \delta T_{Ar} + \delta G_{Ar} \quad (8)$$

By comparing the observed signal of enrichment for ^{15}N and ^{40}Ar the effect size of gravitational and thermal fractionation can be disentangled. Doing so relies on realising that both the thermal enrichment and gravitational enrichment of argon can be expressed as the thermal and gravitational enrichment of nitrogen. The thermal sensitivity of ^{40}Ar was 65% that of ^{15}N , and the gravitational fractionation is approximately 4 times greater for ^{40}Ar than ^{15}N , leading to:

$$\delta^{40}Ar_{obs} = 0.65\delta T_{N_2} + 4 \cdot \delta G_{N_2} \quad (9)$$

From combination with eq. 7 the thermal and gravitational effect can be found (see appendix 1.1):

$$\delta G_{N_2} = \frac{\delta^{40}Ar_{obs} - 0.65 \cdot \delta^{15}N_{obs}}{3.35} \quad (10)$$

$$\delta T_{N_2} = \frac{4 \cdot \delta^{15}N_{obs} - \delta^{40}Ar_{obs}}{3.35} \quad (11)$$

Both the thermal and gravitational effect also play a role in the elemental ratios such as O_2/N_2 and Ar/N_2 , but here it should be noted that a third fractionation effect becomes dominating. Adding to the complexity is the close-off fractionation occurring as a result of different molecules having varying sizes. Based on work from (C. Huber, 2006) it was found that molecules smaller than a critical collision diameter of 3.6\AA was enriched above the close-off depth. This diameter separates O_2 and Ar from N_2 as the diameters are 3.47 , 3.54 and 3.80\AA respectively (H. CRAIG, 1988). The reason given for this is a “window” of 3.6\AA in the structure of the ice-matrix that allowed smaller molecules to pass through. This effect is termed close-off fractionation. Part of the promotion for this is the pressure build-up within the bubbles that occurs with close-off. It should therefore be expected that the small enrichment above the close-off would mirror a depletion in the closed-off bubbles, and that does appear to be the case, with measured elemental ratios O_2/N_2 and Ar/N_2 below the close-off depth being depleted when compared to modern air on the order of -15‰ and -7‰ respectively. This is noticeable as the elemental ratios would be expected to be enriched due to gravitational fractionation. Based on observations O_2/N_2 appears to be usable as a local summer insolation proxy, as the summer insolation affects the physical properties of surface ice grains (Buizert, 2013). When those surface grains make it down to the depth of lock-in-zone it will determine the degree to which the size-dependent fractionation can occur. As argon is also affected by close-off fractionation, it seems likely that Ar/N_2 also could work as a summer insolation proxy in a similar manner.

The amount of air captured in the ice, total air content (TAC) is also a parameter of interest, as it is a product of the pressure and temperature at the point of capture. For that reason it has initially been assumed to be a proxy for surface elevation (LORIUS, 1973), but more recent findings show that the complexity of bubble enclosure complicates matters, as other effects dominate the variation observed. In the work of (Olivier Eicher, 2016) a drop in TAC was observed in response to DO-events in the NGRIP core. The explanation given is that the increase in accumulation coming with the DO-events leads to a temporary enhanced densification reducing the pore size until the firn column has stabilized. If possible this effect will also be investigated.

A final remark regarding the interpretation of gas from firn pertains to the age of the gas in relation to the surrounding ice. Whereas the ice comes in separable layers, the gas diffuses through the firn

column as has been discussed, resulting in a mixing between years. A consequence of this is that the gas that is closed off will be younger than the ice surrounding it. This difference is denoted Δ_{age} and increases with the depth of the close-off zone, and drops with increasing accumulation (Buizert, 2013). A second consequence is that the age distribution will increase with depth, as it has had a longer time and age range to mix in, resulting in a smoothed response. Best conditions for high temporal resolution in gas would be shallow lock-in zone and high accumulation, which is the case for Dye-3. With regards to close-off fractionation, it is expected to follow ice-age rather than gas-age as the effects derive from variation in the ice properties. Timing of gravitational and thermal fractionation is expected to align with gas-age rather than ice-age.

1.1.2 Dye-3

Dye-3 represents one of the earliest deep ice core drillings in Greenland as it was conducted between 1979 to 1981 at the third of the Dye bases as part of the Distant Early Warning line (Dansgaard, 2004). The station and drill site were located a few dozen kilometres east of the local ice-divide at 65°11'N 43°49'W on top of the 2km ice-sheet. The time period covered by the ice core goes through the Holocene down to a depth of 1780m where the transition from the last glacial began. The remaining 250 meters covers the last glacial period and ends with the transition into glacial from the Eemian. The core has already been the subject of campaigns, from the initial measurements of $\delta^{18}O$ for temperature proxy, measuring total air content (Dansgaard, 2004), borehole temperature measurements (D. Dahl-Jensen, 1998) and measurements of gas isotopes from the top 140meter of the ice-sheet (H. CRAIG, 1988). Because CFA was not part of the measurement protocol at the initial cutting of the ice, no pieces have been set aside for it. Samples were therefore taken from the tube archive. Since the core had already been the subject of investigations, the range investigated is therefore suffering from lacking core-bags that have already been used, and presents a few holes in the continuous data with a 44m hole from 1821-1865m covering the onset of the Bølling-Allerød to the end of the stadial 4.

Due to its location east of the local ice-divide, South Dome, the core differs from cores that followed it. This is due to the effects of ice-flow away from the ice-divide resulting in ice found deeper in the core were originally located closer to the summit, but has with time been thinning and flowing out. The older the ice, the further away it originated as can be seen in Figure 3.

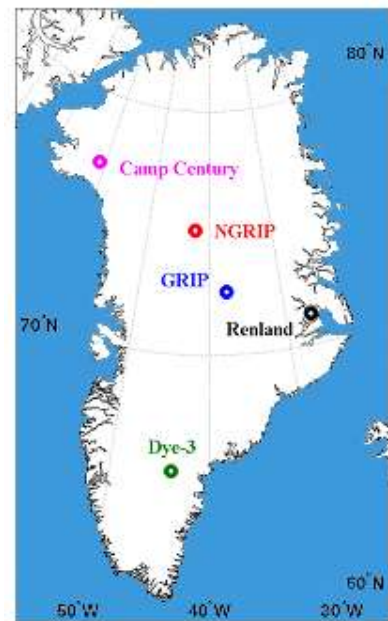


Figure 4: Map of Greenlandic drill sights. (Vinther, 2020)

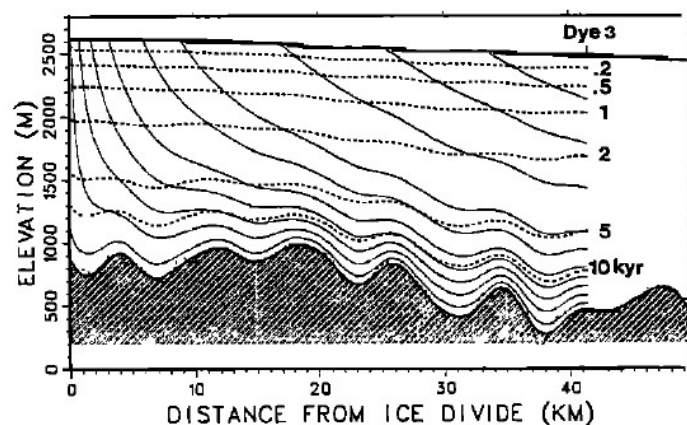


Figure 3: "Flow pattern predicted by the ice flow model. Thin full curves are particle paths (flow lines). Dotted curves are isochrones, with age in thousands of years indicated to the right in the figure" - (N. Reeh, 1985)

In addition to this, the very southern and near costal location of Dye 3 compared to NEEM, GRIP and NGRIP, means that the local conditions are significantly different with regards to temperatures and precipitation. In Figure 5 the average modern conditions can be seen for multiple core sites in both Antarctica and Greenland, and the unusually high accumulation and temperature at Dye 3 result in the smallest Δ age of all the cores. This arises from a relatively shallow firn column, which for the purpose of CFA gas measurements, is desirable, as it means the age distribution will also be significantly smaller, allowing for better temporal resolution. A shallow core also means that the effects of changes to temperature will be more pronounced, as the temperature gradient will be established quicker, resulting in sharper increases in thermal fractionation. The high accumulation in Dye 3 will, however, have the side-effect of increased advective flow. This has already been shown to reduce the gravitational fractionation of $\delta^{15}\text{N}$ from the 0.33‰ expected from eq. 6 with $z=70\text{m}$ and $T=-20^\circ\text{C}$ to 0.22‰ (H. CRAIG, 1988).

An additional point that deserves attention is the aforementioned time the core has been stored. With 40 years since its recovery it has as mentioned had time to relax the clathrates to reform bubbles. This observed morphology points to another potential source of issues, namely loss of gas or contamination from modern air. It is unfortunately possible that the pressure within the core has allowed some of the gas to seep out. This loss would be expected to be a process leading to fractionation in elemental ratios. The reason for this is that O_2 and Ar are small enough that they can escape through the ice matrix, whereas N_2 would be left behind. While there might be diffusion within the ice, only diffusion out of the ice leads to loss, which means that a high volume to surface ratio has a reduced loss. Cracks or fractures in the ice structures increase the surface area and thus increase the loss, leading to core cracking fractionation. As the ice investigated in this campaign is well below the brittle zone, it is expected that all the gas was in the form of clathrates, at the point of excavation. This would provide some protection against core-cracking fractionation as the clathrates would retain the gas better (Bender T. S., 1989) (Bender M. L., 2002). The ice-cores have, however, been stored at ambient pressure, which would promote the reformation of gas-bubbles. From visual inspection of the ice the presence of bubbles in the ice was confirmed. For the purpose of measurements, bubbles are preferred, as the melting of clathrates would result in the captured gas molecule being dissolved at melting. The long storage time of close to 40 years is expected to be sufficient for the majority of clathrates to have collapsed into bubbles, though the exact degree to which this is true is not known.

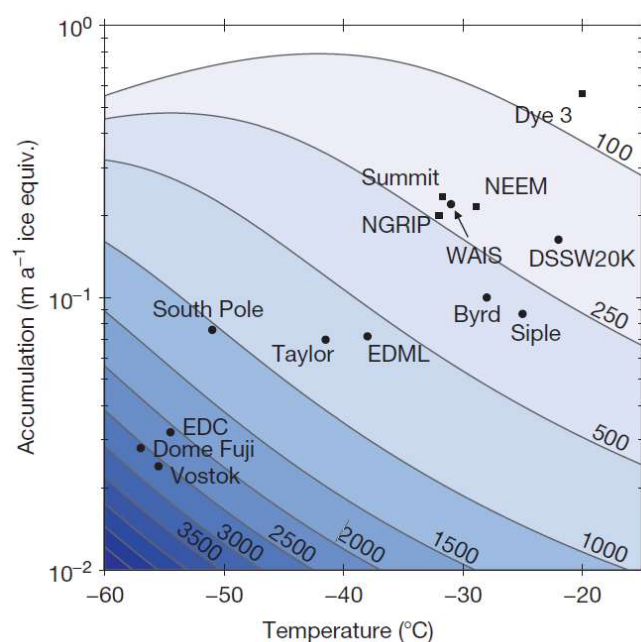


Figure 5: Overview of modern day average yearly accumulation and temperatures for various drilling sites. From this the contour plot of Δ age has been made based on an assumed gas lock-in density of 14kg m^{-3} below the mean close-off density with density profile found from Herron-Langway's model. (Buizert, 2013)

Contamination from modern air is expected to be introduced at macro- or microfractures that have re-frozen sealing in modern air, or during the measurement between two blocks of ice.

1.2 Setup development

The CFA system is based on what has previously been used for campaigns for NEEM, RICE and Renland, and had already been developed to isolate the gas bubbles from the meltwater stream and measure it for methane abundance using the G1101. With the campaign we set out to include isotopic measurements of N₂ and Ar to the gas measurements. The instrument of choice for these measurements was an isotopic ratio mass spectrometer (IRMS), Thermo Delta V, which allows for continuous measurements of a range of different mass to charge ratios.

At the core of a CFA setup is the ice-core itself. Mounted in a frame inside a freezer it is slowly being melted at the bottom where it is placed on a heated unit henceforth named melt-head. This melt-head is constructed in a way that allows for separating the melt-flow from the inner part of the core from the outer. This separation is important as the outside of the core has been in contaminated during storage, sample preparation and from contact with modern air. The outside flow goes to waste, while the inner mix of liquid and gas flow goes towards analysis. The concept builds on the work done by Andreas Sigg (Andreas Sigg, 1994), where the continuous melting of samples from the Greenland Ice core Project (GRIP) allowed for high-resolution measurements of four trace species H₂O₂, HCOHO, NH₄⁺ and Ca²⁺ in the liquid flow. With the development and progress of CFA, it has been used to measure the CH₄ abundance for the core of NEEM (C. Stowasser, 2012), Recap (Vladimirova, 2018). Because of the constant stream of sample generated by the melting of the core, it lends itself to be measured for as many relevant components as possible once melting has started. Components of interest include; Na⁺, Ca²⁺, Cl⁻, NH₄⁺, NO₃⁻, pH, dust, δH₂¹⁸O, CH₄, CO₂, N₂O, δ¹⁵N and δ⁴⁰Ar. This allows for a more complete picture of the past conditions as all the information can be combined to tell parts of the story.

While a functional gas-CFA system was available as originally developed by Christoff Stowasser (C. Stowasser, 2012), and later improved upon by Rachel Rhodes (Rachel H. Rhodes, 2013) and Diana Vladimirova (Vladimirova, 2018), it had to be re-established following the move of February 2019. This opportunity was used to include a number of changes to the original setup as the new location allowed for a more compact setup. Additionally, the campaign of Dye 3 was intended to be a CFA campaign with gas measurements as the main focus. This allowed for implementing changes to the method of gas extraction intended to improve the gas recovery.

The first of these changes was an increased melt-rate to allow for a faster total flow and therefore also greater gas-flow, allowing for a quicker turn-over through the system.

The second change was amplifying the means of gas extraction. In the previous setup the main separation of gas from the liquid flow was done via a debubbler. A debubbler is a unit with a small volume connected to one inlet and two outlets, one at the bottom and one at the tube. Here the gas would gravitationally be separated from the main liquid flow by going towards the up-pointing outlet. The resulting gas flow was volumetrically still half liquid and half gas, and therefore needed further extraction. This was done through the use of a micromodule (MicroModule 0.5" × 1", G591, Membrana GmbH, Germany). The resulting gas stream contains no liquid water, but is still saturated in humidity, therefore requiring additional drying which was accomplished via a Nafion unit. This system allowed for measurements of methane on dry gas, but an unknown part of the sample was lost to the main liquid flow in the debubbler. For the purpose of establishing elemental ratios this can be accounted for via determining the size of this effect via standards, but for the purpose of measuring isotopic enrichment this posed a challenge as dissolution in liquid would lead to fractionation.

To improve this in the new setup, the main liquid flow was redirected along the gas path through a new micromodule (3M, Liqui-Cel MM-0.75X1 Series Membrane Contactor), which allowed for the gas extraction of both the air still in the form of bubbles and to an extent the air dissolved in the liquid.

The efficiency of this module and its dependence on gas pressure, flow rate temperature has been described in the thesis of Janani Venkatesh (Venkatesh, 2020), but the recovery degree was upwards of 90%, depending on the gas to liquid ratio.

The third upgrade was reducing the gas pressure at the dry-side of the micromodule, as that would result in a greater pressure gradient across the membrane. From this we expect an increased gas extraction efficiency.

Fourth was the incorporation of more sensors, tracking the liquid pressure and flow, as well as the temperature and gas flow. This allowed for better control of the setup, for the purpose of trouble shooting and determining the solubility effects as shall be described later.

With these improvements in mind I will account for the setup that was developed while going into detail regarding the used IRMS and oxygen removal method.

1.2.1 Mass spectrometer

Mass Spectrometry (henceforth MS) has been part of the ice-cores science from the beginning from Willi Dansgaard's initial measurements (Dansgaard, 2004). The underlying concept is to charge the incoming sample molecules either by giving them a negative or positive charge. The charged molecules are then passed through a magnetic field that can be controlled to guide certain mass to charge ratios (henceforth m/z) through to the detection, while the rest is deflected. Commonly faraday-cups are used for detection amplifying the signal generated by the charged ion. Common methods for this approach use quadrupoles MS, consisting of four poles maintaining a magnetic field between two pairs, allowing one specific m/z to pass through along the poles while any other ratio is deflected. The magnetic field can then be varied to scan over a range of ratios, though that comes at the price of only measuring one ratio at a time. A method that has been developed that allows for measuring all of m/z 's of interest at the same time is IRMS. This method applies a curved magnetic field that bends the charged sample stream. Depending on the m/z their trajectory gets bent to varying degrees with light molecules getting affected greatly while heavier molecules get their path bent to a smaller degree. This results in the charged molecules leaving the magnetic field in a gradient along m/z . Detection cups can then be installed in the paths of any m/z of interest. The different cups are then equipped with resistances chosen to amplify the data stream up to comparable levels.

With the cup configuration of the Thermo Delta V used in this campaign it was possible to measure m/z 28, 29, 30, 31, 32, 36, 40, 44, 45 and 46 continuously, allowing for measurement of the three main atmospheric components: N_2 , O_2 , Ar and also the isotopic masses for CO_2 . Despite being desirable for measuring argon isotopes the cup configuration unfortunately does allow for m/z 38.

The ionization makes use of electron impact ionization, with a high potential filament charging the molecules passing by.

Part of the benefit of the Thermo Delta V is the small sample volume required for measurements and during the campaign was run with a sample flow of 0.01ml/min.

While MS is a strong tool due to its selectivity for chosen m/z , the instruments tend to have a significant daily drift. The normal intended use is discrete samples, so in order to make sure that the effects of drift are known, a standard was measured immediately before and after every experimental run. To facilitate this, the instrument is equipped with a dual inlet system allowing for shifting between sample and a known standard that can be used for calibration and binding the drift.

1.2.2 CFA setup

The schematics of the CFA setup can be seen in Figure 6, with the entire gas analysis accounted for, while the chemical analysis is only referred to by name. Starting the walkthrough of the system from the melter in the top-right corner, we have the beginning of the CFA setup. Here the 1m ice sticks were placed on the melthead within the freezer. The melthead used in this experiment had a cross-section of 3.5cm*3.5cm with an inner cross-section of 2.6cm*2.6cm and maintained a temperature at 50°C, resulting in a meltspeed of 4-4.5 cm/min. On top of the ice a weight was added with a twofold purpose. As part of the melting is driven by the ice pressing into the melthead, the first purpose is to add mass to the ice even when most of it is already melted. The second purpose is to continuously measure the melt-rate as the weight is attached to an encoder. This measurement was vital for later assigning the measurement to depth.

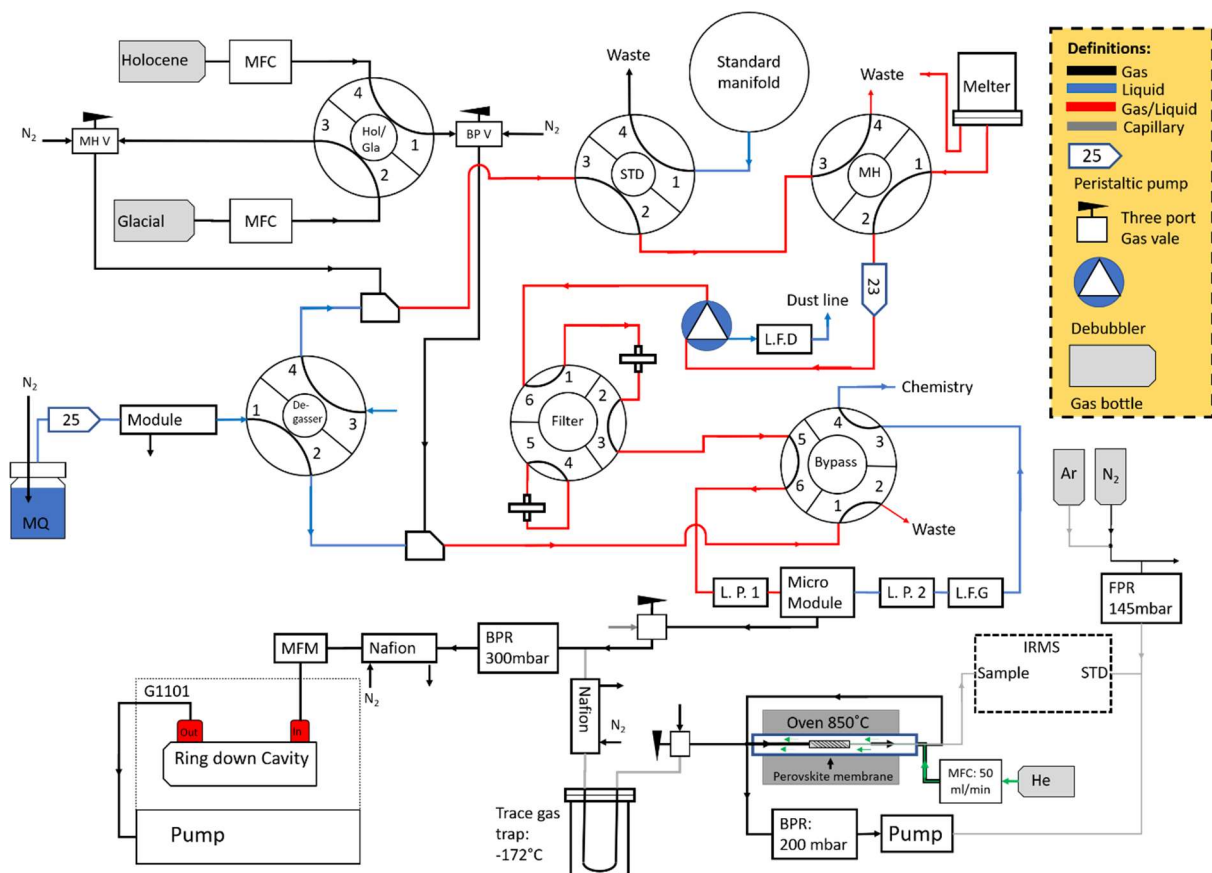


Figure 6: CFA setup with gas side focus. Shown is the vici valves that are controlled by the Labview script. BPR: back-pressure regulator, MFC: mass flow controller, FPR: forward-pressure regulator, L.P. Liquid pressure sensor, L.F. liquid flow meter. All liquid and gas/liquid tubes were 1/8" HPFA tubes, gas tubes (black) were either stainless steel or copper Swagelok tubing or capillaries with inner diameter 340µm.

With the ice melting a flow was generated of mixed air and liquid. This flow was separated as described earlier into the inner flow being directed for measurements and the outer flow discarded as contaminated waste. The inner flow was connected to the MH valve that was used to direct either sample or standard through the full extraction path. In the settings used in the figure the sample is directed towards peristaltic pump set to 23ml/min promoting the inner flow. From the peristaltic pump the sample is connected to a triangular debubbler. Here the majority of liquid flow and approximately the entire gas flow were directed towards the top exit, while a 3ml/min liquid flow was redirected for dust measurements. The flowrate for the dust line was measured by a liquid flowmeter (LS32-1500, Sensirion). The separation was necessary as the following sample treatment was passing the sample through a 20µm particle filter in order to remove particles from the dusty glacial ice. The

dust had to be removed to protect the micromodule used for gas extraction. Two dust filters were installed as loops on a six-port valve, in order to allow exchanging one while the other was in use. After the “filter”-valve, the sample was directed to the “bypass”-valve, where it would either be passed through the micromodule for gas extraction, or bypass it and go directly for chemical analysis. The gas extraction was done via a 0.75” X 1” membrane module, made up of closely-packed microporous, hydrophobic hollow fibre membranes oriented orthogonal to the flow direction (Venkatesh, 2020). By applying under pressure on the shellside of the membrane, gas is passed through the micropores, while the water is retained in the flow-path. Despite the depiction in the schedule the module was oriented vertically, as gas bubbles would tend to get stuck otherwise.

It should also be noted that the connections made to the module was non-conventional, as a Swagelok connection had to be glued to the gas side for a leak-tight connection, while 1/8” HPFA tubing was connected to the liquid inlet and outlet, held in place by a softer broader tubing.

Worth noticing are the two liquid pressure sensors (26PCBFG5G, Honeywell) placed on each side of the micromodule, monitoring the pressure drop associated with gas removal. The average liquid pressure was on the order of 1190mbar. Additionally, a second liquid flowmeter was installed that in combination with the dust flow meter allowed for measuring the total liquid flow. The “bypass”-valve was connected, so that it could switch between degassing the sample or run a readily mixed standard. That concludes it for the sample path. Following will be description of the standard introduction.

The methane standards are situated in the top-left corner and consisted of two bottles, “Holocene” and “Glacial”, mixed to resemble Holocene and glacial trace-gas levels. Both of these bottles were connected to mass-flow-controllers of the type GE50A MKS, connected to the valve named “Hol/Gla”. This valve controls which standard was passed through to the “MH” valve or the “Bypass” valve. The gas going either way would be introduced to a liquid flow through a T-piece, where the gas was introduced via a capillary inserted in line with the liquid flow. This created a segmented flow of bubbles in the liquid very similar to the flow observed for samples. The liquid flow for the standard was generated by a peristaltic pump supplying deionised water. This water was bubbled through by a flow of nitrogen in order to promote the removal of other gasses. The degassing of the water had already started 2.5 hours earlier at a degassing station. The water was further degassed by a module connected to a pump prior to combining with the standard gas.

The standard directed towards the “MH” valve would first pass through the “STD” valve that switched between the gas standards and a manifold with all the necessary liquid standards for chemical analysis calibration. By controlling the ratio between gas and liquid flow varying levels of total air content could be simulated, which would be necessary for the purpose of calibrating the effect of solubility.

All automatic valves, mass flow controllers and meters, back-pressure regulators and liquid pressure meters were either controlled or monitored by a single Labview program running on the computer also controlling the Picarro unit. This program provided a data sheet containing all the monitored data with a 1s frequency.

1.2.3 Gas extraction

For the purpose of discussing the treatment of the extracted gas sample, a zoom-in of this section can be seen in Figure 7. As described, the gas is extracted at the micromodule unit. The extraction is done by maintaining a pressure of 300mbar as controlled by a back-pressure regulator. The pumping for maintaining this pressure is supplied by the pump connected to Picarro G1101 unit. The micromodule is connected to a three-port, installed for the purpose of switching between lab-air or sample. Following the three-port valve the gas-stream is separated into a flow towards the Picarro for the purpose of CH₄ measurements, while a fraction of the main flow is directed towards the mass spectrometer. The connection towards the IRMS is through a capillary with inner diameter of 200µm

limiting the flow. As the pressure was kept regulated at both ends a stable flow of 0.15ml/min went for the IRMS, while the remaining flow went for the Picarro. The final point of interest regarding the Picarro pathway is the mass-flow meter installed in its path. This allowed for measuring the gas flow to the Picarro, which plus the 0.15ml/min accounted for the total gas volume extracted.

On the path from this separation to the MS inlet the sample goes through three sets of purifications. The first means of gas sample preparation is to remove the humidity in the sample stream. Though liquid water could not pass through the micromodule, vapor was still able, and therefore the gas was saturated with moisture. In order to remove it a 34cm Nafion, TT-030 from Perma Pure LLC, was installed, with a 50ml/min N₂ flow running counter to the sample flow. The Nafion is made of extremely hydrophilic material that allows the water molecules to bind to it and travel through it. By having dry gas running with high-flow on the other side of the membrane, the vapor pressure of the water will be kept low as it is continuously removed. With continuous removal on the other side, it will dry out the water from the sample side.

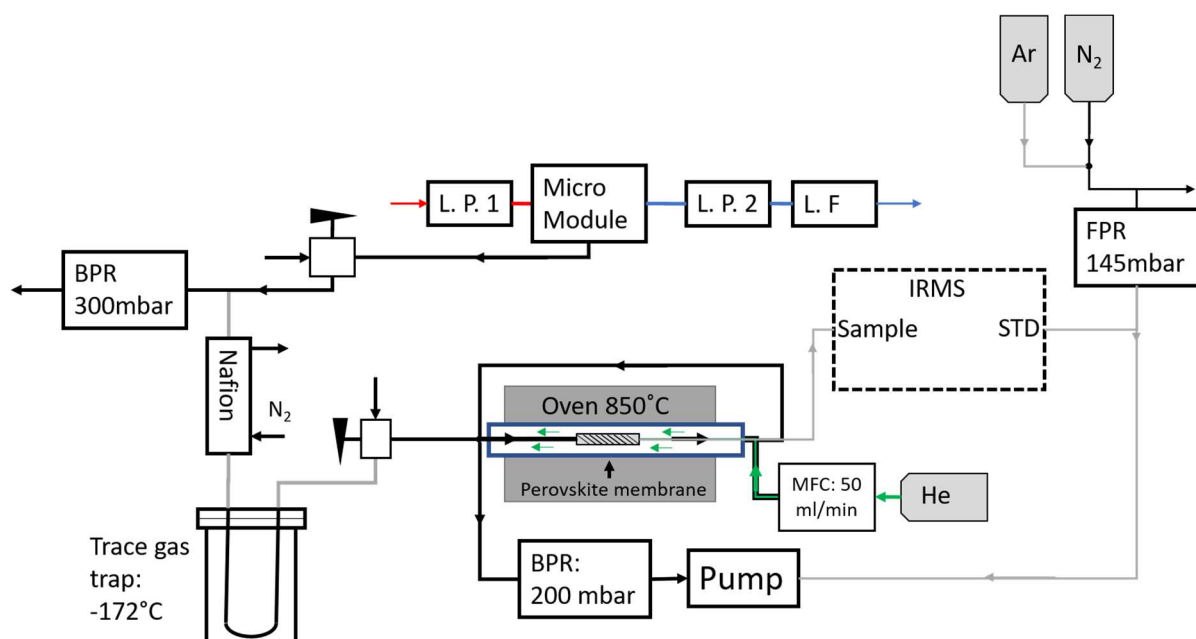


Figure 7: Zoom in on gas sample purification path way. Definitions are identical to previous figure. BPR: back-pressure regulator, MFC: mass flow controller, FPR: forward-pressure regulator, L.P. Liquid pressure sensor, L.F. liquid flow meter.

Following the Nafion a cold-trap was installed for the purpose of removing trace-gases such as CO₂ while also removing additional humidity making it through the Nafion. The cold trap was a 1/16" SS tube of 43.5cm lowered into a dewer filled with liquid nitrogen. Past the cold trap was a connection to another three port valve installed to switch between sample and lab-air. The purpose of which was to determine the combined fractionation effects of the nafion and cold trap.

The output from this valve was connected to the oxygen removal setup that stripped the oxygen content from the gas sample. At the point of entering the oxygen removal setup, all humidity and trace gas levels are expected to be reduced to their respective vapor pressure at -172°C. The oxygen removal setup and its motivation will be described more fully in the following chapter.

From the oxygen reduced sample, a small sample flow was collected by a capillary connected to the IRMS. The capillary had inner diameter of 100µm and a length 164cm. The first 15cm located inside the membrane, had been scorched by a lighter in order to remove the coating. That concludes the sample path, so attention should be drawn to the standard line for the IRMS.

Unlike for the methane setup no static gas was used for the IRMS standard, but was rather dynamically mixed from a flow of ~10ml/min N₂ with a flow of argon kept at around 0.127ml/min. The exact flow was installed so as to match the elemental ratio of lab-air. The combined flow of these two gases would go past a T-piece with the majority of the flow venting to the lab. The other exit of the T-piece was connected to a forward pressure regulator. From here the standard was connected to the IRMS's second inlet via a capillary in order to make use of the dual-inlet function. The forward pressure regulator was used to control the flow to the IRMS so that it was at comparable levels to those on the sample side. It was found that a pressure of 145mbar produces close to identical levels between the standard and lab-air. As a consequence of this pressure and dimensions of the capillary, the flow going through the standard capillary was only 0.01ml/min. This meant that the pumping of the IRMS would not supply sufficient pumping for the forward pressure regulator. For that purpose a second connection was made to the forward pressure regulator going to a pump. The standard could be varied by changing the forward pressure setting or by varying the argon abundance. The idea was that the effect of these changes could always be established by comparing with lab-air that went through the system from the sample side.

1.2.4 Oxygen removal

With the use of the Nafion and the cold trap the majority of trace-gasses should have been removed leaving a gas stream consisting almost exclusively of N₂, O₂, Ar. At this stage we were left with a choice on how to progress. It was desirable to remove O₂ from the sample due to the clumped isotope ¹⁸O₂ overlapping with ³⁶Ar. The atmospheric abundance of oxygen at 20.8% with an isotopic abundance of 0.2% for ¹⁸O would lead to an air abundance of clumped ¹⁸O₂ to be 0.83ppmv compared to the expected 5.88ppmv of ³⁶Ar based on argon abundance of 0.934% and isotopic abundance of ³⁶Ar at 0.063%. The signal of clumped ¹⁸O₂ would result in a 14% higher signal for m/z 36, which is a substantial offset if we desire to measure in the ‰ range. While this effect can be removed to a certain degree by also measuring m/z 32 and extrapolating the expected effect on m/z 36 from the oxygen abundance, variation caused by thermal and gravitational effects will be near impossible to correct for. Part of the reason for this is that the gravitational enrichment of δ¹⁸O₂ will counteract the observed gravitational enrichment of δ⁴⁰Ar, as the m/z 36 is also increased. Based on this relationship a gravitational increase of 1.0‰ would result in a measured increase of only 0.88‰ due to a 124 per meg offset. Such a difference could result in wrongly attributing the observed increases to thermal fractionation rather than gravitational as the ¹⁵N and ⁴⁰Ar response appear to scale nonlinearly. To reduce the effect of oxygen it was deemed necessary to remove it from the sample stream. A removal of 95% of oxygen would reduce the effect to an offset of 7per meg, which would be well below the expected uncertainty of the setup.

The approach for removing O₂ from the sample stream made use of a similar method to that of the Nafion. The sample would flow through a membrane tube selective for oxygen, with a counterflow of helium on the outside. This would allow the oxygen to travel through the membrane and be carried away by the flow of helium. The membrane chosen was a tubular perovskite membrane, from Fraunhofer-Institute for Interfacial Engineering and Biotechnology Inorganic Surfaces and Membranes (Germany). The ceramic membrane had an outer diameter of 1.15mm with an inner diameter in the range of 0.80-0.88mm, and functions as a physical barrier for most gasses. However, it allows diffusion of oxygen through, though the permeability is highly dependent on temperature, necessitating temperatures above 600°C before any oxygen diffusion was observed. As the permeation is based on diffusion it is driven by the difference in partial pressure on each side of the membrane, which is why the counter flow of helium is applied to keep the pressure of oxygen on the other side close to zero.

The membranes had previously been acquired for the purpose of extracting and purifying O₂ for ¹⁷O measurements (Reutenauer, 2016), but due to oxygen being left in the membrane between runs, the project was abandoned. For the purpose of removing O₂ the membrane proved useful however. From initial testing it was found that the permeability increased with temperature, and a working temperature at 850 °C was decided upon based on the limitations of the oven and the diminishing returns at increased temperature.

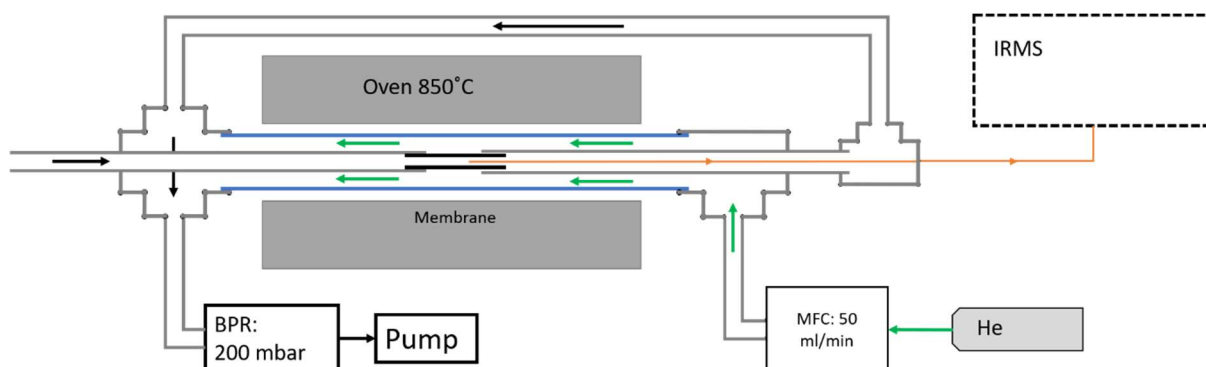


Figure 8: Oven and membrane setup: The thick blue lines represents the quartz tube containing the 2mm SS-tube and the membrane, represented by the thick black lines. The thin orange line connecting to the IRMS from the middle of the membrane is the capillary through which the sample is drawn. The green arrows indicate the flow of helium passing between the SS- and quartz tube. The black arrows indicate the sample flow.

A zoom on the oven setup can be seen in Figure 8. A 12 cm membrane piece was installed between a 2mm SS tube of length 40cm and an 1/8" SS-tube of identical length and the combined setup was inserted into a 6mm quartz glass tube with an inner diameter of 3mm. The connection around the quartz tube was made with two 6mm ultra-torr to 1/4" union fittings. With the SS-tubes inserted in the glass and kept in place by the ultra-torr fittings, the connection would be inserted into the cylindrical oven, after which connections would be made from the ultra-torr fittings to a 1/4" cross for the 2mm SS tube and t-piece for the 1/8" SS tube. The two SS-tubes were small enough to fit through both of these pieces, which allowed for having a sample volume that was separated from the quartz-tube volume. The inlet end of the 2mm SS tube was connected to the aforementioned three-port valve and sample pathway.

The end of the 1/8" SS-tube was connected to one of the "arms" of a 1/8" T-piece. This allowed for inserting a capillary through the opposite "arm" that could then go all the way through the SS-tube into the membrane. This capillary, with an inner diameter of 100µm and a length of 168cm, was left open in the membrane in order to suck in a fraction of the oxygen depleted sample to the IRMS, which it was connected to at one of the dual inlets. The small flow generated by the pumping from the IRMS would only amount to 0.01ml/min, so in order to help promote sample flow, the excess sample gas would be pumped down to a pressure of 200mbar, through a connection from the 1/8" T-piece to the 1/4" cross piece, that was then further connected to a BPR followed by a pump. This BPR would control the pressure of both the sample and the helium flow that was connected via the 1/4" t-piece. The helium flow was introduced by the 1/4" T-piece connected to the 1/8" tubing, and was controlled by a mass-flow controller which was set to 50ml/min for initial experiments but was increased to 70ml/min for the campaign. Increased oxygen removal was observed with increased helium flow, but from 50-70ml/min the effect was minor.

Incorporating this membrane posed some challenges as the membrane did not lend itself easily to be installed in a leak-free manner. The dimensions of it did not fit with any available tubing, so in order to connect it, the inner diameter at the end of 2mm SS-tube was increased in order to fit the membrane inside. While this allowed for connecting the membrane, the connection was still open to

exchange between inside and out. In order to seal this hole a gold-paste, C5754 B from Heraeus, was applied between the membrane and SS-tube. The seal was given a slow heating up to 500°C over the period of three hours, during which the paste would dry and seal around the connection. The reason for choosing this sealant was its heat-resistance, which would be vital at the 850 °C, which the setup would be running with. A lot of attempts were made at sealing the membrane in both ends, by inserting it into another drilled out 2mm SS-tube. This proved an insurmountable task with the tools at hand, as the membrane was too brittle to be locked in place between two SS-tubes. Attempts at steadying the alignment by installing triangular “legs” for the two steel tubes were not sufficient. A break could unfortunately first be confirmed following the installation once the system was running.

Following multiple failed attempts and wasted broken membranes, a less rigid method of connection was attempted, which came at the cost of the membrane connection no longer being leak-tight. The membrane would still be inserted and sealed 0.5cm into the 2mm SS-tube, while the outlet of the membrane would be inserted into the 1/8” SS-tube but not be sealed. The depth of this insertion was increased to approximately 5cm to minimize the flow of helium going past the SS-tube and the membrane into the sample stream. This left roughly 6cm of exposed membrane between the two SS tubes. From the testing done, this fortunately proved to be sufficient as the resulting removal degree was found to be around 98.5% for oxygen.

While the masses of interest are limited to 28, 29, 36 and 40, being able to monitor the O₂ and CO₂ abundance proved to be useful for trouble-shooting, as the final system should remove both of those gases. Increased levels for either of those gasses would indicate that the removal methods are failing or a leak has occurred.

1.2.5 Running the system

The melting campaign was completed over the course of 7 work days, 30th and 31st of October including the 4th, 5th, 6th and 7th of November 2019. The daily measurements consisted on average of 18 ice core bags split over two runs.

Running the system was a full day team-project. The first task of the day was the all-important cutting and logging of the 1m ice sticks which was done in the freezer located next to the laboratory. This included cutting the cross-section of the ice so that it would fit in the melt-head frame of 3.5cm*3.5cm, but also flatten any breaks so that all the pieces would fit together smoothly, not allowing air pockets in-between. The logging of the ice consisted in writing down the length of each core, as well the depth of any break or missing pieces, and account for the ice removed when smoothing breaks. All this was essential for recreating the age scale based on the depth measurements. The ice-cutting needed to be ahead by a few cores, as the ice needed to come continuously once measurements had begun. During the ice-cutting samples were taken for discreet measurements of gas isotopes

While the ice cutting was taking place, the CFA system was started up. This meant installing mQ-water that had been debubbling with N₂ overnight, and start running it through the system by starting the peristaltic pumps. For the IRMS setup it meant turning the heat of the oven up from 600°C to the operational 850°C, increasing the helium flow to the running level, and fill the cold trap with liquid nitrogen.

Initially the chemical standards would run in the liquid tubes allowing for doing a calibration run with the IRMS, by turning the three-port valve from micromodule connection to lab-air connection. A calibration run consisted of running the IRMS in dual-inlet mode, switching between lab-air and the

mixed standard 5 times. From this the enrichment value of the standard when compared to the lab-air was established.

Once the IRMS calibration run was completed and the chemical standards were done, the Holocene standard was introduced to the mQ-flow and the methane calibration could begin by turning the three-port valve back to the micromodule. The standard would be given time to get 15 minutes of stable readings, which normally required 25min total. After the Holocene standard was done, the glacial was introduced in a similar way and left to run until a stable level had been reached for methane. At this point the ice-cutting would be far enough ahead, that the measurements could begin. While the remaining 2 minutes of glacial standard was still running, the first ice-stick would be loaded in the melter. The first ice placed would come with a 7cm block of mQ-ice below it, to start the flow through the system and to have a clear transition to sample. Once the ice was placed in the frame and loaded with the encoder connected weight on top, the "MH" valve would change from standard to sample. Measurements would then begin by heating up the melthead to 50°C leading to a melt-rate of roughly 4cm/min while starting the peristaltic pump with a set-point of 23ml/min. This value was however not reached for the total flow due to restrictions in the flow-path, and was more commonly around 19ml/min.

The IRMS would start measurements at the core being loaded by initially measuring the back-ground level noise for each cup for 30s, before opening up for the standard inlet for 120s. After this it would switch to the sample inlet, where it would sample on the gas there. Normally the first gas measured would be the remaining gas from glacial methane standard, which marked itself by not having any argon. This would last until the melting went past 7cm mQ-ice, as the near zero gas content of the mQ-ice meant no exchange of the gas in the dead-volume between the micromodule and the back-pressure regulator. Once gas sample started arriving at the micromodule this would be detected by a spike in pressure, as the back-pressure regulator started to re-establish stability at 300mbar. Due to the methane standards not having argon, it took 5 minutes before the effect of residual mixing was no longer present, and true sample signal was being measured.

New ice-sticks would be installed whenever the currently melting ice-stick reached 20cm of remaining height. This would cause a short discontinuity of the encoder data, as the weight had to be lifted and placed on top of the new ice. With the melting going on by itself the system only required noting down, whenever breaks were coming up or new ice sticks were installed, so as to match resulting data spikes.

A normal run would take 9 or 10 ice-sticks and last around 3.5 hours, with the final ice-stick coming with 2* 7cm mQ-ice blocks on top to ensure all the sample is passed through the system. After a normal run was over the IRMS would switch to standard inlet again until turned off.

After the completion of a run, the ice-cutting team needed time to get ahead again, which meant that there was time for a second calibration run for the methane and chemistry measurements. For the 31st and 4th this afternoon pause in between runs was unfortunately not utilized for IRMS calibration, but in the later days was used to get a midday calibration run.

Once ice was prepared and calibration schemes were complete the day's second run began, running identically to the first.

After the second run an additional calibration session for chemistry, methane and IRMS would be done, before shutting down the lab for the day.

1.3 Data treatment

Due to the complicated nature of the setup relying on 3 steps of sample preparation, prior the gas extraction from the melt-stream and 4 steps of sample treatment before entering the IRMS, deconvoluting the resulting measurements pose a challenge. For each of the sample preparation steps potential fractionation effects need to be considered:

1. The first potential effect occurred at the melthead. As was mentioned, the campaign made use of a higher melt-rate than previously used at 4cm/min, nearly double the earlier rates, but the resulting liquid and gas flow did not scale accordingly. With the declared melt-rate at a melt-head with an inner surface area of $2.6 \times 2.6 \text{ cm}^2$, we would expect a combined output flow of 27ml/min, but ended on average at 18ml/min. The discrepancy is explained by the missing melt water and gas going to waste with the outer layer of the ice core. By using the measured and liquid gas flow, a general gas ratio (G%) could be found for the sample stream, and was calculated as the flow of gas divided by the total liquid flow plus the gas flow. On average this was found to be around $75 \text{ ml}_{\text{gas}}/\text{ml}_{\text{tot}}$. While being similar this value is not the same as the total air content (henceforth TAC), as that is defined as gas volume per mass of ice, and G% is a volume by volume unit. Calculating TAC directly from the flow measurements, it is found to be around $84 \text{ ml}/\text{kg}_{\text{ice}}$. This was lower than the expected $90\text{-}100 \text{ ml}/\text{kg}_{\text{ice}}$, which suggests a loss. The most preferable type of loss would be gas being dissolved but not extracted, as this effect can be accounted for by solubility correction shown later. Another more problematic reason is that gas is preferentially lost to the waste line or bubbling to the side of the melthead. This loss has a chance of introducing isotopic fractionation effects, though we assess these effects to be minor. Our argument for this is that the mechanism for gas-loss at the MH is almost exclusively in the form of newly formed air-bubbles. As there had been little time for the gas to equilibrate with the liquid, it is assumed that the gas loss does not result in fractionation for the remaining gas. While the preferential gas loss might not lead to detectable fractionation an unfortunate consequence of it is that the total air content cannot be determined accurately, though trends can still be observed.
2. The next step of sample preparation is at the de-bubbler where the gas/liquid sample stream is separated gravitationally, with the major flow containing the air-bubbles going through the top outlet and a sub-flow of $\sim 3 \text{ ml}/\text{min}$ liquid flow goes towards analysis for dust content. The sample reaches this point after 12-15s of travel time, during which the gas had time to start equilibrating with the liquid phase. That means that while all the bubbles were confirmed to flow in the proper direction a small amount of dissolved gas is lost to the dust-line. As this loss is based on solubility of the gases, a fractionation effect will take place here, promoting the loss of heavier molecules due to their higher solubility. This effect is, as for the melthead, assumed to be minor, as the short travel-time combined with the small interface area between gas and liquid does not facilitate the expected equilibrium degree to be reached.
3. The third point of sample preparation is the gas extraction occurring at the micro module. Here, the gas and liquid stream pass through the module where thousands of hydrophobic tubes run orthogonal to the sample stream, allowing the gas to pass through into the shell volume of the micromodule. To promote this transition the pressure at the micromodule is pumped down to 300mbar, where it is maintained by the BPR. The solubility effect is at this point necessary to consider, as the gas and liquid has had a longer time to interact (30-40seconds depending on flowrate). Furthermore, the design of the micromodule means that there is a very large surface area for interaction between the liquid and gas. While this is

desirable approaching complete extraction that relies on providing as close to vacuum on the shell-side as possible, which is far from the case at 300mbar. It is therefore feared that the gas extracted from the air bubbles, will be dissolved to a small degree in the liquid flow. This effect would again promote fractionation, most significantly for the elemental ratios as the difference in molecular solubility is much greater than for isotopic solubility. While it could be argued that an easy fix for this would be to reduce the pressure further, this proved less than ideal as the flow for the IRMS was maintained by the pressure difference between the pressure at the micromodule and the 200mbar maintained at the oven. A compromise had to be reached between selecting as small a pressure as possible to promote extraction, while at the same time maintain sufficient pressure to facilitate a reasonable flow through the setup. For this the 300mbar was selected as an acceptable compromise. The size of the fractionation resulting from solubility was tested in experiments described in one of the later chapters on calibration schemes.

This concludes the interaction between the water and gas and the remaining steps seek to explain the effect varying the gas-sample treatment. In order to understand the following effects a three-way valve was installed that allowed for switching between the sample and lab-air for providing the pressure at the BPR.

4. Following the extraction at the micromodule, the gas flow is split with the main flow going through the BPC towards the Picarro G1301-I for methane analysis, while a flow of 0.15ml/min is going through the remaining sample preparation steps for the IRMS. This splitting of flows can promote a fractionation as well due to the diffusion, as the flow towards the IRMS is going through a capillary with a rather small difference in pressure difference in the end to promote the flow. While this effect should be accounted for by running lab-air through the system, the lab-air introduced at the three-port valve was also administered through a capillary, which would potentially suffer from the same issue. That effect is expected to be negligible as the flow through the lab-air capillary was 20 times larger at 2.6ml/min. But as it was never properly investigated there is a risk that it led to a constant fractionation. The only way to completely rule out those effects would be to run lab-air through the entire system including the micro-module which unfortunately was never done.
5. After the split the sample travels through the capillary to the Nafion. Due to the high selectivity of the Nafion, it is not expected that any gasses of interest were lost, and the sample should therefore not be fractionated. No tests were conducted to test this however.
6. Next in line was the cold trace-gas trap, which did not result in any fractionations. The only effect observed on masses of interest was the immediate drop associated with loading the trap due to sudden pressure drop. This would limit the flow through the system for a short while before a new pressure gradient was established across the setup.
7. The final step of the sample collection was the oxygen removal setup. No effect was expected for this step, as the membrane was reportedly very selective with permeability, and should therefore not affect the nitrogen and argon ratios. In order to assess any effect, we investigated for changes in $\delta^{15}\text{N}$ and $\delta^{40}\text{N}$ when turning on the helium flow, before the oven was turned on. Here an immediate drop in all m/z was observed, due to helium travelling past the unsealed connection around the membrane and into the sample side. After the pressure had been re-established at 200mbar thanks to the BPR, the intensity of m/z would return again. The ratios fortunately did not get enriched or depleted following this. With increased temperature a drop was observed for all masses, though in a proportional manner that did not affect the enrichment to a noticeable degree, though it deserves further investigation. The cause of this effect is the reduced gas concentration arising from maintaining a constant

pressure at increased temperature, as described by the ideal gas law. Running with operating temperature and helium flow mass 32 was removed as intended and the remaining masses increased in signal by roughly 20%. This was to be expected as the remaining gasses would make out a bigger part of the sample flow following the removal of oxygen.

From the treatment of the gas following the extraction, the only potential effect of fractionation not accounted for by running lab-air through the system would be the fractionation described in point 4, which is expected to be minor.

Across the system the biggest source of fractionation was expected to be the solubility and the IRMS itself, as shall be described in the following chapter. A final point of note regarding the setup is that the used lab-air as the final standard to which the dynamically mixed standard (henceforth D.M.STD) should be bound. This decision was based on the assumption that it would have close to constant composition. But that failed to account for the conditions of the laboratory that had poor ventilation, resulting in insufficient air exchange. That meant that the large amount of N₂ introduced from both the gas bottle and the liquid nitrogen shifted the isotopic composition of the air between the days.

1.3.1 Calibration scheme

When applying the corrections for the measurements it is important to apply them in the right order. For the IRMS it meant working backwards from the instrumental effects back to the gas extraction. All of the following calculations were done in a Matlab script that can be seen in appendix (1.2-1.4), where the data from the IRMS along with the depth, methane and Labview data were combined.

The Isodat software that works as the interface between the user and the IRMS, comes with correction and calibration protocols, that for discrete samples would apply the corrections. It is not equipped to correct for continuous measurements, such as was done in this project, and for that reason the corrections have to be applied manually.

The data from the IRMS comes in the form of intensity mV for each cup. The intensity of this signal scales with the amount of charged ions entering the cup, but due to the nature of uncertainty there is a background level of signal that needs to be accounted for in the data processing. Experimentally, this was done by starting each run, with the inlets for the IRMS closed in effect measuring on the vacuum provided by the built-in pump. This allowed for determining the value of the background level that would have to be subtracted from the sample intensities.

$$I_{bc} = I_{mea} - I_{bg} \quad (12)$$

In the equation above I refers to the signal intensity, with definition of the subscripts, bc : background corrected, mea : measured, bg : average background. Having corrected the intensities, it is then possible to use the intensities to determine the ratio between the isotopes using:

$$r_{29} = \frac{int_{bc}(29)}{int_{bc}(28)} \quad (13) \quad r_{36} = \frac{int_{bc}(36)}{int_{bc}(40)} \quad (14) \quad r_{\frac{Ar}{N_2}} = \frac{int_{bc}(40)}{int_{bc}(28)} \quad (15)$$

Here r is the ratio between the background corrected intensities for the respective masses. It should be noted that these intensity ratios are not equal to the elemental or isotopic ratios, as the measured signal has been amplified differently for each cup. In order to scale them it was necessary to compare the ratios to measured ratios of know gas compositions. For this purpose, the use of delta notation is suitable, and will make use of the definition in equation 1.

$$\partial^{15}N = \left(\frac{r_{29}}{r_{29STD}} - 1 \right) \quad (16) \quad \partial^{36}Ar = \left(\frac{r_{36}}{r_{36STD}} - 1 \right) \quad (17) \quad \partial \frac{Ar}{N_2} = \left(\frac{\frac{r_{Ar}}{N_2}}{\frac{r_{Ar}}{N_2}STD} - 1 \right) \quad (18)$$

Equation 16-18 show the equations used to find the enrichment in relation to the standard ratio. While r_{xSTD} was intended to be the ratio of the D.M.STD, we decided to opt for using the average r_{29} , r_{36} and r_{Ar/N_2} of the lab-air measured in the morning and evening calibration run instead. The reason for this was that the lab-air as mentioned was less stable than expected, so binding the D.M.STD to a lab-air ratio that had to be corrected for the daily variation would be double work compared to binding the measurements directly to the daily lab-air measurements. By doing this, we are admittedly making the mistake of assuming that the lab-air has a constant composition, which we know not to be the case. Unfortunately, D.M.STD was also not constant across the campaign. The found daily average ratios can be found in Table 2.

A detail to make note of is that equation 14 and 17, shows the ratio of 36/40 rather than the 40/36 that will later be used. The reason for this is that initially ratio 36/40 was used when the calibration scheme was developed. When the data is presented, after the completion of the data treatment it will be converted to the proper ratio 40/36 as:

$$\partial^{40}Ar = \left(\frac{1}{\partial^{36}Ar+1} - 1 \right) \quad (19)$$

While the measurement of the D.M.STD was no longer used for binding the data to a scale, the measurement of D.M.STD before and after each experimental run was used for determining the drift across the run. Surprisingly the drift was within the uncertainty of the measurements for most days and no correction needed to be applied. The exception was for the 4th of November where the argon supply had accidentally been turned off for the D.M.STD. causing a drop in intensity of m/z 36 and 40. When the flow of argon was re-established in D.M.STD it led to a delayed increase of m/z 40 when compared to m/z36 for the standard and the sample side as well. The exact way that the D.M.STD would affect the sample side is still unknown, but the resulting drift was corrected by:

$$I_{dc}40 = I_{bc}40 - \frac{1}{Dr \cdot (t - t_0)} \quad (20)$$

Where $I_{dc}40$ is the drift corrected intensity of m/z 40 and $I_{bc}40$ is the background corrected value found in eq. 12. Dr is a fitted drift factor based on the measurement of the pre and post experiment D.M.STD measurements. t is the time and the t_0 is the time where the correction was applied. Due to attempts to re-establish the proper elemental ratio in the D.M.STD in between the morning and afternoon run, a second drift effect unfortunately also affected the afternoon run. This led to two values for Dr at two different t_0 seen in Table 1.

Table 1: Drift correction value for int40 with drift origin time t .

Dr (mV/day)	t_0 (hh:mm:ss)
-0.456	11:00:30
-1.00	16:57:03

While the intensities of the measured masses scale with the number of incoming charged molecules, it does not scale linearly, nor equally across different chemical species. These issues manifest in two effects, termed pressure imbalance (MICHAEL L. BENDER, 1994) and chemical slope effect.

The pressure imbalance effect is the non-linearity effect for the individual masses and can be determined by running the system with different inlet pressures, to allow for different flows of sample. Experimentally this was done in dual-inlet mode switching between lab-air passing through normally running gas-treatment setup to the D.M.STD that was maintained at different pressures via the FPR. This resulted in different levels of signal intensity for the standard that could be compared to the

constant lab-air. Here linear scaling of signal intensity would result in constant isotopic ratio, but this was not observed to be the case, as varying levels of enrichment for ^{15}N and ^{36}Ar were observed.

This effect could be linearly fitted by plotting the resulting enrichment of ^{15}N and ^{36}Ar against the offset of the measured intensity of the parent isotope (^{14}N and ^{40}Ar) between the standard and the lab-air. The resulting fractionation termed δ_{Px} , with x being either 29, 36, or Ar/N₂ got defined as:

$$\delta_{P_{29}}(I_{bc}(28)) = P_{29} * (I_{bc}(28) - 10500mV) \quad (21)$$

$$\delta_{P_{36}}(I_{bc}(40)) = P_{36} * (I_{bc}(40) - 8900mV) \quad (22)$$

$$\delta_{\frac{P_{Ar}}{N_2}}(I_{bc}(28)) = \frac{P_{Ar}}{N_2} * (I_{bc}(28) - 10500mV) \quad (23)$$

Where δ_{Px} is the resulting offset of the delta value for mass x in ‰, and Px being the pressure imbalance factor for mass ratio x in units ‰/mV. The values of 10500mV and 8900mV subtracted from the $I_{bc}(28)$ and $I_{bc}(40)$ values were chosen as rounded-off averages for lab-air intensities. The closer the intensity is to that of lab-air the smaller resulting offset in delta value would be observed. The pressure imbalance dependence was established by doing multiple measurements of the standard gas at different pressures, and comparing the gathered delta values when compared to the lab-air that was coming at a constant pressure of 200mbar. The resulting fits can be seen in the appendix 1.5. The pressure imbalance effect can then be corrected by subtracting the pressure imbalance fractionation from the measured delta value:

$$\partial^{29}N_{2P.cor} = \partial^{15}N - \delta_{P_{29}}(I_{bc}(28)) \quad \left[P_{29} = 1.05 \pm 0.21 \cdot 10^{-4} \frac{\text{‰}}{mV} \right] \quad (24)$$

$$\partial^{36}Ar_{P.cor} = \partial^{36}Ar - \delta_{P_{36}}(I_{bc}(40)) \quad \left[P_{36} = 6.76 \pm 0.16 \cdot 10^{-4} \frac{\text{‰}}{mV} \right] \quad (25)$$

$$\partial \frac{Ar}{N_{2MS.cor}} = \partial \frac{Ar}{N_2} - \delta_{\frac{P_{Ar}}{N_2}}(I_{bc}(28)) \quad \left[P_{Ar/N_2} = 5.59 \pm 0.55 \cdot 10^{-4} \frac{\text{‰}}{mV} \right] \quad (26)$$

Following the application of the pressure imbalance correction the effects of chemical slope can be corrected. The chemical slope reflects the readiness of different chemical species towards becoming charged. The chemical slope effect can be characterized, by varying the elemental ratio and observing the resulting fractionation. This was done experimentally by changing the amount of argon added to the D.M.STD, by controlling the pressure of the argon supply. The resulting Ar/N₂ levels spanned ratios from 50%-200% of atmospheric levels. The fitting can be found in the appendix 1.6. It should be noted that the data used for finding the chemical slope had been corrected for the pressure imbalance first, as that effect would also come into play with the resulting increases intensity 40. The effect on isotopes was expressed as a function of the pressure imbalance corrected elemental ratio enrichment.

$$\delta_{C_{29}}\left(\partial \frac{Ar}{N_{2MS.cor}}\right) = a_{29} \cdot \partial \frac{Ar}{N_{2MS.cor}} \quad \left[a_{29} = 4.97 \pm 0.3 \cdot 10^{-5} \frac{\text{‰}}{\text{‰}} \right] \quad (27)$$

The chemical slope effect was minor for $\delta^{15}\text{N}$ which would be expected as the variation in the elemental ratio would not cause a large variation in the nitrogen abundance. The effect was found to follow a linear trend with the elemental ratio $\delta\text{Ar}/\text{N}_2$.

$$\delta_{C_{36}}\left(\partial \frac{Ar}{N_{2MS.cor}}\right) = b_{36} \cdot \left(\partial \frac{Ar}{N_{2MS.cor}}\right)^2 + a_{36} \cdot \partial \frac{Ar}{N_{2MS.cor}} \quad \left[a_{36} = 1.78 \pm 0.05 \cdot 10^{-2} \frac{\text{‰}}{\text{‰}} \right] \quad (28)$$

$$\left[b_{36} = 9.59 \pm 1.4 \cdot 10^{-6} \frac{\text{‰}}{\text{‰}^2} \right]$$

The effects on the argon isotope were more pronounced and could be fitted well by a second order polynomial in the tested range.

The two effects can then be applied to the isotopic delta values accordingly.

$$\partial^{29}N_{MS.cor} = \partial^{29}N_{P.cor} - \delta_{C2} \left(\partial \frac{Ar}{N_2}_{MS.cor} \right) \quad (29)$$

$$\partial^{36}Ar_{MS.cor} = \partial^{36}Ar_{P.cor} - \delta_{C36} \left(\partial \frac{Ar}{N_2}_{MS.cor} \right) \quad (30)$$

After the instrumental corrections for back ground signal, pressure imbalance and chemical slope, had been applied to generate the $\partial x_{MS.cor}$ values, it was necessary to correct for the effect of the daily variation in lab-air ratios. By accounting for the daily variation observed between lab-air measurements, it was possible to bind down the values to a constant scale.

Table 2: overview of the average measurements of daily air ratios and their resulting delta values in relation to their internal average. For the fifth two averages were generated, one for the morning run * and one for the afternoon run **.

Date	Daily ratio			Daily offset (‰)			Uncertainty (‰)		
	r ₂₉	r ₃₆	r _{Ar/N₂}	δ ²⁹ N	δ ³⁶ Ar	δAr/N ₂	δ ²⁹ N	δ ³⁶ Ar	δAr/N ₂
31-Oct	0.740291	0.321742	0.846356	-0.007	0.95	2.57	0.007	0.06	0.2
04-Nov	0.740093	0.323380	0.832760	-0.023	7.53	-12.21	0.015	0.14	0.4
05-Nov*	0.740174	0.320725	0.841558	0.114	-0.65	-1.63	0.013	0.12	0.3
05-Nov**	0.740117	0.320564	0.841625	0.020	-1.24	-1.63	0.012	0.11	0.2
06-Nov	0.740061	0.320241	0.843527	-0.072	-2.35	0.54	0.011	0.09	0.2
07-Nov	0.740007	0.319905	0.844153	-0.031	-3.07	1.35	0.006	0.09	0.2

As can be seen in Table 2, the ratios for the different days do differ, as reflected by the associated daily delta values. The delta values were generated by the same data treatment described above, with the change that the r_x used in eq. 16-18 was the daily ratio, while the r_{xSTD} was the average ratio across the days. The resulting delta values span 0.18‰ for δ²⁹N. With expected values of δ²⁹N in the sample ranging of 0.3-0.5‰ this offset is substantial and needs to be accounted for. For δ³⁶Ar and δAr/N₂ the situation was even more severe with greatest offset seen for the 4th. The daily offset is accounted for in the manner shown below.

$$\partial^{29}N_{air.cor} = ((\partial^{29}N_{MS.cor} + 1) * (\partial^{29}N_{D.air} + 1) - 1) \quad (31)$$

$$\partial^{36}Ar_{air.cor} = ((\partial^{36}Ar_{MS.cor} + 1) * (\partial^{36}Ar_{D.air} + 1) - 1) \quad (32)$$

$$\partial \frac{Ar}{N_2}_{air.cor} = \left(\left(\partial \frac{Ar}{N_2}_{MS.cor} + 1 \right) * \left(\partial \frac{Ar}{N_2}_{D.air} + 1 \right) - 1 \right) \quad (33)$$

Where δ_{x_{air.cor}} was the sample offset from the average air ratio, and δ_{x_{D.air}} was the daily offset for lab-air. Caution should be used when applying these equations as the delta values are in ‰, so as an example the value of δ³⁶Ar_{D,Air} for the 4th would be 0.00753 when used in the equation.

While the binding of the delta values to a local constant scale ought to be the last correction applied, the lab-air used for comparison was introduced right after the point of extraction. For that reason, the daily lab-air can only be used to correct for the effects affecting the measurements from its point of entry till the IRMS. The last effect that could be corrected for is the solubility effect that will be described in the chapter below.

1.3.2 Solubility effect

As discussed in the experimental section, the extraction of gas from the liquid stream happened via the micro module where the pressure at the liquid side of roughly 1190mbar would drive the gas to the shell-side of the module kept at 300mbar. It should be realized that the extraction will not be complete, as the best-case situation being a pressure equilibrium between the two sides of the module, would still leave gas dissolved. It is, however, unlikely that an equilibrium has been reached, and it should rather be considered at a steady state. Whether the resulting steady state will result in more or less gas lost than expected from the equilibrium, will depend on the level of equilibrium reached before the micromodule. For the purpose of discussing this equilibrium I will use the common description of equilibrium between a dissolved gas and its gaseous phase, Henry's law constant (John H. Seinfeld, 2006).

$$H_x = \frac{[x]}{P_x} \quad (34)$$

Henry's law constant (M/atm) is the equilibrium constant between the concentration of dissolved species $[x]$ and its partial pressure P_x . Like all equilibrium constants Henry's law constant is temperature dependent, and its dependence on temperature can be described as:

$$\ln(H_x) = A_x + \frac{B_x}{T} + C_x \cdot \ln(T) \quad (35)$$

With A, B and C being gas specific constants and T being the temperature in kelvin.

Table 3: Overview of N_2 , O_2 and Argons constants for solubility in water for use in eq. 35. (NASA, 2011)

Gas	A	B (K)	C	H(298K) [M/atm]
N₂	-177.1	8640	24.71	6.62E-4
O₂	-161.6	8160	22.39	1.30E-3
Ar	-11.605	1500	0	1.42E-3

From Table 3 the cause for concern can be seen, as N_2 is only half as soluble in water as oxygen and argon. That will lead to depletion in the elemental ratio Ar/ N_2 , as the loss to the liquid will be relatively bigger for Ar than for N_2 .

In order to determine these effects initial experiments investigating the gas loss was performed by Janani Venkatesh, where different flows of the N₂ ranging 1.25ml/min-3.75ml/min was added to varying values of liquid flow in 0.25ml/min steps. This was done for multiple levels of pressure at the BPR to also determine the effect of the pressure at the micro module. From the resulting gas flow an extraction efficiency (henceforth EX) was calculated as the measured gas flow divided by the introduced gas flow. The resulting EX found for one of the sets of experiments with peristaltic pump set to 23ml/min can be seen in Figure 10. Here, the EX for multiple gas ratios, are fitted linearly against the BPR-setting. From the data it would appear that there is a maximum EX of 98.2% with a BPR setting at 0mbar. That is somewhat surprising as one would expect a vacuum to drive the extraction ought to result in an EX of 100%, but this discrepancy is assumed to reflect the steady state of the running system. With steady state it is to be expected that not all gas will have had time to be evacuated, even at maximum extraction potential.

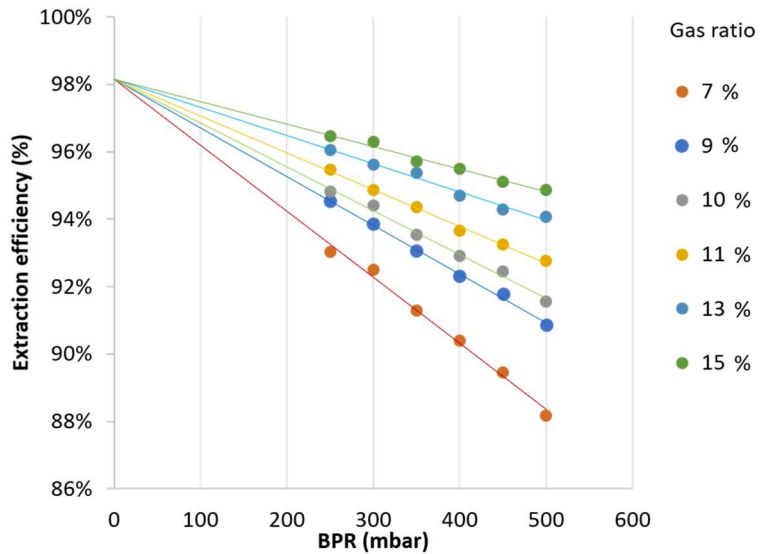


Figure 10: extraction efficiency for N₂ calculated as measured gas flow divided by the introduced gas flow. Multiple different gas ratios have been plotted versus the pressure set at the BPR in mbar.

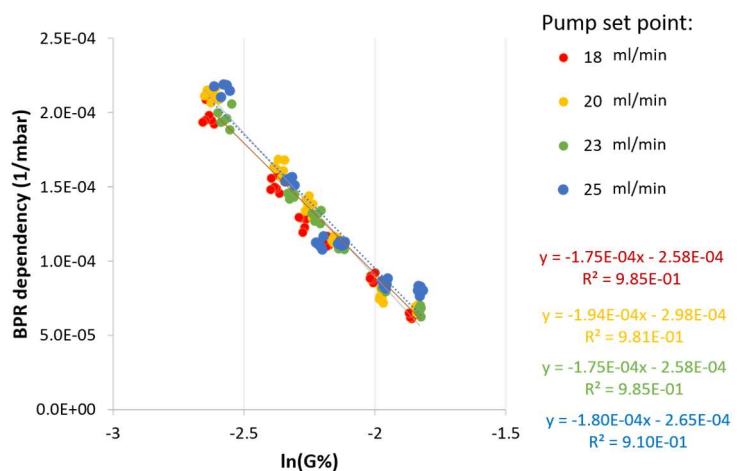


Figure 9: The slopes for BPR dependence in units mbar⁻¹ plotted against the logarithm of the G%. Four different peristaltic pump speeds have been plotted.

At the set-point of 300mbar used throughout the experiments the EX for N₂ spans 92.5-96.3% depending on the measured gas ratio. As expected, the EX increases with the gas ratio, though this increase is not linear. Determining the EX dependence on G% will be important, as G% is the only parameters that can be measured during a sample run that relates to the equilibrium. The way this was done, was to plot the fitted slopes from Figure 10 against the resulting gas ratio leading to Figure 9. In this figure the resulting BPR dependencies for four different pump settings have been plotted against the logarithm of G%, producing comparable linear fits.

$$EX_{N_2} = 1 - ((\ln(G\%) \cdot s + m) \cdot P + 1.84\%) \quad (36)$$

Where EX_{N_2} is the EX for nitrogen, s is the average slope of the fits shown in Figure 9, while m is the average intercept. P is the pressure of the BPR, and 1.84% is the minimum loss to the liquid.

The initial experiments were only done for nitrogen, so the solubility of argon is not accounted for in these results. An approximation for the effect of solubility for argon can be found by comparing the Henry's law constant for argon and nitrogen.

$$EX_{Ar} = 1 - (1 - EX_{N_2}) \cdot \frac{H_{Ar}}{H_{N_2}} \quad (37)$$

At a pressure of 300mbar with a temperature of 25°C and a G% of 10% the EX for nitrogen would be 93.95% and for argon would be only 86.88%. That would result in a drop in the δ_{Ar/N_2} equal to -74.4‰. In general, the fractionation from this can be calculated as:

$$\partial \frac{Ar}{N_2} = \frac{EX_{Ar}}{EX_{N_2}} - 1 \quad (38)$$

The resulting fractionation can be seen plotted against G% in Figure 11.

This only covers the effect on the elemental ratios, but still leaves the effects of isotopes unaccounted for. Unfortunately, it was not possible to find any Henry's Law constants for different isotopes of N₂ and argon. It is expected that the fractionation would lead to depletion of the heavier isotope in the gas-phase, as the heavier isotope would require more energy to shift phase compared to the lighter one. For nitrogen the range of effect has been found to vary between 0.055-0.08% difference in solubility for the heavier isotope compared to the lighter (Jansc , 2001), with greater difference at lower temperatures. In order to investigate these effects, a set of experiments were done where the overflow of the dynamically mixed standard was connected to the MFC in place of the Glacial standard. (see appendix 1.7 for details)

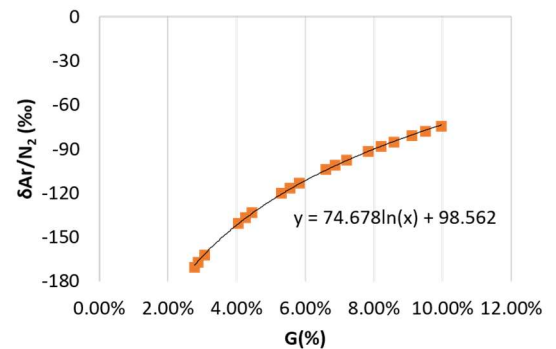


Figure 11: Fractionation of the elemental ratio Ar/N₂ calculated as a function of G%.

This allowed for switching between the standard and sample inlet on the IRMS, and observing the fractionation effects of the complete system, excluding the melthead. Like the initial experiments this was done stepwise, across the gas flow range of 0.75-2ml/min in 0.25 steps in liquid flows 22, 23 and 24ml/min. The result from these experiments can be seen in Figure 12, where the resulting offset between the standard going through the full system and the direct standard line is plotted against the logarithm of the resulting gas ratio. The effect observed for $\delta^{29}N_2$ is minor on the per meg scale, and is therefore at the limit of detectability for the instrument, as can be confirmed by the poor fit. It could reasonably be argued that the correction should not be applied for $\delta^{29}N_2$ based on the R², but it will be included for completeness sake. For both $\delta^{29}N_2$ and $\delta^{36}Ar$ the effect is going in the expected direction, as the heavier isotope is more depleted at lower G%.

$$\partial^{15}N_{cor} = \partial^{29}N_{air.cor} - S_{29} \cdot \ln(G\%) \quad [S_{29} = 5.8 \pm 3.2 \cdot 10^{-3}\text{‰}] \quad (39)$$

$$\partial^{36}Ar_{cor} = \partial^{36}Ar_{air.cor} - S_{36} \cdot \ln(G\%) \quad [S_{36} = -0.30 \pm 0.03\text{‰}] \quad (40)$$

$$\partial \frac{Ar}{N_2}_{cor} = \partial \frac{Ar}{N_2}_{air.cor} - S_{Ar/N_2} \cdot \ln(G\%) \quad [S_{29} = 27.3 \pm 2.5\text{‰}] \quad (41)$$

The final correction function for the data then became as presented in eq. 39-41.

Here it is surprising that the experimentally found dependence on G% for the elemental ratio is 27.3 while the value expected from comparison of EX with Henry's law in eq. 38 was 74.7. It should be noted, however, that the initial experiments were conducted with a different setup, which might have allowed for a greater loss than what was achieved in the final fine-tuned setup. To arrive at the same G% dependence the loss would need to be 0.404 times smaller.

When running the correction in the Matlab script, the G% has been smoothed over 70 seconds, as the variation seen due to bubbles introduced noise dominating the data.

With the solubility effect corrected the data was ready to be cleaned for contamination spikes. These were visually detected and confirmed by comparing the detected signals with the experimental log kept during the campaign tallying the timing of breaks and fractures. Examples of these contaminations can be seen in Figure 13 and Figure 14 where the contamination is documented as spikes in both the elemental ratio and the methane measurements. After the contamination spikes had been removed a smoothing of the data could be applied, without the contamination seeping into the smoothed data. For this a 30 second smoothing applied on the final δ -values. The 30 seconds was chosen as it is well below the smoothing time occurring across the IRMS sample line, so no significant time resolution is expected to be lost.

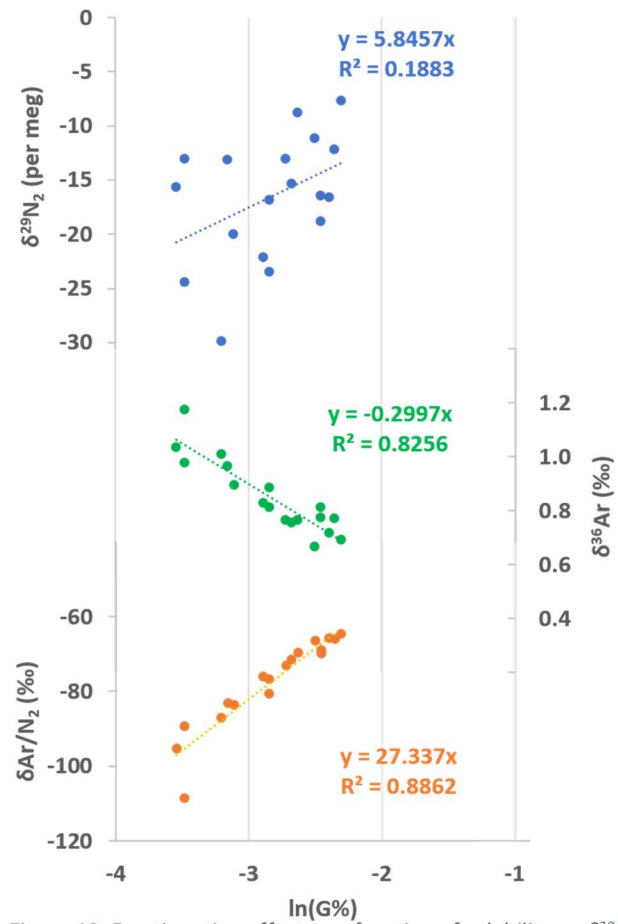


Figure 12: Fractionation effect as a function of solubility on $\delta^{29}\text{N}_2$ (blue) in per meg, on $\delta^{36}\text{Ar}$ (green) in ‰ and on $\delta\text{Ar}/\text{N}_2$ (orange) in ‰ in plot C, all plotted against the logarithm of the gas ratio in percentage. Linear fits forced through 0.

1.3.3 Age assignment

Age assignment of the data is important in order to be able to compare the collected data with other climate records. Age assignment had already been done for the age of ice in Dye 3, and the data for this was provided from personal communication with Bo Vinther, and adheres to the age assignment of GIC05 assignment. Age assignment of the gas thus became a quest to properly assign the measurements to depth.

The depth scale assignment was completed by Janani Venkatesh who was responsible for the methane measurements during the campaign. This first required converting the encoder data at the melthead to depth, based on the melt speed and the data from the ice-core log detailing the core lengths and break locations. From this, the depth corresponding to the ice melted at any specific time was known.

Next step was determining when the melted ice would arrive at the micromodule for gas extraction, and then further reach the gas measurements. Thanks to the addition of sensors for both flow and pressure for gas and liquid, it was possible to reconstruct the travel time for the gas sample from release at the melthead to arrival at the Picarro unit. This was done in two steps, one that used the gas flow and pressure to calculate the travel time from the micromodule to the Picarro. From this a second step was calculated using the liquid and gas flow to go from the micromodule back to the melthead. By accounting for this delay, Janani was able to align the methane measurements with the depth. Because the measurement of methane and isotopes were conducted on two separate sample lines after the gas extraction with different flows, it was necessary to bind them to the same experimental time if the depth assignment of methane should be used. The best time to use for this would be the arrival time at the micromodule as the travel time is the same for the two instruments until then.

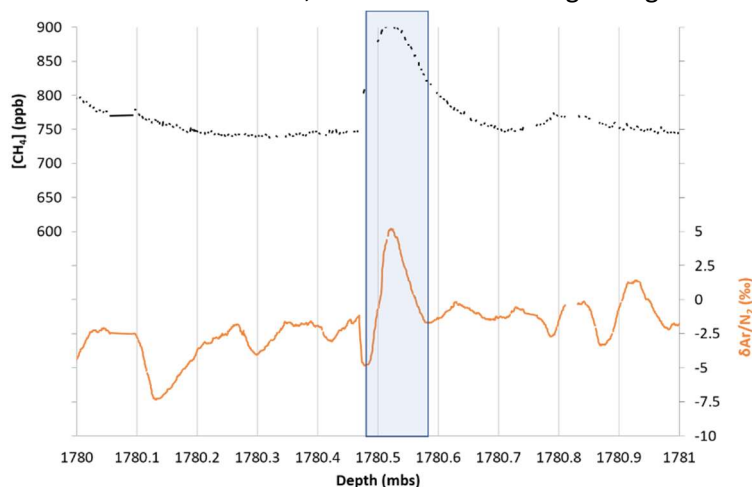


Figure 13: Zoom in on data from depth 1780-17812 meters below surface. Plotted is the $[CH_4]$ in ppb in black and the $\delta Ar/N_2$ in ‰. The blue region highlighted is a contamination spike following a break.

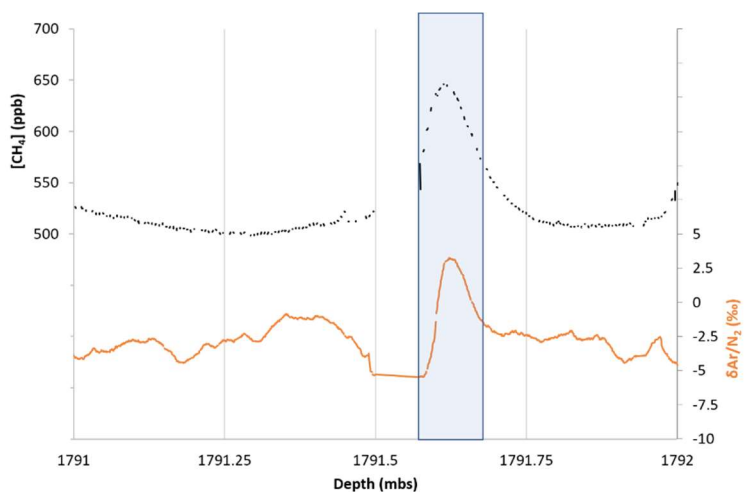


Figure 14: Zoom in on data from depth 1791-1792 meters below surface. Plotted is the $[CH_4]$ in ppb in black and the $\delta Ar/N_2$ in ‰. The blue region highlighted is a contamination spike following a new ice stick.

Unlike for the methane measurements, that had varying delay times due to fluctuating gas flow and pressure, the delay time for the IRMS can be assumed to be constant across all the observed variation, as the flow was kept constant. The delay was estimated based on response time going from the argon-free Holocene and glacial standards to a sample. This delay was found to be 138 seconds. Adding this delay to the travel time from the melthead to the micro module allowed for matching up the IRMS data with the depth profile. Finding the arrival time at the micro module was also essential for determining the solubility effect, as the G% used in eq. 39-41 must be the G% at the time of extraction.

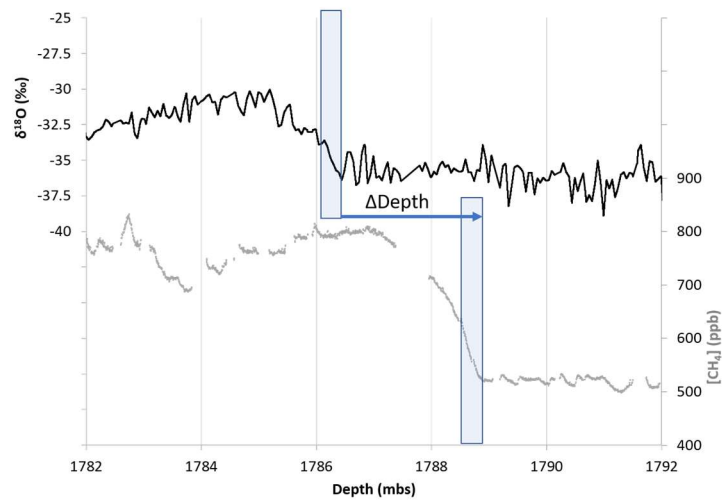


Figure 15: Glacial termination seen in both $\delta^{18}\text{O}$ and methane data. Highlighted are the onset of the termination in the respective data sets.

In order to confirm the quality of the derived depth assignment, the depth assigned methane data and the depth assigned isotope data were compared, to see if contaminations arrived at the same time. The reason for using contamination for this detection rather than the climatic events, is that contaminations were often even more pronounced than DO-events and unlike those the timing of contamination spikes has to be simultaneous. Seen in Figure 13 and Figure 14 are the system's responses to a contamination spike caused by modern air introduced by a gap between two sticks and a fracture in the core. The contamination spike for both methane and elemental ratio data occurs at the same assigned depth, and with the right assignment of the break, seen as jump in depth. There is a greater degree of smoothing for the methane data compared to the IRMS data, but the timing between them agrees. This good agreement between responses confirms the quality of the calculated delay times. The assigned depth can therefore be used for both the methane and IRMS data.

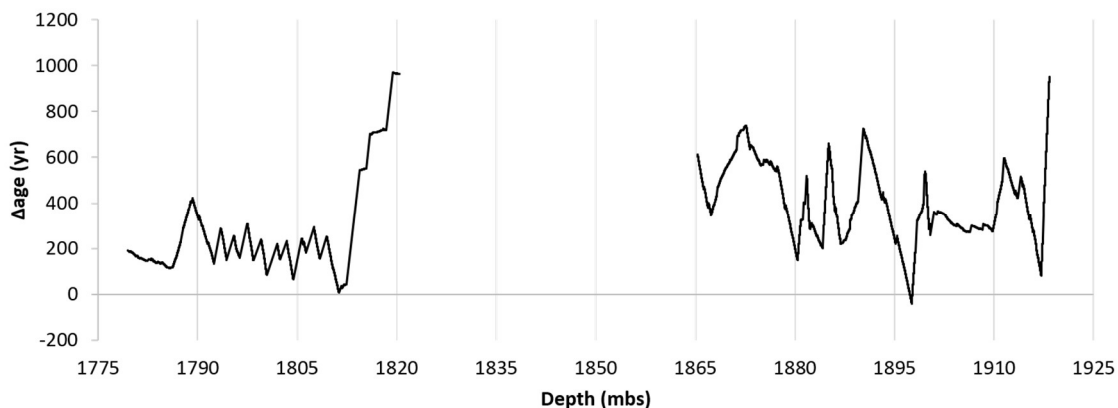


Figure 16: Delta age based on matchmaker fitting plotted against depth in meters below surface.

Dye 3 already had ice-age assigned to depth, as it was found for $\delta^{18}\text{O}$, so assigning the age was done directly from depth to ice-age. The ice-age however does not represent the age scale the gas should be bound up to, as the responses in events are shifted in depth, as can be seen in Figure 15. Here the

termination of the glacial is plotted as an example, and the difference between the ice and gas age can be seen high-lighted as the Δ Depth between the onset of both data sets. In order to arrive at an initial guess of the gas-age the data of $\delta^{18}\text{O}$ was used to find match-points with the methane and isotope data. While it would normally be recommended that the gas-age is assigned by matching the methane record with previously established methane records, this has not been done for this data yet. The resulting difference in age can be seen in Figure 16. The saw-like pattern of the data comes from the linear fit between each match point, and is mostly due to a lack of proper match-points and the poor time resolution of the $\delta^{18}\text{O}$. Additionally, the point at 1897m with a negative Δ age is not lining up with what should be expected, as the gas is never younger than the surrounding ice. With the depth and age assignment complete, it is possible to look at the resulting age along depth scale. This can be seen in Figure 17.

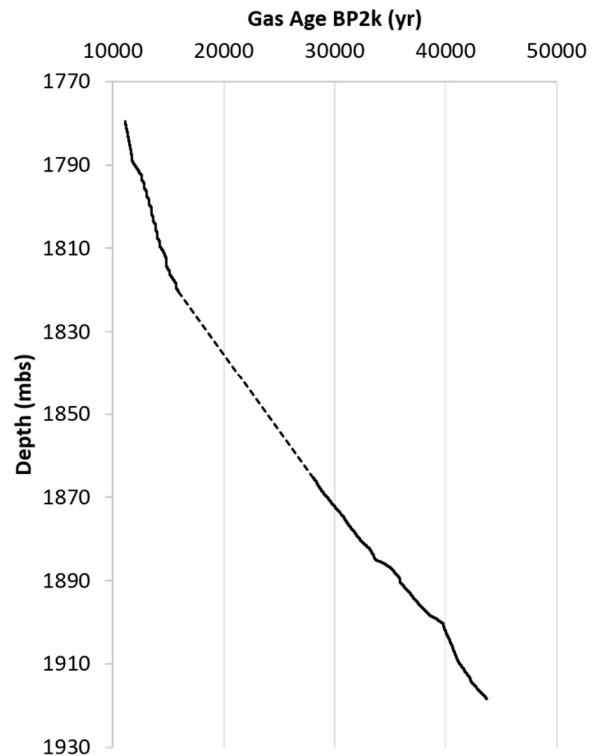


Figure 17: Assigned gas age in years before year 2000, plotted along depth in meter below surface. Dotted region marks the hole in the ice record for the CFA campaign. Minor missing sections are not highlighted indicated.

1.3.2 Uncertainty

For any scientific results to have value the associated uncertainty has to be determined, and it is no different for this campaign. The uncertainties have been calculated for every final data point, based on proper error propagation of both data and correction functions. The uncertainty has been collected from the standard deviation of the intensities of each m/z value in mV, the uncertainty in the found ratios for the daily calibration have been applied for finding the uncertainty in the derived delta-values.

The pressure imbalance correction has some variation in the derived factors from day to day. Part of this is mostly due to the pressure of the used FPR not being completely stable before the measurement. Additional repeated experiments of this would have been able to decrease the associated uncertainty. The effect of these uncertainties is expected to be minor for $\delta^{29}\text{N}_2$ and $\delta\text{Ar}/\text{N}_2$, as the range of $I(28)$ never ventured far from 10500mV, meaning the resulting correction would be minor. For $\delta^{36}\text{Ar}$ the correction, and thus the uncertainty, was more pronounced as $I(40)$ was varying around 8300mV thus resulting in a bigger difference from the used setpoint of 8900mV.

Effects of the chemical slope is only based on one set of experiments, which casts valid concern on the quality of the fit. The uncertainty of the second fit parameter for argon, b36, was also considerable compared to the value of b36. The reason for this is that the fit for $\delta^{36}\text{Ar}$ was only based on 5 data points which is less than ideal.

Another parameter that is not accounted for when applying the chemical slope correction is whether the observed enrichment of $\delta\text{Ar}/\text{N}_2$ is equal to the true enrichment in the standard. It seems reasonable to assume that that would not be the case, but it was not possible to determine with the experiments done here. For that to be feasible greater control of the mixed flows of argon and

nitrogen would be needed to have a better sense of the elemental ratio to expect. For the sample the resulting range of $\delta\text{Ar}/\text{N}_2$ was in between -100 to -50 ‰, which we have to assume is within a range where the difference between observed and real enrichment is minor.

With regards to the solubility correction, this is where the bulk of the uncertainty is introduced. This is both due to the huge spread of G% because of the fluctuating flow with the arrival of bubbles, and the uncertainty of the derived factors for the correction equations. The variation in G% is especially problematic for the elemental ratio, as it has such a great dependence on G%.

The degree to which solubility has been reached for a sample coming from the melthead compared to the standard introduced earlier is unknown. Fortunately, most of the gas volume appeared to arrive at the micro module in the form of bubbles, similar to tests with the standards, hinting that the loss is probably comparable. Complicating a direct comparison between the standard and the sample is the temperature of the gas and water. For the sample it comes directly from the ice at $\sim 0^\circ\text{C}$, and heats up along the way. The temperature profile for the sample line is unknown, whereas for standards it is expected to be room temperature across the entire sample stream. Lower temperatures are expected to lead to more pronounced isotope fractionation, which could mean that the solubility corrections used are not correcting sufficiently.

For the experiments investigating solubility the mQ-water used had been debubbled by N_2 , before being degassed by a module. From observations we know that this subsequent degassing was not sufficient in removing all the gas present in the water, which would mostly be N_2 . As the N_2 used for debubbling was from the same bottle supplying the standard, it is possible that the water was still saturated with nitrogen reducing the fractionation occurring for the introduced standard. That could at least explain the small solubility effect on $\delta^{29}\text{N}_2$, which I would have expected to be only one order of magnitude below the effect on $\delta^{36}\text{Ar}$. It is therefore likely that we are not correcting sufficiently for the solubility of $\delta^{29}\text{N}_2$.

The final effect adding to the uncertainty of the presented data is the smoothing of the data. The resulting uncertainty derived from this was calculated as a combination of the uncertainty of the data point and the standard deviation of the surrounding points smoothed across (in a Pythagorean manner). The resulting uncertainty will be plotted alongside the results.

All of the error propagation can be seen in appendix 1.8-1.10.

1.4 Result and discussion

The melting campaign was completed over the course of 7 work days, 30th and 31st of October including the 4th, 5th, 6th and 7th of November 2019. IRMS measurements were unfortunately not ready at the 30th, so isotope data only covers the depth running over the remaining 6 days. The corrected and smoothed data with contamination spikes removed can be seen in Figure 18 and Figure 19, where the $\delta^{18}\text{O}_{(\text{ice})}$ record collected from (Langway, 1985), is plotted along the methane and isotope measurements. The DO-events have been highlighted and numbered for easier overview. The data is split up in two plots omitting the hole in the ice-record of 1821-1865m.

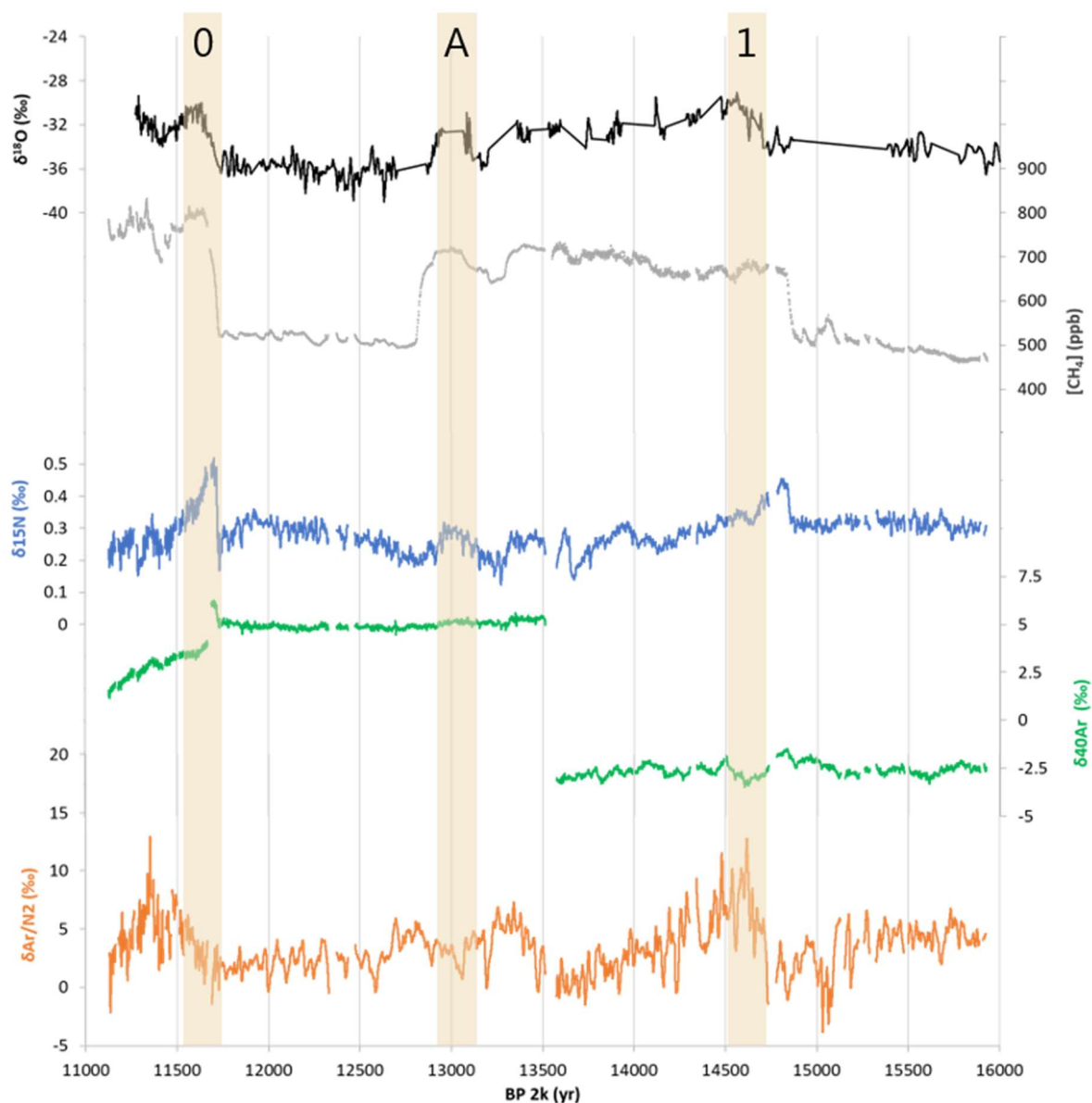


Figure 18: Results from the Dye 3 2019 campaign in the age period 11000-16000 years before year 2000. The $\delta^{18}\text{O}$ of ice (black) in ‰ is plotted along ice-age. Methane (grey), $\delta^{15}\text{N}$ (blue), $\delta^{40}\text{Ar}$ (green) and $\delta\text{Ar}/\text{N}_2$ (orange) are plotted against the assigned gas-age. Ages correspond to the depth 1780-1821m below surface.

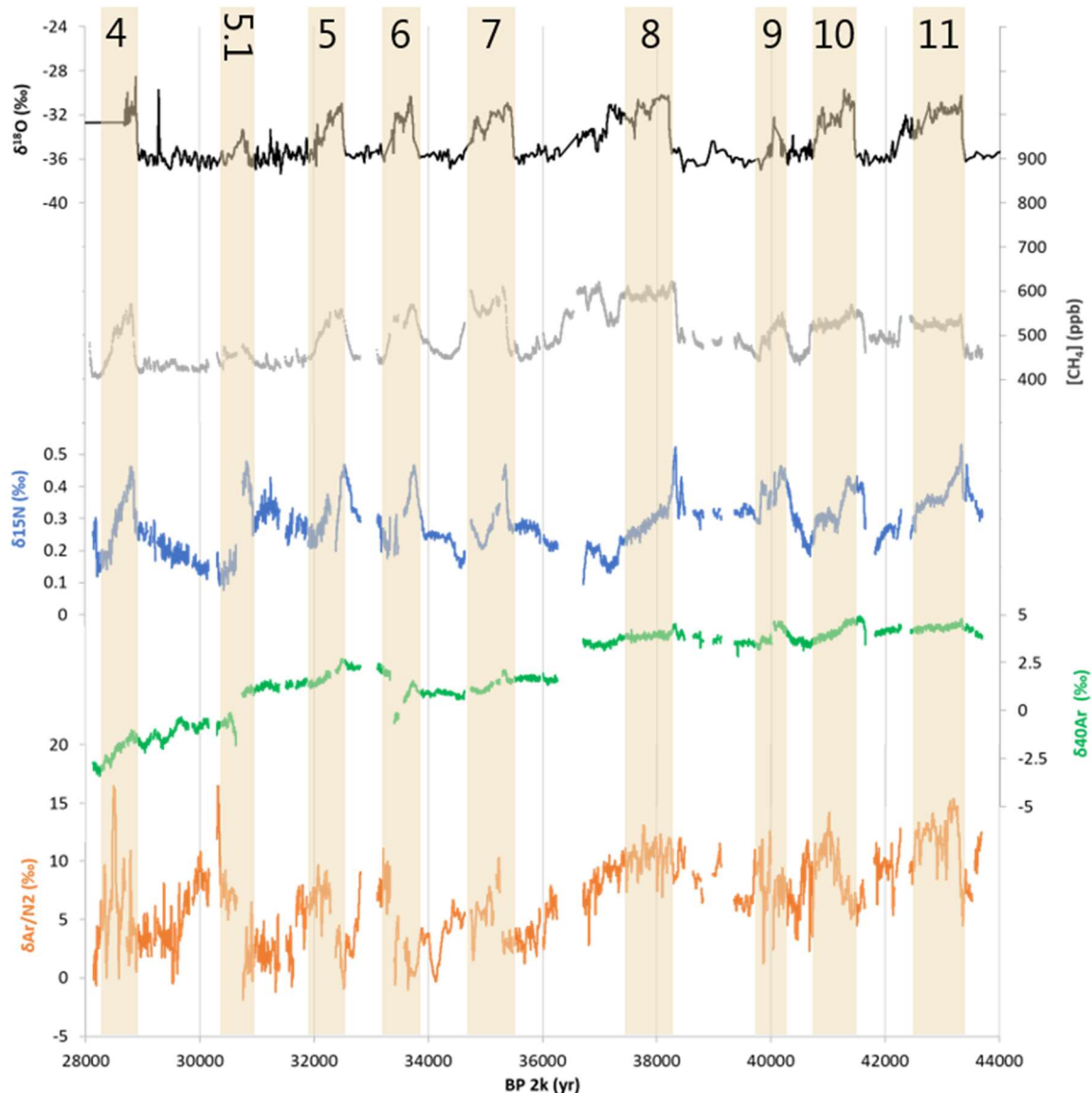


Figure 19: Results from the Dye 3 2019 campaign in the age period 28000-44000 years before year 2000. The $\delta^{18}\text{O}$ of ice (black) in ‰ is plotted along ice-age. Methane (grey), $\delta^{15}\text{N}$ (blue), $\delta^{40}\text{Ar}$ (green) and $\delta\text{Ar}/\text{N}_2$ (orange) are plotted against the assigned gas-age. Ages correspond to the depth 1865-1920m below surface.

Looking at the results presented there are a few things that need to be addressed before any further data discussion can go on. Most eye-catching are the sudden jumps seen for the $\delta^{40}\text{Ar}$ that span a far greater range than expected, from -3 to 7.5‰. Similar discontinuities can be seen for $\delta^{15}\text{N}$ and $\delta\text{Ar}/\text{N}_2$ at the same age, though to a much smaller degree. These jumps happen between two experimental runs and are caused by the instability of the lab-air used as the standard. This effect was expected to be sufficiently corrected for by applying the daily offset correction in eq. 31-33, but is evidently not enough to account for variation in $\delta^{40}\text{Ar}$. This highlights the need to have a constant standard across the measurements.

Secondly, is timing of DO events 1, 8 and 10, where the gas signal arrives prior to the signal in the ice. This is explained by the gas age assignment not yet being adequate, as mentioned in the age assignment chapter.

Thirdly, the elemental ratio is enriched when compared to modern air, which goes against expectations, as the close-off fractionation was expected to leave it depleted rather than enriched.

Having addressed the faults of the data, the attention can be brought back to what can actually be observed. Firstly, there are very clear events in $\delta^{15}\text{N}$ that match up with the methane data, indicating the changes in firn fractionation effects. Similar events can also be seen for $\delta^{40}\text{Ar}$, though it is difficult to make out due to the large range. By comparing the magnitude of these events, it will be possible to determine what effect thermal and gravitational fractionation had leading to the increases.

Looking at the elemental ratio, it is apparent that it differs from the two isotope effects. While there are events that can be made out from the otherwise high variability of the data, these events do not line up with the methane increases.

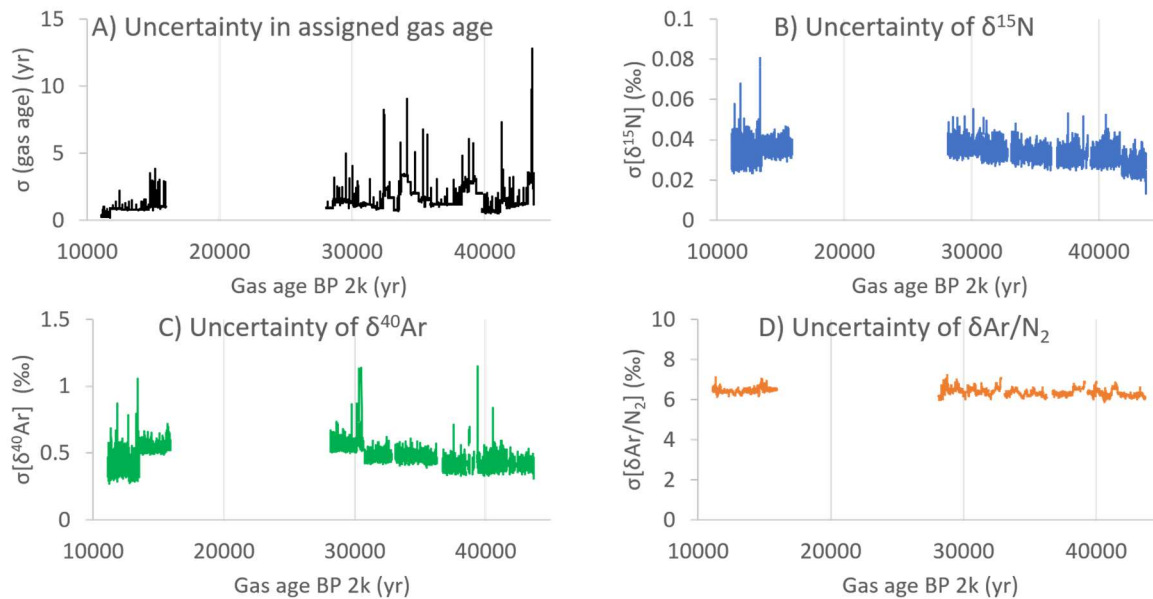


Figure 20: Overview of the error propagated uncertainty based on 30 second smoothing. A is the uncertainty in assigned age in years, based on a 5 sec uncertainty in between methane measurements delay and the IRMS delay. B is the uncertainty in $\delta^{15}\text{N}$ in ‰, C is the uncertainty of $\delta^{40}\text{Ar}$ in ‰ and D is the uncertainty of $\delta\text{Ar}/\text{N}_2$ in ‰.

To determine which values can be considered signals and which are noise it is necessary taking a look at the propagated uncertainties accompanying the data. An overview of this can be seen in Figure 20. Here the first sub-figure, A, shows the uncertainty in age assignment between the ice and gas age based on the uncertainty in the depth assignment. B, C and D show the uncertainty of the IRMS measurements, a. $\delta^{15}\text{N}$ has a rather satisfying uncertainty below 50permeg for the entire core. While better accuracy could be desired, <50permeg uncertainty will still allow for proper data investigation. For $\delta^{40}\text{Ar}$ the uncertainty is considerably higher, around 0.6‰ which is on the order of the expected signals. Most of this uncertainty comes from the relatively high uncertainty of the daily lab-air measurements. This is somewhat apparent with the highest plateau between 13000-30000 corresponding to the measurements of the 4th that had a large daily uncertainty. The uncertainty should therefore rather be interpreted as the accuracy rather than the precision of the measurements. Though as the different runs span a range of 10‰, the uncertainty in accuracy is not sufficient to account for this. The $\delta^{40}\text{Ar}$ should therefore be limited to be investigated for relative change within each run.

Finally, for $\delta\text{Ar}/\text{N}_2$ the uncertainty is at a surprising 6.5‰, which is more than double the expected signals arising from gravitational and thermal fractionation. Some of the variation seen in the data is smaller than this, casting doubt on whether the elemental ratio has any signal at all. With similar line of reasoning as for $\delta^{40}\text{Ar}$, I will argue that it does, as the majority of the uncertainty comes from the

high uncertainty of the solubility correction factor. It accounts for around 87% of the uncertainty for $\delta\text{Ar}/\text{N}_2$. I would therefore argue that it is mostly an uncertainty in the accuracy of the absolute value, but does not reflect the variability of the data. The uncertainty of the absolute value would also explain why the final values are enriched instead of depleted as expected. The variation is rather reflected in the remaining 13% of the uncertainty. Those 13%, however, still make up a variation around 0.9‰, which is still half the expected signal size from gravitational and thermal fractionation making it problematic to recover meaningful signals. With a better understanding of the results, a detailed look into the different aspects will now commence.

1.4.1 $\delta^{15}\text{N}$ record

The $\delta^{15}\text{N}$ data has the most precise data of the IRMS measurements, and it is the IRMS measurement that best lends itself for comparison with previous work. $\delta^{15}\text{N}$ records have already been made for other cores, and for the top 120meter of Dye 3. The general level seen in this campaign for stadial periods is between 0.15-0.3‰, which based on an average temperature

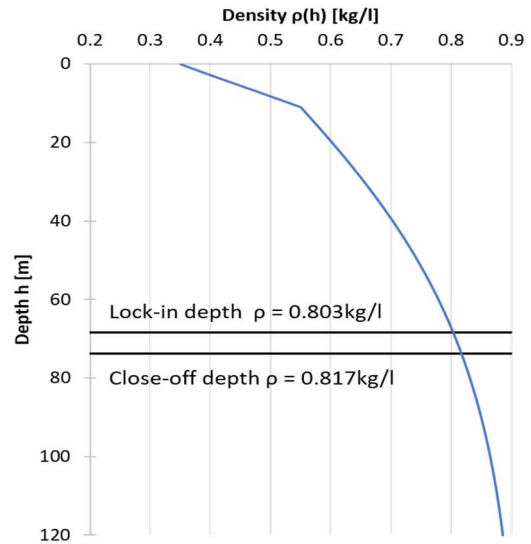


Figure 21 Density profile of Dye 3 as calculated by Herron-Langway's model, with snow density of 0.39kg/l, Temperature: -20°C and accumulation: 0.56m/yr.

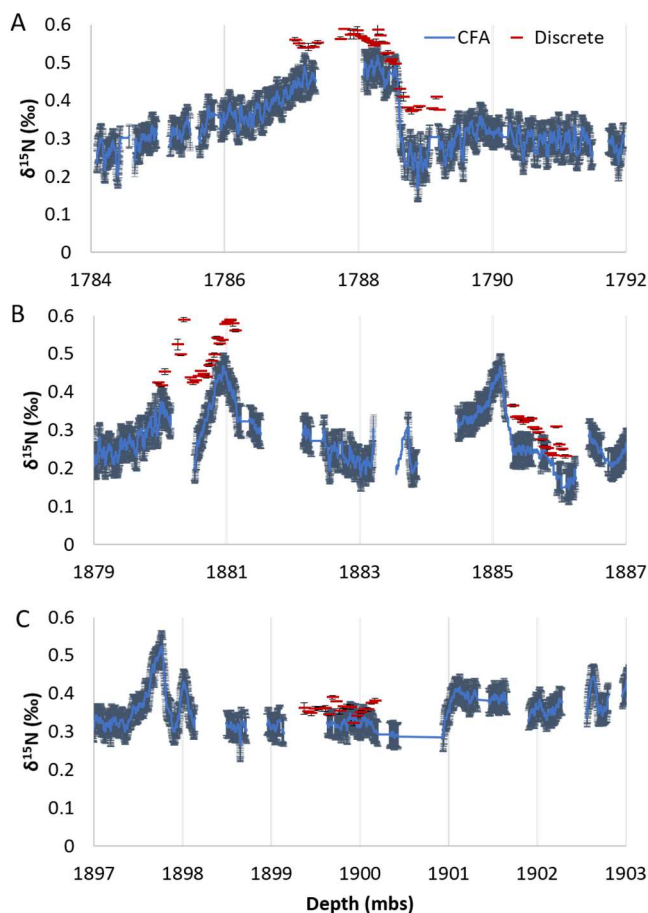


Figure 22: Plot of $\delta^{15}\text{N}$ in ‰ of Dye-3, as measured by discrete measurements (red) and by CFA (blue). Both have associated uncertainty. The discrete data is provided by Todd Sowers, The Earth and Environment Systems Institute, Penn State University

of -36°C (C. Buizert B. A., 2008) would correspond to an unbelievable firn-column height of 30-60meters. That is shallower than the current height around 65-70 meters which stands in contrast to the expectation that the firn at glacial times would be even deeper due to the colder temperatures. A reduced accumulation ratio would help by counteracting this deepening. Since accumulation is expected to scale with temperature, the colder temperatures would result in lower accumulation, due to overall dryer conditions. The explanation might be found elsewhere though, as a discrepancy between firn height and observed $\delta^{15}\text{N}$ already has been documented for the top 80-120m samples of Dye 3 (H. CRAIG, 1988). Here the values found were 0.11‰ (33% of expected value) lower than the value expected. The explanation given for this was the high advective flow as a consequence of the high accumulation. That however complicates matters, as the high accumulation that would increase the

advective flow would also result in a deeper firn-column. The two potential explanations for the lowered signal thus counter each-other.

In order to help assign values more confidently I will make use of discrete measurements performed on Dye 3 (Sowers, 2020). As mentioned, when discussing the ice logging during the campaign, ice was collected for performing discrete measurements by Todd Sowers. These would be able to help determine the precision of the CFA setup, as discrete sampling would be able to get more precise and accurate measurements as it is a well-established method. Unfortunately, due to the limitations brought by the COVID-19 situation in the spring of 2020, the measurements of the discrete samples were postponed, with only three regions measured before the lock-down. These measurements, kindly shared through personal communications with Todd Sowers, can be seen in Figure 22, and are plotted on top of the data collected by CFA. No conclusion should be drawn from the respective level of the two sampling types, and shall exclusively be used for comparison of trends. From looking at the three plots, reasonable agreement can be seen both with regards to timing and size of response. A few discrepancies are observed, but due to the limited amount of data points, nothing final can be said. While the accuracy of the discretely sampled measurements is expected to be higher than that of the CFA, we have refrained from shifting the data to match it, as the discrete data-points represent too few data points across the core. It is possible that proper absolute scale can be assigned to the CFA data, once the remaining discrete data has been collected.

While the absolute scale of the $\delta^{15}\text{N}$ collected is still in question, it is possible to compare the cores response to DO-events to other cores. Figure 23 shows the collected data of $\delta^{15}\text{N}$ for Dye 3 alongside the $\delta^{15}\text{N}$ as recovered from the NGRIP core. The $\delta^{15}\text{N}$ data from NGRIP comes from the discrete measurements of $\delta^{15}\text{N}$ collected as part of the Northern Greenland Ice-core Project (K. K. Andersen, 2004).

The age assignment for NGRIP has been aligned with the Greenland stratigraphic ice core chronology (GICO5) which has been created by layer counting, through visual stratigraphy, electrical conductivity measurements and CFA records (Svensson, 2008). The methane record of the two cores has been added to allow for confirming the quality of the preliminary gas-age assignment of the Dye 3 record, as the timing of $[\text{CH}_4]$ between NGRIP and Dye 3 should be simultaneous. Where the two methane records agree, the gas-age assignment for Dye -3 is acceptable. Looking at the $\delta^{15}\text{N}$ records, there generally seems to be good agreement between the two cores, with all the DO-events reflected in both. Due to improper timing, as confirmed by the methane record, there are a few periods where the onset and peak of events don't agree, as seen with DO#1. With timing accounted for the attention can be brought to the values. Here two main differences manifest on the plots.

Firstly, the difference in stadial levels between the two cores; the $\delta^{15}\text{N}$ of Dye 3 is on average lower than NGRIP by 0.11‰, as would be expected with the deeper firn-column of NGRIP. Though the true difference is smaller, as the Dye 3 values are too low.

The second difference is the response size and time for Dye 3 compared to NGRIP. The increases seen during interstadials brings the enrichment up to the same level as the NGRIP data for many of the events, and does so with a much steeper increase. The transition steepness between the two cores can be compared as is done in Table 4. From the transition times it is clear that the effect of transition is spread out over fewer years for Dye 3, and with bigger increase in $\delta^{15}\text{N}$ for the majority of the events.

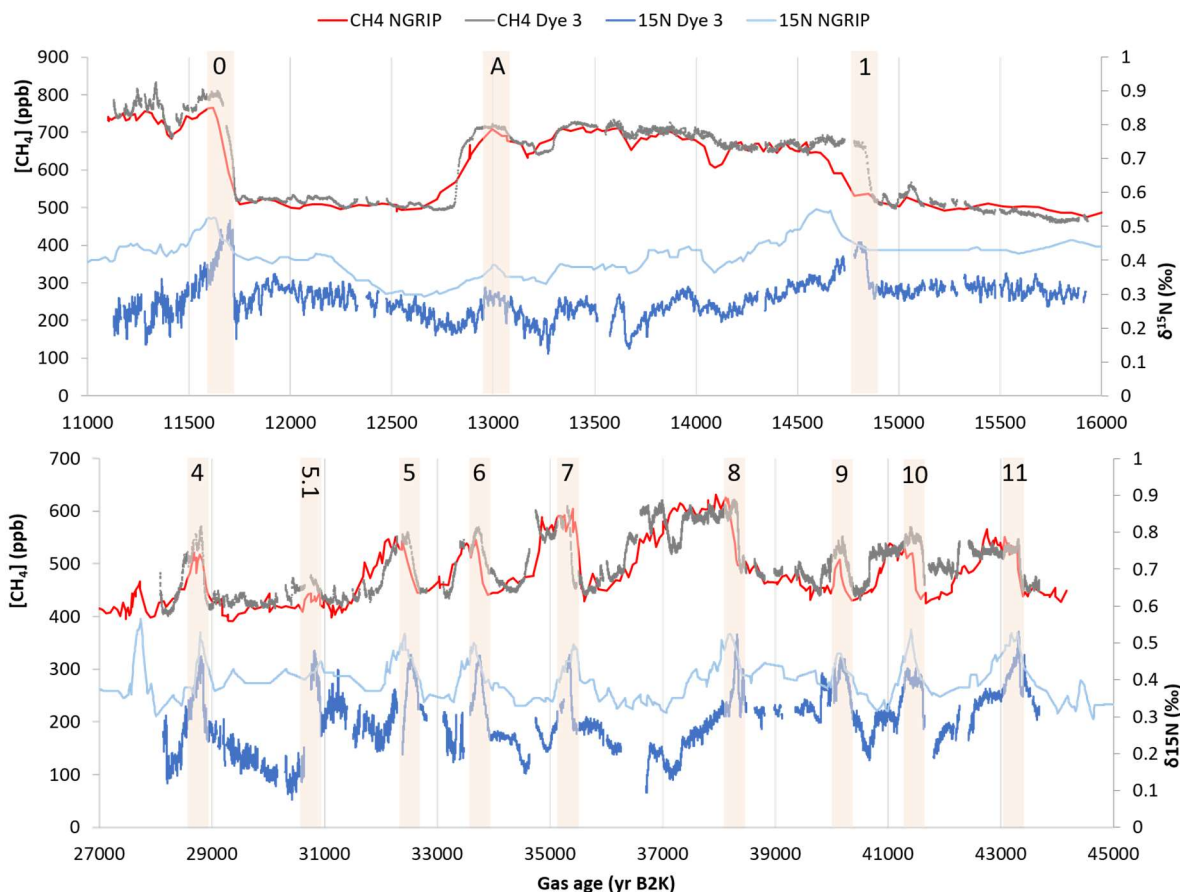


Figure 23: Comparison plots between data from NGRIP as collected from discrete measurements and Dye 3. Along the left axis is plotted the methane record for NGRIP (red) and Dye 3 (grey) in ppb. Along the right axis is plotted the $\delta^{15}\text{N}$ data of NGRIP core (light blue) and the results from Dye 3 (blue) plotted versus gas age before year 2000. The top figure displays the period from 11000-16000 years ago with the bottom displaying the age from 27000-44000 years ago. DO-events for Dye 3 have been highlighted and numbered.

Table 4: compilation of transition time found as time between the onset of $\delta^{15}\text{N}$ increase till the tip of the increase, and accompanying change in $\delta^{15}\text{N}$ between these two periods for NGRIP and Dye 3. Peak and onset have been assigned visually. $\delta^{15}\text{N}$ -slope is the

DO- Event (year)	NGRIP			Dye 3		
	Transition time (yr)	$\Delta\delta^{15}\text{N}$ (‰)	$\delta^{15}\text{N}$ -slope (‰/kyr)	Transition time (yr)	$\Delta\delta^{15}\text{N}$ (‰)	$\delta^{15}\text{N}$ -slope (‰/kyr)
0	117	0.12	1.01	10	0.23	22.78
1	2068	0.11	0.55	35	0.13	3.64
4	213	0.13	0.63	10	0.14	14.41
5	313	0.15	0.46	120	0.12	0.99
6	162	0.10	0.65	145	0.21	1.41
7	119	0.09	0.77	50	0.18	3.60
8	177	0.11	0.61	45	0.19	4.24
9	304	0.11	0.35	190	0.16	0.82
10	325	0.16	0.50	200	0.09	0.47
11	148	0.11	0.72	25	0.15	5.99

The reasons for this difference shall again be found in the difference in firn-height. The first reason for the difference in steepness is that the deeper NGRIP firn column has smoothing across more years

than that of Dye 3, which would reduce the steepness. The increases in value seen with the interstadial transitions are caused by either/or thermal and gravitational fractionation, for which thermal fractionation would be more pronounced at Dye 3. The sudden increase in temperature at the surface will induce a temperature gradient, and that is going to be established across the firn the quicker the shallower it is. A quickly established temperature gradient is going to be steeper which will lead to a bigger thermal fractionation, as eq. 5 would dictate. The temperature profile of the two cores going back to 22000 years before present can be seen in Figure 24 (C. Buizert B. A., 2008), where the average temperature is not only higher for Dye 3, the temperature changes seen were also greater than those for NGRIP. The increase in temperature does not only affect the signal due to thermal fractionation, but will also affect the gravitational fractionation, as the firn densification depends on temperature. Since Dye-3 experiences bigger temperature increases than NGRIP, the expected resulting effect would be a shallower firn column compared to the stadial levels that would lead to a smaller gravitational effect.

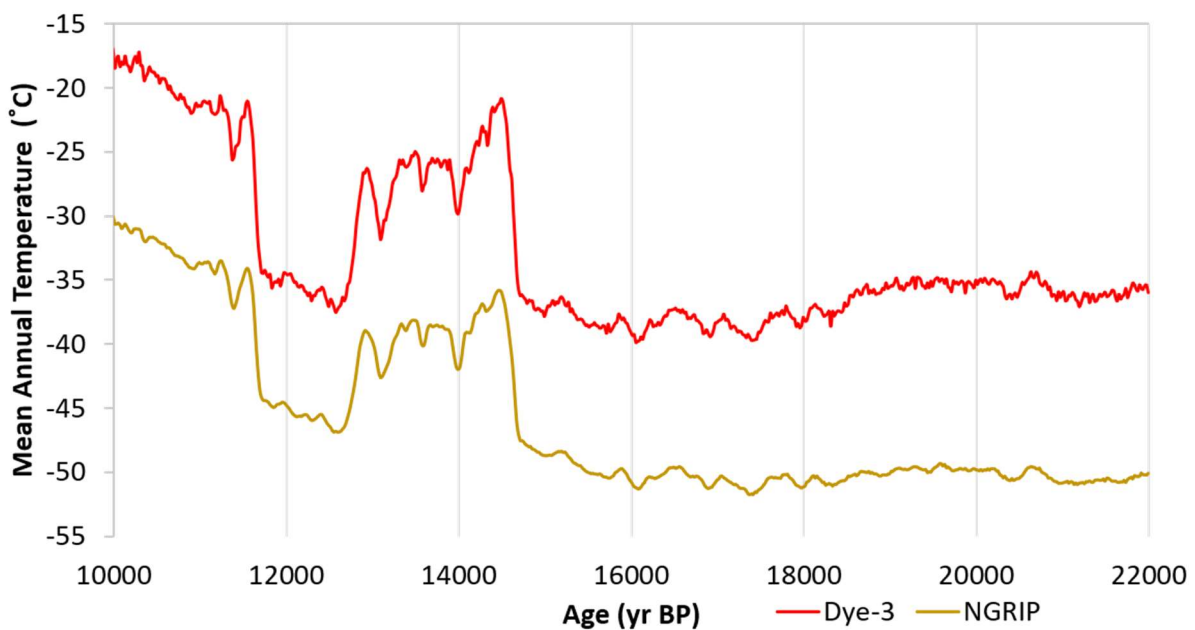


Figure 24: Mean annual temperature in °C for Dye 3 and NGRIP plotted along ice-age in years before present. The data for this was taken from supplemental data for "Greenland-wide seasonal temperatures during the last deglaciation" (C. Buizert B. A., 2008).

But with the increased temperatures comes an increase in accumulation that would dominate the firn-depth, driving the lock-in zone further down. Due to its location Dye 3 would be expected to see more accumulation than NGRIP, as is the case in modern times. The varying effects of the gravitational fractionation at the two places will have to remain unresolved, since no conclusion can be reached without a proper accumulation record.

All that can be concluded from this comparison is that Dye 3 as a more southern drill-site closer to the coast is subject to a greater degree of change related to stadial-interstadial transitions. Due to the relative shallowness of the Dye 3 firn-column the air stored is mixed across years to less of a degree, giving much better temporal resolution.

This high temporal resolution can also be used to compare the timing of transitions between the [CH₄] and δ¹⁵N. This is done in Figure 25, where we see all the DO events and the small increase at Allerød (A) (S. O. Rasmussen, 2006) for [CH₄] and δ¹⁵N plotted along gas age. For most of the events, there appears to be near perfect agreement in timing for the onset of the events, with the exception of

DO#0 where the increase of $[CH_4]$ is going on for a longer time than the sudden increase of $\delta^{15}N$, and DO#11 where the increase starts earlier. An additional point of interest is the two pre-peaks seen in DO#8 and DO#11, where both $[CH_4]$ and $\delta^{15}N$ increase, though the increase for $\delta^{15}N$ is more significant. This increase is not seen in the $\delta^{18}O$, or in the NGRIP data, though that could be explained by the resolution. At the point of writing, I am unaware of these increases being discussed previously.

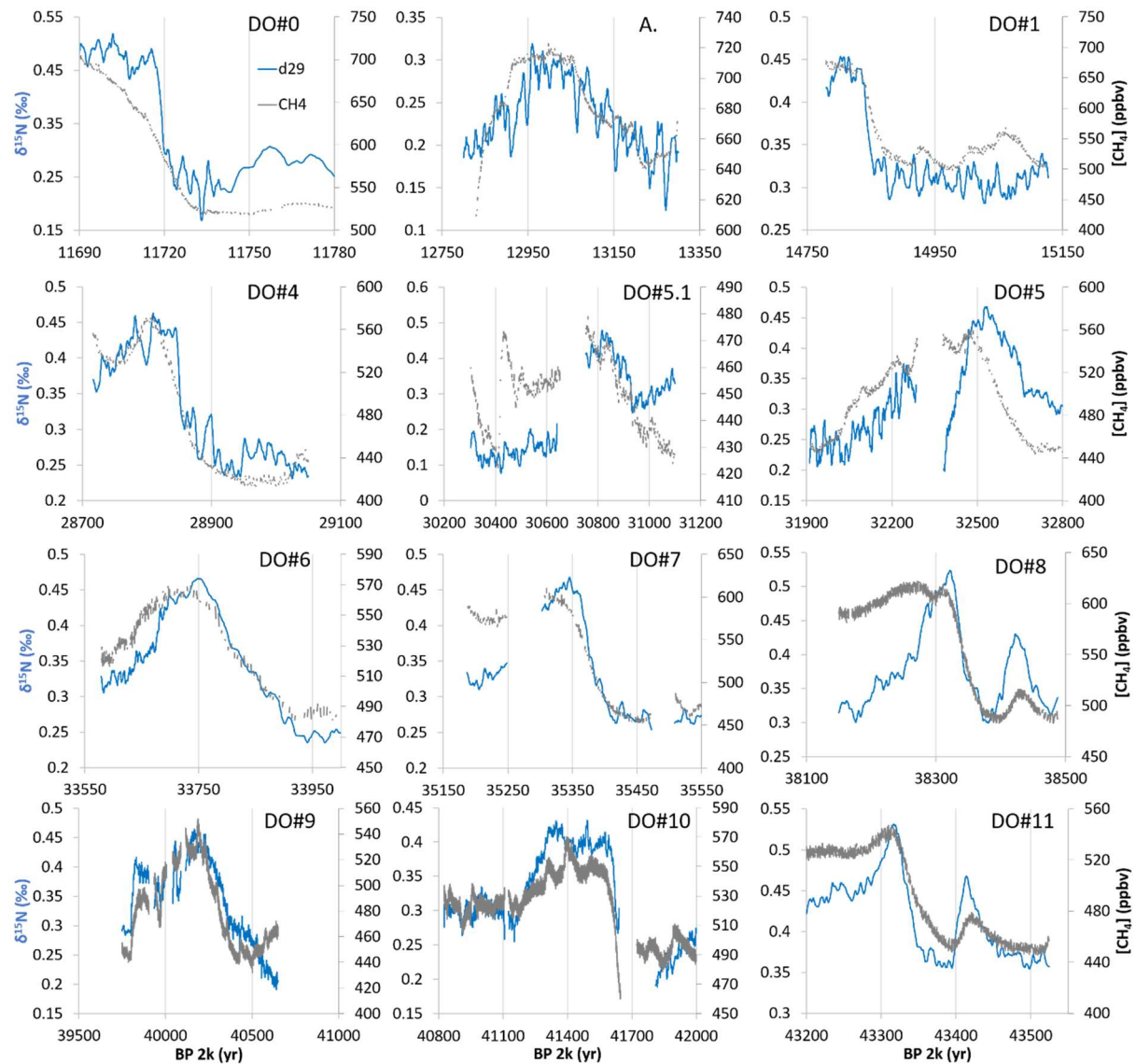


Figure 25: Zoom in on the DO-events with plots featuring $\delta^{15}N$ (blue) in ‰ plotted along the left axis and $[CH_4]$ (grey) in ppbv plotted along the right axis.

1.4.2 Thermal and gravitational fractionation

As described in the chapter on firn, it is possible to discern the effect size of thermal and gravitational fractionation by observing the difference in response between the $\delta^{40}\text{Ar}$ and $\delta^{29}\text{N}_2$ signal. A direct comparison was made difficult by the poor reproducibility of lab-air $\delta^{40}\text{Ar}$ across the different days. In order to remove this effect, a new iteration of the data was produced, separating the data by experimental runs. From each of these separated data groups, a new $\delta^{40}\text{Ar}$ and $\delta^{29}\text{N}_2$ record was created as the difference from the daily mean of each of these values. By doing this, binding the data to an absolute scale was sacrificed, but it allowed for removing the daily variation, thereby aligning it to a relative scale instead. The resulting difference from the mean was also divided by their Δm in order to scale the two isotopes for easy comparison. For $\delta^{29}\text{N}_2$ it meant dividing by one, while for $\delta^{40}\text{Ar}$ it meant dividing by four. The reason for this mass scaling is following the approach by (Jeffrey P. Severinghaus, 1998), that showed that enrichment from gravitational fractionation will be of equal size for the two scaled datasets. By observing where the response is not identical, the effect of thermal fractionation can be observed. The full plot of this scaled data can be seen in Figure 26, where the separated experimental runs have been recombined to the gas-age scale. From this it is possible to make out the variation in the $\delta^{40}\text{Ar}$, and confirm that many of the DO-events are indeed also reflected, and is not just experimental noise.

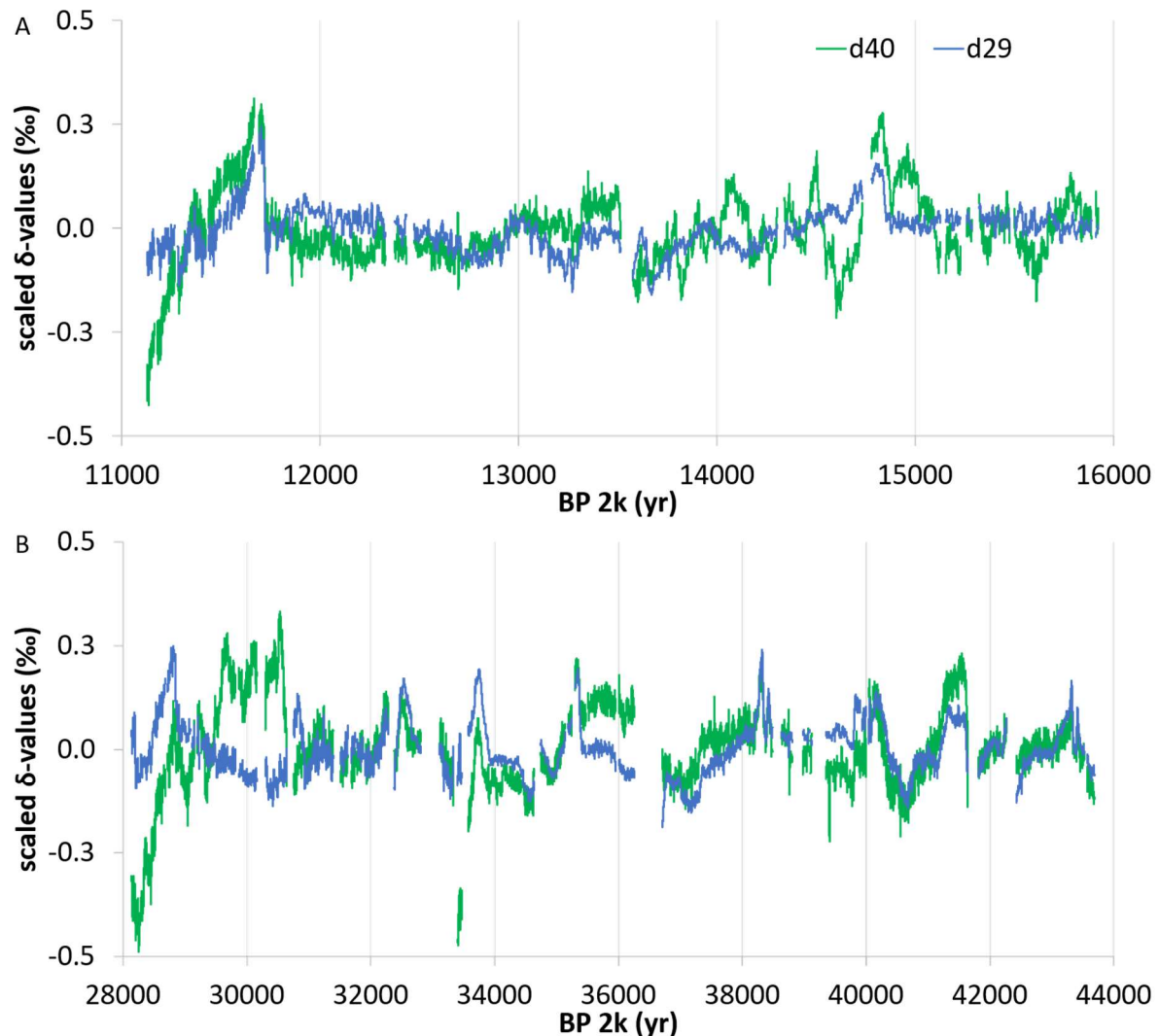


Figure 26: Scaled data for $\delta^{29}\text{N}_2$ (blue) and $\delta^{40}\text{Ar}$ (green). Data has been scaled and "detrended" as described above. Both $\delta^{40}\text{Ar}$ and $\delta^{29}\text{N}_2$ are plotted in ‰ along the relative scale.

There is still a greater degree of variation in the $\delta^{40}\text{Ar}$ than in $\delta^{29}\text{N}_2$, but it seems justified to use the values found to compare the two data sets. To do this, I focused on the DO-events and looked at how the two records responded. This alignment is presented in Figure 27 where the same zoom on DO-events as used in Figure 25 have been applied. Here, the scaled relative values for $\delta^{40}\text{Ar}$ and $\delta^{29}\text{N}_2$ have been aligned along the y-axis so that the onset matches. Because of the long term variation seen in $\delta^{40}\text{Ar}$, the offset needed varied in size. While being plotted along two y axes, they are scaled identically so direct comparison is permitted. From here it is possible to see that there is variation in the responses from the two records. For events like the glacial termination at DO#0 we observe near perfect agreement with response, which would indicate that the fractionation almost exclusively comes from increase in gravitational fractionation, while for events like DO#6 a difference in scale can be seen indicating the thermal fractionation playing a part.

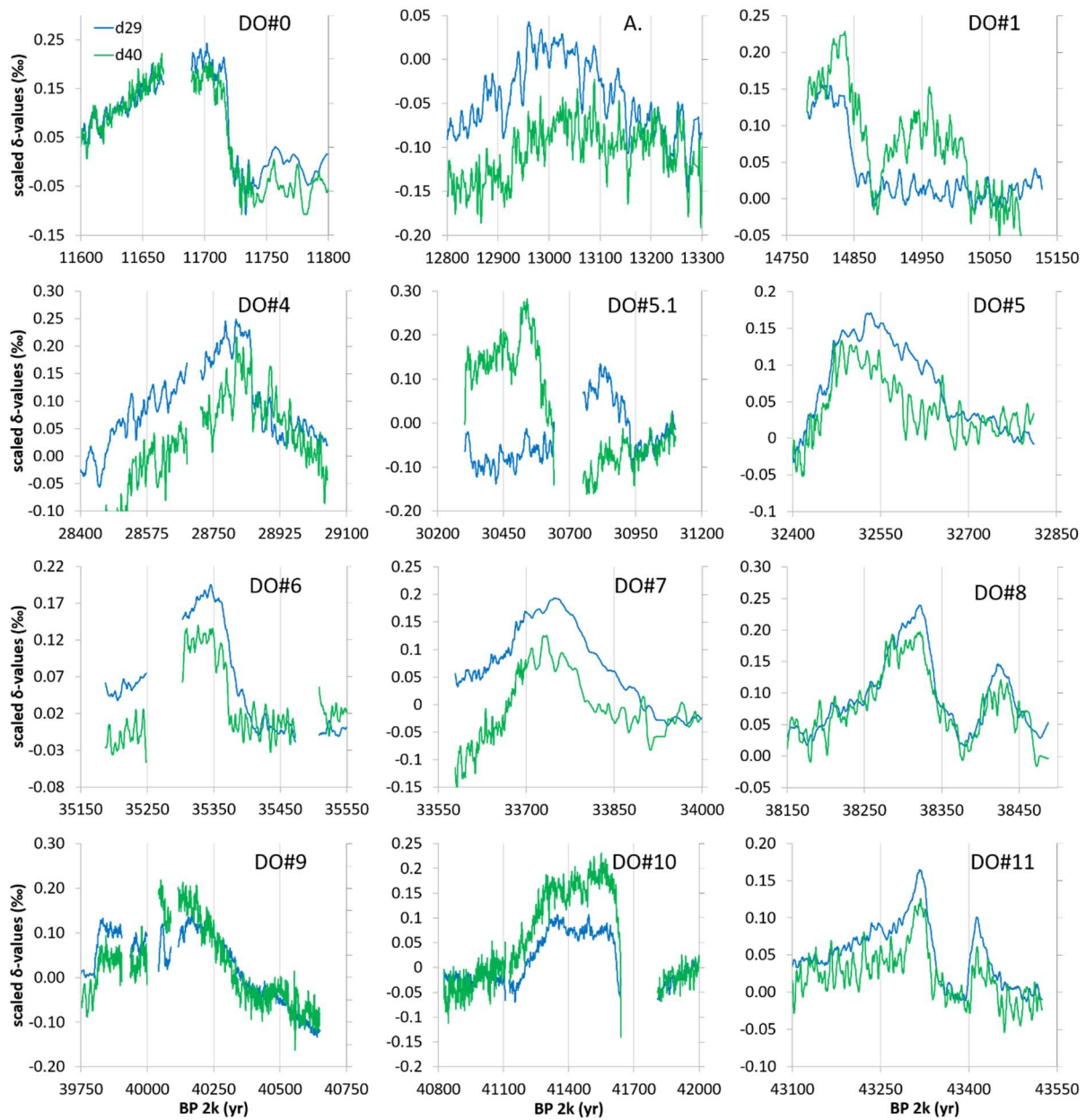


Figure 27: DO-event overview for the relative $\delta^{15}\text{N}$ (blue) and $\delta^{40}\text{Ar}$ (green) in ‰.

In order to quantify these effects, I found the average value at the onset of a DO-event and at the peak. An example of the two mentioned events DO#0 and DO#6 is shown in Figure 28. From these average values the difference can be found reflecting the fractionation associated with DO-event.

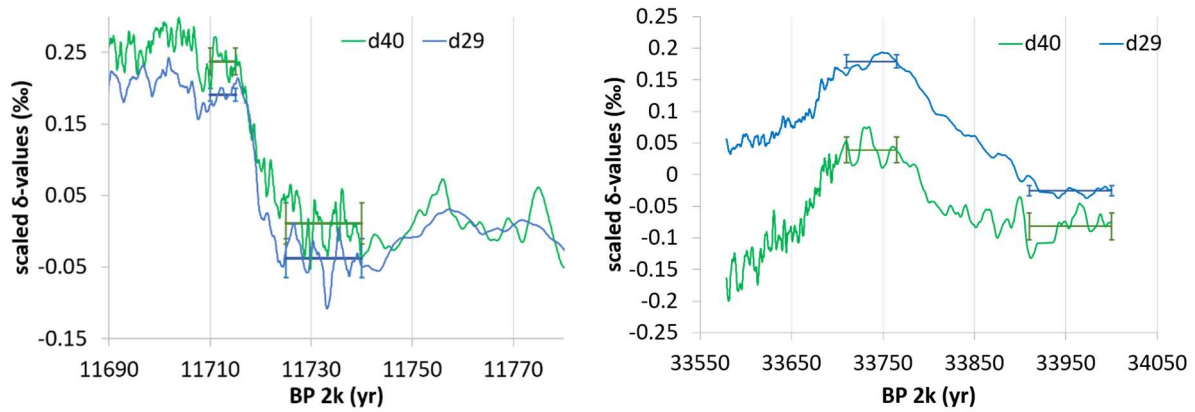


Figure 28: Zoom in on DO#0 to the left and DO#6 to the right. Plotted is the relative scaled δ -value for ^{15}N (blue) and ^{40}Ar (green). In each plot the average and the period it spans, has been shown for both the assigned peak and onset level for both isotope ratios.

In Table 5 the $\Delta\delta^{15}\text{N}$ and $\Delta\delta^{40}\text{Ar}$ has been found and eq. 10 and 11 have been used to find the input from the thermal and gravitational effect. As can be seen the fractionation at the glacial termination appears to come exclusively as a response to increased gravitational fractionation, where for DO#6 it appears to be driven equally between the two effects. These assigned values should be considered the tentative approximations that they are. The uncertainty is high, and the presence of negative values should indicate that no solid conclusion can be drawn from this.

Table 5: Overview of climatic event responses. Peak and onset period marks the time periods used for generating the averages the $\Delta\delta^{15}\text{N}$ and $\Delta\delta^{40}\text{Ar}$ is generated from. The δ_{therm} is thermal fractionation as calculated by eq. 11, while δ_{grav} is gravitational fractionation as calculated by eq. 10. Uncertainty is the error propagated standard deviation of the averages for the two periods.

Event #	Onset period (yr B2K)	Peak period (yr B2K)	$\Delta\delta^{15}\text{N}$ (‰)	$\Delta\delta^{40}\text{Ar}$ (‰)	δ_{therm} (‰)	δ_{grav} (‰)
0	11725-11740	11710-11715	0.23 ± 0.03	0.23 ± 0.03	0.00 ± 0.05	0.23 ± 0.04
A	13150-13220	12950-13010	0.08 ± 0.02	0.00 ± 0.03	0.10 ± 0.04	-0.01 ± 0.03
1	14870-14890	14815-14835	0.13 ± 0.02	0.19 ± 0.03	-0.08 ± 0.04	0.21 ± 0.03
1.5	15025-15075	14950-15010	0.01 ± 0.01	0.09 ± 0.03	-0.09 ± 0.04	0.10 ± 0.04
4	28855-28900	28810-28845	0.14 ± 0.02	0.07 ± 0.04	0.09 ± 0.05	0.06 ± 0.04
5.1	30950-31000	30800-30860	0.17 ± 0.02	-0.01 ± 0.03	0.21 ± 0.05	-0.05 ± 0.04
5	32670-32760	32470-32550	0.12 ± 0.02	0.09 ± 0.02	0.03 ± 0.03	0.09 ± 0.03
6	33910-34000	33710-33765	0.20 ± 0.01	0.12 ± 0.03	0.10 ± 0.04	0.10 ± 0.04
7	35410-35475	35325-35360	0.18 ± 0.01	0.11 ± 0.02	0.08 ± 0.03	0.10 ± 0.03
8	38370-38400	38300-38325	0.19 ± 0.02	0.16 ± 0.02	0.03 ± 0.03	0.16 ± 0.02
8.5	38465-38490	38415-38435	0.10 ± 0.01	0.09 ± 0.02	0.00 ± 0.03	0.09 ± 0.03
9	40390-40500	40160-40200	0.16 ± 0.02	0.20 ± 0.03	-0.05 ± 0.04	0.21 ± 0.04
10	41800-42000	41350-41600	0.09 ± 0.02	0.19 ± 0.03	-0.12 ± 0.04	0.21 ± 0.03
11	43355-43395	43310-43330	0.15 ± 0.02	0.11 ± 0.02	0.05 ± 0.03	0.10 ± 0.02
11.5	43460-43525	43405-43425	0.08 ± 0.01	0.05 ± 0.02	0.04 ± 0.03	0.04 ± 0.02

1.4.3 $\delta\text{Ar}/\text{N}_2$ discussion

Looking at the elemental ratio, it makes sense to address the enriched levels first. As discussed, not much credibility is owed to the absolute scale that the elemental ratio is bound to. In order to quantify the offset from the true values it will eventually be possible to rely on the discrete measurements from Todd Sowers again, as the elemental ratio was also determined during discrete sample measurements. As for the $\delta^{15}\text{N}$ comparison, these preliminary discrete measurements shall only be used for trend comparison. The combined data set of CFA and discrete measurements can be seen in Figure 29, where A, B and C represent the same three regions shown for Figure 22. While the absolute scale of the CFA might be off by a large magnitude, it is still valuable to discuss the trends seen for the three plots. Plot C display good agreement, with a stable level followed by an increase of approximately 5‰ for both the discrete and CFA measurement. Plot B has two regions with discrete data where both are going in the opposite direction to that of CFA. For plot A, there is a rather stable level measured by the CFA data, while there is a clear increase of 21‰ for the discrete measurements. This disagreement in behaviour is difficult to make sense of, as it is unlikely that such an increase would not be captured by the CFA, since the variability of the data is smaller than that. Similar sized increases are observed elsewhere in the data, so it is possible for such increases to be reflected in the CFA- data. Worth mentioning is that the glacial termination as observed in the gas-age occurs at the depth of 1788m, so it is reasonable that an increase should be observed. However, a gas-age bound increase would be driven by thermal and gravitational fractionation, and while I have not found the thermal sensitivity of Ar/N_2 , the overall increase ought to be on the order of 12 times that observed for $\delta^{15}\text{N}$, due to the difference in mass between $^{15}\text{N}/^{14}\text{N}$ and $^{40}\text{Ar}/^{28}\text{N}_2$. As can be confirmed from Figure 27, the increase seen for the glacial termination, named DO#0, the $\delta^{15}\text{N}$ increase was 0.23‰. The expected increase for the elemental ratio would then be about 2.76‰, close to an order of magnitude smaller than observed. Due to the large variation in the CFA data an increase of this size would get lost in the noise. This discrepancy will have to be left unanswered until the remaining discrete samples have been done, so as to allow for determining whether the CFA Ar/N_2 is unusable.

Though the variation in the data is too large for determining gravitational and thermal fractionation effects, there is the third type of fractionation, close-off fractionation that affects the elemental ratio. As discussed, the size of the effect depended on the physical properties of the ice at close-off. The

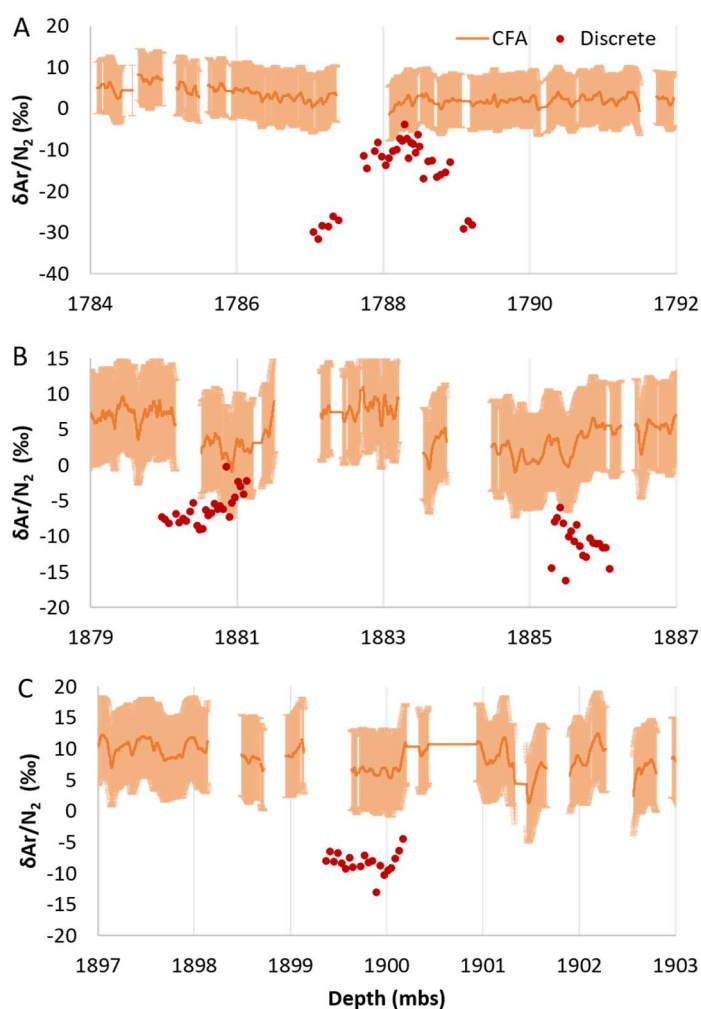


Figure 29: Plot of Ar/N_2 in ‰ of Dye-3, as measured by discrete measurements (red) and by CFA (orange) with error bars. The discrete data is provided by Todd Sowers, The Earth and Environment Systems Institute, Penn State University

effect should then line up with the ice-age rather than gas-age which would explain why no peak is seen in the CFA at 1788m below surface. In Figure 30 the data for $\delta^{18}\text{O}$, $\delta\text{Ar}/\text{N}_2$ and $[\text{CH}_4]$ have been plotted together against depth instead of age. The purpose of this is to determine whether the increases seen in $\delta\text{Ar}/\text{N}_2$ corresponds to events or if it is all due to the variation of the data. By comparing with $\delta^{18}\text{O}$ and $[\text{CH}_4]$ on the depth scale it is possible to determine if the events match with the ice or gas record. From the two plots matching increases can be seen for $\delta\text{Ar}/\text{N}_2$ simultaneous with $\delta^{18}\text{O}$, indicating that the close-off fractionations are dominating the signal with increases of upwards of 8‰. It is unfortunate that many of the transitions in the ice-age are lost, as it makes it impossible to make the same kind of onset-peak comparisons for $\delta\text{Ar}/\text{N}_2$ as done for the isotope effects.

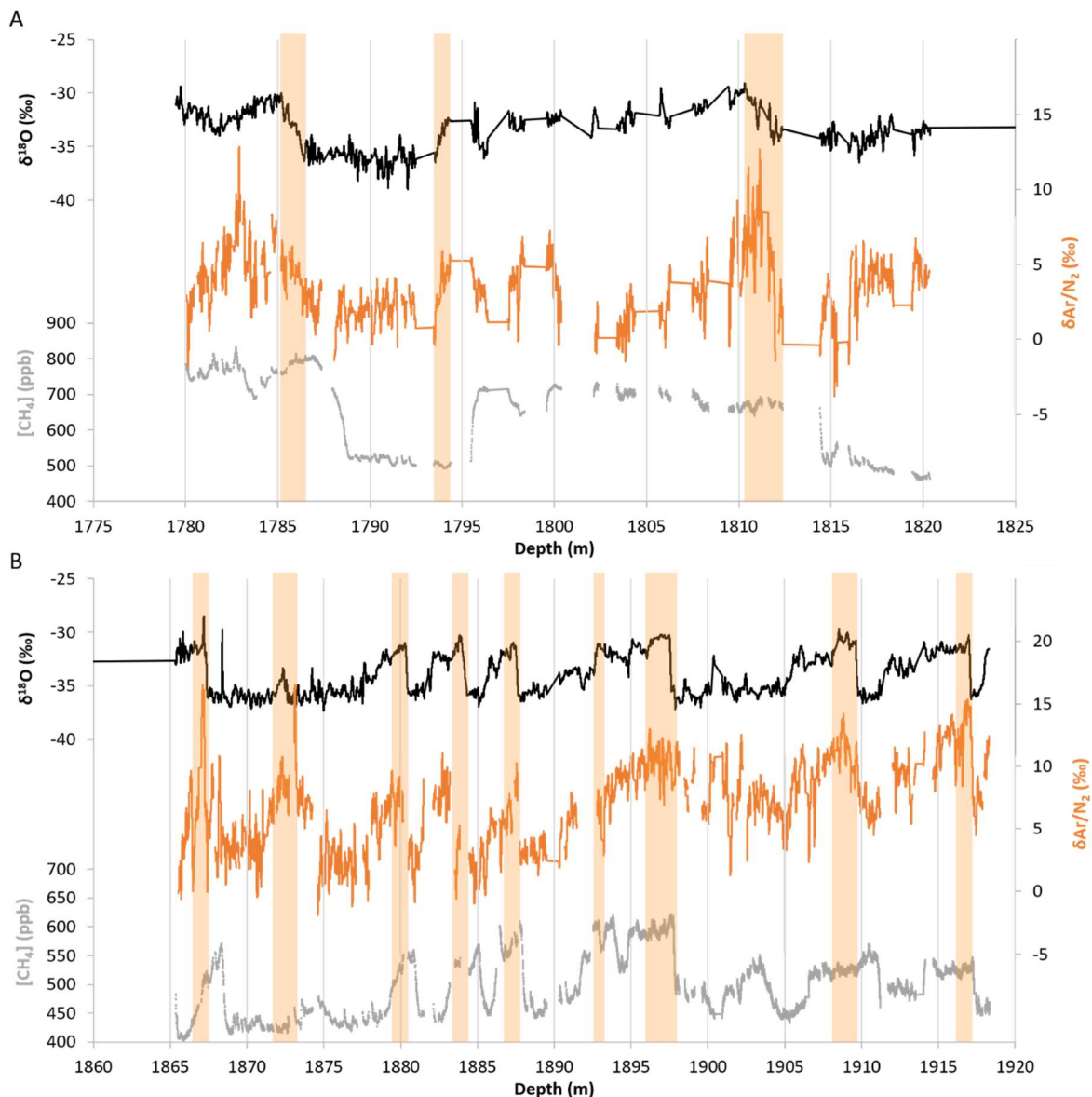


Figure 30: Timing comparison. Plotted is the data for $d^{18}\text{O}$ (black) in ‰, $d\text{Ar}/\text{N}_2$ (orange) in ‰ and $[\text{CH}_4]$ (grey) in ppb. All are plotted against depth.

$\delta\text{O}_2/\text{N}_2$ has been suggested as a proxy for summer insolation, and because of this I investigated if the same would be true for $\delta\text{Ar}/\text{N}_2$. The result of this can be seen in Figure 31.

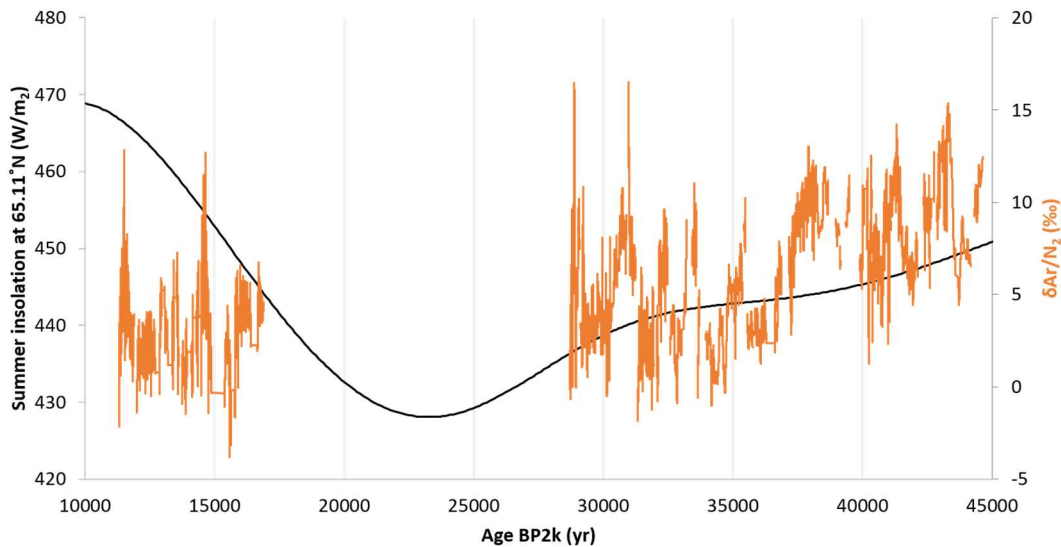


Figure 31: Mean summer insolation at Dye 3 (black) plotted along age, collected $\delta\text{Ar}/\text{N}_2$ data (orange) in ‰ plotted along ice-age.. The insolation has been computed from (Laskar, 2018) and is expressed as the average summer insolation in W/m^2 . The data has been calculated for latitude 65.11°N in 100 year steps, with a solar constant of $1368 \text{ W}/\text{m}^2$. $\delta\text{Ar}/\text{N}_2$ was plotted along ice age.

From observing the comparison between $\delta\text{Ar}/\text{N}_2$ and the calculated insolation, there is a clear discrepancy between the two data sets. While there is semblance of agreement between trends of the two data sets at 28000-45000 years, this break down when compared to the lack of a shared trend between 11000-16000 years. While $\delta\text{O}_2/\text{N}_2$ work as a proxy for summer insolation, from this data it would seem that the driving force for such a relation is not the close-off fractionation, as that would result in correlation with $\delta\text{Ar}/\text{N}_2$. When generating the insolation data, the orbital components going into it; such as eccentricity, climatic precession and obliquity was also generated, and here agreement between the climatic precession and the $\delta\text{Ar}/\text{N}_2$ was observed.

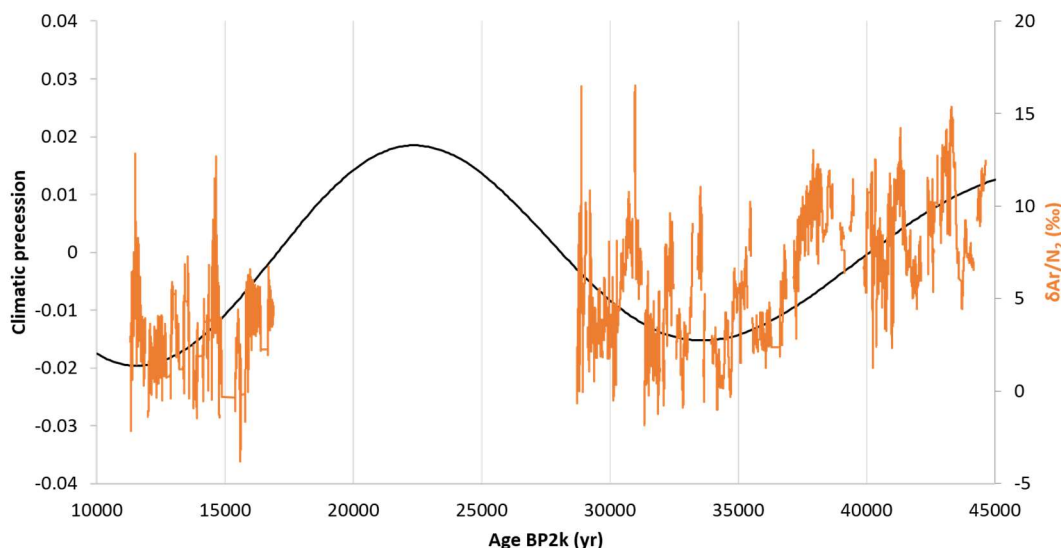


Figure 32: Mean climatic precession (black) plotted along age, collected $\delta\text{Ar}/\text{N}_2$ data (orange) in ‰ plotted along ice-age. The precession has been computed from (Laskar, 2018) and is unitless. The data has been calculated for latitude 65.11°N in 100 year steps. $\delta\text{Ar}/\text{N}_2$ is plotted along ice age.

From the results in Figure 32 a consistent correlation can be observed, though the certainty of it is reduced due to the lacking data in-between 16000-28000yrs that would otherwise confirm correlation at the peak as well. Another potential effect for the increase seen before 35000yrs would be that ice the ice comes from further upstream, where the snow fall conditions are different.

Even if this correlation is able to explain the long-term trends, the timing with DO-events is not explained by the orbital effects. That explanation should be found in the changes in the close-off fractionation as a result of changes in the ice-grain properties. The driver for this change must be bound to temperature, as it increases with the temperature changes seen in the $\delta^{18}\text{O}$ record. Though I have no knowledge or experience in physical properties, I would propose that it is possible that $\delta\text{Ar}/\text{N}_2$ could be used as a proxy for the density of snowfall. The snowfall density would at the very least also be dependent on the snow-grain structure. Increase in the temperature and accumulation would also come with an increase in initial density.

Whether this is the case will have to be determined by further investigation into the physical properties of the ice.

1.4.4 Total air content reconstruction

A final detail that was hoped to be extracted from the data was the total air content. Throughout the work the gas ratio has been used, which is not the same as TAC. The gas ratio was calculated as the gas volume divided by the total sample flow. The TAC can be determined by the CFA measurements, as the gas flow divided by the total liquid flow converted from volumetric to mass flow by converting it via the density of water. For the calculation the density of water at $p(20^\circ\text{C})$ was used which was found to be 0.9982kg/l. The value gained from this is close the TAC, but the loss of dissolved gas needs to be corrected for. The correction eq. 36 was used to calculate the EX of nitrogen. By combining the resulting EX_{N_2} with eq. 37, modified to find EX of oxygen as well as argon, the EX for the three main atmospheric gasses could be found. By weighing their EX with their atmospheric abundance, the total gas EX was found.

$$\text{EX}_{\text{tot}} = \chi_{\text{N}_2} \cdot \text{EX}_{\text{N}_2} + \chi_{\text{O}_2} \cdot \text{EX}_{\text{O}_2} + \chi_{\text{Ar}} \cdot \text{EX}_{\text{Ar}} \quad (42)$$

Dividing the uncorrected TAC by the EX_{tot} , yields the corrected TAC. Here it is approximated that the three main components Oxygen, Nitrogen and argon result in 100% of the atmospheric composition. For completeness' sake, the values for $\delta\text{O}_2/\text{N}_2$ and $\delta\text{Ar}/\text{N}_2$ should be used to correct for variation in the stored abundance, but as $\delta\text{O}_2/\text{N}_2$ was not measured by CFA and the $\delta\text{Ar}/\text{N}_2$ was poorly bound to an absolute scale those variations are not taken into account.

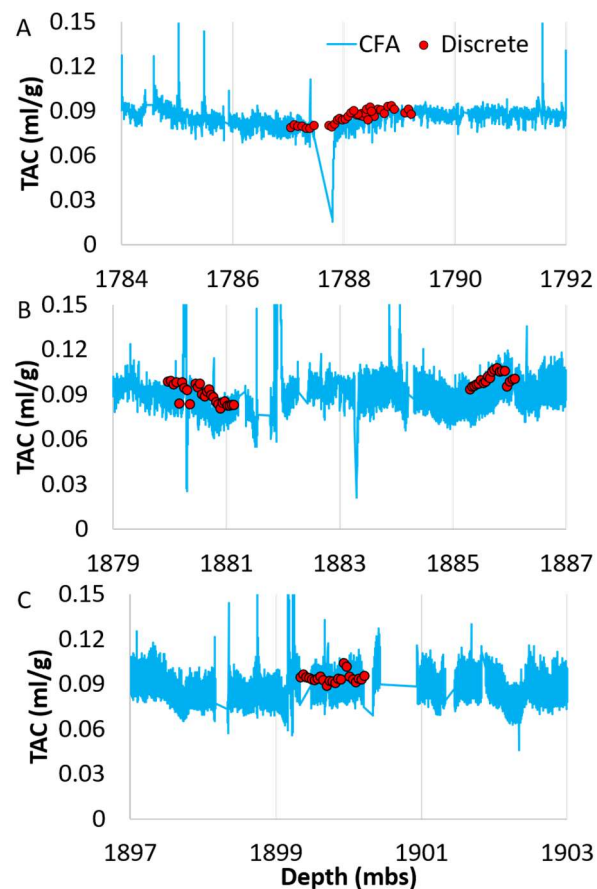


Figure 33: Overview of total air content as collected for CFA (blue) and discrete measurements (red) plotted along depth. Discrete measurements collected by Todd Sowers.

The resulting corrected TAC can be seen in Figure 33, where it is plotted alongside the TAC as collected by discrete samples. There is very good agreement between the two TAC measurements, though the measured TAC_{CFA} is still slightly lower than the discrete measurements. The good agreement between the two types of measurements is reassuring, but because the found TAC_{CFA} is still lower than as determined by discrete measurements the preferential gas loss at the melthead cannot be dismissed.

The behaviour of TAC across the core can be seen in Figure 34, where a 30 sec smoothed TAC record is plotted against depth together with the $\delta^{18}O$ record and TAC as measured from the discrete samples. The 30 sec smoothing was needed to remove the high frequency noise coming from the arrival of bubble bundles. From the plot, agreement can be seen between TAC and $\delta^{18}O$, which is surprising. Warmer temperatures should result in a lower molecule density of the gas, which would lead to lower TAC. Since the discrete samples agree with the observed trends, it seems possible to generate reliable TAC measurements from CFA.

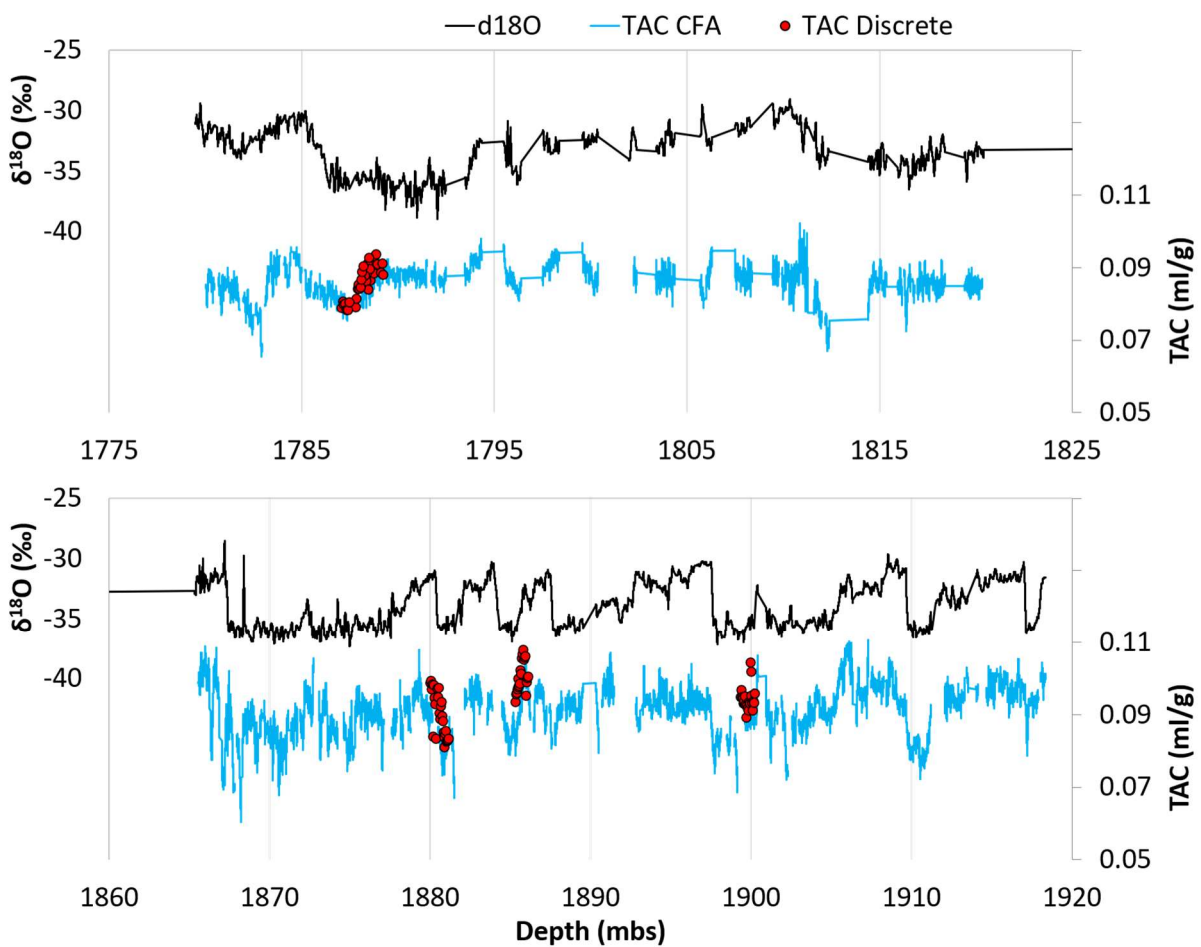


Figure 34: Plot of $\delta^{18}O$ (black) in ‰, and a 30 sec running average of TAC (light blue) in ml/g, plotted along the ice-age.

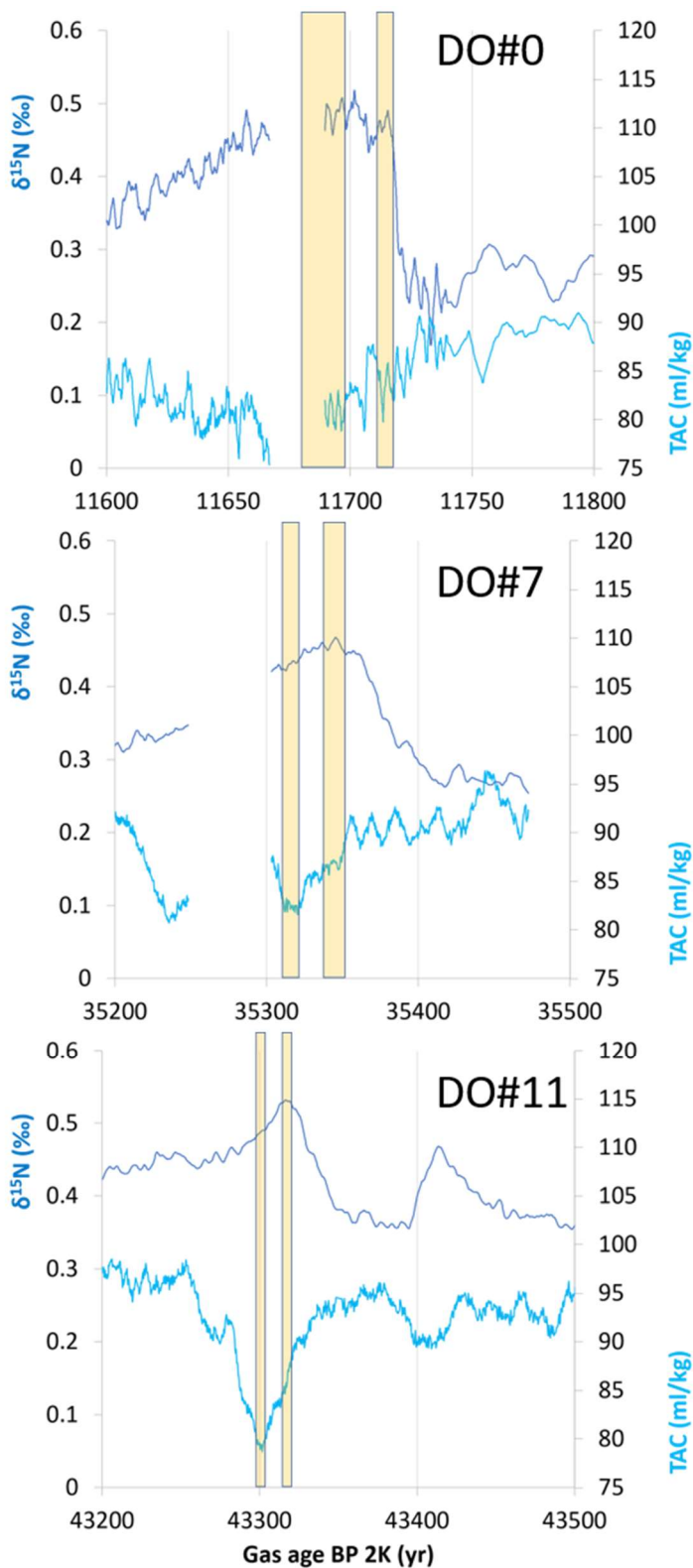


Figure 35: Zoom in on DO#0, DO#7 and DO#11, with $\delta^{15}\text{N}$ (dark blue) along the right axes in ‰, and the 30 sec smoothed TAC (light blue) along the left axes in $\text{ml}/\text{kg}_{\text{ice}}$. Highlighted are the peaks and valleys of the two data sets. Both records are plotted along gas age.

In order to investigate whether the observed drop for TAC prior to DO-events in NGRIP also occurs here, a comparison was made between the $\delta^{15}\text{N}$ record and TAC. A negative correlation between TAC and $\delta^{15}\text{N}$ across the core was found. In order to investigate the decrease seen for TAC at DO-events, event 0, 7 and 11 were magnified in Figure 35. While the absolute value of TAC cannot be trusted, the relative change is representative. From these changes it is possible to see the average drop of around $10\text{ml}_{\text{gas}}/\text{kg}_{\text{ice}}$, slightly is delayed by 20-40 years compared to the $\delta^{15}\text{N}$ for the three events.

In comparison to the findings of (Olivier Eicher, 2016), that reported the effect of the drop lasted upwards of hundreds of years after, the Dye 3 cores seems to be quicker at getting back to normal. This might be explained by the higher temperature at Dye 3 than at NGRIP, which would bring the firn column to equilibrium quicker, thus ending the enhanced densification described. Furthermore, the drop is twice as high as the decrease observed for NGRIP, which can most likely be explained by the higher accumulation at Dye 3 compared to NGRIP, which would increase the enhanced densification effect.

The options for using the relative TAC measurements from the Dye 3 campaign might be a valuable addition for determining the effects influencing the TAC.

1.6 Future work

The work of this campaign was experimental in whether it would be possible to gather continuous measurements of gas isotopes in combination with the CFA. Based on the work presented here I would strongly argue that this is the case, though the current setup leaves room for improvements, as I have been limited to discuss the relative changes rather than the absolute values because of n.

In the following I give suggestions for how to improve the CFA setup to make the measurement of gas isotopes more reproducible.

- The oxygen removal setup could benefit from a redesign. As described, attempts were made to seal the membrane piece in between two SS-tubes, in a manner that allows applying a lower vacuum than the 200mbar used. This would allow for a lower pressure at the micromodule, which increases the EX.
- Standards: Since a static standard was not available, a large source of variation for $\delta^{40}\text{Ar}$ was introduced. and is the main source of variation seen for $\delta^{40}\text{Ar}$. A dynamically mixed standard is still needed for testing the effects chemical slope and solubility, but it needs to be in addition to a static standard.
- If lab-air is to be used for binding the standard, the sampling of it needs to be made from a well-mixed location.
- An easy way of improving the calibration time efficiency would be to attain standards that can work for both methane and isotope measurements, as switching between the two created down time. An additional benefit of this would be that measurements of the solubility effect would be accounted for with every calibration run, compared to the single time it was investigated for this campaign.
- Repetition of the pressure imbalance and chemical slope effects for greater reproducibility.
- Repeat solubility effect experiments with varying levels of starting temperature.
- While it might not be feasible with the methods at hand, producing calibration ice which is loaded with known standard gas could be a powerful tool to get the fractionation effects across the entire sample path.
- Debubbling of mQ-water ought to be done with helium instead of the used N_2 , to avoid loading the water with N_2 which would skew the derived solubility effects.
- The loss of sample at the melthead can be reduced with increased pumping at the inner cross-section of the melthead. The set-point used for the driving peristaltic pump was 23ml/min but due to restrictions at the valves, the targeted flow was not reached. My suggestion is therefore to increase the valve size from 1/16" connections to 1/8" tubes as used throughout most the CFA setup.
- The uncertainty in TAC_{CFA} in general is due to the arrival of bubble bundles, rather than individual bubbles. If these bundles could be split up, the resulting flow will be more even and will allow for smaller uncertainty in TAC assignment and solubility effect correction.
- The IRMS is susceptible to short-term drift, and with measurements running for multiple hours continuously, such drift might cause systematic error. Steady stream of standard gas should be supplied through the system, and left for thrice the time of a measurement run to observe the signal intensity drift across time.

The data presented in this work only represents the gas measurements acquired during the Dye 3 melting, but more data was collected during the campaign. The data from the chemistry side plus the dust content need to be analysed and used for comparison. Additionally, the measurement of all the discrete samples for the gas measurements are not completed yet, and might be valuable to help binding the results to an absolute scale.

1.7 Conclusion

In preparation for the melting campaign of Dye 3 a setup was successfully developed that allowed for measurements of gaseous isotopes extracted from the CFA melt stream. This was done by taking a subsample from the gas extracted for methane analysis. This subsample was then analysed by IRMS, generating isotope data with high temporal resolution. The integral part of this setup was the development of a method for continuous oxygen removal. This was done by the use of a perovskite membrane heated to 850°C, which is permeable to oxygen, while acting as a barrier for other gas components. The removal efficiency was 98% and was stable across experiments.

Because the IRMS used, was designed for discrete measurements, multiple effects offsetting the derived delta value, had to be corrected manually. The effects needing corrections, was the pressure imbalance and chemical slope effects. The most significant of these effects was the solubility of gasses, causing fractionating on the isotopes and most severely on the elemental ratio. Correcting for these relied on empirically derived correction functions, done prior to the campaign.

The developed system was tested out on the bottom 1750-1920m of the old ice core from Dye 3. Dye 3 was found to be a well-suited core for testing the new system, as the response in the isotopes, elemental ratio and TAC was larger and better resolved than for other cores, making full use of the high temporal resolution of the new setup. Thanks to the increased number of sample stream measurements implemented in the combined gas extraction setup, it was possible to determine the varying travel time from the melthead to the gas detection, thereby improving the accuracy of the depth assignment, compared to constant delay assumption used in previous work. Based on the multiple measurements of gas and liquid flow and proper investigation of the solubility effect on gas loss, reconstructing the relative changes of total air content with CFA was possible, and have been confirmed by discrete samples.

The $\delta^{15}\text{N}$ was recorded with an uncertainty <50per meg, which allowed for detailed analysis of the response to climatic events. These responses were compared to those of the $\delta^{15}\text{N}$ record from NGRIP, where the responses in Dye 3 were larger and transpired over fewer years when compared to NGRIP. This highlighted the local differences between the two cores.

The measured average stadial level of 0.25‰, implies an implausibly shallow firn column. This finding can be partially explained by the fact that the solubility fractionation is underestimated for ^{15}N . The explanation for this is assumed to be an underestimation of solubility fractionation.

The $\delta^{40}\text{Ar}$ data suffered from great variation between measurement runs, owing to unstable conditions in the lab-air which was used as the standard. But by taking the mass scaled relative values for each measurement run, a record emerged with climatic responses comparable to those for $\delta^{15}\text{N}$. By closer comparison of the two isotope records, the effect of thermal and gravitational fractionation was determined, though with a high degree of uncertainty.

For the elemental ratio Ar/N_2 the variation was too large to observe thermal and gravitational fractionation, but the close-off fractionation was detectable with increases of 8‰ synchronized with DO-events in the ice-age. Discrepancies were, however, seen in climatic responses when compared to discrete samples.

While the current version of the system could not produce the stability to generate isotope data bound to an absolute scale, the relative measurements acquired in this work are with high precision and allows for detailed analysis. With the coming addition of data from both the liquid analysis of CFA and the remaining discrete gas samples, more data can be extracted from the CFA-gas record.

References

- Amaelle Landais, J. P.-D. (2004, March 20). Evidence for stratigraphic distortion in the Greenland Ice Core Project (GRIP) ice core during Event 5e1 (120 kyr BP) from gas isotopes. *Journal of Geophysical Research*, 109. doi:10.1029/2003JD004193
- Andreas Sigg, K. F. (1994). A Continuous Analysis Technique for Trace Species in Ice Cores. *Environmental science and technology research*, 28(2), pp. 204-209.
- Bender, M. L. (2002, July 19). Orbital tuning chronology for the Vostok climate record supported by trapped gas composition. *Earth and Planetary Science Letters*, pp. 275-289.
- Bender, T. S. (1989, April 20). ELEMENTAL AND ISOTOPIC COMPOSITION OF OCCLUDED O₂ AND N₂ IN POLAR ICE. *JOURNAL OF GEOPHYSICAL RESEARCH*, 94(D4), pp. 5137-5150.
- Buizert, C. (2013). Studies of Firn Air. *Ice Core Methods*, pp. 361-372.
- C. Buizert, B. A. (2008). Greenland-wide seasonal temperatures during the last deglaciation. *Geophysical Review Letters*, pp. 1905-1914. doi:10.1002/2017GL075601
- C. Buizert, P. M. (2012, May 14). Gas transport in firn: multiple-tracer characterisation and model intercomparison for NEEM, Northern Greenland. *Atmospheric chemistry and physics*, pp. 4259-4277. doi:10.5194/acp-12-4259-2012
- C. Huber, U. B. (2006, December 15). Evidence for molecular size dependent gas fractionation in firn air derived from noble gases, oxygen, and nitrogen measurements. pp. 61-73. doi:10.1016/j.epsl.2005.12.036
- C. Stowasser, C. B. (2012, May 9). Continuous measurements of methane mixing ratios from ice cores. *Atmospheric Measurements Techniques*, pp. 999-1013. doi:10.5194/amt-5-999-2012
- D. Dahl-Jensen, K. M. (1998, October 9). Past Temperatures Directly from Greenland Ice Sheet. *Science*, pp. 268-271.
- Dansgaard, W. (2004). *Frozen Annals- Greenland Ice Sheet REsearch*. Odder: Narayana PRes.
- Dieter Lüthi, M. L.-M. (2008, May 15). High-resolution carbon dioxide concentration record 650,000-800,000 years before present. *Nature*, pp. 379-382. doi:10.1038/nature06949
- G. H. Denton, R. F. (2010, June 25). The Last Glacial Termination. *Science*, pp. 1652-1656. doi:10.1126/science.1184119
- H. CRAIG, Y. H. (1988, December 23). Gravitational Separation of Gases and Isotopes in Polar Ice Caps. *AAAS*, pp. 1675-1678.
- J. SCHWANDER, J.-M. B.-. (1993, February 20). The Age of the Air in the Firn and the Ice at Summit, Greenland. *Journal of Geophysical research*, 98(D2), pp. 2831-2838.
- Jansc , G. (2001, October 15). Interpretation of isotope effects on the solubility of gases. *Nukleonika*, pp. S53-S57.
- Jeffrey P. Severinghaus, T. S. (1998, January 8). Timing of abrupt climate change at the end of the Younger Dryas interval from thermally fractionated gases in polar ice. *Nature*, pp. 141-146.

- John H. Seinfeld, S. N. (2006). Chemistry of the atmospheric aqueous phase. In J. H. Pandis, *Atmospheric chemistry and physics: From air pollution to climate change* (Vol. 2, pp. 284-292). John Wiley & sons, inc.
- K. K. Andersen, e. (. (2004, September 9). High-resolution record of Northern Hemisphere climate extending into the last interglacial period. *Nature*, pp. 147-151.
- K. Kawamura, J. P. (2013, November 15). Kinetic fractionation of gases by deep air convection in polar firn. *Atmospheric chemistry and physics*, pp. 11141-11155. doi:10.5194/acp-13-11141-2013
- Kasting, J. F. (2001, August 3). The Rise of Atmospheric Oxygen. *Science*, pp. 819-820.
- KONG Xinggong, W. Y. (2005, June 6). Complicated responses of stalagmite $\delta^{13}\text{C}$ to climate change during the last glaciation from Hulu Cave, Nanjing, China. *Sci. China Ser. D-Earth Sci.* doi:10.1360/04yd0140
- Laetitia Loulergue, A. S.-D.-M. (2008, May 15). Orbital and millennial-scale features of atmospheric CH_4 over the past 800,000 years. *Nature*, pp. 383-386. doi:10.1038/nature06950
- Langway, C. C. (1985). Greenland ice core: geophysics, geochemistry, and the environment. Washington, DC: American Geophysical Union.
- Laskar, J. R. (2018, November 18). Compute insolation quantities derived from the orbital and precessional quantities. doi:10.1051/0004-6361:20041335
- LORIUS, D. R. (1973). Climatic Implications of Total Gas Content in Ice at Camp Century. *Nature*, pp. 283-284.
- Mariotti, A. (1983, June 3). Atmospheric nitrogen is a reliable standard for natural ^{15}N abundance measurements. *Nature*, 303, pp. 685-687. doi:10.1038/303685a0
- MICHAEL L. BENDER, P. P. (1994). A high precision isotope ratio mass spectrometry method for measuring the O_2/N_2 ratio of air. *Geochimica et Cosmochimica Acta*, pp. 4751-4758.
- Michael M. Herron, C. C. (1980). Firn densification: An empirical model. *Journal of Glaciology*, 23(93), pp. 374-385.
- Miller, S. L. (1969, August 1). Clathrate Hydrates of Air in Antarctic Ice. *Science, New Series*, pp. 489-490.
- N. Reeh, S. J.-J. (1985). Dating the Dye 3 Deep ice core by flow model calculations. In H. O. C.C. Langway Jr., *Greenland Ice Core: Geophysics, Geochemistry, and the Environment, Volume 33* (pp. 57-65). Copenhagen: American Geophysical Union. doi:10.1029/GM033p0057
- NASA. (2011). *Chemical Kinetics and Photochemical Data for Use in Atmospheric Studies*. JPL Publication.
- Olivier Eicher, M. B. (2016, October 14). Climatic and insolation control on the high-resolution total air content in the NGRIP ice core. *Climate of the Past*, pp. 1979-1993. doi:10.5194/cp-12-1979-2016
- P. Kindler, M. G. (2014, April 30). Temperature reconstruction from 10 to 120 kyr b2k from the NGRIP ice core. *Climate of the Past*, pp. 887-902. doi:10.5194/cp-10-887-2014

- Rachael H. Rhodes, X. F. (2013, April 3). Continuous methane measurements from a late Holocene Greenland ice core: Atmospheric and in-situ signals. *Earth and Planetary Science Letters*, pp. 9-19. doi:10.1016/j.epsl.2013.02.034
- Reutenauer, C. (2016). *Measuring the triple O2 isotopic composition of air trapped in ice cores and quantifying the causes of $\delta^{18}O_{atm}$ millennial scale variations*. Copenhagen University, Centre for ice and climate.
- Roth-Nebelsick, A. (2004, December 22). Reconstructing atmospheric carbon dioxide with stomata: possibilities and limitations of a botanical pCO_2 -sensor. *Trees*, pp. 251-265. doi:10.1007/s00468-004-0375-2
- Severinghaus, J. P., Grachev, A., & Battle, M. (2001, July 31). Thermal fractionation of air in polar firn by seasonal temperature gradients. *Geochemistry Geophysics Geosystems*, pp. 1525-2027.
- Sowers, T. (2020, February). preliminary data from discrete ice samples from dye 3. *Personal communications*.
- Sune O. Rasmussen, M. B.-J. (2014, October 5). A stratigraphic framework for abrupt climatic changes during the Last Glacial period based on three synchronized Greenland ice-core records: refining and extending the INTIMATE event stratigraphy. *Quaternary Science Reviews*, pp. 14-28. doi:10.1016/j.quascirev.2014.09.007
- Svensson, A. K.-J. (2008, March 31). A 60 000 year Greenland stratigraphic ice core chronology. *Clim. Past*, pp. 47-57.
- Takuro Kobashi, J. P. (2008, July 17). Argon and nitrogen isotopes of trapped air in the GISP2 ice core during the Holocene epoch (0-11,500 B.P.): Methodology and implications for gas loss processes. *Elsevier*, pp. 4675-4686. doi:10.1016/j.gca.2008.07.006
- Venkatesh, J. (2020). *An improved Gas-CFA system for methane measurements and preliminary results from the Dye-3 ice core*. Niels Bohr Institute, Physics of ice, climate and earth. Copenhagen University.
- Vinther, B. (2020, April 29). Retrieved from iceandclimate: http://www.iceandclimate.nbi.ku.dk/research/climatechange/glacial_interglacial/climate_holocene/
- Vladimirova, D. (2018, October 8). High-resolution methane record of the RECAP ice core (Eastern Greenland) over the last climatic cycle. Copenhagen University.

2. Paper on N₂O isotopic measurements using laser spectroscopy; analyser characterization and intercomparison

Presented next is the article based on the work I took part of at Empa in Switzerland.

The article outlines an inter-lab collaboration undertaken at Empa in Switzerland. Here the performance and limitations of ambient measurements of N₂O and its isotopes were compared between different instruments using laser spectroscopy. Effects from trace gas and matrix composition were determined, and the non-linear relationship with N₂O abundance was described. An extensive guideline was developed for how to produce reproducible measurements of N₂O isotopes using these instruments, giving comparable precision to IRMS.

The article can be found on:

<https://www.atmos-meas-tech-discuss.net/amt-2019-451/>



N₂O isotopocule measurements using laser spectroscopy: analyzer characterization and intercomparison

Stephen J. Harris^{1,2,*}, Jesper Liisberg^{3,*}, Longlong Xia⁴, Jing Wei⁵, Kerstin Zeyer⁵, Longfei Yu⁵, Matti Barthel⁶, Benjamin Wolf⁴, Bryce F. J. Kelly¹, Dioni I. Cendón², Thomas Blunier³, Johan Six⁶, and Joachim Mohn⁵

¹School of Biological, Earth and Environmental Sciences, UNSW Sydney, NSW, Australia

²Australian Nuclear Science and Technology Organisation, Lucas Heights, NSW, Australia

³University of Copenhagen, Niels Bohr Institute, Copenhagen, Denmark

⁴Karlsruhe Institute of Technology, IMK-IFU, Garmisch-Partenkirchen, Germany

⁵Empa, Laboratory for Air Pollution/Environmental Technology, Dübendorf, Switzerland

⁶ETH Zürich, Department of Environmental Systems Science, Zürich, Switzerland

*These authors contributed equally to this work.

Correspondence: Joachim Mohn (joachim.mohn@empa.ch)

Received: 25 November 2019 – Discussion started: 5 December 2019

Revised: 15 April 2020 – Accepted: 21 April 2020 – Published:

Abstract. For the past two decades, the measurement of nitrous oxide (N₂O) isotopocules – isotopically substituted molecules ¹⁴N¹⁵N¹⁶O, ¹⁵N¹⁴N¹⁶O and ¹⁴N¹⁴N¹⁸O of the main isotopic species ¹⁴N¹⁴N¹⁶O – has been a promising technique for understanding N₂O production and consumption pathways. The coupling of non-cryogenic and tuneable light sources with different detection schemes, such as direct absorption quantum cascade laser absorption spectroscopy (QCLAS), cavity ring-down spectroscopy (CRDS) and off-axis integrated cavity output spectroscopy (OA-ICOS), has enabled the production of commercially available and field-deployable N₂O isotopic analyzers. In contrast to traditional isotope-ratio mass spectrometry (IRMS), these instruments are inherently selective for position-specific ¹⁵N substitution and provide real-time data, with minimal or no sample pre-treatment, which is highly attractive for process studies.

Here, we compared the performance of N₂O isotope laser spectrometers with the three most common detection schemes: OA-ICOS (N₂-OIA-30e-EP, ABB – Los Gatos Research Inc.), CRDS (G5131-i, Picarro Inc.) and QCLAS (dual QCLAS and preconcentration trace gas extractor (Trex)-mini QCLAS, Aerodyne Research Inc.). For each instrument, the precision, drift and repeatability of N₂O mole fraction [N₂O] and isotope data were tested. The analyzers were then characterized for their dependence on [N₂O], gas matrix composition (O₂, Ar) and spectral in-

terferences caused by H₂O, CO₂, CH₄ and CO to develop analyzer-specific correction functions. Subsequently, a simulated two-end-member mixing experiment was used to compare the accuracy and repeatability of corrected and calibrated isotope measurements that could be acquired using the different laser spectrometers.

Our results show that N₂O isotope laser spectrometer performance is governed by an interplay between instrumental precision, drift, matrix effects and spectral interferences. To retrieve compatible and accurate results, it is necessary to include appropriate reference materials following the identical treatment (IT) principle during every measurement. Remaining differences between sample and reference gas compositions have to be corrected by applying analyzer-specific correction algorithms. These matrix and trace gas correction equations vary considerably according to N₂O mole fraction, complicating the procedure further. Thus, researchers should strive to minimize differences in composition between sample and reference gases. In closing, we provide a calibration workflow to guide researchers in the operation of N₂O isotope laser spectrometers in order to acquire accurate N₂O isotope analyses. We anticipate that this workflow will assist in applications where matrix and trace gas compositions vary considerably (e.g., laboratory incubations, N₂O liberated from wastewater or groundwater), as well as extend to

future analyzer models and instruments focusing on isotopic species of other molecules.

1 Introduction

Nitrous oxide (N₂O) is a long-lived greenhouse gas with a 100-year global warming potential nearly 300 times that of carbon dioxide (CO₂; Forster et al., 2007) and is the largest emission source of ozone-depleting nitrogen oxides in the stratosphere (Ravishankara et al., 2009). In 2019, the globally averaged [N₂O] reached approximately 332 ppb compared to the pre-industrial level of 270 ppb (NOAA/ESRL, 2019). While this increase is known to be linked primarily to increased fertilizer use in agriculture (Bouwman et al., 2002; Mosier et al., 1998; Tian et al., 2015), understanding the underlying microbial processes producing and consuming N₂O has proved more challenging, and individual source contributions from sectors such as agricultural soils, wastewater management and biomass burning to global bottom-up estimates of N₂O emissions have large uncertainties (Denman et al., 2007). Stable isotopes are an effective tool for distinguishing N₂O sources and determining production pathways, which is critical for developing appropriate mitigation strategies (Baggs, 2008; Ostrom and Ostrom, 2011; Toyoda et al., 2017).

The N₂O molecule has an asymmetric linear structure (NNO), with the following most abundant isotopocules: ¹⁴N¹⁵N¹⁶O (¹⁵N^α-N₂O); ¹⁵N¹⁴N¹⁶O (¹⁵N^β-N₂O); ¹⁴N¹⁴N¹⁸O (¹⁸O-N₂O); and ¹⁴N¹⁴N¹⁶O (Yoshida and Toyoda, 2000). The terms ¹⁵N^α and ¹⁵N^β refer to the respective central and terminal positions of nitrogen (N) atoms in the NNO molecule (Toyoda and Yoshida, 1999). Isotopic abundances are reported in δ notation, where $\delta^{15}\text{N} = R(^{15}\text{N}/^{14}\text{N})_{\text{sample}}/R(^{15}\text{N}/^{14}\text{N})_{\text{reference}} - 1$ denotes the relative difference in per mil (‰) of the sample versus atmospheric N₂ (AIR-N₂). The isotope ratio $R(^{15}\text{N}/^{14}\text{N})$ equals $x(^{15}\text{N})/x(^{14}\text{N})$, with x being the absolute abundance of ¹⁴N and ¹⁵N, respectively. Similarly, Vienna Standard Mean Ocean Water (VSMOW) is the international isotope-ratio scale for δ¹⁸O. In practice, the isotope δ value is calculated from measurement of isotopocule ratios of sample and reference gases, with the latter being defined on the AIR-N₂ and VSMOW scales. By extension, δ¹⁵N^α denotes the corresponding relative difference of isotope ratios for ¹⁴N¹⁵N¹⁶O/¹⁴N¹⁴N¹⁶O, and δ¹⁵N^β for ¹⁵N¹⁴N¹⁶O/¹⁴N¹⁴N¹⁶O. The site-specific intramolecular distribution of ¹⁵N within the N₂O molecule is termed ¹⁵N-site preference (SP) and is defined as $\text{SP} = \delta^{15}\text{N}^{\alpha} - \delta^{15}\text{N}^{\beta}$ (Yoshida and Toyoda, 2000). The term δ¹⁵N^{bulk} is used to express the average δ¹⁵N value and is equivalent to $\delta^{15}\text{N}^{\text{bulk}} = (\delta^{15}\text{N}^{\alpha} + \delta^{15}\text{N}^{\beta})/2$.

Extensive evidence has shown that SP, δ¹⁵N^{bulk} and δ¹⁸O can be used to differentiate N₂O source processes and

biogeochemical cycling (Decock and Six, 2013; Denk et al., 2017; Heil et al., 2014; Lewicka-Szczebak et al., 2014, 2015; Ostrom et al., 2007; Sutka et al., 2003, 2006; Toyoda et al., 2005, 2017; Wei et al., 2017). Isotopocule abundances have been measured in a wide range of environments, including the troposphere (Harris et al., 2014a; Röckmann and Levin, 2005; Toyoda et al., 2013), agricultural soils (Buchen et al., 2018; Ibraim et al., 2019; Köster et al., 2011; Mohn et al., 2012; Ostrom et al., 2007; Park et al., 2012; Pérez et al., 2001, 2006; Toyoda et al., 2011; Verhoeven et al., 2018, 2019; Well et al., 2008; Well and Flessa, 2009; Wolf et al., 2015), mixed urban-agricultural environments (Harris et al., 2017), coal and waste combustion (Harris et al., 2014b; Ogawa and Yoshida, 2005), fossil fuel combustion (Toyoda et al., 2008), wastewater treatment (Harris et al., 2015a, b; Wunderlin et al., 2012, 2013), groundwater (Koba et al., 2009; Minamikawa et al., 2011; Nikolenko et al., 2019; Well et al., 2005, 2012), estuaries (Erler et al., 2015), mangrove forests (Murray et al., 2018), stratified water impoundments (Yue et al., 2018), and firn air and ice cores (Bernard et al., 2006; Ishijima et al., 2007; Prokopiou et al., 2017). While some applications like laboratory incubation experiments allow for analysis of the isotopic signature of the pure source, most studies require analysis of the source diluted in ambient air. This specifically applies to terrestrial ecosystem research, since N₂O emitted from soils is immediately mixed with background atmospheric N₂O. To understand the importance of soil emissions for the global N₂O budget, two-end-member mixing models commonly interpreted using Keeling or Miller-Tans plots are frequently used to back-calculate the isotopic composition of N₂O emitted from soils (Keeling, 1958; Miller and Tans, 2003).

N₂O isotopocules can be analyzed by isotope-ratio mass spectrometry (IRMS) and laser spectroscopic techniques, with currently available commercial spectrometers operating in the mid-infrared (MIR) region to achieve highest sensitivities. IRMS analysis of the N₂O intramolecular ¹⁵N distribution is based on quantification of the fragmented (NO⁺, m/z 30 and 31) and molecular (N₂O⁺, m/z 44, 45 and 46) ions to calculate isotope ratios for the entire molecule (¹⁵N/¹⁴N and ¹⁸O/¹⁶O) and the central (N^α) and terminal (N^β) N atom (Toyoda and Yoshida, 1999). The analysis of N₂O SP by IRMS is complicated by the rearrangement of N^α and N^β in the ion source, while analysis of δ¹⁵N^{bulk} (45/44) involves correction for NN¹⁷O (mass 45). IRMS can achieve repeatability as good as 0.1‰ for δ¹⁵N, δ¹⁸O, δ¹⁵N^α and δ¹⁵N^β (Potter et al., 2013; Röckmann and Levin, 2005), but an interlaboratory comparison study showed substantial deviations in measurements of N₂O isotopic composition, in particular for SP (up to 10‰) (Mohn et al., 2014).

The advancement of mid-infrared laser spectroscopic techniques was enabled by the invention and availability of non-cryogenic light sources which have been coupled with different detection schemes, such as direct absorption quantum cascade laser absorption spectroscopy (QCLAS; Aerodyne

Research Inc. (ARI); Wächter et al., 2008), cavity ring-down spectroscopy (CRDS; Picarro Inc.; Berden et al., 2000) and off-axis integrated cavity output spectroscopy (OA-ICOS; ABB – Los Gatos Research Inc.; Baer et al., 2002) to realize compact field-deployable analyzers. In short, the emission wavelength of a laser light source is rapidly and repetitively scanned through a spectral region containing the spectral lines of the target N_2O isotopocules. The laser light is coupled into a multi-path cell filled with the sample gas, and the mixing ratios of individual isotopic species are determined from the detected absorption using Beer's law. The wavelengths of spectral lines of N_2O isotopocules with distinct ^{17}O , ^{18}O or position-specific ^{15}N substitution are unique due to the existence of characteristic rotational-vibrational spectra (Rothman et al., 2005). Thus, unlike IRMS, laser spectroscopy does not require mass-overlap correction. However, the spectral lines may have varying degrees of overlap with those of other gaseous species, which, if unaccounted for, may produce erroneous apparent absorption intensities. One advantage of laser spectroscopy is that instruments can analyze the N_2O isotopic composition in gaseous mixtures (e.g., ambient air) in a flow-through mode, providing real-time data with minimal or no sample pretreatment, which is highly attractive to better resolve the temporal complexity of N_2O production and consumption processes (Decock and Six, 2013; Heil et al., 2014; Köster et al., 2013; Winther et al., 2018).

Despite the described inherent benefits of laser spectroscopy for N_2O isotope analysis, applications remain challenging and are still scarce for four main reasons:

1. Two pure N_2O isotopocule reference materials (USGS51, USGS52) have only recently been made available through the United States Geological Survey (USGS) with provisional values assigned by the Tokyo Institute of Technology (Ostrom et al., 2018). The lack of N_2O isotopocule reference materials was identified as a major reason limiting interlaboratory compatibility (Mohn et al., 2014).
2. Laser spectrometers are subject to drift effects (e.g., due to moving interference fringes), particularly under fluctuating laboratory temperatures, which limits their performance (Werle et al., 1993).
3. If apparent δ values retrieved from a spectrometer are calculated from raw uncalibrated isotopocule mole fractions, referred to here as a δ -calibration approach, an inverse concentration dependence may be introduced. This can arise if the analyzer measurements of isotopocule mole fractions are linear, yet the relationship between measured and true mole fractions has a non-zero intercept (e.g., Griffith et al., 2012; Griffith, 2018), such as due to baseline structures (e.g., interfering fringes; Tuzson et al., 2008).

4. Laser spectroscopic results are affected by mole fraction changes of atmospheric background gases (N_2 , O_2 and Ar), herein called gas matrix effects, due to the difference of pressure-broadening coefficients (Nara et al., 2012) and potentially by spectral interferences from other atmospheric constituents (H_2O , CO_2 , CH_4 , CO , etc.), herein called trace gas effects, depending on the selected wavelength region. The latter is particularly pronounced for N_2O due to its low atmospheric abundance in comparison to other trace gases.

Several studies have described some of the above effects for CO_2 (Bowling et al., 2003, 2005; Griffiths et al., 2004; Griffith et al., 2012; Friedrichs et al., 2010; Malowany et al., 2015; Pataki et al., 2006; Pang et al., 2016; Rella et al., 2013; Vogel et al., 2013; Wen et al., 2013), CH_4 (Eyer et al., 2016; Griffith et al., 2012; Rella et al., 2013) and recently N_2O isotope laser spectrometers (Erler et al., 2015; Harris et al., 2014; Ibrahim et al., 2018; Wächter et al., 2008). However, a comprehensive and comparative characterization of the above effects for commercially available N_2O isotope analyzers is lacking.

Here, we present an intercomparison study of commercially available N_2O isotope laser spectrometers with the three most common detection schemes: (1) OA-ICOS (N_2O OIA-30e-EP, ABB – Los Gatos Research Inc.); (2) CRDS (G5131-i, Picarro Inc.); (3) QCLAS (dual QCLAS and trace gas extractor (TREX)-mini QCLAS, ARI). Performance characteristics including precision, repeatability, drift and dependence of isotope measurements on $[\text{N}_2\text{O}]$ were determined. Instruments were tested for gas matrix effects (O_2 , Ar) and spectral interferences from enhanced trace gas mole fractions (CO_2 , CH_4 , CO , H_2O) at various $[\text{N}_2\text{O}]$ to develop analyzer-specific correction functions. The accuracy of different spectrometer designs was then assessed during a laboratory-controlled mixing experiment designed to simulate two-end-member mixing, in which results were compared to calculated expected values, as well as to those acquired using IRMS (δ values) and gas chromatography (GC, N_2O concentration). In closing, we provide a calibration workflow that will assist researchers in the operation of N_2O and other trace gas isotope laser spectrometers in order to acquire accurate isotope analyses.

2 Materials and methods

2.1 Analytical techniques

Operational details of the laser spectrometers tested in this study, including wavenumber regions, line positions and line strengths of N_2O , are provided in Table 1. In Fig. 1, selected N_2O rotational lines are shown in combination with the absorption lines of the atmospheric most abundant IR-active trace gases (H_2O , CO_2 , CH_4 , CO and O_3) within the different wavenumber regions used by the analyzers. Figure 1 can

be used to rationalize possible spectral interferences within different wavenumber regions.

2.1.1 OA-ICOS (ABB – Los Gatos Research Inc.)

The N₂-OIA-30e-EP (model 914-0027, serial number 15-830, ABB – Los Gatos Research Inc., USA) tested in this study was provided by the University of New South Wales (UNSW Sydney, Australia) and is herein referred to as OA-ICOS I (Table 1). The instrument employs the OA-ICOS technique integrated with a quantum cascade laser (QCL) (Baer et al., 2002). In short, the QCL beam is directed off axis into the cavity cell with highly reflective mirrors, providing an optical path of several kilometers. For further details on the OA-ICOS technique, the reader is referred to the webpage of ABB – Los Gatos Research Inc. (ABB – Los Gatos Research Inc., 2019) and Baer et al. (2002).

The specific analyzer tested here was manufactured in June 2014 and has had no hardware modifications since then. It is also important to note that a more recent N₂-OIA-30e-EP model (model 914-0060) is available, that in addition quantifies $\delta^{17}\text{O}$. We are unaware of any study measuring N₂O isotopocules at natural abundance and ambient mole fractions with the N₂-OIA-30e-EP. The only studies published so far reporting N₂O isotope data apply the N₂-OIA-30e-EP either at elevated [N₂O] in a standardized gas matrix or using ¹⁵N labeling, including Soto et al. (2015), Li et al. (2016), Kong et al. (2017), Brase et al. (2017), Wassenaar et al. (2018) and Nikolenko et al. (2019).

2.1.2 CRDS (Picarro Inc.)

Two G5131-i analyzers (Picarro Inc., USA) were used in this study: a 2015 model (referred to as CRDS I, serial number 5001-PVU-JDD-S5001, delivered September 2015) provided by the Niels Bohr Institute, University of Copenhagen, Denmark; and a 2018 model (referred to as CRDS II, serial number 5070-DAS-JDD-S5079, delivered June 2018) provided by Karlsruhe Institute of Technology, Germany (Table 1). In CRDS, the beam of a single-frequency continuous wave (cw) laser diode enters a three-mirror cavity with an effective pathlength of several kilometers to support a continuous traveling light wave. A photodetector measures the decay of light in the cavity after the cw laser diode is shut off to retrieve the mole fraction of N₂O isotopocules. For more details, we refer the reader to the webpage of Picarro Inc. (Picarro Inc., 2019) and Berden et al. (2000).

Importantly, the manufacturer-installed flow restrictors were replaced in both analyzer models, as we noted reduced flow rates due to clogging during initial reconnaissance testing. In CRDS I, a capillary (inner diameter, ID: 150 μm , length: 81 mm, flow: 25.2 cm³ min⁻¹) was installed, while CRDS II was equipped with a critical orifice (ID: 75 μm , flow: 12.5 cm³ min⁻¹). Both restrictors were tested and confirmed leakproof. Both analyzers had manufacturer-installed

permeation driers located prior to the inlet of the cavity, which were not altered for this study. In December 2017, CRDS I received a software and hardware update as per the manufacturer's recommendations. The CRDS II did not receive any software or hardware upgrades as it was acquired immediately prior to testing.

To the best of our knowledge, the work presented in Lee et al. (2017) and Ji and Grundle (2019) discusses the only published uses of G5131-i models. A prior model (the G5101-i), which employs a different spectral region and does not offer the capability for $\delta^{18}\text{O}$, was used by Peng et al. (2014), Erler et al. (2015), Li et al. (2015), Lebegue et al. (2016) and Winther et al. (2018).

2.1.3 QCLAS (Aerodyne Research Inc.)

Three QCLAS instruments (ARI, USA; CW-QC-TILDAS-SC-D) were used in this study. One instrument (QCLAS I, serial number 046), purchased in 2013, was provided by Karlsruhe Institute of Technology, Germany, and two instruments, purchased in 2014 (QCLAS II, serial number 065) and 2016 (QCLAS III, serial number 077), were supplied by ETH Zürich, Switzerland (Table 1). QCLAS I was used in all experiments presented in this study, while QCLAS II and III were only used to assess the reproducibility of drift reported in Sect. 3.1.

All instruments were dual-cw QCL spectrometers, equipped with mirror optics guiding the two laser beams through an optical anchor point to assure precise coincidence of the beams at the detector. On the way to the detector, the laser beams are coupled into an astigmatic multipass cell with a volume of approximately 2100 cm³ in which the beams interact with the sample air. The multiple passes through the absorption cell result in an absorption path length of approximately 204 m. The cell pressure can be selected by the user and was set to 53.3 mbar as a trade-off between line separation and sensitivity. This set point is automatically maintained by the TDLWintel software (version 1.14.89 ARI, MA, USA), which compensates for variations in vacuum pump speed by closing or opening a throttle valve at the outlet of the absorption cell.

QCLAS instruments offer great liberty to the user as the system can also be operated with different parameter settings, such as the selection of spectral lines for quantification, wavenumber calibration, sample flow rate and pressure. Thereby, different applications can be realized, from high-flow eddy covariance studies or high-mole-fraction process studies to high-precision measurements coupled to a customized inlet system. In addition, spectral interferences and gas matrix effects can be taken into consideration by multi-line analysis, inclusion of the respective spectroscopic parameters in the spectral evaluation or adjustment of the pressure-broadening coefficients. The spectrometers used in this study (QCLAS I–III) were tested under standard settings but were not optimized for the respective experiments.

Table 1. Overview of the wavelength regions, line positions and line strengths of N₂O isotopocules and key operating parameters for each laser spectrometer tested in this study. [C12](#)

Detection scheme (model; manufacturer)	N ₂ O range (ppb)	Wavenumber region (cm ⁻¹)	Isotopocules	Line positions (cm ⁻¹ /line strength (cm ⁻¹ /molecule cm ⁻²))	Flow rate (cm ³ min ⁻¹)	Cell temperature (°C)	Cell pressure (fPa)	Internal pumping volume (cm ³)	Effective volume at NTP (cm ³)	Measurement frequency (s)	References	
OAACOS I (N ₂ OIA-30s-EP; ABB – Los Gatos Research Inc.)	300–100000	2192.1–2192.5	1 ⁴ N ¹ 1 ⁴ N ¹ 1 ⁶ O	2192.40/4.919 × 10 ⁻²¹	60	43.6	61	930	60.50	1.00	Baer et al. (2002), ABB – Los Gatos Research Inc. (2019)	
			1 ⁴ N ¹ 1 ⁴ N ¹ 1 ⁶ O	2192.44/4.919 × 10 ⁻²⁰	60							
			1 ⁴ N ¹ 1 ⁴ N ¹ 1 ⁶ O	2192.48/3.375 × 10 ⁻¹⁹	60							
			1 ⁴ N ¹ 1 ⁴ N ¹ 1 ⁶ O	2192.31/3.31 × 10 ⁻²¹	60							
			1 ⁴ N ¹ 1 ⁴ N ¹ 1 ⁶ O	2192.33/2.968 × 10 ⁻²¹	60							
1 ⁴ N ¹ 1 ⁴ N ¹ 1 ⁶ O	2192.13/1.113 × 10 ⁻²¹	60										
CRDS I & II (G5131+; Picarro Inc.)	300–1500	2195.7–2196.3	1 ⁴ N ¹ 1 ⁴ N ¹ 1 ⁶ O	2196.21/5.161 × 10 ⁻²⁰	25.2 (CRDS I)	40.2	100	40	4.22	3.41 (CRDS I) 2.54 (CRDS II)	Picarro Inc. (2019)	
			1 ⁴ N ¹ 1 ⁴ N ¹ 1 ⁶ O	2196.24/5.161 × 10 ⁻²⁰	12.5 (CRDS II)							
			1 ⁴ N ¹ 1 ⁴ N ¹ 1 ⁶ O	2195.76/2.734 × 10 ⁻²¹	12.5 (CRDS II)							
			1 ⁴ N ¹ 1 ⁴ N ¹ 1 ⁶ O	2195.80/2.197 × 10 ⁻²¹	12.5 (CRDS II)							
1 ⁴ N ¹ 1 ⁴ N ¹ 1 ⁶ O	2195.95/1.431 × 10 ⁻²¹	12.5 (CRDS II)										
QCLAS I, II & III (CW-QC-TILDAS-SC-D; Aerodyne Research Inc.)	300–90000	2187.7–2188.15 and 2203.1–2203.4	1 ⁴ N ¹ 1 ⁴ N ¹ 1 ⁶ O	2188.04/2.601 × 10 ⁻²¹	130 ^a	20 ^a	53.3 ^a	2100	10 ^a	1.00 ^a	Nelson et al. (2008) Wickler et al. (2008)	
			1 ⁴ N ¹ 1 ⁴ N ¹ 1 ⁶ O	2187.94/3.294 × 10 ⁻²¹								
			1 ⁴ N ¹ 1 ⁴ N ¹ 1 ⁶ O	2187.85/3.274 × 10 ⁻²¹								
			1 ⁴ N ¹ 1 ⁴ N ¹ 1 ⁶ O	2203.28/1.794 × 10 ⁻²¹								
			1 ⁴ N ¹ 1 ⁴ N ¹ 1 ⁶ O	2203.10/2.710 × 10 ⁻²¹								
TREX-QCLAS I (modified CW-QC-TILDAS-76-CS; Aerodyne Research Inc.)	300–15000 ^b	2203.1–2203.4 ^a	1 ⁴ N ¹ 1 ⁴ N ¹ 1 ⁶ O	2203.11/1.435 × 10 ⁻²¹ 2203.36/9.798 × 10 ⁻²² 2203.20/7.016 × 10 ⁻²² 2203.28/1.794 × 10 ⁻²¹	^b	20 ^a	35.6 ^a	620	20 ^a	1.00 ^a	Ibrahim et al. (2018)	

^a Dual QC-TILDAS and mini QC-TILDAS are flexible spectrometer platforms which can be used with different parameter settings. The indicated numbers were chosen for the described experiments. ^b The mini QC-TILDAS spectrometer is used in combination with a pre-concentration device (Ibrahim et al., 2018); the indicated N₂O concentration range is prior to pre-concentration. ^c The pre-concentration – mini QC-TILDAS system is used in a repetitive batch cycle without a continuous sample gas flow (Ibrahim et al., 2018, 2020).

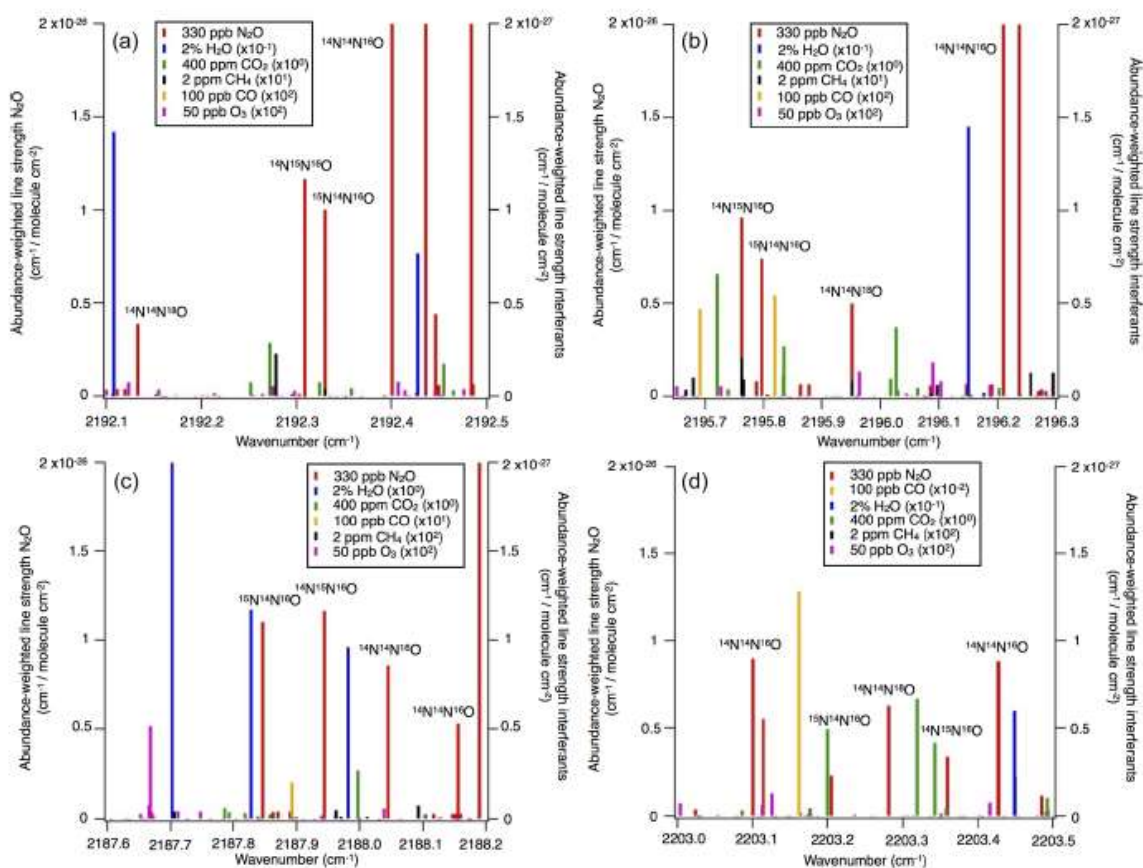


Figure 1. N_2O isotopocule absorption line positions in the wavenumber regions selected for (a) OA-ICOS, (b) CRDS and (c, d) QCLAS techniques. Regions of possible spectral overlap from interfering trace gases such as H_2O , CO_2 , CH_4 and CO are shown. The abundance-scaled line strengths of trace gases have been scaled with 10^{-1} to 10^2 (as indicated) because they are mostly weaker than those of the N_2O isotopocules.

QCLAS I was operated as a single laser instrument using laser 1, to optimize spectral resolution of the frequency sweeps. It is important to note the mixing ratios returned by the instrument are solely based on fundamental spectroscopic constants (Rothman et al., 2005), so that corrections such as the dependence of isotope ratios on $[\text{N}_2\text{O}]$ have to be implemented by the user in the postprocessing.

To our knowledge, QCLAS instruments have so far predominantly been used for determination of N_2O isotopic composition in combination with preconcentration (see below) or at enhanced mole fractions (Harris et al., 2015; Heil et al., 2014; Köster et al., 2013), except for Yamamoto et al. (2014), who had used a QCLAS (CW-QC-TILDAS-SC-S-N2OISO; ARI, USA) with one laser (2189 cm^{-1}) in combination with a closed chamber system. To achieve the precision and accuracy levels reported in their study, Yamamoto et al. (2014) corrected their measurements for mixing ratio de-

pendence and minimized instrumental drift by measuring N_2 gas every 1 h for background correction. These authors also showed that careful temperature control of their instrument in an air-conditioned cabinet was necessary for achieving optimal results.

2.1.4 TREX-QCLAS

A compact mini QCLAS device (CW-QC-TILDAS-76-CS, serial number 074, ARI, USA) coupled with a preconcentration system (TREX) was provided by Empa, Switzerland. The spectrometer comprises a continuous-wave mid-infrared quantum cascade laser source emitting at 2203 cm^{-1} and an astigmatic multipass absorption cell with a path length of 76 m and a volume of approximately 620 cm^3 (Ibraim et al., 2018) (Table 1). The TREX unit was designed and manufactured at Empa and is used to separate the N_2O from

the sample gas prior to QCLAS analysis. Thereby, the initial [N₂O] is increased by a factor of 200–300, other trace gases are removed, and the gas matrix is set to standardized conditions. Before entering the TREX device, CO is oxidized to CO₂ using a metal catalyst (Sofnocat 423, Molecular Products Limited, GB). Water and CO₂ in sample gases were removed by a permeation dryer (PermaPure Inc., USA) in combination with a sodium hydroxide (NaOH)/magnesium perchlorate (Mg(ClO₄)₂) trap (Ascarite: 6 g, 10–35 mesh, Sigma Aldrich, Switzerland, bracketed by Mg(ClO₄)₂, 2 × 1.5 g, Alfa Aesar, Germany). Thereafter, N₂O is adsorbed on a HayeSep D (Sigma Aldrich, Switzerland) filled trap, cooled down to 125.1 ± 0.1 K by attaching it to a copper baseplate mounted on a high-power Stirling cryocooler (CryoTel GT, Sunpower Inc., USA). N₂O adsorption requires 5.080 ± 0.011 L of gas to have passed through the adsorption trap. For N₂O desorption, the trap is decoupled from the copper baseplate, while slowly heating it to 275 K with a heat foil (diameter 62.2 mm, 100 W, HK5549, Minco Products Inc., USA). Desorbed N₂O is purged with 1–5 cm³ min⁻¹ of synthetic air into the QCLAS cell for analysis. By controlling the flow rate and trapping time, the [N₂O] in the QCLAS cell can be adjusted to 60–80 ppm at a cell pressure of 35.6 ± 0.04 mbar. A custom-written LabVIEW program (Version 18.0.1, National Instruments Corp., USA) allows remote control and automatic operation of the TREX. So far, the TREX-QCLAS system has been successfully applied to determine N₂O emission, as well as N₂O isotopic signatures from various ecosystems (e.g., Mohn et al., 2012; Harris et al., 2014; Wolf et al., 2015; Ibraim et al., 2019).

2.1.5 GC-IRMS

IRMS analyses were conducted at ETH Zürich using a gas preparation unit (Trace Gas, Elementar, Manchester, UK) coupled to an IsoPrime100 IRMS (Elementar, Manchester, UK). [N₂O] analysis using gas chromatography was also performed at ETH Zürich (456-GC, Scion Instruments, Livingston, UK). GC-IRMS analyses were conducted as part of experiments described further in Sect. 2.4.8. Further analytical details are provided in Sect. S1 in the Supplement (TS10).

2.2 Sample and reference gases

2.2.1 Matrix and interference test gases

Table 2 provides O₂, Ar and trace gas mole fractions of matrix gases and interference test gases used during testing. The four matrix gases comprised synthetic air (matrix a, TSI, Messer Schweiz AG, Switzerland); synthetic air with Ar (matrix b, Carbagas AG, Switzerland); synthetic air with Ar, CO₂, CH₄ and CO at near-ambient mole fractions (matrix c, Carbagas AG, Switzerland); and high-purity nitrogen gas (N₂, Messer Schweiz AG, Switzerland). Matrix gases were analyzed in the World Meteorological Organization (WMO)

Global Atmosphere Watch (GAW) World Calibration Center at Empa (WCC Empa) for CO₂, CH₄, H₂O (G1301, Picarro Inc., USA), and N₂O and CO (CW-QC-TILDAS-76-CS; ARI, USA) against standards of the National Oceanic and Atmospheric Administration/Earth System Research Laboratory/Global Monitoring Division (NOAA/ESRL/GMD). The [N₂O] in all matrix gases and N₂ were below 0.3 ppb. The three gas mixtures used for testing of spectral interferences contained higher mole fractions of either CO₂, CH₄ or CO in matrix gas b (Carbagas AG, Switzerland), which prevented spectroscopic analysis of other trace substances.

2.2.2 Reference gases (S1, S2) and pressurized air (PA1, PA2)

Preparation of pure and diluted reference gases

Two reference gases (S1, S2) with different N₂O isotopic composition were used in this study. Pure N₂O reference gases were produced from high-purity N₂O (Linde, Germany) decanted into evacuated Luxfer aluminum cylinders (S1: P3333N, S2: P3338N) with ROTAREX valves (Matar, Italy) to a final pressure of maximum 45 bar to avoid condensation. Reference gas 1 (S1) was high-purity N₂O only. For reference gas 2 (S2), high-purity N₂O was supplemented with defined amounts of isotopically pure (> 98 %) ¹⁴N¹⁵NO (NLM-1045-PK), ¹⁵N¹⁴NO (NLM-1044-PK) (Cambridge Isotope Laboratories, USA) and NN¹⁸O using a 10-port two-position valve (EH2C10WEPH with 20 mL sample loop, Valco Instruments Inc., Switzerland). Since NN¹⁸O was not commercially available, it was synthesized using the following procedure: (1) ¹⁸O exchange of HNO₃ (1.8 mL, Sigma Aldrich) with 97 % H₂¹⁸O (5 mL, Medical Isotopes Inc.) under reflux for 24 h; (2) condensation of NH₃ and reaction controlled by LN₂; and (3) thermal decomposition of NH₄NO₃ in batches of 1 g in 150 mL glass bulbs with a breakseal (Glasbläserei Möller AG, Switzerland) to produce NN¹⁸O. The isotopic enrichment was analyzed after dilution in N₂ (99.9999 %, Messer Schweiz AG) with a Vision 1000C quadrupole mass spectrometer (QMS) equipped with a customized ambient pressure inlet (MKS Instruments, UK). Triplicate analysis provided the following composition: 36.25 ± 0.10 % of NN¹⁶O and 63.75 ± 0.76 % of NN¹⁸O.

High [N₂O] reference gases (S1-a₉₀ppm, S1-b₉₀ppm, S1-c₉₀ppm, S2-a₉₀ppm) with a target mole fraction of 90 ppm were prepared in different matrix gases (a, b, c) using a two-step procedure. First, defined volumes of S1 and S2 were dosed into Luxfer aluminum cylinders (ROTAREX valve, Matar, Italy) filled with matrix gas (a, b and c) to ambient pressure using N₂O calibrated mass flow controllers (MFCs) (Vögtlin Instruments GmbH, Switzerland). Second, the N₂O was gravimetrically diluted (ICS429, Mettler Toledo GmbH, Switzerland) with matrix gas to the target mole fraction. Ambient [N₂O] reference gases (S1-c₃₃₀ppb, S2-c₃₃₀ppb) with a target mole fraction of 330 ppb were prepared by dosing

Table 2. O₂, Ar content and trace gas concentrations for matrix and interference test gases. Trace gas concentrations of matrix gases were analyzed by WMO GAW WCC Empa against standards of the NOAA/ESRL/GMD. For trace gas concentrations of interference test gases, manufacturer specifications are given. Reported O₂ and Ar content is according to manufacturer specifications. The given uncertainty is the uncertainty stated by the manufacturer or the standard deviation for analysis of *n* cylinders of the same specification.

Gas	Abbreviation	O ₂ ^a (%)	Ar ^a (%)	CO ₂ ^b (ppm)	CH ₄ ^b (ppb)	CO ^b (ppb)	N ₂ O ^b (ppb)	<i>n</i>
Matrix gases								
Synthetic air	Matrix a	20.5 ± 0.5	–	< 1	< 25	< 200	< 0.25	4
Synthetic air + Ar	Matrix b	20.95 ± 0.2	0.95 ± 0.01	< 0.5	< 15	< 150	< 0.15	3
Synthetic air + ArCO ₂ + CH ₄ + CO	Matrix c	20.95 ± 0.4	0.95 ± 0.02	397 ± 3	2004 ± 20	195 ± 3	< 0.15	9
Nitrogen (6.0)	N ₂	< 0.00003	< 0.0001	< 0.2	< 1	< 1	< 0.05	2
		O ₂ ^a (%)	Ar ^a (%)	CO ₂ ^a (%)	CH ₄ ^a (ppm)	CO ^a (ppm)	N ₂ O ^a (ppb)	<i>n</i>
Interference test gases								
CO ₂ in synthetic air + Ar	CO ₂ in matrix b	21.06 ± 0.2	0.94 ± 0.01	4.02 ± 0.04	n.a.	n.a.	n.a.	–
CH ₄ in synthetic air + Ar	CH ₄ in matrix b	20.79 ± 0.4	0.96 ± 0.02	n.a.	199 ± 4	n.a.	n.a.	–
CO in synthetic air + Ar	CO in matrix b	20.95 ± 0.4	0.95 ± 0.02	n.a.	n.a.	20.6 ± 0.4	n.a.	–

^a Manufacturer specifications. ^b Analyzed at WMO GAW WCC Empa. "n.a." indicates data not analyzed due to very high concentration of one trace substance, which affects spectroscopic analysis of other species.

S1-c₉₀ppm or S2-c₉₀ppm into evacuated cylinders with a calibrated MFC, followed by gravimetric dilution with matrix c.

Analysis of reference gases and pressurized air

Table 3 details the trace gas mole fractions and N₂O isotopic composition of high and ambient [N₂O] reference gases, as well as commercial pressurized air (PA1 and PA2) used during testing. Trace gas mole fractions of high [N₂O] reference gases were acquired from the trace gas levels in the respective matrix gases (Table 2), while ambient [N₂O] reference gases and target as well as background gases were analyzed by WCC Empa. The isotopic composition of high [N₂O] isotope reference gases in synthetic air (S1-a₉₀ppm, S2-a₉₀ppm) was analyzed in relation to N₂O isotope standards (Ca11–Ca13) in an identical matrix gas (matrix a) using laser spectroscopy (CW-QC-TILDAS-200; ARI, Billerica, USA). The composition of Ca11–Ca13 is outlined in Sect. S2.

For high-mole-fraction reference gases in matrix **b** and **c** (S1-b₉₀ppm, S1-c₉₀ppm, S2-c₉₀ppm), the δ values acquired for S1-a₉₀ppm and S2-a₉₀ppm were assigned, since all S1 and S2 reference gases (irrespective of gas matrix) were generated from the same source of pure N₂O gas. Direct analysis of S1-b₉₀ppm, S1-c₉₀ppm and S2-c₉₀ppm by QCLAS was not feasible, as no N₂O isotope standards in matrix **b** and **c** were available. The absence of significant difference (< 1 ‰) in N₂O isotopic composition between S1-b₉₀ppm and S1-c₉₀ppm in relation to S1-a₉₀ppm (and S2-c₉₀ppm to S2-a₉₀ppm) was assured by first statically diluting S1-b₉₀ppm, S1-c₉₀ppm and S2-c₉₀ppm to ambient N₂O mole fractions with synthetic air. This was followed by analysis using TREX-QCLAS (as described in Sect. 2.1.4) against the same standards used for S1-a₉₀ppm, S2-a₉₀ppm isotope analysis.

Ambient mole fraction N₂O isotope reference gases (S1-c₃₃₀ppb, S2-c₃₃₀ppb) and PA1 and PA2 were analyzed by TREX-QCLAS (Sect. 2.1.4) using N₂O isotope standards (Ca11–Ca15) as outlined in Sect. S2.

2.3 Laboratory setup, measurement procedures and data processing

2.3.1 Laboratory setup

All experiments were performed at the Laboratory for Air Pollution/Environmental Technology, Empa, Switzerland, during June 2018 and February 2019. The laboratory was air conditioned to 295 K (±1 K), with ±0.5 K diel variations (Saveris 2, Testo AG, Switzerland), with the exception of a short period (7 to 8 July 2018), where the air conditioning was deactivated to test the temperature dependence of analyzers. Experiments were performed simultaneously for all analyzers, with the exception of the TREX-QCLAS, which requires an extensive measurement protocol and additional time to trap and measure N₂O (Ibraim et al., 2018) and thus could not be integrated concurrently with the other analyzers.

Figure 2 shows a generalized experimental setup used for all experiments. Additional information for specific experiments is given in Sect. 2.4, and individual experimental setups are depicted in Sect. S3. Gas flows were controlled using a set of MFCs (model high-performance, Vögtlin Instruments GmbH, Switzerland) integrated into a MFC control unit (Contrec AG, Switzerland). All MFCs were calibrated by the manufacturer for whole air, which according to Vögtlin Instruments is valid for pure N₂ and pure O₂ as well. Operational ranges of applied MFCs ranged from 0–25 to 0–5000 cm³ min⁻¹ and had reported uncertainties of 0.3 % of

their maximum flow and 0.5 % of actual flow. To reduce the uncertainty of the flow regulation, the MFC with the smallest maximum flow range available was selected. The sum of dosed gas flows was always higher than the sum of gas consumption by analyzers, with the overflow exhausted to room air. Gas lines between gas cylinders and MFCs, as well as between MFCs and analyzers, were 1/8" stainless steel tubing (type 304, Supelco, Sigma Aldrich, Switzerland). Manual two-way (SS-1RS4 or SS-6H-MM, Swagelok, Switzerland) or three-way valves (SS-42GXS6MM, Swagelok, Switzerland) were used to separate or combine gas flows.

2.3.2 Measurement procedures, data processing and calibration

With the exception of Allan variance experiments performed in Sect. 2.4.1, all gas mixtures analyzed during this study were measured by the laser spectrometers for a period of 15 min, with the last 5 min used for data processing. Customized R scripts (R Core Team, 2017) were used to extract the 5 min averaged data for each analyzer. Whilst the OA-ICOS and QCLAS instruments provide individual $^{14}\text{N}^{14}\text{N}^{16}\text{O}$, $^{14}\text{N}^{15}\text{N}^{16}\text{O}$, $^{15}\text{N}^{14}\text{N}^{16}\text{O}$ and $^{14}\text{N}^{14}\text{N}^{18}\text{O}$ mole fractions, the default data output generated by the CRDS analyzers are δ values, with underlying calculation schemes inaccessible to the user. Therefore, to remain consistent across analyzers, uncalibrated δ values were calculated for OA-ICOS and QCLAS instruments first, using literature values for the $^{15}\text{N}/^{14}\text{N}$ (0.0036782) and $^{18}\text{O}/^{16}\text{O}$ (0.0020052) isotope ratios of AIR-N2 and VSMOW (Werner and Brand, 2001).

Each experiment was performed over the course of 1 d and consisted of three phases: (1) an initial calibration phase; (2) an experimental phase; and (3) a final calibration phase. During phases (1) and (3), reference gases S1-c₃₃₀ppb and S2-c₃₃₀ppb were analyzed. On each occasion (i.e., twice a day), this was followed by the analysis of PA1, which was used to determine the long-term (day-to-day) repeatability of the analyzers. Phase (2) experiments are outlined in Sect. 2.4. Throughout all three phases, all measurements were systematically alternated with an Anchor gas measurement, the purpose of which was two-fold: (1) to enable drift correction and (2) as a means of quantifying deviations of the measured $[\text{N}_2\text{O}]$ and δ values caused by increasing $[\text{N}_2\text{O}]$ (Sect. 2.4.4), the removal of matrix gases (O_2 and Ar in Sect. 2.4.5) or addition of trace gases (CO_2 , CH_4 and CO in Sect. 2.4.6). Accordingly, the composition of the Anchor gas varied across experiments (see Sect. 2.4) but remained consistent throughout each experiment. A drift correction was applied to the data if a linear or non-linear model fitted to the Anchor gas measurement over the course of an experiment was statistically significant at $p < 0.05$. Otherwise, no drift correction was applied.

In Sect. 2.4.3 (repeatability experiments) and 2.4.8 (two-end-member mixing experiments), trace gas effects were

corrected according to Eqs. (1), (2) and (3) using derived analyzer-specific correction functions because the CO_2 , CH_4 and CO composition of PA1 in Sect. 2.4.3 and the gas mixtures in Sect. 2.4.8 varied from those of the calibration gases S1-c₃₃₀ppb (S1) and S2-c₃₃₀ppb (S2):

$$[\text{N}_2\text{O}]_{\text{tc}, G} = [\text{N}_2\text{O}]_{\text{meas}, G} - \sum_x (\Delta[\text{N}_2\text{O}] (\Delta[x]_G, [\text{N}_2\text{O}]_{\text{meas}, G})) \quad (1)$$

$$\delta_{\text{tc}, G} = \delta_{\text{meas}, G} - \sum_x (\Delta\delta (\Delta[x]_G, \delta_{\text{meas}, G})) \quad (2)$$

and

$$\Delta[x]_G = [x]_G - \frac{[x]_{\text{S1}} + [x]_{\text{S2}}}{2}, \quad (3)$$

where $[\text{N}_2\text{O}]_{\text{tc}, G}$ and $\delta_{\text{tc}, G}$ refer to the trace-gas-corrected $[\text{N}_2\text{O}]$ and δ values ($\delta^{15}\text{N}^\alpha$, $\delta^{15}\text{N}^\beta$ or $\delta^{18}\text{O}$) of sample gas G, respectively; $[\text{N}_2\text{O}]_{\text{meas}, G}$ and $\delta_{\text{meas}, G}$ are the raw uncorrected $[\text{N}_2\text{O}]$ and δ values measured by the analyzer for sample gas G, respectively; $\Delta[\text{N}_2\text{O}]$ and $\Delta\delta$ refer to the offset on the $[\text{N}_2\text{O}]$ or δ values, respectively, resulting from the difference in trace gas mole fraction between sample gas G and reference gases, denoted $\Delta[x]_G$; $[x]_G$ is the mole fraction of trace gas x (CO_2 , CH_4 or CO) in sample gas G; and $[x]_{\text{S1}}$ and $[x]_{\text{S2}}$ are the mole fractions of trace gas x in reference gases S1-c₃₃₀ppb and S2-c₃₃₀ppb. It is important to note that the differences in CO_2 and CH_4 mole fractions in S1-c₃₃₀ppb and S2-c₃₃₀ppb are 2 orders of magnitude smaller than the differences with PA1.

Thereafter, δ values of trace-gas-corrected, mole-fraction-corrected (Sect. 2.4.8 only) and drift-corrected measurements from the analyzers were normalized to δ values on the international isotope-ratio scales using a two-point linear calibration procedure derived from values of S1-c₃₃₀ppb (S1) and S2-c₃₃₀ppb (S2) calculated using Eq. (4) (Gröning, 2018):

$$\delta_{\text{Cal}, G} = \frac{\delta_{\text{reftrue}, \text{S1}} - \delta_{\text{reftrue}, \text{S2}}}{\delta_{\text{corrmeas}, \text{S1}} - \delta_{\text{corrmeas}, \text{S2}}} \cdot (\delta_{\text{corrlineal}, G} - \delta_{\text{corrmeas}, \text{S1}}) + \delta_{\text{reftrue}, \text{S1}}, \quad (4)$$

where $\delta_{\text{Cal}, G}$ is the calibrated δ value for sample gas G normalized to international isotope-ratio scales; $\delta_{\text{reftrue}, \text{S1}}$ and $\delta_{\text{reftrue}, \text{S2}}$ are the respective δ values assigned to reference gases S1-c₃₃₀ppb and S2-c₃₃₀ppb; $\delta_{\text{corrmeas}, \text{S1}}$ and $\delta_{\text{corrmeas}, \text{S2}}$ are the respective δ values measured for the reference gases S1-c₃₃₀ppb and S2-c₃₃₀ppb which, if required, were drift corrected; and $\delta_{\text{corrlineal}, G}$ is the trace-gas-corrected, mole-fraction-corrected (Sect. 2.4.8 only) and drift-corrected (if required) δ value measured for the sample gas G.

2.4 Testing of instruments

An overview of all experiments performed in this study, including applied corrections and instruments tested, is provided in Table 4.

Table 3. Trace gas concentrations and N₂O isotopic composition of high and ambient N₂O concentration reference gases, and pressurized air. Trace gas concentrations of high concentration reference gases were retrieved from the composition of matrix gases used for their production (see Table 2); trace gas concentrations in ambient concentration reference gases and pressurized air were analyzed by WMO GAW WCC Empa against standards of the NOAA/ESRL/GMD. The N₂O isotopic composition was quantified by laser spectroscopy (QCLAS) and pre-concentration – laser spectroscopy (TRES-QCLAS) against reference gases previously analyzed by the Tokyo Institute of Technology.

Gas	CO ₂ (ppm)	CH ₄ (ppb)	CO (ppb)	N ₂ O (ppb)	$\delta^{15}\text{N}^{\alpha}$ vs. AIR-N ₂ (‰)	$\delta^{15}\text{N}^{\beta}$ vs. AIR-N ₂ (‰)	$\delta^{18}\text{O}$ vs. VSMOW (‰)
High N ₂ O concentration reference gases							
S1-a ₉₀ ppm	< 1	< 25	< 200	~ 90 000	0.54 ± 0.17	1.15 ± 0.06	39.46 ± 0.01
S1-b ₉₀ ppm	< 0.5	< 15	< 150	~ 90 000	0.54 ± 0.17	1.15 ± 0.06	39.46 ± 0.01
S1-c ₉₀ ppm	397 ± 3	2004 ± 20	195 ± 3	~ 90 000	0.54 ± 0.17	1.15 ± 0.06	39.46 ± 0.01
S2-a ₉₀ ppm	< 1	< 25	< 200	~ 90 000	51.43 ± 0.06	55.14 ± 0.09	100.09 ± 0.03
S2-c ₉₀ ppm	397 ± 3	2004 ± 20	195 ± 3	~ 90 000	51.43 ± 0.06	55.14 ± 0.09	100.09 ± 0.03
Ambient N ₂ O concentration reference gases							
S1-c ₃₃₀ ppb	399.78 ± 0.04	2022 ± 0.2	195 ± 0.3	327.45 ± 0.06	0.92 ± 0.39	1.44 ± 0.25	39.12 ± 0.18
S2-c ₃₃₀ ppb	398.62 ± 0.04	2020 ± 0.2	193 ± 0.3	323.97 ± 0.06	52.38 ± 0.10	55.61 ± 0.12	99.59 ± 0.03
High N ₂ O concentration source gas (SG) for two-end-member mixing experiments (Sect. 2.4.8)							
SG1-a ₉₀ ppm	< 1	< 25	< 200	~ 90 000	-24.35 ± 0.32	-22.94 ± 0.33	31.79 ± 0.12
SG2-a ₉₀ ppm	< 1	< 25	< 200	~ 90 000	51.43 ± 0.06	55.14 ± 0.09	100.09 ± 0.03
Pressurized air							
Pressurized air (PA1)	200.55 ± 0.07	2582 ± 0.2	187 ± 0.2	326.51 ± 0.06	15.83 ± 0.03	-3.39 ± 0.14	44.66 ± 0.02
Pressurized air (PA2)	437.99 ± 0.36	2957 ± 0.3	275 ± 0.4	333.50 ± 0.09	15.81 ± 0.07	-3.31 ± 0.004	44.72 ± 0.04

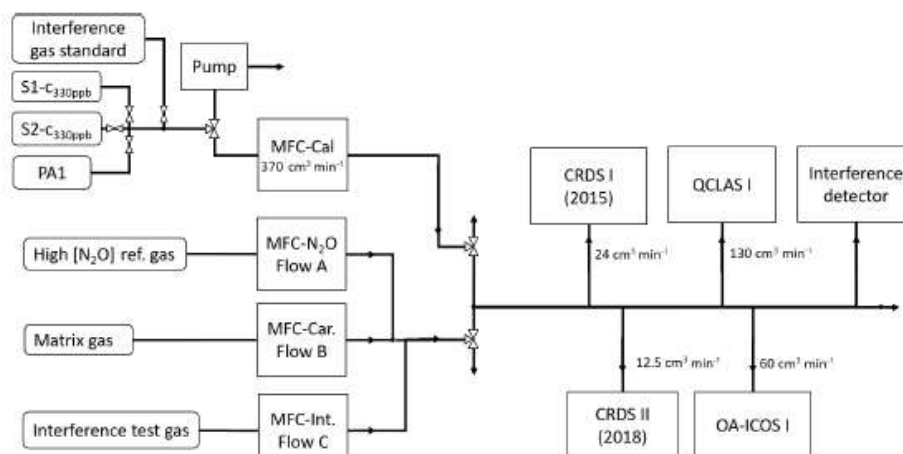


Figure 2. The generalized experimental setup used for all experiments conducted in this study. The gases introduced via MFC flows A, B and C were changed according to the experiments outlined in Sect. 2.4. Tables 2 and 3 provide the composition of the matrix gases (MFC B), interference test gases (MFC C) and high [N₂O] concentration reference gases (MFC A). Laboratory setups for each individual experiment are provided in Sect. S3.

Table 4. Overview of the experiments performed in this study.

Experiment	Sections	Aims	Corrections applied	Instruments tested	Comments
Instrumental precision (Allan deviation)	2.4.1 3.1	Short-term precision, optimal integration time/maximum precision and drift	None	OA-ICOS I CRDS I & II QCLAS I QCLAS II & III (ambient only) TREX-QCLAS I	Conducted at N ₂ O concentrations ~ 326, 1000, 10 000 ppb
Temperature effects	2.4.2 3.2	Temperature effects on [N ₂ O] and isotope deltas	None	OA-ICOS I CRDS I & II QCLAS I	
Repeatability (short term, ~ 2 h)	2.4.3 3.3	Repeatability	Drift	OA-ICOS I CRDS I & II QCLAS I TREX-QCLAS I	Conducted at N ₂ O concentrations ~ 326, 1000, 10 000 ppb
Repeatability (long term, ~ 2 weeks)	2.4.3 3.3	Repeatability	Drift, delta calibration, trace gas effect ^a	OA-ICOS I CRDS I & II QCLAS I TREX-QCLAS I	Conducted at ~ 326 ppb N ₂ O using PA1
N ₂ O mole fraction effects	2.4.4 3.4	[N ₂ O] effects on isotope deltas, and derive correction functions	Drift	OA-ICOS I CRDS I & II QCLAS I	CRDS: 300 to 1500 ppb N ₂ O, OA-ICOS, QCLAS: 300 to 90 000 ppb
Gas matrix effects (N ₂ , O ₂ and Ar)	2.4.5 3.5	Gas matrix effects on [N ₂ O] and isotope deltas and derive correction functions	Drift	OA-ICOS I QCLAS I TREX-QCLAS I	Conducted at N ₂ O concentrations ~ 330, 660, 990 ppb
Trace gas effects (H ₂ O, CO ₂ , CH ₄ , CO)	2.4.6 3.6	Trace gas effects on [N ₂ O] and isotope deltas and derive correction functions	Drift	OA-ICOS I CRDS I & II QCLAS I TREX-QCLAS I (except H ₂ O)	Conducted at N ₂ O concentrations ~ 330, 660, 990 ppb
CO ₂ and CO removal	2.4.7 3.6	Effects of removal of CO ₂ (Ascarite) and CO (Sofnocat) on [N ₂ O] and isotope deltas	Drift	OA-ICOS I CRDS I & II QCLAS I	Conducted at N ₂ O concentrations ~ 330 ppb
Two-end-member mixing	2.4.8 3.7	Test the ability of the instruments to extrapolate a N ₂ O source using a Keeling plot approach	Drift, three-point concentration dependence, δ calibration, trace gas effect ^a , and scaled with N ₂ O ^b	OA-ICOS I (Exps. 1–6) CRDS I & II (Exps. 1–4) QCLAS I (Exps. 1–6) TREX-QCLAS I (Exps. 1–2) GC [N ₂ O], IRMS [δ] (Exps. 1–6)	The workflow provided in Sect. 4.3 was applied

^a Derived from trace gas effect determined in Sect. 3.6. ^b Derived from scaling effects described in Sect. 3.6.2.

2.4.1 Allan precision

The precision of the laser spectrometers was determined using the Allan variance technique (Allan, 1966; Werle et al., 1993). Experiments were conducted at different [N₂O]: ambient, 1000 and 10 000 ppb. For the Allan variance testing conducted at ambient [N₂O], a continuous flow of PA1 was measured continuously for 30 h. For testing conducted

at 1000 and 10 000 ppb [N₂O], S1-c₉₀ppm was dynamically diluted to 1000 or 10 000 ppb [N₂O] with matrix gas c for 10 h. CRDS I and II were disconnected for the 10 000 ppb measurement because [N₂O] exceeded the specified measurement range. Daily drifts were estimated using the slope of the linear regression over the measurement period normalized to 24 h (i.e., ppb d⁻¹ and ‰ d⁻¹).

2.4.2 Temperature effects

To investigate instrumental sensitivities to variations in ambient temperature, PA1 was simultaneously and continuously measured by all analyzers in flow-through mode for a period of 24 h, while the air conditioning of the laboratory was turned off for over 10 h. This led to a rise in temperature from 21 to 30 °C, equating to an increase in temperature of approximately 0.9 °C h⁻¹. The increase in laboratory room temperature was detectable shortly after the air conditioning was turned off due to considerable heat being released from several other instruments located in the laboratory. Thereafter, the air conditioning was restarted and the laboratory temperature returned to 21 °C over the course of 16 h, equating to a decrease of roughly 0.6 °C h⁻¹, with most pronounced effects observable shortly after restart of air conditioning when temperature changes were highest.

2.4.3 Repeatability

Measurements of PA1 were taken twice daily over ~ 2 weeks prior to and following the experimental measurement period to test the long-term repeatability of the analyzers. Measurements were sequentially corrected for differences in trace gas concentrations (Eqs. 1–3), drift (if required) and then δ calibrated (Eq. 4). No matrix gas corrections were applied because the N₂, O₂ and Ar composition of PA1 was identical to that of S1-C₃₃₀ ppb and S2-C₃₃₀ ppb. TREX-QCLAS I measurements for long-term repeatability were collected separately from other instruments over a period of 6 months. Repeatability over shorter time periods (2.5 h) was also tested for each analyzer by acquiring 10 repeated 15 min measurements at different N₂O mole fractions: ambient (PA1), 1000 and 10 000 ppb N₂O.

2.4.4 N₂O mole fraction dependence

To determine the effect of changing [N₂O] on the measured δ values, S1-C₉₀ ppm was dynamically diluted with matrix c to various [N₂O] spanning the operational ranges of the instruments. For both CRDS analyzers mole fractions between 300 to 1500 ppb were tested, while for the OA-ICOS I and QCLAS I mixing ratios ranged from 300 to 90 000 ppb. Between each [N₂O] step change, the dilution ratio was systematically set to 330 ppb N₂O to perform an Anchor gas measurement. For each instrument, the effect of increasing [N₂O] on δ values was quantified by comparing the measured δ values at each step change to the mean measured δ values of the Anchor gas and was denoted $\Delta\delta$ such that $\Delta\delta = \delta_{\text{measured}} - \delta_{\text{Anchor}}$ and $\Delta\delta_{\text{Anchor}} = 0$. The experiment was repeated on three consecutive days to test day-to-day variability.

2.4.5 Gas matrix effects (O₂ and Ar)

Gas matrix effects were investigated by determining the dependence of [N₂O] and isotope δ values on the O₂ or Ar mixing ratio of a gas mixture. For O₂ testing, Gases 1, 2 and 3 (N₂) were mixed to incrementally change mixing ratios of O₂ (0%–20.5% O₂) while maintaining a consistent [N₂O] of 330 ppb. As an Anchor gas, Gas 1 (S1-a₉₀ ppm) was dynamically diluted with Gas 2 (matrix a) to produce 330 ppb N₂O in matrix a (Table 5). O₂ mole fractions in the various gas mixtures were analyzed with a paramagnetic O₂ analyzer (Servomex, UK) and agreed with expected values to within 0.3% (relative). For Ar testing, Gas 1 (S1-b₉₀ ppm) was dynamically diluted with Gas 2 (matrix b) to produce an Anchor gas with ~ 330 ppb N₂O in matrix b. Gases 1, 2 and 3 (N₂ + O₂) were then mixed to incrementally change mixing ratios of Ar (0.003%–0.95% Ar), while a consistent [N₂O] of 330 ppb was maintained. Ar compositional differences were estimated based on gas cylinder manufacturer specifications and selected gas flows. The effects of decreasing O₂ and Ar on [N₂O] and δ values were quantified by comparing the measured [N₂O] and δ values at each step change to the mean measured [N₂O] and δ values of the Anchor gas and were denoted $\Delta[\text{N}_2\text{O}]$ and $\Delta\delta$, similar to Sect. 2.4.4. Deviations in O₂ and Ar mixing ratios were quantified by comparing the [O₂] and [Ar] at each step change to the mean [O₂] and [Ar] of the Anchor gas and were denoted ΔO_2 and ΔAr such that, for example, $\Delta\text{O}_2 = \text{O}_{2\text{measured}} - \text{O}_{2\text{Anchor}}$ and $\Delta\text{O}_{2\text{Anchor}} = 0$. Both O₂ and Ar experiments were triplicated.

In addition, O₂ and Ar effects were derived for N₂O mole fractions of ~ 660 and ~ 990 ppb. These experiments were undertaken in a way similar to those described above, except Anchor gas measurements were conducted once (not triplicated).

2.4.6 Trace gas effects (CO₂, CH₄, CO and H₂O)

The sensitivity of [N₂O] and δ values on changing trace gas concentrations was tested in a similar way to those described in Sect. 2.4.5. In short, Gas 1 (S1-b₉₀ ppm) was dynamically diluted with Gas 2 (matrix b) to create an Anchor gas with 330 ppb N₂O in matrix b. Gases 1, 2 and 3 (either CO₂, CH₄ or CO in matrix gas b) were mixed to incrementally change the mixing ratios of the target substances (1.7–2030 ppm CO₂, 0.01–10.25 ppm CH₄ and 0.14–2.14 ppm CO) while maintaining a consistent gas matrix and [N₂O] of 330 ppb (Table 5). Trace gas mole fractions in the produced gas mixtures were analyzed with a Picarro G2401 (Picarro Inc., USA) and agreed with predictions within better than 2%–3% (relative). Similar to Sect. 2.4.4, the effects of increasing CO₂, CH₄ and CO on [N₂O] and δ values were quantified by comparing the measured [N₂O] and δ values at each step change to the mean measured [N₂O] and δ values of the Anchor gas and were denoted $\Delta[\text{N}_2\text{O}]$ and $\Delta\delta$. Similar to Sect. 2.4.5, deviations in CO₂, CH₄ and CO mix-

Table 5. Gas mixtures used to test effects of gas matrix (O₂, Ar) or trace gases (CO₂, CH₄ and CO) on [N₂O] and isotope deltas. Gas 1 was dynamically diluted with Gas 2 to make up an Anchor gas with [N₂O] of ~ 330 ppb which was systematically measured throughout the experiments to (1) enable drift correction and (2) quantify deviations of the measured [N₂O] and δ values caused by the removal of matrix gases (O₂ and Ar in Sect. 2.4.5) or addition of trace gases (CO₂, CH₄ and CO in Sect. 2.4.6). Gases 1, 2 and 3 were combined in different fractions to make up sample gas with identical [N₂O] but varying mixing ratio of the target compound.

Target compound	Gas 1	Gas 2	Gas 3	Mixing range
O ₂	S1-a ₉₀ ppm (N ₂ O + N ₂ + O ₂)	N ₂ + O ₂ ^a	N ₂	0%–20.5% O ₂
Ar	S1-b ₉₀ ppm (N ₂ O + N ₂ + O ₂ + Ar)	N ₂ + O ₂ + Ar ^b	N ₂ + O ₂ ^a	0.003%–0.95% Ar
CO ₂	S1-b ₉₀ ppm (N ₂ O + N ₂ + O ₂ + Ar)	N ₂ + O ₂ + Ar ^b	CO ₂ in N ₂ + O ₂ + Ar ^b	1.72–2030 ppm CO ₂
CH ₄	S1-b ₉₀ ppm (N ₂ O + N ₂ + O ₂ + Ar)	N ₂ + O ₂ + Ar ^b	CH ₄ in N ₂ + O ₂ + Ar ^b	0.014–10.25 ppm CH ₄
CO	S1-b ₉₀ ppm (N ₂ O + N ₂ + O ₂ + Ar)	N ₂ + O ₂ + Ar ^b	CO in N ₂ + O ₂ + Ar ^b	0.14–2.13 ppm CO

^a Matrix a: 20.5% O₂ in N₂. ^b Matrix b: 20.95% O₂, 0.95% Ar in N₂.

ing ratios were quantified by comparing the measured [CO₂], [CH₄] and [CO] at each step change to the mean measured [CO₂], [CH₄] and [CO] of the Anchor gas. Each experiment was triplicated. The interference effects were also tested at

~ 660 ppb and ~ 990 ppb N₂O.

The sensitivity of the analyzers to water vapor was tested by firstly diluting Gas 1 (S1-c₉₀ppm) with Gas 2 (matrix c) to produce an Anchor gas with 330 ppb N₂O. This mixture was then combined with Gas 3 (also matrix c) which had been passed through a humidifier (customized setup by Glasbläserei Möller, Switzerland) set to 15 °C (F20 Julabo GmbH, Germany) dew point. By varying the flows of Gases 2 and 3, different mixing ratios of water vapor ranging from 0 to 13 800 ppm were produced and measured using a dew-point meter (model 973, MBW, Switzerland). H₂O effects were quantified as described above, but [N₂O] results were additionally corrected for dilution effects caused by the addition of water vapor into the gas stream. Water vapor dependence testing was not performed on the TREX-QCLAS I, as the instrument is equipped with a permeation dryer at the inlet.

2.4.7 CO₂ and CO removal using NaOH (Ascarite) and Sofnocat

The efficiency of NaOH and Sofnocat for removing spectral effects caused by CO₂ and CO was assessed by repeating CO₂ and CO interference tests (Sect. 2.4.6) but with the respective traps connected in line. These experiments were triplicated but only undertaken at ~ 330 ppb N₂O. NaOH traps were prepared using stainless steel tubing (OD 2.54 cm, length 20 cm) filled with 14 g Ascarite (0–30 mesh, Sigma Aldrich, Switzerland) bracketed by 3 g Mg(ClO₄)₂ (Alfa Aesar, Germany) each separated by glass wool. The Sofnocat trap was prepared similarly using stainless steel tubing (OD 2.54 cm, length 20 cm) filled with 50 g Sofnocat (Sofnocat 423, Molecular Products Limited, GB) and capped on each side with glass wool.

2.4.8 Two-end-member mixing

The ability of the instruments to accurately extrapolate N₂O source compositions was tested using a simulated two-end-member mixing scenario in which a gas with high N₂O concentration, considered to be a N₂O source gas (SG), was dynamically diluted into a gas with ambient N₂O concentration (PA2), considered to be background air. N₂O mole fractions were raised above ambient levels (denoted as Δ N₂O) in three different scenarios ranging (1) 0–30 ppb, (2) 0–700 ppb and (3) 0–10 000 ppb. In each scenario, two isotopically different source gases with high N₂O concentration were used; one source gas (SG1-a₉₀ppm) was ¹⁵N depleted compared to PA2, and a second source gas (SG2-a₉₀ppm) was ¹⁵N enriched compared to PA2 (Table 3). The three different mixing scenarios and two different source gases resulted in a total of six mixing scenarios (referred to as Exps. 1–6). During each experiment, PA2 was alternated with PA2 + SG in four different mixing ratios to give a span of N₂O concentrations and isotopic compositions required for Keeling plot analysis. Each experiment was triplicated. OA-ICOS I and QCLAS I were used in all experiments (Exps. 1–6), CRDS was used for Δ N₂O 0–30 ppb and 0–700 ppb (Exps. 1–4) and TREX-QCLAS was only used for Δ N₂O 0–30 ppb (Exps. 1–2).

To test the robustness of trace gas correction equations derived for each analyzer in Sect. 3.6, NaOH and Sofnocat traps were placed in line between the PA2 + SG mixtures and the analyzers such that we could ensure a difference in CO₂ and CO mole fractions between the measured gas mixture and reference gases (S1-c₃₃₀ppb, S2-c₃₃₀ppb). The experiments were also bracketed by two calibration phases (S1-c₃₃₀ppb, S2-c₃₃₀ppb) to allow for δ calibration, followed by two phases where the N₂O concentration dependence was determined.

Gas samples for GC-IRMS analysis were taken in the same phase (last 5 min of 15 min interval) used during the minute prior to the final 5 min used for averaging by the laser-based analyzers. The gas was collected at the common overflow port of the laser spectrometers using a 60 mL syringe connected via a Luer lock three-way valve to the nee-

dle and port. The 200 mL samples were taken at each concentration step. A 180 mL gas sample was stored in pre-evacuated 110 mL serum crimp vials for isotopic analysis using IRMS. IRMS analyses were conducted at ETH Zürich using a gas preparation unit (Trace Gas, Elementar, Manchester, UK) coupled to an IsoPrime100 IRMS (Elementar, Manchester, UK). The remaining 20 mL were injected in a pre-evacuated 12 mL Labco exetainer for $[\text{N}_2\text{O}]$ analysis using gas chromatography equipped with an electron capture detector (ECD) performed at ETH Zürich (Bruker, 456-GC, Scion Instruments, Livingston, UK). After injection, samples were separated on HayeSep D packed columns with a 5% CH_4 in Ar mixture (P5) as carrier and make-up gas. The GC was calibrated using a suite of calibration gases at N_2O concentrations of 0.393 (Carbagas AG, Switzerland), 1.02 (PanGas AG, Switzerland) and 3.17 ppm (Carbagas AG, Switzerland). For further analytical details, see Verhoeven et al. (2019) and Sect. S1.

For the laser-based analyzers, data were processed as described in Sect. 2.3.2 using the following sequential order: (1) analyzer-specific correction functions, determined in Sect. 3.6, were applied to correct for differences in trace gas concentrations (CO_2 , CO) between sample gas and calibration gases; (2) the effect of $[\text{N}_2\text{O}]$ changes was corrected using a three-point correction; (3) a drift correction based on repeated measurements of PA2 was applied if necessary; and (4) δ values standardized to international scales (Eq. 4) using $\text{S1-C}_{330\text{ppb}}$ and $\text{S2-C}_{330\text{ppb}}$.

3 Results

Note that due to the large number of results acquired in this section, only selected results are shown in Figs. 3 to 14. The complete datasets (including $[\text{N}_2\text{O}]$, $\delta^{15}\text{N}^\alpha$, $\delta^{15}\text{N}^\beta$ and $\delta^{18}\text{O}$ acquired by all instruments tested) are provided in Sect. S4.

3.1 Allan precision

Allan deviations (square root of Allan variance) for 5 and 10 min averaging times, often reported in manufacturer specifications, at ~ 327 , 1000 and 10 000 ppb $[\text{N}_2\text{O}]$ are shown in Table 6.

At near-atmospheric N_2O mole fractions of ~ 326.5 ppb, both CRDS analyzers showed the best precision and stability for the measurement of $\delta^{15}\text{N}^\alpha$, $\delta^{15}\text{N}^\beta$ and $\delta^{18}\text{O}$ (0.32‰–0.41‰, 0.41‰–0.45‰, 0.41‰–0.46‰ at 300 s averaging time, respectively), while for the precision of $[\text{N}_2\text{O}]$, the OA-ICOS I and the CRDS II showed best performance (1.7×10^{-2} ppb at 300 s averaging time) (Figs. 3 and S4-1; Table 6). The Allan precision of CRDS and OA-ICOS analyzers further improved with increasing averaging times, and optimal averaging times typically exceeded 1.5–3 h. The precision and daily drift of the OA-ICOS I and both CRDS analyzers were in agreement with manufacturer specifications

(ABB – Los Gatos Research Inc., 2019; Picarro Inc., 2019). The CRDS II outperformed the CRDS I for precision, presumably due to manufacturer upgrades/improvements in the newer model. The QCLAS spectrometers exhibited significant differences between instruments, which might be due to differences in the instrument hardware/design, as instruments were manufactured between 2012 and 2016, or in the parameter setting (such as cell pressure and tuning parameters) of different analyzers.

Generally, short-term (approximately up to 100 s) precision of QCLAS instruments was compatible or superior to CRDS or OA-ICOS, but data quality was decreased for longer averaging times due to drift effects. Nonetheless, the performance of QCLAS I, II and III generally agrees with Allan precision measurements executed by Yamamoto et al. (2014), who reported 1.9‰–2.6‰ precision for δ values at ambient N_2O mole fractions and 0.4‰–0.7‰ at 1000 ppb N_2O . QCLAS I, which was tested further in Sect. 3.2–3.7, displayed the poorest performance of all QCLAS analyzers, in particular for $\delta^{15}\text{N}^\beta$. The primary cause of the observed excess drift in QCLAS I was fluctuating spectral baseline structure (ARI, personal communication, 2019), which can be significantly reduced by applying an automatic spectral correction method developed by ARI. This methodology is currently in a trial phase and thus not yet implemented in the software that controls the QCLAS instruments. A brief overview of the methodology is provided in Sect. S5, and corrected results for QCLAS I are provided in Table 6. This methodology is not discussed in detail here as it is beyond the scope of this work. Nonetheless, QCLAS I achieved Allan deviations of ~ 0.4 ‰ at 300 s averaging time for $\delta^{15}\text{N}^\alpha$ and $\delta^{15}\text{N}^\beta$ at ambient N_2O mole fractions when this correction method was applied by ARI.

At $[\text{N}_2\text{O}]$ of 1000 ppb, the precision of δ values measured by all analyzers, except CRDS I, significantly improved due to greater signal-to-noise ratios. Whilst the performance of OA-ICOS I was similar to that of CRDS II for $\delta^{15}\text{N}^\alpha$ and $\delta^{15}\text{N}^\beta$ (0.24‰ and 0.24‰ for CRDS II; 0.28‰ and 0.37‰ for OA-ICOS I at 300 s averaging time), CRDS II displayed the best precision for $\delta^{18}\text{O}$ (0.21‰ at 300 s averaging time). Also notable was the improved performance of the 2018 model (CRDS II) compared to the 2015 model (CRDS I). QCLAS analyzers showed the best 1 s precision for δ values, but beyond 100 s, δ measurements were still heavily affected by instrumental drift resulting in lower precision, especially for QCLAS I. When the spectral correction method described in Sect. S5 was applied, QCLAS I achieved Allan deviations of ~ 0.2 ‰ at 300 s averaging time for $\delta^{15}\text{N}^\alpha$ and $\delta^{15}\text{N}^\beta$ at 1000 ppb N_2O .

At $[\text{N}_2\text{O}]$ of 10 000 ppb, all analyzers showed excellent precision, with QCLAS I, II and III outperforming OA-ICOS I for precision of $\delta^{15}\text{N}^\alpha$ and $\delta^{15}\text{N}^\beta$ (collectively better than 0.10‰ at 300 s averaging time for both $\delta^{15}\text{N}^\alpha$ and $\delta^{15}\text{N}^\beta$). QCLAS II had the best precision for $[\text{N}_2\text{O}]$ (1.2 ppb at 300 s averaging time). OA-ICOS I and QCLAS III were the only

analyzers tested in this study that could be used to measure $\delta^{18}\text{O}$ at 10 000 ppb N_2O . OA-ICOS I attained a precision of 0.17 ‰, while QCLAS III attained a precision of 0.48 ‰, both with 300 s averaging time. QCLAS I achieved Allan deviations of $\sim 0.02\text{‰}$ – 0.03‰ at 300 s averaging time for $\delta^{15}\text{N}^\alpha$ and $\delta^{15}\text{N}^\beta$ at 10 000 ppb N_2O when the spectral correction method (Sect. S5) was applied.

The precision of instruments on $[\text{N}_2\text{O}]$ measurements at 1000 and 10 000 ppb N_2O might not be representative because of small fluctuations in the final gas mixture produced by the MFCs, which were likely amplified due to the small dilution ratios. Moreover, the different relative increases in Allan deviation compared to measurements at 326.5 ppb might have been caused by the different internal plumbing volumes, flow rates and spectral fits used for the analyzers, which could scale or add to the increased Allan deviation introduced via the MFCs. Therefore, the indicated $[\text{N}_2\text{O}]$ precisions should be considered as a pessimistic estimate. Nonetheless, the observed decline in $[\text{N}_2\text{O}]$ precision for all analyzers was around 1 order of magnitude when changing from atmospheric N_2O mole fractions to 1000 ppb N_2O and from 1000 ppb to 10 000 ppb N_2O .

3.2 Temperature effects

All instruments tested showed significant effects, albeit to varying degrees, on their measurements due to the change in laboratory temperature (Figs. 4 and S4-2). The OA-ICOS I displayed no clear temperature effects for $[\text{N}_2\text{O}]$, $\delta^{15}\text{N}^\alpha$ and $\delta^{15}\text{N}^\beta$ but displayed a moderate temperature dependence for $\delta^{18}\text{O}$ measurements (up to 14 ‰ deviation from the mean), with measurement drift closely paralleling the laboratory temperature ($r^2 = 0.78$). Both CRDS instruments displayed smaller shifts in $[\text{N}_2\text{O}]$ (up to 0.14 ppb deviation from the mean), $\delta^{15}\text{N}^\alpha$, $\delta^{15}\text{N}^\beta$ and $\delta^{18}\text{O}$ that occurred particularly when the laboratory temperature had an acute change. QCLAS I showed a strong temperature dependence on $\delta^{15}\text{N}^\alpha$ ($r^2 = 0.85$) and $\delta^{15}\text{N}^\beta$ ($r^2 = 0.96$).

3.3 Repeatability

The best long-term repeatability for δ values was achieved by TREX-QCLAS I with 0.60 ‰ for $\delta^{15}\text{N}^\alpha$, 0.37 ‰ for $\delta^{15}\text{N}^\beta$ and 0.46 ‰ for $\delta^{18}\text{O}$, even though measurements were taken over a 6-month period (Table 7). The best repeatability without preconcentration was achieved by CRDS analyzers with 0.52 ‰– 0.75‰ for CRDS II and 0.79 ‰– 0.83‰ for CRDS I for all δ values. OA-ICOS I achieved repeatability between 1 ‰– 2‰ (1.47 ‰, 1.19 ‰ and 2.17 ‰ for $\delta^{15}\text{N}^\alpha$, $\delta^{15}\text{N}^\beta$ and $\delta^{18}\text{O}$, respectively). QCLAS I isotopic measurements attained repeatability of 5.4 ‰ and 8.6 ‰ for $\delta^{15}\text{N}^\alpha$ and $\delta^{15}\text{N}^\beta$, respectively. Short-term repeatability results for 10 repeated 15 min measurements periods over 2.5 h are provided in Sect. S6.

3.4 Dependence of isotopic measurements on N_2O mole fraction

There was an offset in measured δ values resulting from the change in $[\text{N}_2\text{O}]$ introduced to the analyzers (Figs. 5 and S4-3). A linear relationship between $\Delta\delta^{15}\text{N}^{\alpha,\beta}$ and $\Delta\delta^{18}\text{O}$ values with $[1/\text{N}_2\text{O}]$ was observed across all analyzers that were tested. However, examination of the residuals from the linear regression revealed varying degrees of residual curvature, highlighting that further non-linear terms would be required to adequately describe, and correct for, this mole fraction dependence. Repeated analysis of $[\text{N}_2\text{O}]$ dependencies on consecutive days showed similar trends, indicating that the structure of non-linear effects might be stable over short periods of time. Nevertheless, there were small variabilities in δ values at a given N_2O mole fraction, which could be due to the inherent uncertainty of the measurement and/or day-to-day variations in the mole fraction dependence. The standard deviation of individual 5 min averages of $\delta^{15}\text{N}^{\alpha,\beta}$ and $\delta^{18}\text{O}$ also varied according to the $[\text{N}_2\text{O}]$ measured by each analyzer due to variations in the signal-to-noise ratio (Sect. S7).

3.5 Gas matrix effects (O_2 and Ar)

3.5.1 Gas matrix effects at ambient N_2O mole fractions

With the exception of TREX-QCLAS I, all instruments displayed strong O_2 dependencies for $[\text{N}_2\text{O}]$ and δ values (Figs. 6 and S4-4). For these instruments, linear regressions best described the offset of measured $[\text{N}_2\text{O}]$ and δ values resulting from the change in O_2 composition of the matrix gas. Importantly, CRDS I and II displayed different degrees of O_2 interference on $[\text{N}_2\text{O}]$ and δ values, suggesting that these dependencies were either analyzer-specific or differences were due to hardware/software modifications between different production years. Preconcentration prior to analysis, as performed in TREX-QCLAS I, eliminated O_2 dependencies as the gas matrix was normalized to synthetic air (20.5 % O_2).

The change in Ar composition of the matrix gas caused minor, yet measurable, interferences on $[\text{N}_2\text{O}]$ and δ measurements (Fig. S4-5). The range investigated was between approximately 0 % and 0.95 % Ar, as anticipated for N_2O in synthetic air (no Ar) reference gas versus a whole air (with Ar) sample gas. The effects observed for a 0.95 % change in [Ar] were significantly smaller than that observed for O_2 but might extend to a similar range for sample and reference gases with higher differences in [Ar]. The interference effects were found to be best described by second-order polynomial functions, though we expect that a linear fit would serve equally well if a larger change in [Ar] was investigated. Although most functions to describe the dependence on Ar across all instruments were statistically significant ($p < 0.05$), maximum effects did not transgress the repeatability.

Table 6. Key parameters for instrument stability retrieved from Allan variance experiments for $[\text{N}_2\text{O}]$, $\delta^{15}\text{N}^\alpha$, $\delta^{15}\text{N}^\beta$ and $\delta^{18}\text{O}$: precision (1σ) at 300 and 600 s averaging times, and daily drift at various N_2O concentrations. The 1σ data refer to Allan deviation (square root of Allan variance).

Instrument	1σ N_2O (ppb) (300 s)	1σ N_2O (ppb) (600 s)	N_2O drift (ppb d^{-1})	1σ $\delta^{15}\text{N}^\alpha$ (‰) (300 s)	1σ $\delta^{15}\text{N}^\alpha$ (‰) (600 s)	$\delta^{15}\text{N}^\alpha$ drift (‰ d^{-1})	1σ $\delta^{15}\text{N}^\beta$ (‰) (300 s)	1σ $\delta^{15}\text{N}^\beta$ (‰) (600 s)	$\delta^{15}\text{N}^\beta$ drift (‰ d^{-1})	1σ $\delta^{18}\text{O}$ (‰) (300 s)	1σ $\delta^{18}\text{O}$ (‰) (600 s)	$\delta^{18}\text{O}$ drift (‰ d^{-1})
326.5 ppb N_2O												
CRDS I	3.0×10^{-2}	2.3×10^{-2}	2.0×10^{-2}	0.41	0.27	0.22	0.45	0.38	0.18	0.46	0.34	0.03
CRDS II	1.7×10^{-2}	1.2×10^{-2}	3.2×10^{-2}	0.32	0.23	3.5×10^{-3}	0.41	0.31	0.14	0.41	0.28	0.10
OA-ICOS I	1.7×10^{-2}	1.3×10^{-2}	1.5×10^{-2}	1.08	0.82	0.07	0.79	0.52	0.50	1.69	1.14	2.34
QCLAS I	6.3×10^{-2}	4.6×10^{-2}	3.7×10^{-2}	1.24	1.41	6.80	3.45	4.22	15.81	n.d.	n.d.	n.d.
QCLAS I*	2.1×10^{-2}	2.4×10^{-2}	0.12	0.39	0.37	0.71	0.42	0.55	4.83	n.d.	n.d.	n.d.
QCLAS II	9.5×10^{-3}	1.1×10^{-2}	1.00	1.08	1.44	0.20	0.60	0.72	0.05	n.d.	n.d.	n.d.
QCLAS III	2.5×10^{-2}	3.6×10^{-2}	0.75	0.81	1.23	0.09	0.78	1.22	0.04	0.97	1.51	0.13
~ 1000 ppb N_2O												
CRDS I	7.7×10^{-1}	6.0×10^{-1}	0.29	0.88	0.67	0.67	0.89	0.73	1.39	0.81	0.67	0.32
CRDS II	2.1×10^{-1}	1.3×10^{-1}	0.54	0.24	0.20	0.36	0.24	0.18	0.23	0.21	0.13	0.86
OA-ICOS I	1.7×10^{-1}	1.2×10^{-1}	1.02	0.28	0.23	0.93	0.37	0.25	0.54	0.67	0.44	0.15
QCLAS I	3.3×10^{-1}	2.4×10^{-1}	1.03	0.47	0.61	7.25	0.83	1.11	8.01	n.d.	n.d.	n.d.
QCLAS I*	1.4×10^{-1}	1.0×10^{-1}	1.2×10^{-3}	0.19	0.23	0.61	0.20	0.22	0.11	n.d.	n.d.	n.d.
QCLAS II	2.0×10^{-1}	2.4×10^{-1}	4.11	0.52	0.49	0.04	0.22	0.19	4.3×10^{-3}	n.d.	n.d.	n.d.
QCLAS III	1.0×10^{-1}	1.6×10^0	1.61	0.81	1.37	0.06	0.72	1.18	0.03	0.38	0.54	0.05
~ 10000 ppb N_2O												
OA-ICOS I	1.7×10^0	1.3×10^0	1.30	0.12	0.10	0.12	0.15	0.09	0.54	0.17	0.12	0.35
QCLAS I	3.3×10^0	2.3×10^0	3.74	0.06	0.07	1.09	0.09	0.11	0.82	n.d.	n.d.	n.d.
QCLAS I*	4.6×10^{-1}	3.8×10^{-1}	0.10	0.03	0.03	0.02	0.02	0.03	0.10	n.d.	n.d.	n.d.
QCLAS II	1.2×10^0	9.9×10^{-1}	35.1	0.09	0.07	2.9×10^{-3}	0.09	0.08	7.0×10^{-3}	n.d.	n.d.	n.d.
QCLAS III	1.3×10^0	1.6×10^0	66.1	0.10	0.17	3.4×10^{-3}	0.10	0.13	5.8×10^{-3}	0.48	0.65	2.8×10^{-3}

* Data were reprocessed by Aerodyne Research Inc. technicians using an automatic spectral correction method. This method corrects data that were influenced by changing baseline structure. Further information on this method is provided in Sect. S5. "n.d." indicates not determined.

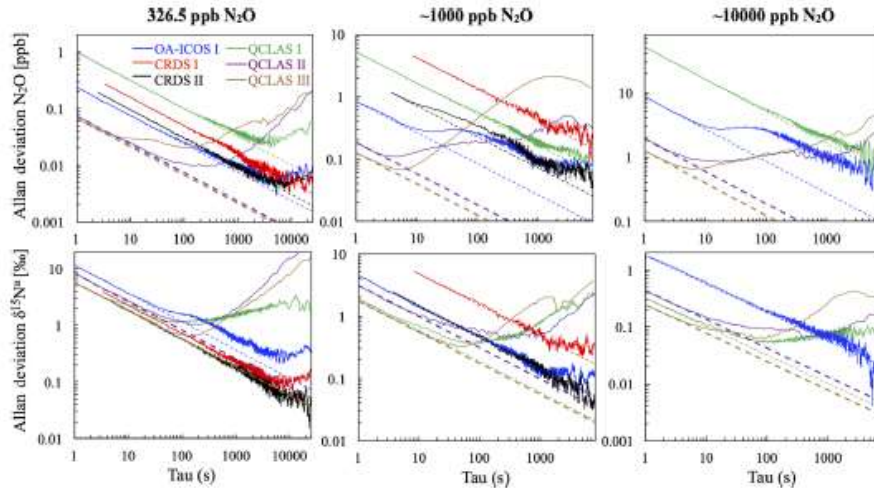


Figure 3. Allan deviation (square root of Allan variance) plots for the OA-ICOS I (blue), CRDS I (red), CRDS II (black), QCLAS I (green), QCLAS II (purple) and QCLAS III (brown) at different N_2O mole fractions (~ 327, 1000 and 10 000 ppb). The dashed lines represent a slope of -0.5 (log–log scale) and indicate the expected behavior for Gaussian white noise in each analyzer. The Allan deviations of all analyzers tested were reproducible on three separate occasions prior to the test results presented here. Allan deviation plots for $\delta^{15}\text{N}^\beta$ and $\delta^{18}\text{O}$ are provided in Sect. S4 (Fig. S4-1 in the Supplement).

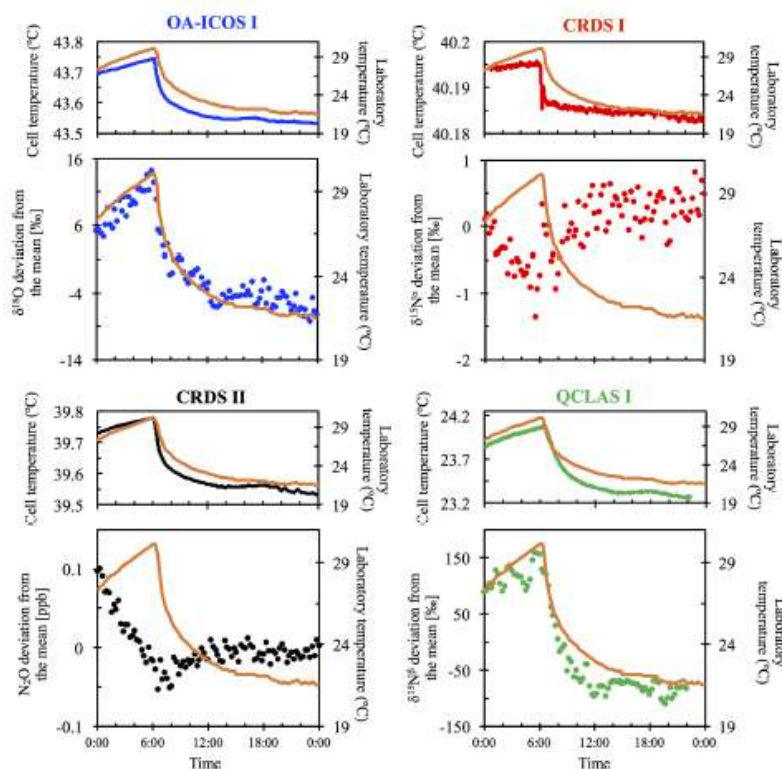


Figure 4. Examples of the dependency of different measurements on laboratory temperature ($^{\circ}\text{C}$) for OA-ICOS I (blue), CRDS I (red), CRDS II (black) and QCLAS I (green). The complete dataset is provided in Sect. S4 (Fig. S4-2). The laboratory temperature is indicated by a solid orange line and was allowed to vary over time. Cell temperatures for each instrument are also plotted for comparison. The analyzers began acquiring measurements at 00:00 LT [15 Jul](#) on 8 July 2018 [15 Jul](#), capturing the end of the rising limb of the laboratory temperature. Results are plotted as the deviation from the mean, without any anchoring to reference gases.

Table 7. Summary of the measured $[\text{N}_2\text{O}]$, $\delta^{15}\text{N}^{\alpha}$, $\delta^{15}\text{N}^{\beta}$ and $\delta^{18}\text{O}$ and associated 1σ at 300 s averaging times based on repeated measurements of PA1.

Instrument	n	N_2O (ppb)	1σ N_2O (ppb)	$\delta^{15}\text{N}^{\alpha}$ (‰)	1σ $\delta^{15}\text{N}^{\alpha}$ (‰)	$\delta^{15}\text{N}^{\beta}$ (‰)	1σ $\delta^{15}\text{N}^{\beta}$ (‰)	$\delta^{18}\text{O}$ (‰)	1σ $\delta^{18}\text{O}$ (‰)
CRDS I	22	326.66	0.30	15.86	0.79	-2.30	0.83	44.48	0.81
CRDS II	22	326.72	0.26	15.71	0.52	-2.86	0.64	44.40	0.75
OA-ICOS I	22	326.49	0.07	15.29	1.47	-2.11	1.19	44.01	2.17
QCLAS I	22	326.82	0.16	13.92	5.35	-2.97	8.57	–	–
TREX-QCLAS I	28	326.70	1.29	15.72	0.60	-2.82	0.37	44.31	0.46
Empa-assigned values	3	326.51	0.06	15.81	0.07	-3.31	0.004	44.72	0.04

bility (1σ) of the Anchor gas measurements. TREX-QCLAS I measurements were not impaired by gas matrix effects.

3.5.2 Continuity of gas matrix corrections at higher N_2O mole fractions

When mole fractions of 660 and 990 ppb N_2O were measured by the laser spectrometers, O_2 interference effects on

$[\text{N}_2\text{O}]$ and δ values were well described using linear regression, albeit with different slopes to those obtained for 330 ppb N_2O (Figs. 6 and S4-4; Sect. S8).

We could not adequately predict the nature in which the slopes of the interference effects scaled with N_2O mole fractions. Overall, this suggests that interference effects were analyzer-specific and varied according to instrument-specific

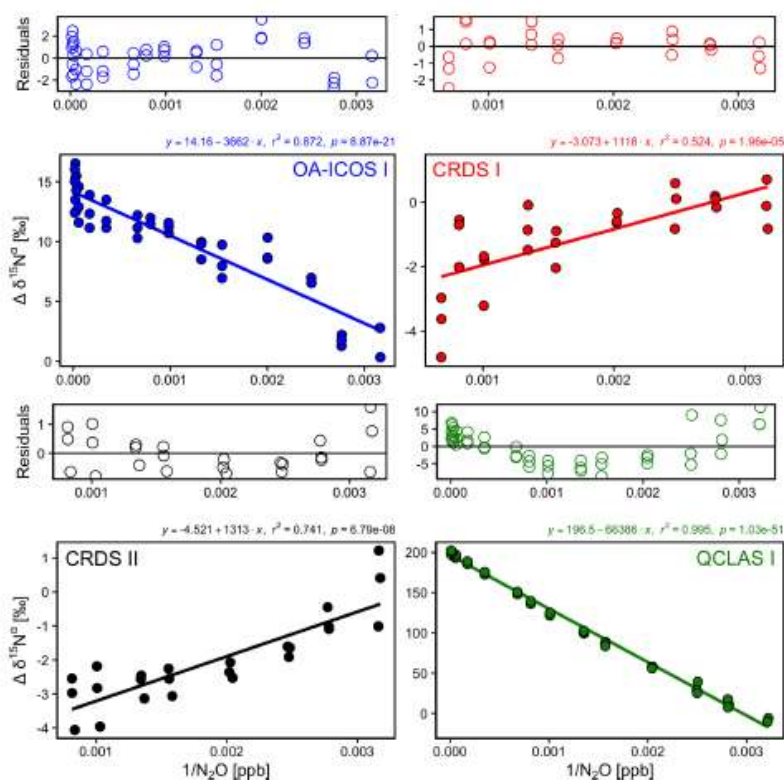


Figure 5. Deviations of the measured $\delta^{15}\text{N}^\alpha$, $\delta^{15}\text{N}^\beta$ and $\delta^{18}\text{O}$ values according to $1/[\text{N}_2\text{O}]$ for the OA-ICOS I (blue), CRDS I (red), CRDS II (black) and QCLAS I (green). Measurements span the manufacturer-specified operational ranges of the analyzers. The experiment was repeated on three separate days. A linear regression is indicated by the solid line, and a residual plot is provided above each plot. Individual linear equations, coefficients of determination (r^2) and p values are indicated above each plot. The remaining plots for $\delta^{15}\text{N}^\beta$ and $\delta^{18}\text{O}$ are provided in Sect. S4 (Fig. S4-3).

parameters, rather than due to bona fide scaling of the pressure-broadening effect. Therefore, to account for combined effects of $[\text{O}_2]$ and $[\text{N}_2\text{O}]$ changes on measurements, a user would be required to perform a series of laboratory tests across the range of expected $[\text{O}_2]$ and $[\text{N}_2\text{O}]$. In an exemplary approach, we applied a series of empirical equations (Eqs. 5–6) to predict the offset of measured $[\text{N}_2\text{O}]$ and δ values caused by changes in $[\text{O}_2]$ as a function of $[\text{N}_2\text{O}]$ introduced to the analyzers in this study:

$$\Delta[\text{N}_2\text{O}]_{\text{meas, mix}}(\Delta[\text{O}_2]_A, [\text{N}_2\text{O}]_{\text{exp, mix}}) = (A \cdot [\text{N}_2\text{O}]_{\text{exp, mix}}^2 + B \cdot [\text{N}_2\text{O}]_{\text{exp, mix}}) \cdot \Delta[\text{O}_2]_A \quad (5)$$

$$\Delta\delta_{\text{meas, mix}}(\Delta[\text{O}_2]_A, [\text{N}_2\text{O}]_{\text{exp, mix}}) = (a \cdot [\text{N}_2\text{O}]_{\text{exp, mix}}^2 + b \cdot [\text{N}_2\text{O}]_{\text{exp, mix}} + c) \cdot \Delta[\text{O}_2]_A, \quad (6)$$

where $\Delta[\text{N}_2\text{O}]_{\text{meas, mix}}$ and $\Delta\delta_{\text{meas, mix}}$ are the measured offsets on $[\text{N}_2\text{O}]$ and δ values for the gas mixtures introduced to the analyzers as reported in Sect. 3.5.1, respectively; $\Delta[\text{O}_2]_A$

is the difference in O_2 mole fraction between the gas mixture and Anchor gas as reported in Sect. 3.5.1; $[\text{N}_2\text{O}]_{\text{exp, mix}}$ is the expected $[\text{N}_2\text{O}]$ of gas mixtures introduced to the analyzer, calculated based on gas flows and cylinder compositions of Gases 1, 2 and 3 as reported in Sect. 2.4.5; A and B , and a , b and c are analyzer-specific constants.

Using Eqs. (5) and (6) to fit values for the constants A and B for $\Delta[\text{N}_2\text{O}]_{\text{meas, mix}}$, and a , b and c for $\Delta\delta_{\text{meas, mix}}$ resulted in a total of 11 analyzer-specific values (Sect. S8). With gas-specific constants established, interferences on $[\text{N}_2\text{O}]$ and δ measurements for a sample gas G for a given analyzer can be corrected using Eqs. (7)–(8):

$$[\text{N}_2\text{O}]_{\text{mc, G}} = \frac{-(1 + B \cdot \Delta[\text{O}_2]_G) + \sqrt{(1 + B \cdot \Delta[\text{O}_2]_G)^2 + 4 \cdot A \cdot \Delta[\text{O}_2]_G \cdot [\text{N}_2\text{O}]_{\text{meas, G}}}}{2 \cdot A \cdot \Delta[\text{O}_2]_G} \quad (7)$$

$$\delta_{\text{mc, G}} = \delta_{\text{meas, G}} - (a \cdot [\text{N}_2\text{O}]_{\text{mc, G}}^2 + b \cdot [\text{N}_2\text{O}]_{\text{mc, G}} + c) \cdot \Delta[\text{O}_2]_G, \quad (8)$$

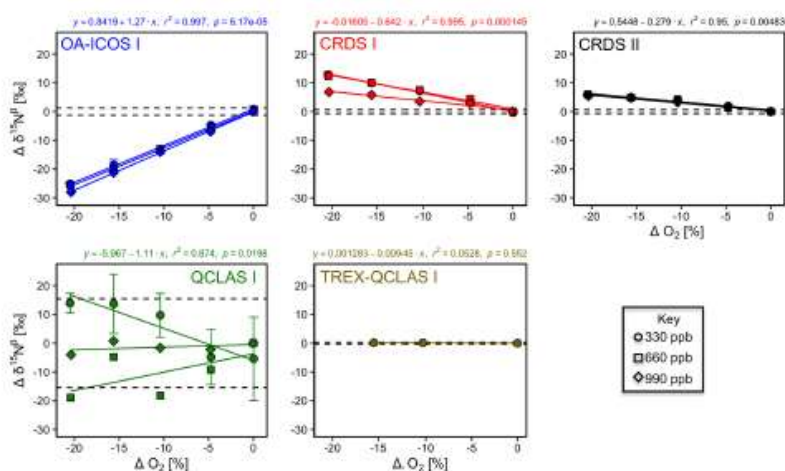


Figure 6. Deviations of the measured $[\text{N}_2\text{O}]$, $\delta^{15}\text{N}^\alpha$, $\delta^{15}\text{N}^\beta$ and $\delta^{18}\text{O}$ values according to ΔO_2 (%) at different N_2O mole fractions (330, 660 and 990 ppb) for the OA-ICOS I (blue), CRDS I (red), CRDS II (black), QCLAS I (green) and TREX-QCLAS I (brown). The remaining plots for $[\text{N}_2\text{O}]$, $\delta^{15}\text{N}^\alpha$ and $\delta^{18}\text{O}$ are provided in Sect. S4 (Fig. S4-4). The standard deviation of the Anchor gas ($\pm 1\sigma$) is indicated by dashed lines. Data points represent the mean and standard deviation (1σ) of triplicate measurements. Dependencies are best described using linear regressions, which are indicated by a solid line. Individual equations, coefficients of determination (r^2) and p values are indicated above each plot for the 330 ppb N_2O data only.

where $[\text{N}_2\text{O}]_{\text{mc}, G}$ and $\delta_{\text{mc}, G}$ are the matrix-corrected $[\text{N}_2\text{O}]$ and δ values of sample gas G (Fig. 2), respectively; $\Delta[\text{O}_2]_G$ is the difference in O_2 mole fraction between sample gas G and reference gases. Correction using Eqs. (7)–(8) removes the O_2 effect to a degree that corrected measurements from Sect. 3.5.1 are typically within the uncertainty bounds of the anchor (Sect. S8).

Although Ar effects seemingly scaled with increased N_2O mole fractions, we did not derive scaling coefficients for Ar because the derived Ar correction equations at 330, 660 and 990 ppb N_2O were typically not statistically significant at $p < 0.05$. These interferences also did not always exceed the repeatability of Anchor gas measurements. Although we could have tested for effects for $[\text{Ar}]$ changes greater than 0.95 %, we limited our experiments to $[\text{Ar}]$ expected in tropospheric samples.

3.6 Trace gas effects (H_2O , CO_2 , CH_4 and CO)

3.6.1 Trace gas effects at ambient N_2O mole fractions

The apparent offset of $[\text{N}_2\text{O}]$ and δ values resulting from the change in CO_2 composition of the matrix gas was best described by linear functions (Figs. 7 and S4-6). OA-ICOS I exhibited discrete and well-defined linear interference effects of CO_2 on $[\text{N}_2\text{O}]$, $\delta^{15}\text{N}^\alpha$, $\delta^{15}\text{N}^\beta$ and $\delta^{18}\text{O}$ (all $r^2 > 0.95$), likely due to crosstalk between CO_2 absorption lines situated near 2192.46 and 2192.33 cm^{-1} . Both CRDS instruments showed CO_2 interference effects of smaller magnitude for $[\text{N}_2\text{O}]$, $\delta^{15}\text{N}^\alpha$ and $\delta^{18}\text{O}$, presumably due to CO_2 absorption

lines at 2196.21, 2195.72 and 2196.02 cm^{-1} . QCLAS I displayed less well-defined CO_2 interference effects for $\delta^{15}\text{N}^\beta$, which was possibly due to several overlapping absorption lines of CO_2 located near 2187.85 cm^{-1} . All linear functions derived for the TREX-QCLAS I were not statistically significant at $p < 0.05$. As shown in Figs. 7 and S4-6, the NaOH trap was effective in removing the CO_2 effect (if present) across the mole fraction ranges tested for all instruments.

Similarly, CH_4 effects on apparent $[\text{N}_2\text{O}]$ and δ values were well described by linear functions (Figs. 8 and S4-7). The largest effects were for CRDS I and II, which both displayed strong CH_4 dependencies for $\delta^{15}\text{N}^\alpha$ and $\delta^{18}\text{O}$ of similar magnitude. This might be due to crosstalk of $^{14}\text{N}^{15}\text{N}^{16}\text{O}$ and $^{14}\text{N}^{14}\text{N}^{18}\text{O}$ absorption lines with the respective CH_4 lines located at 2195.76 and 2195.95 cm^{-1} . For OA-ICOS I, minor CH_4 effects were observed for $\delta^{15}\text{N}^\beta$, due to absorption line overlap at 2192.33 cm^{-1} . QCLAS I did not display any CH_4 interference effect over the tested $[\text{CH}_4]$ range. Linear functions derived for the TREX-QCLAS I were not statistically significant at $p < 0.05$. The similarity between the $[\text{N}_2\text{O}]$ dependencies on CH_4 mole fractions for OA-ICOS I, CRDS I, II and QCLAS I suggests that the apparent effects may be due to small fluctuations in the gas mixtures produced by the MFCs, rather than a discrete spectral interference effect.

The CRDS analyzers showed minor interference effects for $\delta^{15}\text{N}^\alpha$ and $\delta^{15}\text{N}^\beta$ on $[\text{CO}]$ (0.14–2.14 ppm) (Fig. S4-8), likely due to crosstalk with CO absorption lines located at 2195.69 and 2195.83 cm^{-1} . The magnitude of these effects

was similar for both models. QCLAS I displayed interference effects for $\delta^{15}\text{N}^\alpha$ and $\delta^{15}\text{N}^\beta$ caused by a CO absorption line located near 2187.9 cm^{-1} , although this effect did not exceed the repeatability of the Anchor gas (containing no CO) over the measurement range. The effects of [CO] on δ values acquired using OA-ICOS I and TREX-QCLAS I were not statistically significant at $p < 0.05$. Similar to CH_4 , the resemblance of [CO] effects to $[\text{N}_2\text{O}]$ measurements for OA-ICOS I, CRDS I, II and QCLAS I suggests that the apparent effects may be due to inaccuracies in the dynamic dilution process, rather than a discrete spectral interference effect. The Sofno-cat trap was effective in removing CO (if present) across the mole fraction ranges tested for all instruments.

OA-ICOS I exhibited large effects of $[\text{H}_2\text{O}]$ (0–13 800 ppm) on $\delta^{15}\text{N}^\beta$ (up to -10‰) and $\delta^{18}\text{O}$ (up to -15‰), and minor dependencies for $\delta^{15}\text{N}^\alpha$ (up to 4‰) and $[\text{N}_2\text{O}]$ (up to 1 ppb) across the range tested (Fig. S4–9). For QCLAS I, the H_2O effect was largest for $\delta^{15}\text{N}^\alpha$ (up to 20‰), whilst minor effects for $[\text{N}_2\text{O}]$ (up to 2 ppb) were observed in relation to the Anchor gas (no H_2O). In contrast, both CRDS instruments showed no significant effects across the range tested, which is attributable to the installation of permeation dryers inside the analyzers by the manufacturer.

3.6.2 Continuity of trace gas corrections at higher N_2O mole fractions

Interference effects from CO_2 , CH_4 and CO on apparent δ values, where significant, inversely scaled with increasing $[\text{N}_2\text{O}]$ (Figs. 7, 8, S4–8 and Sect. S8). The scaling of trace gas effects can be explained by simple spectral overlap of the $^{14}\text{N}^{15}\text{N}^{16}\text{O}$, $^{15}\text{N}^{14}\text{N}^{16}\text{O}$ and $^{14}\text{N}^{14}\text{N}^{18}\text{O}$ lines with those of the trace gas, which results in the interference effects being inversely proportional to the mixing ratio of N_2O . However, there may be additional spectral overlap between the trace gas and the $^{14}\text{N}^{14}\text{N}^{16}\text{O}$ peak resulting in an offset for the measured $[\text{N}_2\text{O}]$, which introduces a further shift in the δ values (as shown in Sect. 3.4). The effect on the apparent $[\text{N}_2\text{O}]$ was less clear and was possibly confounded by inaccuracies during dynamic gas mixing. In this study, the scaling of interference effects from trace gases as a function of the $[\text{N}_2\text{O}]$ introduced to the analyzers could be described using Eqs. (9) and (10):

$$\begin{aligned} \Delta[\text{N}_2\text{O}]_{\text{meas, mix}}(\Delta[x]_A, [\text{N}_2\text{O}]_{\text{exp, mix}}) \\ = \left(A_x \frac{1}{[\text{N}_2\text{O}]_{\text{exp, mix}}} + B_x \right) \cdot \Delta[x]_A \end{aligned} \quad (9)$$

$$\begin{aligned} \Delta\delta_{\text{meas, mix}}(\Delta[x]_A, [\text{N}_2\text{O}]_{\text{exp, mix}}) \\ = \left(a_x \cdot \frac{1}{[\text{N}_2\text{O}]_{\text{exp, mix}}} + b_x \right) \cdot \Delta[x]_A, \end{aligned} \quad (10)$$

where $\Delta[\text{N}_2\text{O}]_{\text{meas, mix}}$ and $\Delta\delta_{\text{meas, mix}}$ are the measured offsets on $[\text{N}_2\text{O}]$ and δ values for the gas mixtures introduced to the analyzers as reported in Sect. 3.6.1, respectively; $\Delta[x]_A$ is the difference in trace gas mole fraction between the gas

mixture and Anchor gas as reported in Sect. 3.6.1; and A_x , B_x , a_x and b_x are constants that are trace gas and instrument specific. The constant b_x only occurs when there is spectral overlap from the trace gas and $^{14}\text{N}^{14}\text{N}^{16}\text{O}$ absorption lines.

For a sample gas G, the effect can then be corrected by using Eqs. (11) and (12):

$$[\text{N}_2\text{O}]_{\text{tc, G}} = [\text{N}_2\text{O}]_{\text{meas, G}} - \sum_x \left(\left(A_x \frac{1}{[\text{N}_2\text{O}]_{\text{meas, G}}} + B_x \right) \cdot \Delta[x]_G \right) \quad (11)$$

$$\delta_{\text{tc, G}} = \delta_{\text{meas, G}} - \sum_x \left(\left(a_x \frac{1}{[\text{N}_2\text{O}]_{\text{meas, G}}} + b_x \right) \cdot \Delta[x]_G \right). \quad (12)$$

In Eqs. (11)–(12), the sum of the effect of all interfering gases with overlapping absorption lines is taken into account. Similar to Sect. 3.5.2, correction using Eqs. (11)–(12) removes the trace gas interference effects to the extent that corrected measurements from Sect. 3.6.1 are within the repeatability bounds of the Anchor gas (Sect. S8). Similar inverse relationships have been described by Malowany et al. (2015) for H_2S interferences on $\delta^{13}\text{C}$ – CO_2 .

3.7 Two-end-member mixing

Results for the two-end-member mixing experiment were evaluated in two different ways. First, results for individual gas mixtures acquired by laser spectroscopy and GC-IRMS were compared to expected $[\text{N}_2\text{O}]$ and δ values calculated from N_2O mole fractions and isotopic composition of end-members and mixing fractions. Second, source values were extrapolated using a weighted total least squares regression analysis, known as Keeling plot analysis (Keeling, 1958), and compared to assigned δ values of the source gas used in each experiment.

3.7.1 Comparison with expected $[\text{N}_2\text{O}]$ and δ values

Triplicate measurements (mean $\pm 1\sigma$) obtained using the laser spectrometers and GC-IRMS were plotted against expected $[\text{N}_2\text{O}]$ and δ values calculated using MFC flow rates, N_2O mole fractions and isotopic composition of background and source gases (Figs. 12–15). Comparisons between individual laser spectrometer measurements and GC-IRMS are plotted in Sect. S9 and are discussed only briefly below.

OA-ICOS I

Generally, there was good agreement of $[\text{N}_2\text{O}]$ between the OA-ICOS I and expected values, although the analyzer overestimated mole fractions at higher $\Delta\text{N}_2\text{O}$ during Exps. 5 and 6. There was excellent agreement between the OA-ICOS I and calculated expected δ values (all $r^2 > 0.95$; Figs. 9 and S4–10). Measurements for $\delta^{15}\text{N}^\alpha$ were mostly within $\pm 2.4\text{‰}$ of expected values, while $\delta^{15}\text{N}^\beta$, $\delta^{15}\text{N}^{\text{bulk}}$ and SP

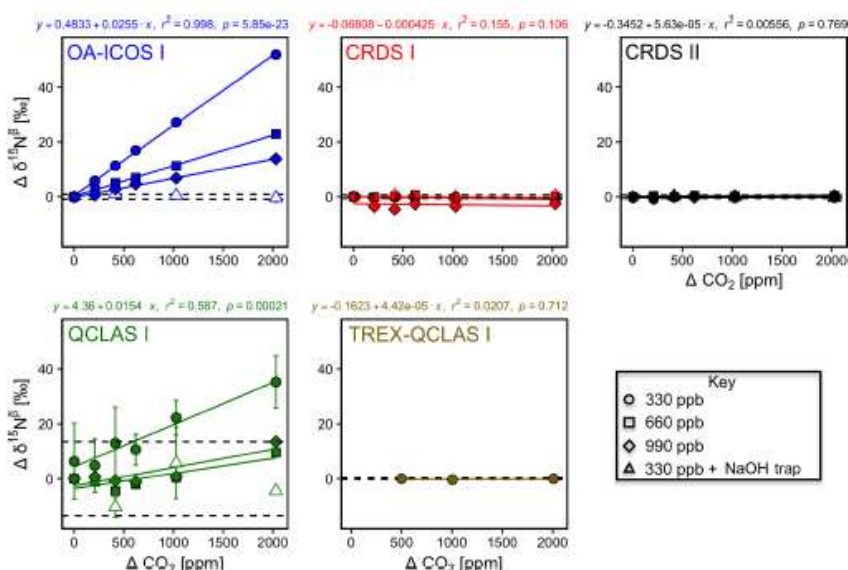


Figure 7. Deviations of the measured [N₂O], δ¹⁵N^α, δ¹⁵N^β and δ¹⁸O values according to ΔCO₂ (ppm) at different N₂O mole fractions (330, 660 and 990 ppb) for the OA-ICOS I (blue), CRDS I (red), CRDS II (black), QCLAS I (green) and TREX-QCLAS I (brown). The remaining plots for [N₂O], δ¹⁵N^α and δ¹⁸O are provided in Sect. S4 (Fig. S4-6). The standard deviation of the Anchor gas (±1σ) is indicated by dashed lines. Data points represent the mean and standard deviation (1σ) of triplicate measurements. Dependencies are best described by linear fits, which are indicated by solid lines. Individual equations, coefficients of determination (r²) and p values are indicated above each plot for the 330 ppb N₂O data only.

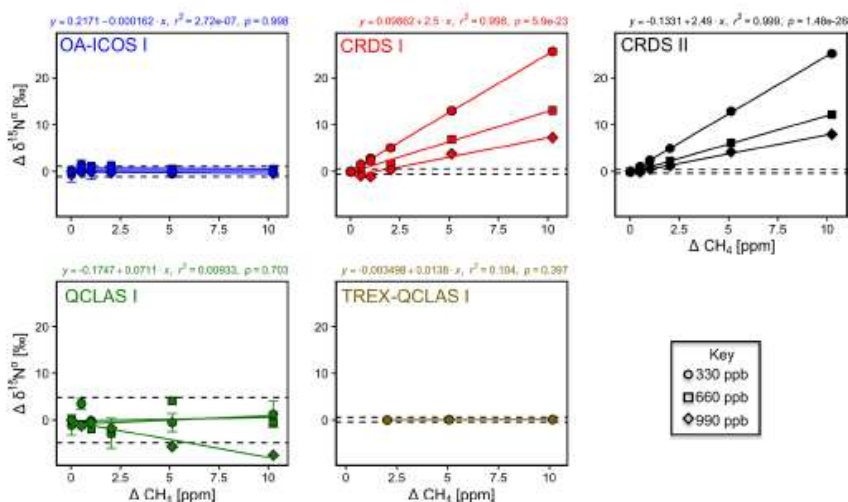


Figure 8. Deviations of the measured [N₂O], δ¹⁵N^α, δ¹⁵N^β and δ¹⁸O values according to ΔCH₄ (ppm) at different N₂O mole fractions (330, 660 and 990 ppb) for the OA-ICOS I (blue), CRDS I (red), CRDS II (black), QCLAS I (green) and TREX-QCLAS I (brown). The remaining plots for [N₂O], δ¹⁵N^α and δ¹⁸O are provided in Sect. S4 (Fig. S4-7). Data points represent the mean and standard deviation (1σ) of triplicate measurements. Dependencies are best described by linear fits, which are indicated by solid lines. Individual equations, coefficients of determination (r²) and p values are indicated above each plot for the 330 ppb N₂O data only.

were all within $\pm 2\%$ of expected values. $\delta^{18}\text{O}$ measurements were the poorest performing but were typically within $\pm 3.6\%$ of expected values. Similarly, there was excellent agreement between OA-ICOS I and IRMS isotope values (all $r^2 > 0.95$), which agreed within 1.7% – 2.4% (Fig. S9-2). The standard deviations of triplicate isotope measurements decreased dramatically with increasing $\Delta\text{N}_2\text{O}$, improving from 1% to 2% during Exps. 1 and 2 to typically better than 0.1% during Exps. 5 and 6. Conversely, the standard deviations of triplicate sample measurements for $[\text{N}_2\text{O}]$ increased with increasing $\Delta\text{N}_2\text{O}$, rising from < 0.1 ppb during Exps. 1–4 to > 1 ppb during Exps. 5 and 6. Nonetheless, all OA-ICOS I $[\text{N}_2\text{O}]$ measurements had better 1σ repeatability than those acquired using GC. The repeatability of the triplicate isotope measurements with OA-ICOS I was typically better than IRMS exclusively at higher $\Delta\text{N}_2\text{O}$ (> 700 ppb).

CRDS I

$[\text{N}_2\text{O}]$ acquired by CRDS I were in good agreement with expected values, although the analyzer slightly underestimated mole fractions at higher $\Delta\text{N}_2\text{O}$ during Exps. 3 and 4. There was excellent agreement between the CRDS I and calculated expected isotope values (all $r^2 > 0.95$; Figs. 10 and S4-11). Measurements for $\delta^{15}\text{N}^\alpha$ and $\delta^{15}\text{N}^\beta$ were mostly better than $\pm 1.1\%$ of expected values, while $\delta^{15}\text{N}^{\text{bulk}}$ was within $\pm 0.5\%$ of expected values. SP and $\delta^{18}\text{O}$ measurements were typically within $\pm 1.5\%$ of expected values. There was excellent agreement between CRDS I and IRMS isotope values (all $r^2 > 0.93$), which agreed to within 0.5% – 1.9% (Fig. S9-3). In general, the standard deviations of triplicate isotope measurements increased as a function of $\Delta\text{N}_2\text{O}$, with the lowest deviations of 0.1% – 1% occurring when $\Delta\text{N}_2\text{O} < 100$ ppb. However, two triplicated measurements for $\delta^{15}\text{N}^{\text{bulk}}$ had standard deviations better than 0.1% . The standard deviations of triplicate measurements for $[\text{N}_2\text{O}]$ also increased with increasing $\Delta\text{N}_2\text{O}$ mole fractions, rising from 0.03 – 0.07 ppb when $\Delta\text{N}_2\text{O} \approx 0$ ppb (i.e., ambient conditions) to ~ 1 ppb when $\Delta\text{N}_2\text{O} \approx 700$ ppb. With the exception of one triplicate measurement, all CRDS I $[\text{N}_2\text{O}]$ measurements had better 1σ repeatability than those acquired using GC. Overall, IRMS had slightly better repeatability (most ranging from 0.1% to 1%) than CRDS I (most ranging from 0.1% to 2%) for isotopic measurements.

CRDS II

Similar to results for CRDS I, $[\text{N}_2\text{O}]$ acquired by CRDS II were in good agreement with expected values but slightly underestimated mole fractions at higher $\Delta\text{N}_2\text{O}$ during Exps. 3 and 4. There was excellent agreement between the CRDS II and calculated expected isotope values (all $r^2 > 0.99$; Figs. 11 and S4-12). Measurements for $\delta^{15}\text{N}^\alpha$ and SP were typically better than $\pm 0.8\%$ of expected values, while

$\delta^{15}\text{N}^\beta$, $\delta^{15}\text{N}^{\text{bulk}}$ measurements were all within $\pm 0.4\%$ of expected values. $\delta^{18}\text{O}$ measurements were within $\pm 1.0\%$ of expected values. There was excellent agreement between CRDS II and IRMS isotope values (all $r^2 > 0.98$), which agreed within $\pm 0.6\%$ – 1.4% (Fig. S9-4). The standard deviations of triplicate isotope measurements typically decreased as a function of $\Delta\text{N}_2\text{O}$, with the lowest deviations of $< 0.1\%$ – 0.3% occurring when $\Delta\text{N}_2\text{O} \approx 700$ ppb. Conversely, the standard deviations of triplicate sample measurements for $[\text{N}_2\text{O}]$ increased with increasing $\Delta\text{N}_2\text{O}$, rising from 0.04 – 0.09 ppb when $\Delta\text{N}_2\text{O} \approx 0$ ppb (i.e., ambient conditions) to ~ 0.4 ppb when $\Delta\text{N}_2\text{O} \approx 700$ ppb. All CRDS II $[\text{N}_2\text{O}]$ measurements had better 1σ repeatability than those acquired using GC. There was no clear distinction between CRDS II and IRMS triplicate repeatability, with both achieving triplicate repeatability ranging from 0.1% to 1% for most isotopic measurements. However, the repeatability of SP CRDS II measurements was mostly better than IRMS, achieving triplicate repeatability between 0.1% and 0.6% , compared to 0.2% – 1% for IRMS.

QCLAS I

There was good agreement of $[\text{N}_2\text{O}]$ between QCLAS I and expected values; however, the analyzer underestimated mole fractions at higher $\Delta\text{N}_2\text{O}$ during Exps. 5 and 6. Unfortunately, it is clear from the large spread of isotope values depicted in Fig. 12 that the standardized calibration scheme selected for the two-end-member mixing tests was insufficient for acquiring accurate and precise isotopic measurements using QCLAS I. For this reason, we urge researchers not to overinterpret such results, as the implementation of a QCLAS-specific calibration procedure (in line with results from Sect. 3.1 and 3.3) would improve results dramatically. Nonetheless, QCLAS I obtained accurate results at higher N_2O mole fractions (indicated in red in Figs. 12 and S4-13), such that when $\Delta\text{N}_2\text{O} < 700$ ppb measurements were excluded, $\delta^{15}\text{N}^\alpha$, $\delta^{15}\text{N}^\beta$, $\delta^{15}\text{N}^{\text{bulk}}$ and SP were within $\pm 3.0\%$, 1.4% , 1.4% and 3.8% of calculated expected values, respectively. Similarly, QCLAS I showed good agreement with IRMS only at higher $\Delta\text{N}_2\text{O}$ (> 700 ppb; Fig. S9-5). Similar to OA-ICOS I, the standard deviations of QCLAS I triplicate isotope measurements decreased dramatically with increasing $\Delta\text{N}_2\text{O}$, improving from $\sim 10\%$ during Exps. 1 and 2 to typically between 0.1% and 1% during Exps. 5 and 6. Conversely, the standard deviations of triplicate sample measurements for $[\text{N}_2\text{O}]$ increased with increasing $\Delta\text{N}_2\text{O}$, rising from < 0.1 ppb during Exps. 1–4, to > 1 ppb during Exps. 5 and 6. All QCLAS I $[\text{N}_2\text{O}]$ measurements had better 1σ repeatability than those acquired using GC. QCLAS I had triplicate isotope measurement standard deviations comparable to IRMS only at higher $\Delta\text{N}_2\text{O}$ (> 700 ppb).

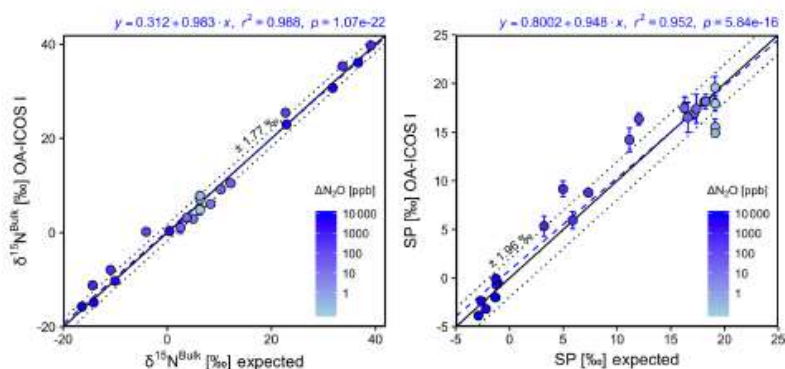


Figure 9. Correlation diagrams for $\delta^{15}\text{N}^{\text{bulk}}$ and SP measurements at various $\Delta\text{N}_2\text{O}$ mole fractions analyzed by OA-ICOS I plotted against expected values. The remaining plots for $[\text{N}_2\text{O}]$, $\delta^{15}\text{N}^\alpha$, $\delta^{15}\text{N}^\beta$ and $\delta^{18}\text{O}$ are provided in Sect. S4 (Fig. S4-10). The solid black line denotes the 1 : 1 line, while the dotted line indicates $\pm 1\sigma$ of the residuals from the 1 : 1 line. The dashed blue line represents a linear fit to the data. Individual equations, coefficients of determination (r^2) and p values are indicated above each plot. Each data point represents the mean and standard deviation (1σ) of triplicate measurements. The inset plots indicate the standard deviation (1σ) of the triplicate measurements achieved at different $\Delta\text{N}_2\text{O}$ mole fractions, and the 1 : 1 line is similarly a solid line.

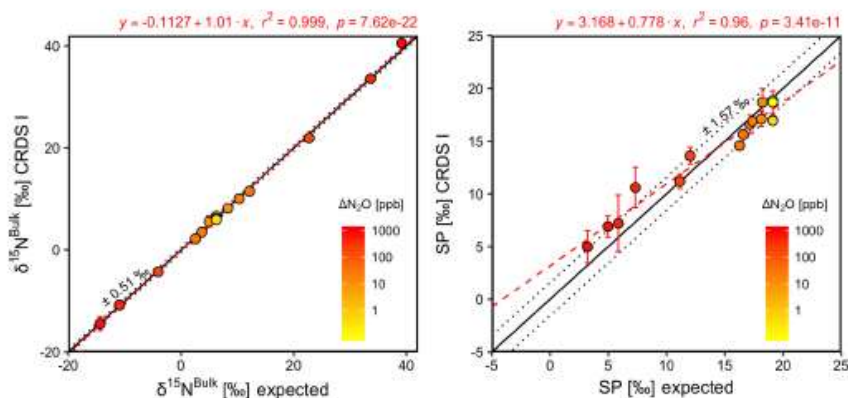


Figure 10. Correlation diagrams for $\delta^{15}\text{N}^{\text{bulk}}$ and SP measurements at various $\Delta\text{N}_2\text{O}$ mole fractions analyzed by CRDS I plotted against expected values. The remaining plots for $[\text{N}_2\text{O}]$, $\delta^{15}\text{N}^\alpha$, $\delta^{15}\text{N}^\beta$ and $\delta^{18}\text{O}$ are provided in Sect. S4 (Fig. S4-11). The solid black line denotes the 1 : 1 line, while the dotted line indicates $\pm 1\sigma$ of the residuals from the 1 : 1 line. The dashed red line represents a linear fit to the data. Individual equations, coefficients of determination (r^2) and p values are indicated above each plot. Each data point represents the mean and standard deviation (1σ) of triplicate measurements. The inset plots indicate the standard deviation (1σ) of the triplicate measurements achieved at different $\Delta\text{N}_2\text{O}$ mole fractions, and the 1 : 1 line is similarly a solid line.

TREX-QCLAS I

There was good agreement of N_2O mixing ratios between the TREX-QCLAS I and expected values. Similarly, there was excellent agreement between the TREX-QCLAS I and calculated expected isotope values (all $r^2 > 0.97$; Figs. 13 and S4-14). Measurements for $\delta^{15}\text{N}^\alpha$, $\delta^{15}\text{N}^\beta$, $\delta^{15}\text{N}^{\text{bulk}}$ and SP were within $\pm 0.29\text{‰}$, 0.32‰ , 0.23‰ and 0.41‰ of expected values, respectively. $\delta^{18}\text{O}$ measurements were typically within $\pm 0.24\text{‰}$ of expected values. Generally, the standard deviations of triplicate isotope measurements de-

creased with increasing $\Delta\text{N}_2\text{O}$, improving from typically 0.2‰ – 0.3‰ at low $\Delta\text{N}_2\text{O}$ mole fractions (ambient) to close to or better than 0.1‰ when $\Delta\text{N}_2\text{O}$ reached 30 ppb. Conversely, the standard deviations of triplicate sample measurements for $[\text{N}_2\text{O}]$ increased with increasing $\Delta\text{N}_2\text{O}$, rising from < 0.3 to ~ 1 ppb. No comparison could be made between TREX-QCLAS I and IRMS measurements because TREX-QCLAS measurements were undertaken separately from the other instruments.

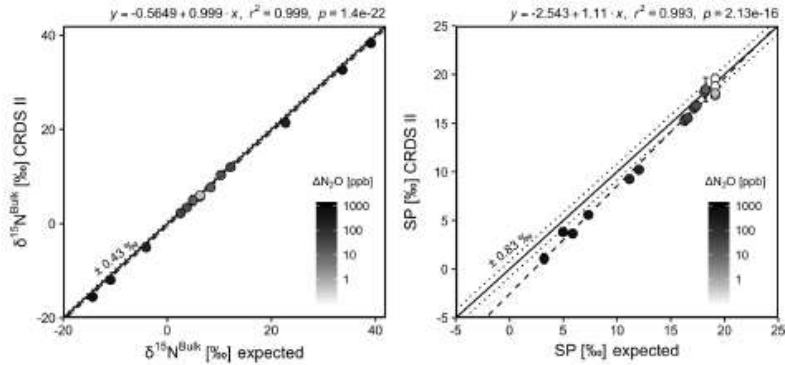


Figure 11. Correlation diagrams for $\delta^{15}\text{N}^{\text{bulk}}$ and SP measurements at various $\Delta\text{N}_2\text{O}$ mole fractions analyzed by CRDS II plotted against expected values. The remaining plots for $[\text{N}_2\text{O}]$, $\delta^{15}\text{N}^{\alpha}$, $\delta^{15}\text{N}^{\beta}$ and $\delta^{18}\text{O}$ are provided in Sect. S4 (Fig. S4-12). The solid black line denotes the 1 : 1 line, while the dotted line indicates $\pm 1\sigma$ of the residuals from the 1 : 1 line. The dashed black line represents a linear fit to the data. Individual equations, coefficients of determination (r^2) and p values are indicated above each plot. Each data point represents the mean and standard deviation (1σ) of triplicate measurements. The inset plots indicate the standard deviation (1σ) of the triplicate measurements achieved at different $\Delta\text{N}_2\text{O}$ mole fractions, and the 1 : 1 line is similarly a solid line.

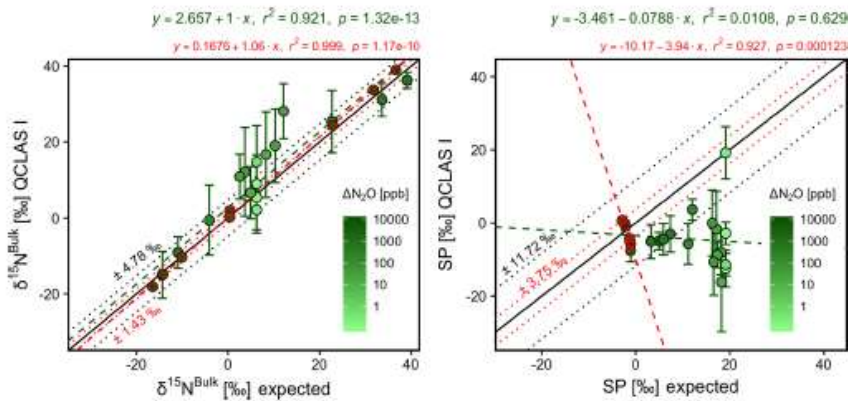


Figure 12. Correlation diagrams for $\delta^{15}\text{N}^{\text{bulk}}$ and SP measurements at various $\Delta\text{N}_2\text{O}$ mole fractions analyzed by QCLAS I plotted against expected values. The remaining plots for $[\text{N}_2\text{O}]$, $\delta^{15}\text{N}^{\alpha}$, $\delta^{15}\text{N}^{\beta}$ and $\delta^{18}\text{O}$ are provided in Sect. S4 (Fig. S4-13). The solid black line denotes the 1 : 1 line, while the dotted line indicates $\pm 1\sigma$ of the residuals from the 1 : 1 line. The dashed green line represents a linear fit to the data. Individual equations, coefficients of determination (r^2) and p values are indicated above each plot. Each data point represents the mean and standard deviation (1σ) of triplicate measurements. The inset plots indicate the standard deviation (1σ) of the triplicate measurements achieved at different $\Delta\text{N}_2\text{O}$ mole fractions, and the 1 : 1 line is similarly a solid line. Results for Exps. 5–6 are highlighted in red, with the dashed red line indicating a linear fit to this data.

3.7.2 Source identification using Keeling analysis

Despite the excellent agreement between expected and measured values across all experiments for OA-ICOS I, CRDS I and II, and TREX-QCLAS I, the extrapolated source intercept values acquired using Keeling analysis showed large standard errors, especially for Exps. 1 and 2 ($\Delta\text{N}_2\text{O} = 30$ ppb) (Figs. 14 and S4-15; Sect. S10). This was mostly due to the small mole fraction range (i.e., large inverse mole fraction range) over which the regression line was extrapo-

lated in order to acquire the intercept value. The cause of the erroneous intercept values was likely two-fold: (1) the extrapolated source was highly susceptible to measurements acquired at background levels, and due to the inherent greater uncertainty associated with measurements acquired at ambient N_2O mole fractions, intercepts can be skewed accordingly; and (2) any further non-linearity that could not be taken into account in the three-point concentration dependence correction applied. Overall, this implies that N_2O isotope source studies using laser spectroscopy focusing on

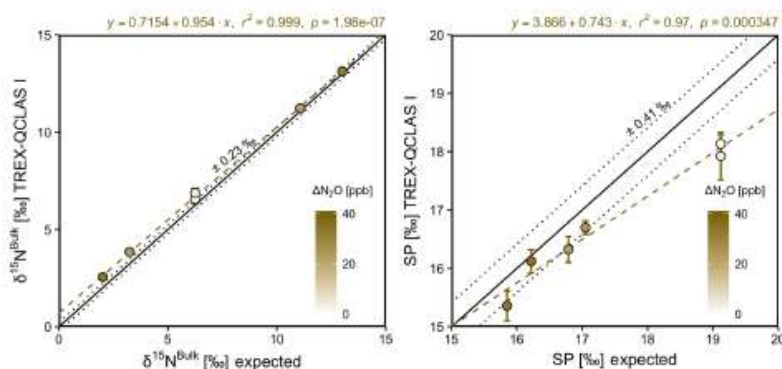


Figure 13. Correlation diagrams for $\delta^{15}\text{N}^{\text{bulk}}$ and SP measurements at various $\Delta\text{N}_2\text{O}$ mole fractions analyzed by OA-ICOS I plotted against expected values. The remaining plots for $[\text{N}_2\text{O}]$, $\delta^{15}\text{N}^\alpha$, $\delta^{15}\text{N}^\beta$ and $\delta^{18}\text{O}$ are provided in Sect. S4 (Fig. S4-14). The solid black line denotes the 1 : 1 line, while the dotted line indicates $\pm 1\sigma$ of the residuals from the 1 : 1 line. The dashed green line represents a linear fit to the data. Individual equations, coefficients of determination (r^2) and p values are indicated above each plot. Each data point represents the mean and standard deviation (1σ) of triplicate measurements. The inset plots indicate the standard deviation (1σ) of the triplicate measurements achieved at different $\Delta\text{N}_2\text{O}$ mole fractions, and the 1 : 1 line is similarly a solid line.

near-ambient N_2O variations remain a challenging undertaking, and one should expect large uncertainty in source estimates over small mole fraction changes.

For Exps. 3–6, however, the accuracy of the source intercept and its standard error improved dramatically for all analyzers on account of the decreasing uncertainty in measurement. OA-ICOS I and both CRDS analyzers typically achieved within $\pm 2\%$ – 5% of the assigned values for $\delta^{15}\text{N}^\alpha$, $\delta^{15}\text{N}^\beta$, $\delta^{15}\text{N}^{\text{bulk}}$, SP and $\delta^{18}\text{O}$, and had performance comparable to or better than the GC-IRMS approach (Figs. 14 and S4-15). Similarly, the standard error of all intercepts decreased dramatically for Exps. 3–6, and all analyzers typically achieved better than $\pm 1\%$ standard error on derived intercepts in Exps. 5 and 6.

4 Discussion

4.1 Factors affecting the precision and accuracy of N_2O isotopocule measurements using laser spectroscopy

A summary of results is presented in Table 8. Our results highlight that the precision at which laser-based analyzers acquire N_2O isotopocule measurements is a function of N_2O mole fraction, the selected measuring and averaging times and calibration frequency according to measurement stability. The degree of accuracy obtained using different laser spectrometers is ultimately a function of the robustness of corrections aimed at removing matrix and trace gas effects, and the selected calibration procedure aimed at standardizing the data to international scales.

All spectrometers tested displayed temperature effects on isotope measurements, which can be attributed to differences in the lower state energies of the probed N_2O isotopocule

lines (Sect. S11) (e.g., Wächter et al., 2008). The temperature sensitivities of all analyzers tested necessitates that, especially when deployed in the field, they be operated under temperature-controlled conditions (such as in maintained field stations).

The experiments performed in this study were undertaken using a standardized protocol. Calibration was performed on isotope δ values derived from raw uncalibrated isotopocule amount fractions, thus requiring $[\text{N}_2\text{O}]$ dependence corrections. Alternative approaches aimed at calibrating isotopocule amount fractions prior to deriving δ values were not included in our study but have the potential to remove the need for this correction (e.g., Wen et al., 2013; Flores et al., 2017; Griffith, 2018) if appropriate reference materials become available. Isotopocule calibration approaches would require a set of N_2O standard gases with high-accuracy mole fractions in addition to assigned δ values.

All analyzers tested in this study showed significant effects from changing O_2 composition of the gas matrix. Although the magnitude of this effect ultimately varied across the analyzers and was dependent on N_2O mixing ratios, the effect of a change in O_2 composition of 20.5% was typically on the order of 10% to 30% for δ values. Similar O_2 dependencies have been reported by Erler et al. (2015) for CRDS N_2O isotope laser spectrometers, as well as for CRDS H_2O isotope analyzers (Johnson and Rella, 2017). The underlying reason for this effect is differences in N_2 versus O_2 (and Ar) broadening parameters of the probed N_2O isotopocule lines. In short, the N_2 , O_2 (and Ar) broadening parameters depend on rotational quantum numbers of the respective N_2O lines (Henry et al., 1985; Sect. S11). Thus, differences in the rotational quantum numbers for a pair of isotopocules (e.g., $^{14}\text{N}^{15}\text{N}^{16}\text{O}/^{14}\text{N}^{14}\text{N}^{16}\text{O}$) relate to a difference in their N_2 , O_2

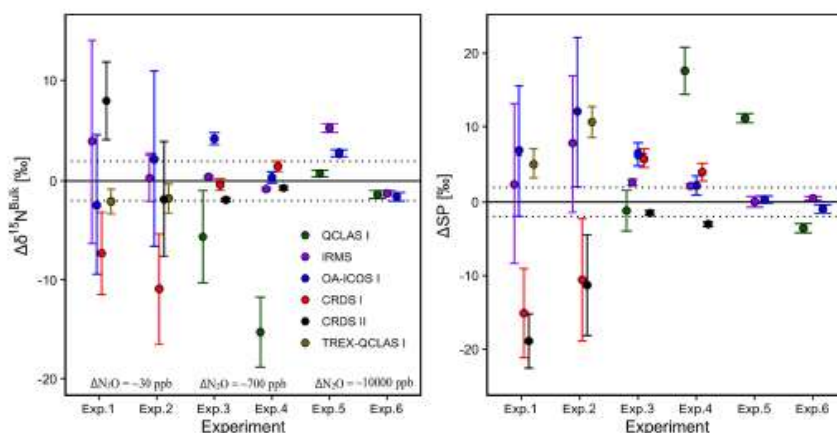


Figure 14. $\Delta\delta^{15}\text{N}^{\text{bulk}}$ and $\Delta\text{SP}(\text{Estimated}_{\text{Source}} - \text{True}_{\text{Source}})$ values derived from the OA-ICOS I (blue), CRDS I (red), CRDS II (black), QCLAS I (green) and IRMS (purple) via Keeling analysis of the two-end-member mixing scenario. The remaining plots for $\delta^{15}\text{N}^{\alpha}$, $\delta^{15}\text{N}^{\beta}$ and $\delta^{18}\text{O}$ are provided in Sect. S4 (Fig. S4-15). $\text{Estimated}_{\text{Source}} = \text{True}_{\text{Source}}$ is indicated by a solid black line at $y = 0$, and the dotted lines indicated $\pm 2\text{‰}$ deviation from $y = 0$. The change in concentration exceeding that of the background gas is indicated for Exps. 1–2 ($\Delta\text{N}_2\text{O} \sim 30$ ppb), 3–4 ($\Delta\text{N}_2\text{O} \sim 700$ ppb) and 5–6 ($\Delta\text{N}_2\text{O} \sim 10000$ ppb). Note that the QCLAS I results for Exps. 1 and 2 are not depicted to maintain clarity, as they exceed the selected y-axis scale.

Table 8. Summary of main findings presented in this study.

Detection scheme (model; manufacturer)	OA-ICOS I (N2OIA-30e-EP)	CRDS I & II (G5131-i)	QCLAS I (CW-QC-TILDAS-SC-D)	TREX-QCLAS I (CW-QC-TILDAS-76-CS)
Allan precision (300 s)				
$\delta^{15}\text{N}^{\alpha}$, $\delta^{15}\text{N}^{\beta}$, $\delta^{18}\text{O}$ [‰]				
326.5 ppb N_2O	0.79–1.69	0.32–0.46	0.39–3.45 ^a	n.d.
~ 1000 ppb N_2O	0.28–0.67	0.21–0.89	0.19–0.83 ^a	n.d.
~ 10000 ppb N_2O	0.12–0.17	n.d.	0.02–0.48 ^a	n.d.
Repeatability (326.5 ppb N_2O)				
N_2O [ppb]	0.07	0.26–0.30	0.16	1.29
$\delta^{15}\text{N}^{\alpha}$, $\delta^{15}\text{N}^{\beta}$, $\delta^{18}\text{O}$ [‰]	1.19–2.17	0.52–0.83	5.35–8.57	0.37–0.60
Temperature effect (326.5 ppb N_2O)				
N_2O [ppb K^{-1}]	0.01	0.02	0.10	n.d.
$\delta^{15}\text{N}^{\alpha}$, $\delta^{15}\text{N}^{\beta}$, $\delta^{18}\text{O}$ [‰ K^{-1}]	0.36–2.60	0.25–0.65	31.29–37.32	n.d.
N_2O mole fraction dependence				
$\delta^{15}\text{N}^{\alpha}$, $\delta^{15}\text{N}^{\beta}$, $\delta^{18}\text{O}$ [‰ppb ($\Delta 1/\text{N}_2\text{O}$)]	–8296 to 2544	–458 to 1353	–66 386 to 15 833	n.d.
O_2 matrix effect (330 ppb N_2O)				
N_2O [ppb ‰^{-1} (ΔO_2)]	–0.044	0.24–0.305	0.351	n.s.
$\delta^{15}\text{N}^{\alpha}$, $\delta^{15}\text{N}^{\beta}$, $\delta^{18}\text{O}$ [‰ ‰^{-1} (ΔO_2)]	0.874–1.270	–0.279 to (–1.364)	–1.111	n.s.
CO_2 trace gas effects (330 ppb N_2O)				
N_2O [ppb ppm^{-1} (ΔCO_2)]	0.0011	0.0005	n.s.	n.s.
$\delta^{15}\text{N}^{\alpha}$, $\delta^{15}\text{N}^{\beta}$, $\delta^{18}\text{O}$ [‰ ppm^{-1} (ΔCO_2)]	–0.009 to 0.026	n.s. to (–0.0019)	n.s. to 0.0154	n.s.
CH_4 trace gas effects (330 ppb N_2O)				
N_2O [ppb ppm^{-1} (ΔCH_4)]	n.s. ^b	–0.039 to (–0.056)	n.s. ^b	n.s. ^b
$\delta^{15}\text{N}^{\alpha}$, $\delta^{15}\text{N}^{\beta}$, $\delta^{18}\text{O}$ [‰ ppm^{-1} (ΔCH_4)]	0.173	0.085–2.50	n.s.	n.s.
CO trace gas effects (330 ppb N_2O)				
N_2O [ppb ppm^{-1} (ΔCO)]	–0.29	–0.15 to (–0.24)	–0.19	n.s.
$\delta^{15}\text{N}^{\alpha}$, $\delta^{15}\text{N}^{\beta}$, $\delta^{18}\text{O}$ [‰ ppm^{-1} (ΔCO)]	n.s.	–0.53 to (–2.41)	n.s. to (–4.04)	n.s.

^a Includes QCLAS I, II and III. ^b Likely due to inaccuracies during dynamic dilution (see text for details). n.d.: not determined, n.s.: not statistically significant at $p < 0.05$ and/or $r^2 < 0.5$.

and Ar broadening parameters. Consequently, differences in the O₂ or Ar content of the sample gas matrix and that of the reference gas affect measured isotope ratios and lead to changes in apparent δ values. Nonetheless, the magnitude of effects reported for the CRDS analyzers in this study varied across CRDS I (a 2015 model) and CRDS II (a 2018 model), as well as from those reported by Erler et al. (2015). Therefore, we recommended that in applications where O₂ concentrations vary, such as groundwater, estuaries, stratified waterbodies and incubation studies, researchers test individual analyzers for their specific dependencies to allow for correction. This is especially important given that N₂O production and reduction processes in such environments are strongly controlled by O₂ availability. Although the Ar effects characterized in this study were not large, it is nonetheless recommended as a precautionary measure that researchers ensure, where possible, the standard calibration gas Ar composition is similar to that of the sample gas.

The CO₂ effects for OA-ICOS and CH₄ effects for CRDS analyzers must be considered for applications of these analyzers where CO₂ and CH₄ may also co-vary, such as during diel atmospheric monitoring, in soil-flux chamber measurements, incubation studies and even waterbodies (e.g., Erler et al., 2015). These effects need to be either characterized and corrected for by the user, or the interfering gas quantitatively removed. To our knowledge, there is currently no commercially available technique to remove CH₄ from a gas stream without affecting N₂O, and therefore independent co-analysis of CH₄ is ultimately required to correct for these effects post-measurement. Similarly, while water vapor effects can in theory be characterized and corrected for all instruments, we recommend that researchers remove water vapor from the gas stream prior to analysis. Although not tested here, other studies have highlighted possible spectral interference effects associated with elevated H₂S and volatile organic compounds (Erler et al., 2015; Ostrom and Ostrom, 2017), but these may also be removed from gas streams using chemical traps (e.g., Cu and activated carbon traps, respectively).

The scaling of gas matrix and trace gas effects with [N₂O] has important implications for any measurement setup that relies on post-measurement correction equations. An equation developed to correct for CH₄ effects that was derived using a [N₂O] of 330 ppb should not be implemented for a sample gas containing 990 ppb N₂O. For example, as shown in Fig. 8, the measured interference effect on $\delta^{15}\text{N}^{\alpha}$ measurements acquired using CRDS II for 10 ppm [CH₄] at 330 ppb N₂O was 24.9‰, while at 990 ppb N₂O it was 8.1‰, resulting in a 16.8‰ difference. The scaling of interference effects from trace gases has been reported previously for CO₂/CH₄ laser spectrometers (Assan et al., 2017; Malowany et al., 2015). This underlines the usefulness of removing H₂O, CO₂ and CO with scrubbers prior to measurement, as this removes the need for correction equations to begin with and the scaling of corrections that can ensue. We are unaware

of any studies that have shown that O₂ interferences caused by pressure-broadening linewidth effects change as a function of N₂O mole fraction. While we were unable to describe the scaling of the O₂ effect sufficiently using correction functions based on theoretical deductions, empirical equations based on experimental testing, such as those developed in Sect. 3.5.2 and 3.6.2, could be implemented by researchers when covariation in both O₂ and N₂O in the sample gas is expected. Alternatively, as shown in this study, matrix and/or trace gas effects can be removed by automated N₂O preconcentration devices such as TREX (Ibraim et al., 2018; Mohn et al., 2010), similar to IRMS. However, such devices are not commercially available, complex to build and operate, and restrict sample frequency.

4.2 Pre-measurement considerations

Our study clearly shows that knowledge/estimation of the matrix and trace gas composition of both reference standards and sample gases, and the differences between them, are critical for accurate N₂O isotopocule analysis using laser spectroscopy. We acknowledge, however, that this may be difficult to predict in certain applications without prior testing of the sample gas, and therefore researchers should err on the side of caution.

As a prerequisite to acquiring measurements using N₂O isotope laser spectrometers, researchers will be required to consider the accessory gas mixtures required to characterize their instrument. For applications with significant variations in matrix (O₂, Ar) or trace gas (CO₂, CH₄, CO) compositions, researchers will require gas mixtures containing the gas of interest in order to characterize the associated interference effects for their laser spectrometer. This also necessitates that appropriate interference detectors are implemented, especially O₂ and CH₄ analyzers given that these effects cannot be mitigated using chemical traps.

In this study, interference effects, and the associated scaling of these effects according to the co-measured N₂O mole fraction, were derived via dynamic dilution with various gas mixtures using MFCs. This allowed for the introduction of a wide range of gas mixtures to the analyzers for interference testing, and consequently only a small amount of gas mixtures were required for all of the experiments outlined in Sect. 2.4. In comparison, a much larger number of individual gas mixtures would have been required had they been prepared using static dilution techniques (see Erler et al., 2015). The scaling of interference effects was sufficiently distinguished by undertaking testing at three different N₂O mole fractions (N₂O = 330, 660 and 990 ppb), and we therefore recommend this as a minimum criterion for researchers wishing to characterize this effect.

Researchers should also consider the sample gas volume required for a given measurement application using a specific laser spectrometer. In our experience, ensuring that five laser cavity cell volumes have been flushed prior to measurement

is best practice to negate any memory effects when these instruments are operated using continuous flow-through configurations (as opposed to discrete sample measurements in a closed laser cavity). By following this procedure and using the operating parameters selected in this study (Table 1), the sample gas volume required for a single 300 s measurement is approximately 80 mL for CRDS II, 150 mL for CRDS I, 600 mL for OA-ICOS I and 1200 mL for QCLAS I. By comparison, TREX-QCLAS I requires approximately 5 L of sample gas to allow for N₂O preconcentration. These sample gas volumes represent typical numbers for atmospheric applications; however, instrument parameter settings such as flow rate and cell pressure, which ultimately change the required sample volume, can be optimized depending on the measurement application. This is particularly the case for QCLAS instruments, which can be operated with different user-adjustable settings. For applications requiring discrete sample analysis (e.g., the headspace analysis of $\delta^{15}\text{N}$ and $\delta^{18}\text{O}$ in N₂O derived from dissolved NO₃⁻), high N₂O concentration gas samples with lower volumes can be introduced to these instruments using injection ports and dilution gases (e.g., Soto et al., 2015; Wassenaar et al., 2018); however, we did not test these capabilities in our study.

4.3 Measurement workflow

In line with our results, we propose a step-by-step workflow that can be followed by researchers to acquire N₂O isotopocule measurements (Fig. 15). This workflow seeks to cover all sources of potential error tested in our study. Not all steps will be applicable because interference effects vary across analyzers. For QCLAS analyzers, which offer high versatility, interference effects can also be approached by multi-line analysis, inclusion of interfering spectral lines or adaption of pressure-broadening parameters in the spectral fitting algorithm. For specific applications, such as incubation experiments with He, accessory injection units and setups using TREX, related actions have to be taken. While we tested several mono-variant (e.g., changes in [CH₄] at constant [N₂O]) and some bi-variant (e.g., changes in [CH₄] and [N₂O]) systems in our study, more complex systems (e.g., changes in [CH₄], [O₂] and [N₂O]) were not tested, and deviations from additive behavior are to be expected. Depending on the desired precision, users may vary the measurement and averaging times, and calibration frequency.

4.4 What degree of accuracy can be achieved using this workflow?

The simulated two-end-member mixing experiments conducted in this study show that, when the workflow proposed above is applied, accuracy within $\pm 0.5\%$ can be achieved for TREX-QCLAS, $\pm 0.4\%$ – 1.6% for CRDS analyzers and $\pm 1.6\%$ – 3.6% for OA-ICOS analyzers. Likewise, the comparison between the laser spectrometers and IRMS highlights

that cross-technique compatibility within $\pm 1\%$ – 2.5% can be achieved for most N₂O isotopocule measurements. However, it is clear that the balanced (i.e., non-analyzer-specific) approach applied for the purpose of this comparative study did not cater to QCLAS I. Therefore, a more specific calibration protocol for the QCLAS I will likely yield better performance, as shown in Table 6. It is worth noting that, although the results of our study are representative of the performance of the instruments tested, the magnitude of reported effects and the performance are likely to vary within the same analyzer models.

Whilst the laboratory-simulated mixing experiment is not fully representative of naturally occurring two-end-member mixing per se, the results are useful in comparing intercept accuracy and uncertainty amongst analyzers and against IRMS. Our results show that large uncertainties exist for N₂O source apportionment using Keeling analysis performed at near-ambient N₂O mole fractions. Given the amount of corrections that are required in the experiment, we have not detailed individual analyzer uncertainty budgets to quantify individual sources of error on the intercept, as it is beyond the scope of this study. Nonetheless, the reduction of uncertainty with increasing $\Delta\text{N}_2\text{O}$ shown in Exps. 1–6 in Sect. 3.7 has also been shown in previous studies (e.g., Wolf et al., 2015). Therefore, by extension, it is reasonable to assume that the current largest source of uncertainty for ambient N₂O measurements using laser spectroscopy is the inherent signal-to-noise ratio of the measurement.

5 Conclusions

In this study, we characterized and compared N₂O isotope laser-based analyzers with the three most common detection schemes, including OA-ICOS, CRDS and QCLAS. Our results show a number of factors that need to be carefully considered to ensure precise and accurate measurements of N₂O isotopocules using laser spectroscopy. The performance of N₂O isotope laser spectrometers depends on a complex interplay between instrumental precision, drift, matrix gas composition and associated spectral interferences that ultimately vary as a function of N₂O mole fraction. On this basis, we echo recommendations from Ostrom and Ostrom (2017), who cautioned not to underestimate the need for the careful consideration of analyzer-specific corrections. These analyzers clearly do not represent “plug and play” devices – instead, one needs to carefully consider the desired application, precision and accuracy, and develop appropriate calibration strategies to achieve these outcomes.

Consequently, we recommend calibration schemes that have (1) a calibration frequency that is adequate for constraining instrument drift over experimental period/long-term measurements; (2) temperature stability during measurement, or the temperature effect adequately characterized and corrected; (3) a three-point or higher [N₂O] effect correc-

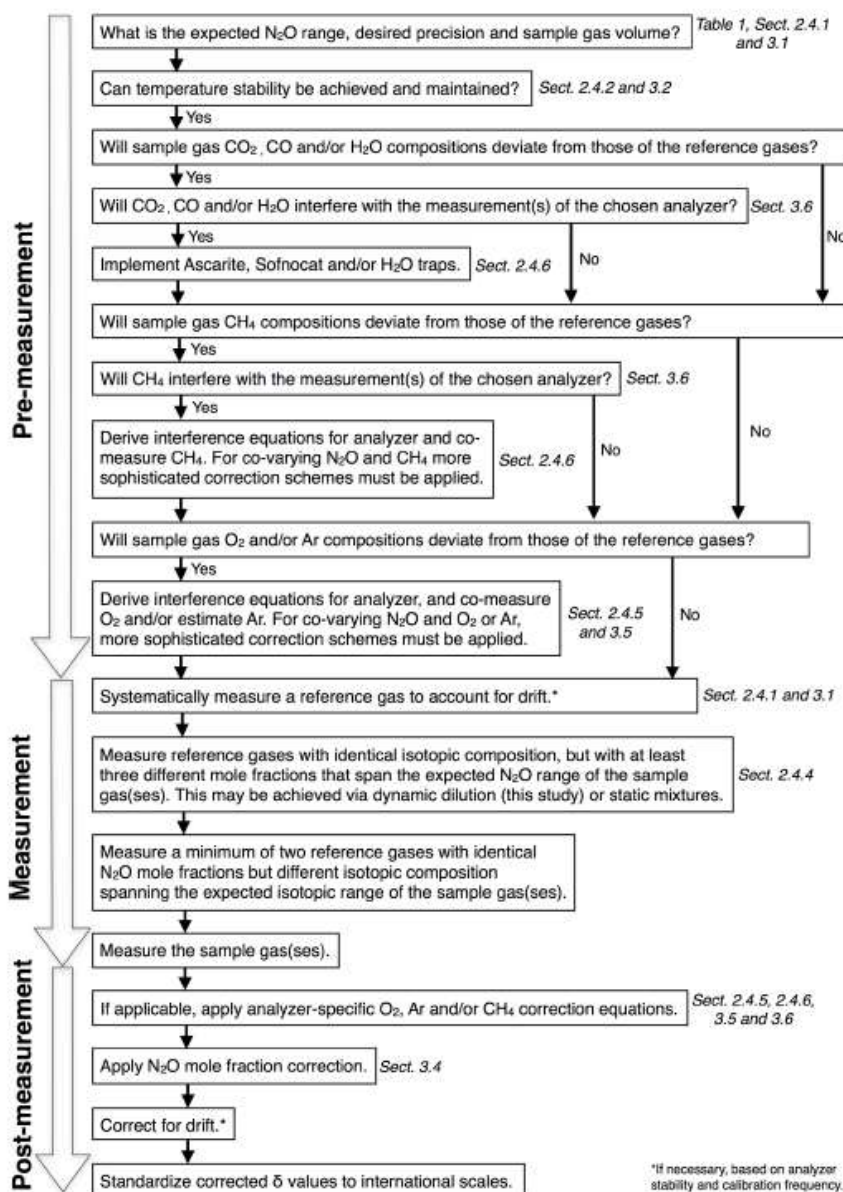


Figure 15. Proposed measurement workflow for the operation of N_2O isotope laser spectrometers. Relevant sections of this study are shown next to each step.

tion that spans the range of expected $[\text{N}_2\text{O}]$ (if calibration relies on raw δ values derived from uncalibrated isotopocule amount fractions; i.e., a δ -calibration approach); and (4) accounted for the differences in matrix and trace gas composition between the sample gas and reference gases, whereby either analyzer-specific interference corrections have been

carefully characterized and applied, or where possible interfering substances (CO_2 , CO , H_2O) removed using chemical traps. Correcting for interference effects becomes significantly more complicated once $[\text{N}_2\text{O}]$ exceeds ambient levels, requiring a multitude of analyzer- and gas-specific constants that inevitably increase the number of gas mixtures required

by the user, as well as the uncertainty of the measurement. Researchers should therefore strive to implement measurement setups that require as few corrections as possible, and this will inherently decrease the combined uncertainty in the measurement.

Data availability. All data are available from the corresponding author upon request.

Supplement. The supplement related to this article is available online at: <https://doi.org/10.5194/amt-13-1-2020-supplement>.

Author contributions. SJH and JL, guided by JM, designed the study, established the setup and coordinated the experiments. Responsibilities of the analyzers were as follows: SJH, BFJK and DIC were responsible for OA-ICOS; JL and TB were responsible for CRDS I; LX and BW were responsible for QCLAS I and CRDS II; JW and KZ were responsible for TREX-QCLAS I; MB and JS were responsible for QCLAS II, QCLAS III and GC-IRMS. JM prepared the non-commercial gas mixtures used in this study. LY referenced the δ values of applied gas mixtures to international scales. SJH and JL performed the main data analysis and together with JM developed correction algorithms. SJH and JL wrote the manuscript with input from all co-authors.

Competing interests. The authors declare that they have no conflict of interest.

Acknowledgements. We extend our thanks to Doug Baer, Rob Provencal and Frederick Despagne from ABB – Los Gatos Research Inc., Renato Winkler, Magdalena Hofmann and Paulos Getachew from Picarro Inc., and Dave Nelson and Barry McManus from Aerodyne Research Inc. for their helpful discussions and assistance concerning the analyzers. We thank Christoph Zellweger for his assistance in analyzing matrix gas cylinders and providing the Picarro G2401 for matrix interference testing, and the NABEL laboratory at Empa for providing the dew-point generator for water vapor testing. We want to thank Kristýna Kantnerová from Empa and Daniel Zindel from ETH for the synthesis of ^{18}O -labeled N_2O . This study was supported by the European Metrology Programme for Innovation and Research (EMPIR) 16ENV06 project “Metrology for Stable Isotope Reference Standards (SIRS)”. The EMPIR initiative is co-funded by the European Union’s Horizon 2020 research and innovation program and the EMPIR participating states. Furthermore, this research was supported by grants from the Cotton Research and Development Corporation (CRDC) and was facilitated by an Endeavour Research Fellowship acquired by Stephen Harris from the Australian Government. Stephen Harris is supported by PhD scholarships from the Australian Government, the Australian Institute of Nuclear Science and Engineering (AINSE), Australian Nuclear Science and Technology Organisation (ANSTO) and CRDC. The UNSW Sydney $\text{N}_2\text{-OIA-30e-EP}$ was purchased using funds from the Australian National Collaborative

Research Infrastructure Strategy (NCRIS) Groundwater Infrastructure Project. Jing Wei and Longfei Yu were supported by the Swiss National Science Foundation (SNSF) within grants CRSII5_170876 and 200021_163075, as well as the EMPAPOSTDOCS-II program, which received funding from the European Union’s Horizon 2020 research and innovation program under the Marie Skłodowska-Curie grant agreement no. 754364.

Financial support. This research has been supported by the Australian Endeavour Leadership Program (grant no. ERF_RDDH_6743_2018), the European Union’s Horizon 2020 research and innovation program and the EMPIR Participating States (European Metrology Programme for Innovation and Research (EMPIR); grant no. 16ENV06), the Cotton Research and Development Corporation (grant no. ANSTO1801) and the H2020 Marie Skłodowska-Curie Actions (EMPAPOSTDOCS-II; grant no. 754364).

Review statement. This paper was edited by Huilin Chen and reviewed by three anonymous referees.

References

- ABB-Los Gatos Research Inc.: Off-Axis Integrated Cavity Output Spectroscopy (OA-ICOS), available at: <http://www.lgrinc.com/advantages/> (last access: 2019), 2019.
- Allan, D. W.: Statistics of atomic frequency standards, P. IEEE, 54, 221–230, 1966.
- Anderson, B., Bartlett, K., Frolking, S., Hayhoe, K., Jenkins, J., and Salas, W.: Methane and Nitrous Oxide Emissions from Natural Sources, Office of Atmospheric Programs, US EPA, EPA 430-R-10-001, Washington DC, 2010.
- Assan, S., Baudic, A., Guemri, A., Ciais, P., Gros, V., and Vogel, F. R.: Characterization of interferences to in situ observations of $\delta^{13}\text{C}$ and C_2H_6 when using a cavity ring-down spectrometer at industrial sites, Atmos. Meas. Tech., 10, 2077–2091, <https://doi.org/10.5194/amt-10-2077-2017>, 2017.
- Baer, D. S., Paul, J. B., Gupta, M., and O’Keefe, A.: Sensitive absorption measurements in the near-infrared region using off-axis integrated-cavity-output spectroscopy, Appl. Phys. B-Lasers O., 75, 261–265, <https://doi.org/10.1007/s00340-002-0971-z>, 2002.
- Baggs, E. M.: A review of stable isotope techniques for N_2O source partitioning in soils: recent progress, remaining challenges and future considerations, Rapid Commun. Mass Sp., 22, 1664–1672, <https://doi.org/10.1002/rcm.3456>, 2008.
- Berden, G., Peeters, R., and Meijer, G.: Cavity ring-down spectroscopy: Experimental schemes and applications, Int. Rev. Phys. Chem., 19, 565–607, <https://doi.org/10.1080/014423500750040627>, 2000.
- Bernard, S., Röckmann, T., Kaiser, J., Barnola, J.-M., Fischer, H., Blunier, T., and Chappellaz, J.: Constraints on N_2O budget changes since pre-industrial time from new firn air and ice core isotope measurements, Atmos. Chem. Phys., 6, 493–503, <https://doi.org/10.5194/acp-6-493-2006>, 2006.
- Bouwman, A. F., Boumans, L. J. M., and Batjes, N. H.: Modeling global annual N_2O and NO emissions from

- fertilized fields, *Global Biogeochem. Cy.*, 16, 1080, <https://doi.org/10.1029/2001GB001812>, 2002.
- Bowling, D. R., Sargent, S. D., Tanner, B. D., and Ehleringer, J. R.: Tunable diode laser absorption spectroscopy for stable isotope studies of ecosystem-atmosphere CO₂ exchange, *Agr. Forest Meteorol.*, 118, 1–19, [https://doi.org/10.1016/s0168-1923\(03\)00074-1](https://doi.org/10.1016/s0168-1923(03)00074-1), 2003.
- Bowling, D. R., Burns, S. P., Conway, T. J., Monson, R. K., and White, J. W. C.: Extensive observations of CO₂ carbon isotope content in and above a high-elevation subalpine forest, *Global Biogeochem. Cy.*, 19, GB3023, <https://doi.org/10.1029/2004gb002394>, 2005.
- Brase, L., Bange, H. W., Lentdt, R., Sanders, T., and Dähnke, K.: High Resolution Measurements of Nitrous Oxide (N₂O) in the Elbe Estuary, *Front. Mar. Sci.*, 4, 162, <https://doi.org/10.3389/fmars.2017.00162>, 2017.
- Buchen, C., Lewicka-Szczebak, D., Flessa, H., and Well, R.: Estimating N₂O processes during grassland renewal and grassland conversion to maize cropping using N₂O isotopocules, *Rapid Commun. Mass Sp.*, 32, 1053–1067, <https://doi.org/10.1002/rcm.8132>, 2018.
- Decock, C. and Six, J.: How reliable is the intramolecular distribution of ¹⁵N in N₂O to source partition N₂O emitted from soil?, *Soil Biol. Biochem.*, 65, 114–127, <https://doi.org/10.1016/j.soilbio.2013.05.012>, 2013.
- Denk, T. R., Mohn, J., Decock, C., Lewicka-Szczebak, D., Harris, E., Butterbach-Bahl, K., Kiese, R., and Wolf, B.: The nitrogen cycle: A review of isotope effects and isotope modeling approaches, *Soil Biol Biochem.*, 105, 121–137, <https://doi.org/10.1016/j.soilbio.2016.11.015>, 2017.
- Denman, K. L., Brasseur, G., Chidthaisong, A., Ciais, P., Cox, P. M., Dickinson, R. E., Hauglustaine, D., Heinze, C., Holland, E., Jacob, D., Lohmann, U., Ramachandran, S., da Silva Dias, P. L., Wofsky, S. C., and Zhang, X.: Couplings between changes in the climate system and biogeochemistry, in: *Climate change 2007, the physical science basis, contribution of working group I to the Fourth Assessment Report of the Intergovernmental Panel on Climate Change*, edited by: Solomon, S., Qin, D., Manning, M., Chen, Z., Marquis, M., Averyt, K. B., Tignor, M., and Miller, H. L., Cambridge University Press, Cambridge, United Kingdom and New York, NY, USA, 499–587, 2007.
- Erler, D. V., Duncan, T. M., Murray, R., Maher, D. T., Santos, I. R., Gatland, J. R., Mangion, P., and Eyre, B. D.: Applying cavity ring-down spectroscopy for the measurement of dissolved nitrous oxide mole fractions and bulk nitrogen isotopic composition in aquatic systems: Correcting for interferences and field application, *Limnol. Oceanogr.-Meth.*, 13, 391–401, <https://doi.org/10.1002/lom3.10032>, 2015.
- Eyer, S., Tuzson, B., Popa, M. E., van der Veen, C., Röckmann, T., Rothe, M., Brand, W. A., Fisher, R., Lowry, D., Nisbet, E. G., Brennwald, M. S., Harris, E., Zellweger, C., Emmenegger, L., Fischer, H., and Mohn, J.: Real-time analysis of δ¹³C- and δD-CH₄ in ambient air with laser spectroscopy: method development and first intercomparison results, *Atmos. Meas. Tech.*, 9, 263–280, <https://doi.org/10.5194/amt-9-263-2016>, 2016.
- Flores, E., Viallon, J., Moussay, P., Griffith, D. W., and Wielgosz, R. I.: Calibration strategies for FT-IR and other isotope ratio infrared spectrometer instruments for accurate δ¹³C and δ¹⁸O measurements of CO₂ in air, *Anal. Chem.*, 89, 3648–3655, <https://doi.org/10.1021/acs.analchem.6b05063>, 2017.
- Forster, P., Ramaswamy, V., Artaxo, P., Bernsten, T., Betts, R., Fahey, D. W., Haywood, J., Lean, J., Lowe, D. C., Myhre, G., Nganga, J., Prinn, R., Raga, G., Schulz, M., and Van Dorland, R.: *Climate Change 2007: Changes in Atmospheric Constituents and in Radiative Forcing*, The Physical Science Basis: Contribution of Working Group I to the Fourth Assessment Report of the Intergovernmental Panel on Climate Change, edited by: Solomon, S., Qin, D., Manning, M., Chen, Z., Marquis, M., Averyt, K. B., Tignor, M., and Miller, H. S., Cambridge University Press, Cambridge, UK, New York, NY, USA, 2007.
- Friedrichs, G., Bock, J., Temps, F., Fietzek, P., Körtzinger, A., and Wallace, D. W.: Toward continuous monitoring of seawater ¹³CO₂/¹²CO₂ isotope ratio and pCO₂: Performance of cavity ringdown spectroscopy and gas matrix effects, *Limnol. Oceanogr.-Meth.*, 8, 539–551, <https://doi.org/10.4319/lom.2010.8.539>, 2010.
- Griffis, T. J., Baker, J. M., Sargent, S. D., Tanner, B. D., and Zhang, J.: Measuring field-scale isotopic CO₂ fluxes with tunable diode laser absorption spectroscopy and micrometeorological techniques, *Agr. Forest Meteorol.*, 124, 15–29, <https://doi.org/10.1016/j.agrformet.2004.01.009>, 2004.
- Griffith, D. W. T.: Calibration of isotopologue-specific optical trace gas analysers: a practical guide, *Atmos. Meas. Tech.*, 11, 6189–6201, <https://doi.org/10.5194/amt-11-6189-2018>, 2018.
- Griffith, D. W. T., Deutscher, N. M., Caldow, C., Kettlewell, G., Riggensbach, M., and Hammer, S.: A Fourier transform infrared trace gas and isotope analyser for atmospheric applications, *Atmos. Meas. Tech.*, 5, 2481–2498, <https://doi.org/10.5194/amt-5-2481-2012>, 2012.
- Gröning, M.: TEL Technical Note No. 01. SICalib User Manual (Stable Isotope Calibration for routine δ-scale measurements) Ver 2.16j, 2018.
- Harris, E., Nelson, D. D., Olszewski, W., Zahniser, M., Potter, K. E., McManus, B. J., Whitehill, A., Prinn, R. G., and Ono, S.: Development of a spectroscopic technique for continuous online monitoring of oxygen and site-specific nitrogen isotopic composition of atmospheric nitrous oxide, *Anal. Chem.*, 86, 1726–1734, <https://doi.org/10.1021/ac403606u>, 2014.
- Harris, E., Joss, A., Emmenegger, L., Kipf, M., Wolf, B., Mohn, J. and Wunderlin, P.: Isotopic evidence for nitrous oxide production pathways in a partial nitrification-anammox reactor, *Water Res.*, 83, 258–270, <https://doi.org/10.1016/j.watres.2015.06.040>, 2015a.
- Harris, E., Zeyer, K., Kegel, R., Müller, B., Emmenegger, L., and Mohn, J.: Nitrous oxide and methane emissions and nitrous oxide isotopic composition from waste incineration in Switzerland, *Waste Manage.*, 35, 135–140, <https://doi.org/10.1016/j.wasman.2014.10.016>, 2015b.
- Harris, E., Henne, S., Hüglin, C., Zellweger, C., Tuzson, B., Ibraim, E., Emmenegger, L., and Mohn, J.: Tracking nitrous oxide emission processes at a suburban site with semicontinuous, in situ measurements of isotopic composition, *J. Geophys. Res.-Atmos.*, 122, 1850–1870, <https://doi.org/10.1002/2016JD025906>, 2017.
- Heil, J., Wolf, B., Brüggemann, N., Emmenegger, L., Tuzson, B., Vereecken, H., and Mohn, J.: Site-specific ¹⁵N isotopic signatures of abiotically produced N₂O, *Geochim. Cosmochim. Ac.*, 139, 72–82, <https://doi.org/10.1016/j.gca.2014.04.037>, 2014.

- Henry, A., Margottin-Maclou, M., and Lacombe, N.: N₂- and O₂-broadening parameters in the ν_3 band of $^{14}\text{N}_2^{16}\text{O}$, *J. Mol. Spectrosc.*, 111, 291–300, [https://doi.org/10.1016/0022-2852\(85\)90006-2](https://doi.org/10.1016/0022-2852(85)90006-2), 1985.
- Ibraim, E., Harris, E., Eyer S., Tuzson, B., Emmenegger, L., Six, J., and Mohn, J.: Development of a field-deployable method for simultaneous, real-time measurements of the four most abundant N₂O isotopocules, *Isot. Environ. Health S.*, 54, 1–5, <https://doi.org/10.1080/10256016.2017.1345902>, 2018.
- Ibraim, E., Wolf, B., Harris, E., Gasche, R., Wei, J., Yu, L., Kiese, R., Eggleston, S., Butterbach-Bahl, K., Zeeman, M., Tuzson, B., Emmenegger, L., Six, J., Henne, S., and Mohn, J.: Attribution of N₂O sources in a grassland soil with laser spectroscopy based isotopocule analysis, *Biogeosciences*, 16, 3247–3266, <https://doi.org/10.5194/bg-16-3247-2019>, 2019.
- Ishijima, K., Sugawara, S., Kawamura, K., Hashida, G., Morimoto, S., Murayama, S., Aoki, S., and Nakazawa, T.: Temporal variations of the atmospheric nitrous oxide mole fraction and its $\delta^{15}\text{N}$ and $\delta^{18}\text{O}$ for the latter half of the 20th century reconstructed from firm air analyses, *J. Geophys. Res.*, 112, D03305, <https://doi.org/10.1029/2006JD007208>, 2007.
- Ji, Q. and Grundle, D. S.: An automated, laser-based measurement system for nitrous oxide isotope and isotopomer ratios at nanomolar levels, *Rapid Commun. Mass Sp.*, 33, 1553–1564, <https://doi.org/10.1002/rcm.8502>, 2019.
- Johnson, J. E. and Rella, C. W.: Effects of variation in background mixing ratios of N₂, O₂, and Ar on the measurement of $\delta^{18}\text{O}$ -H₂O and $\delta^2\text{H}$ -H₂O values by cavity ring-down spectroscopy, *Atmos. Meas. Tech.*, 10, 3073–3091, <https://doi.org/10.5194/amt-10-3073-2017>, 2017.
- Keeling, C. D.: The mole fraction and isotopic abundances of atmospheric carbon dioxide in rural areas, *Geochim. Cosmochim. Ac.*, 13, 322–334, [https://doi.org/10.1016/0016-7037\(58\)90033-4](https://doi.org/10.1016/0016-7037(58)90033-4), 1958.
- Koba, K., Osaka, K., Tobarı, Y., Toyoda, S., Ohte, N., Katsuyama, M., Suzuki, N., Itoh, M., Yamagishi, H., Kawasaki, M., and Kim, S. J.: Biogeochemistry of nitrous oxide in groundwater in a forested ecosystem elucidated by nitrous oxide isotopomer measurements, *Geochim. Cosmochim. Ac.*, 73, 3115–3133, <https://doi.org/10.1016/j.gca.2009.03.022>, 2009.
- Kong, X., Duan, Y., Schramm, A., Eriksen, J., Holmstrup, M., Larsen, T., Bol, R., and Petersen, S.O.: Mitigating N₂O emissions from clover residues by 3,4-dimethylpyrazole phosphate (DMPP) without adverse effects on the earthworm *Lumbricus terrestris*, *Soil Biol. Biochem.*, 104, 95–107, <https://doi.org/10.1016/j.soilbio.2016.10.012>, 2017.
- Köster, J. R., Cárdenas, L., Senbayram, M., Bol, R., Well, R., Butler, M., Mühlıng, K. H., and Dittert, K.: Rapid shift from denitrification to nitrification in soil after biogas residue application as indicated by nitrous oxide isotopomers, *Soil Biol. Biochem.*, 43, 1671–1677, <https://doi.org/10.1016/j.soilbio.2011.04.004>, 2011.
- Köster, J. R., Well, R., Tuzson, B., Bol, R., Dittert, K., Giesemann, A., Emmenegger, L., Manninen, A., Cárdenas, L., and Mohn, J.: Novel laser spectroscopic technique for continuous analysis of N₂O isotopomers – application and intercomparison with isotope ratio mass spectrometry, *Rapid Commun. Mass Sp.*, 27, 216–222, <https://doi.org/10.1002/rcm.6434>, 2013.
- Lebeque, B., Schmidt, M., Ramonet, M., Wastine, B., Yver Kwok, C., Laurent, O., Belviso, S., Guemri, A., Philippon, C., Smith, J., and Conil, S.: Comparison of nitrous oxide (N₂O) analyzers for high-precision measurements of atmospheric mole fractions, *Atmos. Meas. Tech.*, 9, 1221–1238, <https://doi.org/10.5194/amt-9-1221-2016>, 2016.
- Lee, A., Winther, M., Priemé, A., Blunier, T., and Christensen, S.: Hot spots of N₂O emission move with the seasonally mobile oxic-anoxic interface in drained organic soils, *Soil Biol. Biochem.*, 115, 178–186, <https://doi.org/10.1016/j.soilbio.2017.08.025>, 2017.
- Lewicka-Szczczak, D., Well, R., Köster, J. R., Fuß, R., Senbayram, M., Dittert, K., and Flessa, H.: Experimental determinations of isotopic fractionation factors associated with N₂O production and reduction during denitrification in soils, *Geochim. Cosmochim. Ac.*, 134, 55–73, <https://doi.org/10.1016/j.gca.2014.03.010>, 2014.
- Lewicka-Szczczak, D., Well, R., Bol, R., Gregory, A. S., Matthews, G. P., Misselbrook, T., Whalley, W. R., and Cardenas, L. M.: Isotope fractionation factors controlling isotopocule signatures of soil-emitted N₂O produced by denitrification processes of various rates, *Rapid Commun. Mass Sp.*, 29, 269–282, <https://doi.org/10.1002/rcm.7102>, 2015.
- Li, P., Wang, S., Peng, Y., Liu, Y., and He, J.: The synergistic effects of dissolved oxygen and pH on N₂O production in biological domestic wastewater treatment under nitrifying conditions, *Environ. Technol.*, 36, 1623–1631, <https://doi.org/10.1080/09593330.2014.1002862>, 2015.
- Li, X., Sørensen, P., Olesen, J. E., and Petersen, S. O.: Evidence for denitrification as main source of N₂O emission from residue-amended soil, *Soil Biol. Biochem.*, 92, 153–160, <https://doi.org/10.1016/j.soilbio.2015.10.008>, 2016.
- Malowany, K., Stix, J., Van Pelt, A., and Lucic, G.: H₂S interference on CO₂ isotopic measurements using a Picarro G1101-i cavity ring-down spectrometer, *Atmos. Meas. Tech.*, 8, 4075–4082, <https://doi.org/10.5194/amt-8-4075-2015>, 2015.
- Miller, J. B. and Tans, P. P.: Calculating isotopic fractionation from atmospheric measurements at various scales, *Tellus B*, 55, 207–214, <https://doi.org/10.1034/j.1600-0889.2003.00020.x>, 2003.
- Minamikawa, K., Nishimura, S., Nakajima, Y., Osaka, K.I., Sawamoto, T., and Yagi, K.: Upward diffusion of nitrous oxide produced by denitrification near shallow groundwater table in the summer: a lysimeter experiment, *Soil Sci. Plant Nutr.*, 57, 719–732, <https://doi.org/10.1080/00380768.2011.625556>, 2011.
- Mohn, J., Guggenheim, C., Tuzson, B., Vollmer, M. K., Toyoda, S., Yoshida, N., and Emmenegger, L.: A liquid nitrogen-free preconcentration unit for measurements of ambient N₂O isotopomers by QCLAS, *Atmos. Meas. Tech.*, 3, 609–618, <https://doi.org/10.5194/amt-3-609-2010>, 2010.
- Mohn, J., Tuzson, B., Manninen, A., Yoshida, N., Toyoda, S., Brand, W. A., and Emmenegger, L.: Site selective real-time measurements of atmospheric N₂O isotopomers by laser spectroscopy, *Atmos. Meas. Tech.*, 5, 1601–1609, <https://doi.org/10.5194/amt-5-1601-2012>, 2012.
- Mohn, J., Wolf, B., Toyoda, S., Lin, C. T., Liang, C. M., Brüggemann, N., Wissel, H., Steiker, A. E., Dyckmans, J., Szwed, L., Ostrom, N. E., Casciotti, K. L., Forbes, M., Giesemann, A., Well, R., Doucett, R. R., Yarnes, C. T., Ridley, A. R., Kaiser, J., and Yoshida, N.: Inter-Laboratory assessment of nitrous oxide isotopomer analysis of isotopomer analysis by isotope ratio mass spectrometry and laser spectroscopy: current status

- and perspectives, *Rapid Commun. Mass Sp.*, 28, 1995–2007, <https://doi.org/10.1002/rcm.6982>, 2014.
- Mosier, A., Kroeze, C., Nevison, C., Oenema, O., Seitzinger, S., and Van Cleemput, O.: Closing the global N₂O budget: nitrous oxide emissions through the agricultural nitrogen cycle, *Nutr. Cycl. Agroecosys.*, 52, 225–248, <https://doi.org/10.1023/A:1009740530221>, 1998.
- Murray, R., Erler, D., Rosentreter, J., Maher, D., and Eyre, B.: A seasonal source and sink of nitrous oxide in man-groves: Insights from mole fraction, isotope, and isotopomer measurements, *Geochim. Cosmochim. Ac.*, 238, 169–192, <https://doi.org/10.1016/j.gca.2018.07.003>, 2018.
- Nara, H., Tanimoto, H., Tohjima, Y., Mukai, H., Nojiri, Y., Katsumata, K., and Rella, C. W.: Effect of air composition (N₂, O₂, Ar, and H₂O) on CO₂ and CH₄ measurement by wavelength-scanned cavity ring-down spectroscopy: calibration and measurement strategy, *Atmos. Meas. Tech.*, 5, 2689–2701, <https://doi.org/10.5194/amt-5-2689-2012>, 2012.
- Nikolenko, O., Orban, P., Jurado, A., Morana, C., Jamin, P., Robert, T., Knöller, K., Borges, A. V., and Brouyère, S.: Dynamics of greenhouse gases in groundwater: hydrogeological and hydrogeochemical controls, *Appl. Geochem.*, 105, 31–44, <https://doi.org/10.1016/j.apgeochem.2019.04.009>, 2019.
- NOAA/ESRL: Combined Nitrous Oxide data, NOAA/ESRL Global Monitoring Division, 2019. <https://www.noaa.gov/esrl/gmd/>
- Ogawa, M. and Yoshida, N.: Intramolecular distribution of stable nitrogen and oxygen isotopes of nitrous oxide emitted during coal combustion, *Chemosphere*, 61, 877–887, <https://doi.org/10.1016/j.chemosphere.2005.04.096>, 2005.
- Ostrom, N. E. and Ostrom, P. H.: The Isotopomers of Nitrous Oxide: Analytical Considerations and Application to Resolution of Microbial Production Pathways, in: *Handbook of Environmental Isotope Geochemistry*, edited by: Baskaran, M., Springer Berlin Heidelberg, Berlin, Heidelberg, 1, 453–476, 2011.
- Ostrom, N. E. and Ostrom, P. H.: Mining the isotopic complexity of nitrous oxide: a review of challenges and opportunities, *Biogeochemistry*, 132, 359–372, <https://doi.org/10.1007/s10533-017-0301-5>, 2017.
- Ostrom, N. E., Pitt, A., Sutka, R., Ostrom, P. H., Grandy, A. S., Huizinga, K. M., and Robertson, G. P.: Isotopologue effects during N₂O reduction in soils and in pure cultures of denitrifiers, *J. Geophys. Res.*, 112, G02005, <https://doi.org/10.1029/2006JG000287>, 2007.
- Ostrom, N. E., Gandhi, H., Coplen, T. B., Toyoda, S., Böhlke, J. K., Brand, W. A., Casciotti, K. L., Dyckmans, J., Giesemann, A., Mohn, J., and Well, R.: Preliminary assessment of stable nitrogen and oxygen isotopic composition of USGS51 and USGS52 nitrous oxide reference gases and perspectives on calibration needs, *Rapid Commun. Mass Sp.*, 32, 1207–1214, <https://doi.org/10.1002/rcm.8157>, 2018.
- Pang, J., Wen, X., Sun, X., and Huang, K.: Intercomparison of two cavity ring-down spectroscopy analyzers for atmospheric ¹³CO₂/¹²CO₂ measurement, *Atmos. Meas. Tech.*, 9, 3879–3891, <https://doi.org/10.5194/amt-9-3879-2016>, 2016.
- Park, S., Croteau, P., Boering, K. A., Etheridge, D. M., Ferretti, D., Fraser, P. J., Kim, K. R., Krummel, P. B., Langenfelds, R. L., Van Ommen, T. D., and Steele, L. P.: Trends and seasonal cycles in the isotopic composition of nitrous oxide since 1940, *Nat. Geosci.*, 5, 261–265, <https://doi.org/10.1038/NGEO1421>, 2012.
- Pataki, D. E., Bowling, D. R., Ehleringer, J. R., and Zobitz, J. M.: High resolution atmospheric monitoring of urban carbon dioxide sources, *Geophys. Res. Lett.*, 33, L03813, <https://doi.org/10.1029/2005gl024822>, 2006.
- Peng, L., Ni, B. J., Erler, D., Ye, L., and Yuan, Z.: The effect of dissolved oxygen on N₂O production by ammonia-oxidizing bacteria in an enriched nitrifying sludge, *Water Res.*, 66, 12–21, <https://doi.org/10.1016/j.watres.2014.08.009>, 2014.
- Pérez, T., Trumbore, S. E., Tyler, S. C., Matson, P. A., Ortiz-Monasterio, I., Rahn, T., and Griffith, D. W. T.: Identifying the agricultural imprint on the global N₂O budget using stable isotopes, *J. Geophys. Res.*, 106, 9869–9878, <https://doi.org/10.1029/2000JD900809>, 2001.
- Pérez, T., García-Montiel, D., Trumbore, S., Tyler, S., Cargano, P. D., Moreira, M., Piccolo, M., and Cerri, C.: Nitrous oxide nitrification and denitrification ¹⁵N enrichment factors from Amazon forest soils, *Ecol. Appl.*, 16, 2153–2167, [https://doi.org/10.1890/1051-0761\(2006\)016\[2153:NONADN\]2.0.CO;2](https://doi.org/10.1890/1051-0761(2006)016[2153:NONADN]2.0.CO;2), 2006.
- Picarro Inc.: Cavity Ring-Down Spectroscopy (CRDS), available at <https://www.picarro.com/company/technology/crds> (last access: 15 Feb 2019), 2019.
- Potter, K. E., Ono, S., and Prinn, R. G.: Fully automated, high-precision instrumentation for the isotopic analysis of tropospheric N₂O using continuous flow isotope ratio mass spectrometry, *Rapid Commun. Mass Sp.*, 27, 1723–1738, <https://doi.org/10.1002/rcm.6623>, 2013.
- Prokopiou, M., Martinerie, P., Sapart, C. J., Witrant, E., Montéil, G., Ishijima, K., Bernard, S., Kaiser, J., Levin, I., Blunier, T., Etheridge, D., Dlugokencky, E., van de Wal, R. S. W., and Röckmann, T.: Constraining N₂O emissions since 1940 using firm air isotope measurements in both hemispheres, *Atmos. Chem. Phys.*, 17, 4539–4564, <https://doi.org/10.5194/acp-17-4539-2017>, 2017.
- R Core Team.: R: A language and environment for statistical computing, R Foundation for Statistical Computing, Vienna, Austria, available at: <https://www.R-project.org/> (last access: 15 Feb 2019), 2017.
- Ravishankara, A. R., Daniel, J. S., and Portmann, R. W.: Nitrous oxide (N₂O): the dominant ozone-depleting substance emitted in the 21st century, *Science*, 326, 123–125, 2009.
- Rella, C. W., Chen, H., Andrews, A. E., Filges, A., Gerbig, C., Hatakka, J., Karion, A., Miles, N. L., Richardson, S. J., Steinbacher, M., Sweeney, C., Wastine, B., and Zellweger, C.: High accuracy measurements of dry mole fractions of carbon dioxide and methane in humid air, *Atmos. Meas. Tech.*, 6, 837–860, <https://doi.org/10.5194/amt-6-837-2013>, 2013.
- Röckmann, T. and Levin, I.: High-precision determination of the changing isotopic composition of atmospheric N₂O from 1990 to 2002, *J. Geophys. Res.*, 110, D21304, <https://doi.org/10.1029/2005JD006066>, 2015.
- Rothman, L. S., Jacquemart, D., Barbe, A., Benner, D. C., Birk, M., Brown, L. R., Carleer, M. R., Chackerian Jr., C., Chance, K., Coudert, L. E. A., and Dana, V.: The HITRAN 2004 molecular spectroscopic database, *J. Quant. Spectrosc. Ra.*, 96, 139–204, <https://doi.org/10.1016/j.jqsrt.2004.10.008>, 2005.
- Soto, D. X., Koehler, G., and Hobson, K. A.: Combining denitrifying bacteria and laser spectroscopy for isotopic analyses

- ($\delta^{15}\text{N}$, $\delta^{18}\text{O}$) of dissolved nitrate, *Anal. Chem.*, 87, 7000–7005, <https://doi.org/10.1021/acs.analchem.5b01119>, 2015.
- Sutka, R. L., Ostrom, N. E., Ostrom, P. H., Gandhi, H., and Breznak, J. A.: Nitrogen isotopomer site preference of N_2O produced by *Nitrosomonas europaea* and *Methylococcus capsulatus* bath, *Rapid Commun. Mass Sp.*, 17, 738–745, <https://doi.org/10.1002/rcm.968>, 2003.
- Sutka, R. L., Ostrom, N. E., Ostrom, P. H., Breznak, J. A., Gandhi, H., Pitt, A. J., and Li, F.: Distinguishing nitrous oxide production from nitrification and denitrification on the basis of isotopomer abundances, *Appl. Environ. Microb.*, 72, 638–644, <https://doi.org/10.1128/AEM.72.1.638-644.2006>, 2006.
- Tian, H., Chen, G., Lu, C., Xu, X., Ren, W., Zhang, B., Banger, K., Tao, B., Pan, S., Liu, M., Zhang, C., Bruhwiler, L., and Wofsy, S.: Global methane and nitrous oxide emissions from terrestrial ecosystems due to multiple environmental changes, *Ecosyst. Health Sustain.*, 1, 1–20, <https://doi.org/10.1890/ehs14-0015.1>, 2015.
- Toyoda, S. and Yoshida, N.: Determination of nitrogen isotopomers of nitrous oxide on a modified isotope ratio mass spectrometer, *Anal. Chem.*, 71, 4711–4718, <https://doi.org/10.1021/ac9904563>, 1999.
- Toyoda, S., Mutobe, H., Yamagishi, H., Yoshida, N., and Tanji, Y.: Fractionation of N_2O isotopomers during production by denitrifier, *Soil Biol. Biochem.*, 37, 1535–1545, <https://doi.org/10.1016/j.soilbio.2005.01.009>, 2005.
- Toyoda, S., Yano, M., Nishimura, S., Akiyama, H., Hayakawa, A., Koba, K., Sudo, S., Yagi, K., Makabe, A., Tobari, Y., Ogawa, N. O., Ohkouchi, N., Yamada, K., and Yoshida, N.: Characterization and production and consumption processes of N_2O emitted from temperate agricultural soils determined via isotopomer ratio analysis, *Globl Biogeochem. Cy.*, 25, GB2008, <https://doi.org/10.1029/2009GB003769>, 2011.
- Toyoda, S., Kuroki, N., Yoshida, N., Ishijima, K., Tohjima, Y., and Machida, T.: Decadal time series of tropospheric abundance of N_2O isotopomers and isotopologues in the Northern Hemisphere obtained by the long-term observation at Hateruma Island, Japan, *J. Geophys. Res.-Atmos.*, 118, 3369–3381, <https://doi.org/10.1002/jgrd.50221>, 2013.
- Toyoda, S., Yoshida, N., and Koba, K.: Isotopocule analysis of biologically produced nitrous oxide in various environments, *Mass Spectrom. Rev.*, 36, 135–160, <https://doi.org/10.1002/mas.21459>, 2017.
- Tuzson, B., Mohn, J., Zeeman, M. J., Werner, R. A., Eugster, W., Zahniser, M. S., Nelson, D. D., McManus, J. B., and Emmenegger, L.: High precision and continuous field measurements of $\delta^{13}\text{C}$ and $\delta^{18}\text{O}$ in carbon dioxide with a cryogen-free QCLAS, *Appl. Phys. B*, 92, 451, <https://doi.org/10.1007/s00340-008-3085-4>, 2008.
- Verhoeven, E., Decock, C., Barthel, M., Bertora, C., Sacco, D., Romani, M., Stutel, S., and Six, J.: Nitrification and coupled nitrification-denitrification at shallow depths are responsible for early season N_2O emissions under alternate wetting and drying management in an Italian rice paddy system, *Soil Biol. Biochem.*, 120, 58–69, <https://doi.org/10.1016/j.soilbio.2018.01.032>, 2018.
- Verhoeven, E., Barthel, M., Yu, L., Celi, L., Said-Pullicino, D., Stutel, S., Lewicka-Szczepak, D., Six, J., and Decock, C.: Early season N_2O emissions under variable water management in rice systems: source-partitioning emissions using isotope ratios along a depth profile, *Biogeosciences*, 16, 383–408, <https://doi.org/10.5194/bg-16-383-2019>, 2019.
- Vogel, F. R., Huang, L., Ernst, D., Giroux, L., Racki, S., and Worthy, D. E. J.: Evaluation of a cavity ring-down spectrometer for in situ observations of $^{13}\text{CO}_2$, *Atmos. Meas. Tech.*, 6, 301–308, <https://doi.org/10.5194/amt-6-301-2013>, 2013.
- Wächter, H., Mohn, J., Tuzson, B., Emmenegger, L., and Sigrist, M. W.: Determination of N_2O isotopomers with quantum cascade laser based absorption spectroscopy, *Opt. Express*, 16, 9239–9244, <https://doi.org/10.1364/OE.16.009239>, 2008.
- Wassenaar, L. I., Douance, C., Altabet, M. A., and Aggarwal, P. K.: N and O isotope ($\delta^{15}\text{N}^\alpha$, $\delta^{15}\text{N}^\beta$, $\delta^{18}\text{O}$, $\delta^{17}\text{O}$) analyses of dissolved NO_3^- and NO_2^- by the Cd-azide reduction method and N_2O laser spectrometry, *Rapid Commun. Mass Sp.*, 32, 184–194, <https://doi.org/10.1002/rcm.8029>, 2018.
- Wei, J., Zhou, M., Vereecken, H., and Brüggemann, N.: Large variability in CO_2 and N_2O emissions and in ^{15}N site preference of N_2O from reactions of nitrite with lignin and its derivatives at different pH, *Rapid Commun. Mass Sp.*, 31, 1333–1343, <https://doi.org/10.1002/rcm.7912>, 2017.
- Well, R. and Flessa, H.: Isotopologue signatures of N_2O produced by denitrification in soils, *J. Geophys. Res.*, 114, G02020, <https://doi.org/10.1029/2008JG000804>, 2009.
- Well, R., Flessa, H., Jaradat, F., Toyoda, S., and Yoshida, N.: Measurement of isotopomer signatures of N_2O in groundwater, *J. Geophys. Res.*, 110, G02006, <https://doi.org/10.1029/2005JG000044>, 2005.
- Well, R., Flessa, H., Xing, L., Xiaotang, J., and Römhild, V.: Isotopologue ratios of N_2O emitted from microcosms with NH_4^+ fertilized arable soils under conditions favoring nitrification, *Soil Biol. Biochem.*, 40, 2416–2426, <https://doi.org/10.1016/j.soilbio.2008.06.003>, 2008.
- Well, R., Eschenbach, W., Flessa, H., von der Heide, C., and Weymann, D.: Are dual isotope and isotopomer ratios of N_2O useful indicators for N_2O turnover during denitrification in nitrate-contaminated aquifers?, *Geochim. Cosmochim. Ac.*, 90, 265–282, <https://doi.org/10.1016/j.gca.2012.04.045>, 2012.
- Wen, X.-F., Meng, Y., Zhang, X.-Y., Sun, X.-M., and Lee, X.: Evaluating calibration strategies for isotope ratio infrared spectroscopy for atmospheric $^{13}\text{CO}_2/^{12}\text{CO}_2$ measurement, *Atmos. Meas. Tech.*, 6, 1491–1501, <https://doi.org/10.5194/amt-6-1491-2013>, 2013.
- Werle, P. O., Mücke, R., and Slemr, F.: The limits of signal averaging in atmospheric trace-gas monitoring by tunable diode-laser absorption spectroscopy (TDLAS), *Appl. Phys. B*, 57, 131–139, <https://doi.org/10.1007/BF00425997>, 1993.
- Werner, R. A. and Brand, W. A.: Referencing strategies and techniques in stable isotope ratio analysis, *Rapid Commun. Mass Sp.*, 15, 501–519, <https://doi.org/10.1002/rcm.258>, 2001.
- Winther, M., Balslev-Harder, D., Christensen, S., Priemé, A., Elberling, B., Crosson, E., and Blunier, T.: Continuous measurements of nitrous oxide isotopomers during incubation experiments, *Biogeosciences*, 15, 767–780, <https://doi.org/10.5194/bg-15-767-2018>, 2018.
- Wolf, B., Merbold, L., Decock, C., Tuzson, B., Harris, E., Six, J., Emmenegger, L., and Mohn, J.: First on-line isotopic characterization of N_2O above intensively managed grassland, *Biogeo-*

- sciences, 12, 2517–2531, <https://doi.org/10.5194/bg-12-2517-2015>, 2015.
- Wunderlin, P., Mohn, J., Joss, A., Emmenegger, L., and Siegrist, H.: Mechanisms of N_2O production in biological wastewater treatment under nitrifying and denitrifying conditions, *Water Res.*, 46, 1027–1037, <https://doi.org/10.1016/j.watres.2011.11.080>, 2012.
- Wunderlin, P., Lehmann, M. F., Siegrist, H., Tuzson, B., Joss, A., Emmenegger, L., and Mohn, J.: Isotope signatures of N_2O in a mixed microbial population system: constraints on N_2O producing pathways in wastewater treatment, *Environ. Sci. Technol.*, 47, 1339–1348, <https://doi.org/10.1021/es303174x>, 2013.
- Yamamoto, A., Uchida, Y., Akiyama, H., and Nakajima, Y.: Continuous and unattended measurements of the site preference of nitrous oxide emitted from an agricultural soil using quantum cascade laser spectrometry with intercomparison with isotope ratio mass spectrometry, *Rapid Commun. Mass Spectr.*, 28, 1444–1452, <https://doi.org/10.1002/rcm.6916>, 2014.
- Yoshida, N. and Toyoda, S.: Constraining the atmospheric N_2O budget from intramolecular site preference in N_2O isotopomers, *Nature*, 405, 330–334, <https://doi.org/10.1038/35012558>, 2000.
- Yue, F. J., Li, S. L., Liu, C. Q., Mostofa, K. M., Yoshida, N., Toyoda, S., Wang, S. L., Hattori, S., and Liu, X. L.: Spatial variation of nitrogen cycling in a subtropical stratified impoundment in southwest China, elucidated by nitrous oxide isotopomer and nitrate isotopes, *Inland Waters*, 8, 186–195, <https://doi.org/10.1080/20442041.2018.1457847>, 2018.

3. Cl-initiated Methane oxidation

Because of the methane interference discovered for the Picarro G5131-I shown in the previous article, a method was developed for continuously removing methane from a sample flow by the use of chlorine radical initiated oxidation.

This work was a collaboration between Physics of Ice Climate and Earth and Copenhagen Centre for Atmospheric Research, both part of Copenhagen University.

The article presented is an unreviewed draft before getting finished for final assessment by co-authors.

My share of the work has included; design of experiment, data collection and treatment, writing and editing.

Cl-initiated Methane oxidation

Merve Polat¹, Jesper Baldtzer Liisberg², Morten Krogsbøll¹, Thomas Blunier², and Matthew Stanley Johnson¹

¹Copenhagen Center for Atmospheric Research, Department of Chemistry, University of Copenhagen, Universitetsparken 5, 2100 Copenhagen, Denmark

²Physics of Ice Climate and Earth, Niels Bohr Institute, University of Copenhagen, Denmark

Correspondence: Merve Polat (mp@chem.ku.dk)

Abstract. The development of laser spectroscopy has made it possible to measure the minute changes in the absorption of trace gasses and their isotopes. Due to the low magnitude signal from these species, it is essential that no cross-talk of other absorbing gas species interfere with the observations. To scrub the sample stream and prepare it for measurements there are many options including traps and membranes that remove common atmospheric trace gases such as CO₂ and H₂O. The options for removing CH₄, however, are limited. We demonstrate a novel method for CH₄ removal through chlorine initiated oxidation. This is accomplished through a developed setup with the essential photochemical device used for generating the chlorine radicals. We have developed a simple kinetic model with the intention of predicting the removal efficiency when varying the four parameters in the system; CH₄, J_{Cl_2} , Cl₂ and residence time. Besides, the model exhibits great agreement with the experimental data. The stable removal of the experiments could be maintained and with a peak removal efficiency level of >98% achieved for ambient levels of methane. The system seems viable as an option for continuous methane scrubbing.

Copyright statement. TEXT

1 Introduction

Laser spectroscopy offers a fast and non-destructive way for measuring gas samples that easily lend itself to monitoring purposes, as many of the available instruments require little maintenance. The continued development and improvement of spectrometers extent the spectra of gas species that can be measured. The commercially available instruments can measure isotopic enrichment based on the finely resolved spectra of the vib-rot absorption in the infrared region. Here laser spectroscopy is encroaching on the territory that was normally reserved for mass spectrometry. The advancement in this field can give the impression, that the instrument can be used in a "plug and play" manner. That is not the case, as there are still limitations dictating the accuracy and reproducibility of the measurements. In a recent study investigating the performance of currently available laser spectroscopic N₂O isotope analyzers (Harris et al. (2019)), an array of interference's from other trace gasses was determined based on spectral overlap between N₂O and the vib-rot spectra of trace-gasses. The result of this was observed false increases in isotopic values arising exclusively from increased trace-gas concentration. A common use for these instruments is

for measurements of agricultural soils, (Ibraim et al. (2019), Wolf et al. (2015)) where the variations in the isotopic composition are of interest for monitoring the biological activity in the soil. Complicating measurement changes in these isotopic compositions will commonly be accompanied by changes in the abundance of the interfering trace-gasses such as CH₄, CO₂, and water. Without a method for removing or accounting for these effects, it will be impossible to get any meaningful data. One solution to this obstacle is applying multi-line analysis or co-measurement of the interfering gas by a second instrument, which allows for quantifying the interference magnitude. These efficient options are not readily available for every user of these specialized instruments, as it will either require a redesign of the instrument or investment in an additional instrument. For that reason, the more common method would be to separate the sample from the interfering species. The measurements of discrete samples can be accomplished by the use of gas chromatography. For continued measurements, well-established methods include chemical traps and membranes are readily available for the removal of CO₂, CO, and humidity. However, to the best of our knowledge, no method for continued removal of methane is available, safe for catalyzed combustion (CULLIS and WILLATT (1983)) which requires high temperatures and the addition of oxygen thereby altering the gas matrix. It was hence desired to develop a method for removing CH₄ and potentially other VOCs in a manner that would not introduce changes to the matrix composition. Inspiration for the method investigated in this work was taken from the oxidation pathways taking place in the atmosphere. Here the majority of methane is oxidized through initial reaction with OH radicals (Rigby et al. (2017)) under the formation of water and CH₃. The reactivity of chlorine atoms toward various climate-relevant gases, e.g. CH₄, and other volatile organic compounds (VOCs) has proven to be a faster alternative to the reaction with OH radicals. Chlorine could hence represent a potentially important tropospheric oxidation initiator: generally, the reaction rates of Cl with VOCs exceed the analogous ones with OH by at least one order of magnitude; The known NIST rate constants values for methane's reaction with Cl atoms is $1.07 \cdot 10^{-13} \frac{cm^3}{molecules \cdot s}$ (Bryukov et al. (2002)) and with hydroxyl radicals is $6.20 \cdot 10^{-15} \frac{cm^3}{molecules \cdot s}$ (Bonard et al. (2002)) The mechanism proposed in this study is the Cl-initiated methane oxidation technology (R1)-(R6)



The design of the mechanism is based on the natural self-cleaning process in the Earth's atmosphere called the Gas Phase Advanced Oxidation (GPAO) air pollution management (Johnson et al. (2014)), and the observed destruction of ozone on the Antarctic caused by active chlorine. The high levels of chlorine are maintained through ozone destruction by an effective recycling process called the HCl null cycle. (Müller et al. (2018))

Preliminary experiments

Prior to the work presented here preliminary experiments were conducted to investigating the feasibility of the proposed

mechanism. In these an ambient air standard was enriched in Cl_2 by in-situ production of Cl_2 through electrolysis of a saltwater mixture. Following the addition of chlorine to the standard air mixture, the sample was photolyzed in a photochemical device generating Cl radicals that would initiate the oxidation of methane. The resulting drop in methane was monitored with a Cavity Ring-Down Spectrometer, Picarro G1301. The preliminary experimental setups A, B1, B2, C1, and C2 are described in Appendix A. The photochemical device used was comprised of 28 LEDs (385 nm)(UV LED LAMP-VAOL-5EUV8T4) spaced evenly in a PVS plastic chamber to generate the photolyzing light. The last set of experiments substituted the LEDs with a high-pressure Xenon lamp (ILC technology R100-IB) equipped with an optical filter at 335 nm for generating the light at an optimal cross-section. The resulting peak removal efficiencies for the preliminary experiments are presented in 1.

Table 1. Removal Efficiencies for the Preliminary Experiment

EXPERIMENT	HIGHEST RE% (DATA)	CH_4 (STAND.)
A (17/4)	68%	2 ppm
A (23/4)	67.75%	1.98 ppm
A (24/4)	76.48%	1.98 ppm
B1 (26/4)	78.52%	2 ppm
B2 (30/4)	80.16%	2 ppm
C2 (26/5)	98.20%	2 ppm

The system yielded an average methane depletion of 86.63% with a peak depletion at 98.2%. Various parameters were changes throughout the experiments, and it was determined that methane depletion is highly dependent on both the flow, chlorine production, and the light source. It is therefore believed that with better control of these parameters a higher and steadier RE% can be obtained for each experiment. The goal of this work then became:

- Improve upon the system used in preliminary experiments, by making the relevant parameters, Cl_2 , CH_4 , reaction time, and light intensity tunable.
- Determine the effect of these variables
- Reach removal above 99% at ambient methane levels.
- Develop a model describing the system to help determine the mechanism of removal.

2 Method

2.1 Experimental approach

Based on the findings from the preliminary experiments, a setup was designed to better characterize the dynamics of the ongoing reactions. The first step in achieving this was to confine the $[\text{Cl}_2]$ abundance, by supplying it from an external high

Table 2. Table of the gas bottles used in the experiments

Bottle name	CH_4 (ppm)	Cl_2 (ppm)	Matrix composition	Flow range (ml/min)
A	0	100 ± 2.5	$>99\% N_2$	6-23
B	$2.003 \pm 5 \cdot 10^{-4}$	0	Atmospheric air	1-29
C	78 ± 2	0	$20.95\% O_2 + >79\% N_2$	0.3-1.2

concentration source rather than in-situ production. The second step was to add a high concentration CH_4 source to allow for generating various levels of $[CH_4]$. Additionally, the chlorine sensor was moved out of the main flow line, greatly reducing the dead volume of the setup, allowing for higher time-resolution. Four different iterations of the setup are utilized for the presented results; Repeated experiment using high-pressure Xenon lamp (Figure B1), single tube hexagonal photochemical device experiments with (Figure B3) and without flow-controlled chlorine waste (Figure B2) and multiple tubes Hexagonal photochemical device experiments (Figure 1).

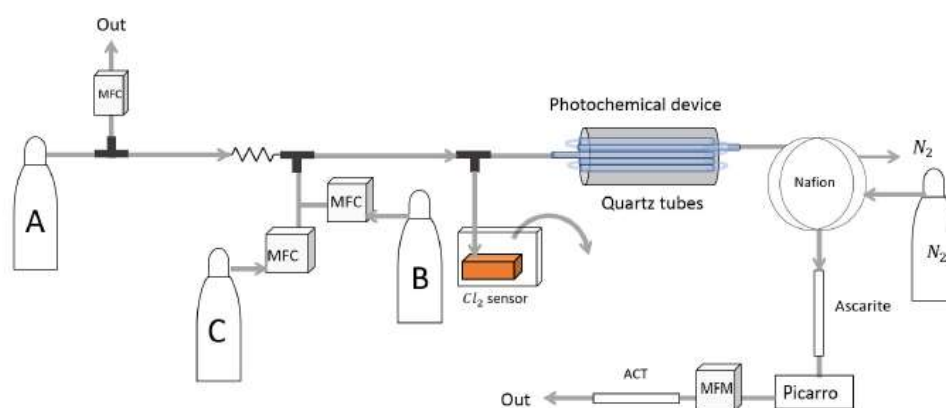


Figure 1. Experimental setup of Hexagonal photochemical device experiments with increased Residence Time.

The inlet of the system consists of two channels: the methane channel and the chlorine gas channel. The methane channel is providing a flow of a dynamically mixed sample, combining flow from bottle B and C as defined in Table 2. Through controlling the ratio between the two gasses diverging levels of $[CH_4]$ could be maintained. The flows were controlled by two mass flow controllers of type GE50A from MKS. Chlorine supply from bottle A was added to the methane mixture through a glass capillary of length 23cm with an inner diameter of 0.1mm functioning as a static flow restrictor. In order to promote flow through the capillary an over-pressure on the order of 0.8-1.6bar compared to the atmospheric pressure in the setup, was maintained by the bottle regulator to get the desired flow. A flow controller would have been preferable, the corrosive

nature of the high Cl_2 limited the options for material choices. An additional consequence of the high corrosives was the need to incorporate an overflow waste line between bottle A and the capillary, regulated to maintain a high flow of $>100\text{ml}/\text{min}$ through the bottle regulator, as it was found to consume a substantial amount of chlorine at flow-rates below $20\text{ml}/\text{min}$. This loss of chlorine is still unexplained, as Cl_2 is not reactive with metals under dry conditions at room temperature. The most likely hypothesis was that the pressure regulator had not been sufficiently flushed by dry air prior to being used. As the regulator had been exposed to ambient air prior to installation, it is likely that a thin film of humidity has bound to it. The chlorine would then be able to bind to this water under the formation of hydrochloric and hypochlorous acid. (Institute (2020)) The loss of Cl_2 above flows of $50\text{ ml}/\text{min}$ was minimized substantially. This overflow was initially controlled by a forward pressure controller but was replaced with a manual mass flow controller in later experiments to limit chlorine-waste. The combined flow from the chlorine and methane channel was in the range of $25\text{-}30\text{ ml}/\text{min}$ and varied with the desired mixing ratio. A flow of roughly $5.6\text{ ml}/\text{min}$ of chlorine mixture was expected with a pressure of 2 atm at the capillary inlet and an assumed pressure of 1 atm at the point of mixing with methane. The flow containing methane and chlorine gas is split at a T-piece, where the main flow, controlled by the pump of the Picarro, proceeds through the photochemical device while the overflow goes towards a Cl_2 sensor. (Chlorine Gas Detector 0-20PPM Cl_2 with Alarms Datalogger and USB Charging).

The Photochemical device

The photochamber in "Repeated experiment using high-pressure Xenon lamp" uses a quartz tube with dimensions (20 cm in length, $1/2\text{ inches}(12.7\text{ mm})$ in outer diameter) placed in the Xenon lamp (XL) photochemical device as described in "Electrochemical device setup C1-2 - High-pressure xenon lamp experiments" (A4 and A5)

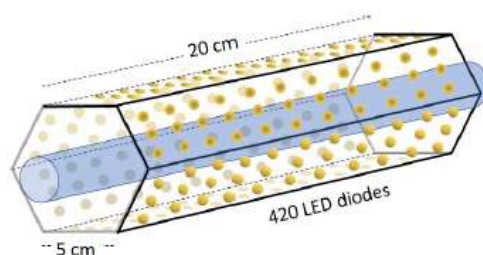


Figure 2. Hexagonal photochemical device consisting of connected circuit boards of 420 LED at 365 nm

The initial experiments with the XL confirm that the supply of chlorine could be tuned. The XL was replaced with a new photolysis chamber consisting of 420 LED at 365 nm (Figure 1, B2 and B3) peak wavelength connected by circuit boards in a hexagonal cylinder. The inner diameter between the lamps was approximately 2 cm to ensure that the previously used quartz tube could pass through it, see Figure 2. The LED diodes run in a parallel circuit with a forward voltage and forward current (from positive to negative). The max current is 13.2 mA for each LED with a max voltage of 3.8 V . The same voltage runs through the LEDs, resulting in a total current across the system of 5.5 A . The difference between the two similar setups "Hexagonal photochemical device with MFC and without MFC" is illustrated in Figures B3 and B2, respectively. The forward

pressure valve is exchanged with a mass flow controller, as minimum flow from the forward pressure valve was needlessly large. Installing the mass flow controller allowed for a smaller and more stable level of waste flow. The quartz tube of the previous experiments is substituted with seven smaller quartz tubes to yield a longer residence time in the photochemical device in the last experimental setup utilized, see Figure 1. The seven quartz tubes are arranged in hexagonal shape for optimal packing and consist of five 8.33 mm in outer diameter with a 20 cm length, and two tubes with an outer diameter of 8.00mm and a length of 25 cm. The extra 5 cm of the two last tubes were outside the photolysis chamber to connect with the setup. The volume inside the photolysis chamber at 42.8cm^3 supplies a 2.7 times increase in residence time in the photolysis chamber compared to the previous setup. The tubes were connected in series via Tygon tubes, Tygon R3603, of length 5cm. The insides of these tubes were coated with krytox, GPL-206 Grease Lubricant O-Rings SCUBA, to stop the consumption of Cl_2 that was observed for any soft tubing.

After the photochemical device

A 35cm Nafion membrane, TT-030 from Perma Pure LLC, was installed following the photochemical device. A counter-flow of 50ml/min N_2 on the outside of the membrane to remove water. Post drying the sample passed through an ascarite trap. The trap consisted of a quartz tube filled with a central layer of NaOH settled in between two layers of MgClO_4 separated by glass wool. These types of traps are normally used for the removal of CO_2 and H_2O (Harris et al. (2019)), but to our benefit it was found to likewise remove HCl and Cl_2 . The corrosive compounds cleaned gas stream was pumped into a CRDS Picarro G1301 as described in the electrochemical device experiments. The G1301 unit was run with a cavity pressure of 45Torr maintained by a built-in pump. The flow through the instrument is controlled by the ratio between the inlet and outlet of the cavity, with the flow monitored by an external flowmeter installed in-between the cavity and the pump. The normal settings of the flow were maintained at approximately 15 ml/min. However, for experiments involving variation in residence time, this flow was changed accordingly. The outlet of the Picarro has an activated carbon trap labeled "ACT" attached which is mainly utilized for scrubbing for chlorinated species. This trap has proved to be useful in removing the chlorinated species in the preliminary experiments.

2.2 Theoretical approach

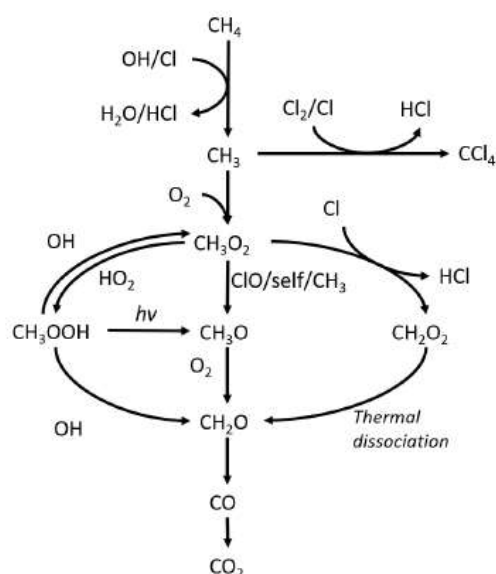
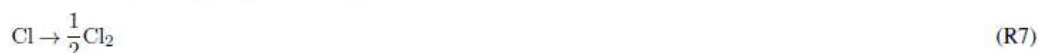


Figure 3. Reaction scheme for the oxidation of methane to CO_2

A model made with the software Kintecus, version 6.8, (Ianni (2012)) is used to get an understanding of the dynamics within the photochemical device. Kintecus is based on deterministic methods, specifically the Arrhenius equations, and uses Microsoft Office Excel as an interface. The software is designed to show the reaction processes by displaying the concentration of species of interest as a function of time. The desired Kintecus model was made by providing it the relevant reactions with rates for chlorine radical production and removal, methane oxidation, and formation of chlorinated species. The model was kept as simple as possible while still capturing the majority of the relevant reactions. The reactions and their rates used in the model are found in Tables D1-D2. A simplified reaction-scheme is shown in Figure 3. Different experiments can then be modeled by setting the concentration of both the initial and external concentration of used species and the residence time within the chamber. Some parameters were fixed in the simulation model as a continuous flow through the model by setting the initial and external concentrations of gases flowing to be the same value. This is done for the gases Cl_2 , CH_4 , N_2 and O_2 . The software also takes into account the relevant physical condition e.g. temperature and pressure as inputs, which is set in the parameter section. All rates in the model set to be temperature independent. The physical parameters are fixed as well. The temperature at 298 K, starting integration time to 10^{-6} s (starting step for the integrated model), maximum integration time to 1 s, simulation length equal to residence time plus 5 sec, the accuracy of digits to 10^{-4} . Furthermore, the energy barrier unit kcal was selected, and the unit of concentration selected to be molecules/cc. Due to the reactive nature of radicals, a set of radical terminating reactions

had to be incorporated into the model, reflecting radicals reacting with the walls of the quartz tube. These four additional wall reactions R7-R10 are added to the Kintecus model.



The rate constant of the wall reactions and the photolysis rate had to be determined. The wall reaction rates were estimated based on the diffusion rate of the radicals and the diffusion length calculated as the average distance from the wall. Because two different sizes of tubes were used throughout the experiments the wall reactions should reflect that. The diffusion length was calculated as

$$l = r \cdot \left(1 - \frac{1}{\sqrt{2}}\right) \quad (1)$$

l being the diffusion length and r being the inner radius of the tube

$$k = \frac{4 \cdot D}{l^2} \quad (2)$$

The rate of the wall reactions is defined by equation 2 which is dependent on the diffusion constant D and the diffusion length. The diffusion constants, diffusion lengths, and estimated wall reaction rates are shown in Table D3.

The model intends to recreate the experimental results and variation performed on the Cl-initiated methane oxidation mechanism. The desired output from the model was the initiating Cl_2 photodissociation-rate, J_{Cl_2} , which was the only rate varied throughout the experimental models. A second output from the model was the determination of the abundance of $[\text{Cl}]$ within the photochamber and finally of unwanted side-products with a focus on CCl_4 . This compound is the end product of continued reaction of CH_3 with Cl_2 and Cl . It is toxic with a recommended exposure limit at 2ppm (NIOSH (2020)). J_{Cl_2} for the simulations is estimated in two ways. The first approach was fitting of J_{Cl_2} in Kintecus to generate the observed removal efficiencies from experimental results. These fittings were only produced for experiments investigating the effect of power. The resulting J_{Cl_2} was related to power via a calculation of the effective power to light conversion based on the absorption cross-section of Cl_2 and the wavelength distribution of the LEDs. Two sets of power to J_{Cl_2} was determined in this manner, one for the single tube experiments and one for the multiple tubes experiments. A second method of estimating J_{Cl_2} and relating it to power input was done, as two sets of experiments could not be adequately covered by the method described above. This method estimated J_{Cl_2} through simplified kinetic calculations relating it to power via the same method as for the Kintecus derived J_{Cl_2} .

The photolysis rate of R1 is dependent on power input, therefore, it needs to be tunable in the model. This was calculated by the estimation of the light output as energy. Based on observations this was fitted well by a second-order polynomial for calculating the effective light output as a function of power.

$$P_{eff}(W) = (a \cdot W + b) \cdot W \quad (3)$$

Where P_{eff} is the effective power and the constants a, with unit $1/W$, and b, unitless, are setup dependent constants, that scales the effectivity of effective power output P_{eff} . From the effective power output the photolysis rate J_{Cl_2} could be calculated by multiplying P_{eff} with a scaling factor.

$$J_{Cl_2}(W) = P_{eff}(W) \cdot J_{scale} \quad (4)$$

Here J_{scale} is the scaling-factor with unit $1/J$, and was calculated from the cross-section of Cl_2 , the wavelength distribution of the generated light, and the expected photon density. The density of photons would depend on the volume and cross-section of the tube within the photochemical device. A detailed walkthrough of the calculation of J_{scale} can be found in the supplement. The J_{Cl_2} is fit to data collected on the of 26 February and the 9 March, values for the constants a and b could be found. The 26 February reflects the single tube system while the 9 March reflect the optimized multiple tubes setup. From the fitted a, b, and calculated J_{scale} the photolysis rate could be calculated for the other experiments.

3 Results and discussion

3.1 Experimental results

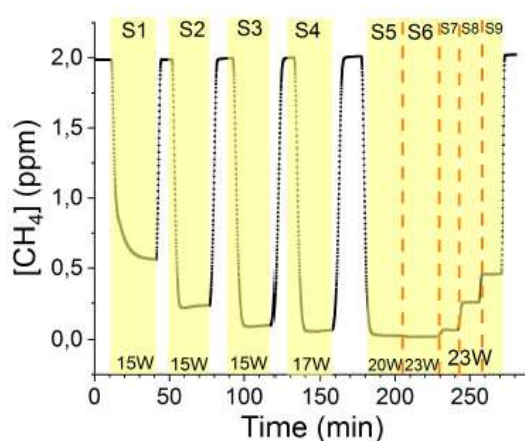


Figure 4. Experiment conducted on the 5 March. The CH_4 is seen as a function of time. The highlight indicates the times where light was turned on. The experimental step is indicated in the top of the highlights, while the power input in watts is indicated in the bottom.

Experiments were conducted over the span of eight days, where each day a different combination of settings for the four parameters; $[CH_4]_{Initial}$, $[Cl_2]$, residence time and power were tested. An overview of the settings and resulting removal can be seen in Tables C1, C2 and C3. The results from the 5 March are shown in Figure 4. The experiments of the 5 March were

carried out with the constant $[\text{CH}_4]_{\text{initial}}$ at $2.000 \pm 0.003 \text{ ppm}$ and Cl_2 mixing ratio at 50.5 ppm , but with mixed settings of residence time and power. The first three steps were done with constant power at 14.8 W with residence times ranging from $164\text{--}350 \text{ s}$. Then keeping residence time around 350 s three steps (S3-S6) of increasing power were tested, ranging from $14.8\text{--}22.8 \text{ W}$. In between steps 4 and 5 a fan was installed, in order to see if cooling at the higher power settings could improve the efficiency. In the previous experiments usually a drop in efficiency is observed at this level of power input. However, this wasn't observed and, therefore, the power was increased for step 6 without turning off the lamp. The removal remained stable across the 15 minutes, so the light was left on as the final 3 steps (S7-S9) were tested. Throughout steps (S6-S9) the power remained at 22.8 W and stepped through reduced residence time from $342\text{--}130 \text{ s}$. Usually, the photochemical device has shown some difficulties at working at higher power inputs, however, the results in Figure C16 present a great improvement due to the silicone removal and inclusion of cooling. All the experimental days two unwanted effects affected the measurements: The first few steps of each experiment did not see removal efficiencies close to the level expected. The cause for this effect is still undetermined, but it is assumed that the effect is due to insufficient flushing of the setup. This effect will be referred to as early-experiment-deviation. The second effect was a pressure drop from the chlorine flow across an experiment, which would subtly increase $[\text{CH}_4]$ and decrease $[\text{Cl}_2]$ during the experiment. The effect was insignificant, but it adds to the uncertainty of the $[\text{Cl}_2]$ values.

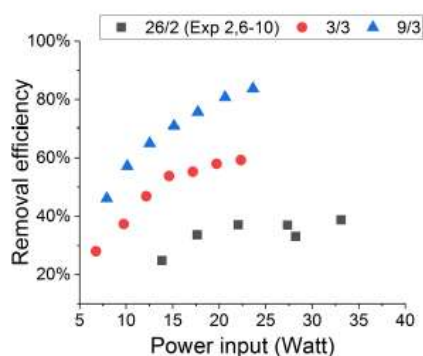


Figure 5. Removal efficiency of methane plotted against power input in W. The result from three experiments, 26 February (black), 3 March (red) and 9 March (blue) have different settings in residence time, $[\text{CH}_4]$ and $[\text{Cl}_2]$.

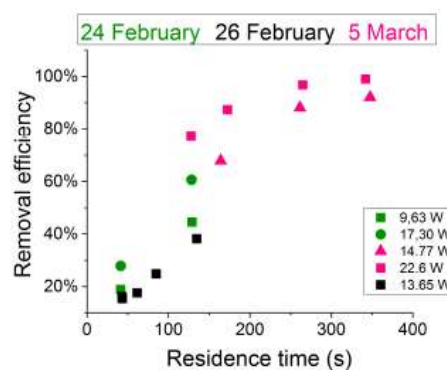


Figure 6. Removal efficiency of methane plotted against residence time in s. The result from three experiments, 24 February (green), 26 February (black) and 5 March (pink) have different settings in power input, $[\text{CH}_4]$ and $[\text{Cl}_2]$.

3.1.1 The effect of power:

The effect of power was the most tested parameter, as it varied on six of the eight days. The result from the three days with a focus on testing power is depicted in Figure 5. Here the improvement in the setup can be followed from the 26 February to the 9 March. As presented for the 26 February the system reaches a maximum removal, where increasing the power does not

yield significantly higher removal efficiencies. This effect also appears to occur on the 3 March. The higher removal is reached thanks to longer residence time and higher $[Cl_2]$, but the system still struggles with greater power inputs, and the efficiency also flattens out. The reason for this was found to be overheating of the device, as was confirmed when the silicone glue holding it together started to melt at the higher power inputs. As a result of this the system went through another upgrade after completing the experiments on the 3 March. This included rewiring the circuit board and removing the silicone glue that appears to increase the resistance of the system. The experiment of the 9 March is additionally equipped with a fan to help dissipate the heat, which resulted in a trend going asymptotically towards 100% removal with power input. Comparing the settings between the 3 March and the 9 March the single difference is the $[CH_4]$ which was lower for the 9 March. This would lead to higher removal, but the solution to the heat issue is the main force behind their difference.

3.1.2 Effect of residence time:

Increasing the time spent in the photochemical device will result in increased removal. Experiments highlighting the effect of varying residence time can be seen in Figure 6. The residence time was investigated in two regions, one for the single tube experiments and one for the multiple tubes experiments. The same flow equals longer residence time for the multiple tubes setup due to the 2.7 fold volume increase in the photochemical device. The expected trend of asymptotically approaching 100% can be depicted for the 5 March where the higher power approach this quicker. The effective light output and residence time are lower for the 24 and 26 February compared to the 5 March. The resulting removal efficiency is accordingly lower. Residence time is an easy method of increasing the removal efficiency, but it comes at the cost of the response time of the system.

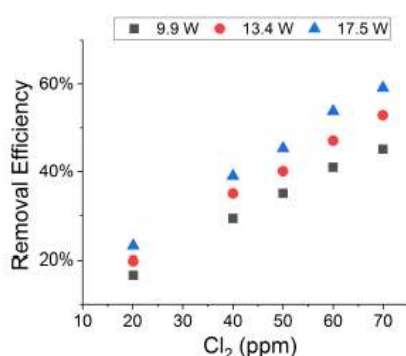


Figure 7. The Figure presents the removal efficiency as a function of the chlorine mixing ratio. Step one is an example of early-experiments-derivation, therefore, it is removed. The dots represent different power inputs of the photochemical device

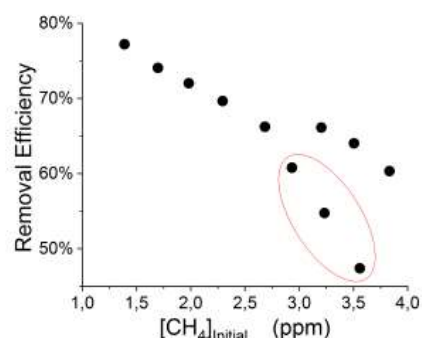


Figure 8. The removal efficiency is displayed as a function of the initial methane concentration with the remaining fixed parameters such as Cl_2 mixing ratio, residence time, and power input. The three encircled points in the Figure represent steps suffering from early- experiments-derivation.

3.1.3 Effect of [Cl₂]

The [Cl₂] was changed during the days. The experiment of 27 February was utilized for determining the effect of [Cl₂]. The results from the 27 February are depicted in Figure 7, and the chlorine mixing ratio is ranged from 20 ppm to 70ppm. The change of chlorine mixing ratios required considerable stabilization time, hence, three steps of power were tested for each step of [Cl₂]. The trend is clear, higher [Cl₂] results in a higher removal rate. Since the resulting removal is still below 60% the trend appears linear with [Cl₂]. Following the results from the 27 February a [Cl₂] level of 50ppm was chosen for the remaining experiments.

3.1.4 Effect of [CH₄]:

The initial [CH₄] had been altered during some of the days, but similar to the [Cl₂] only one experiment depicts the effects of changing [CH₄]. Here the 4 March experiment spans the [CH₄] in the range 1.4-4.1 ppm as plotted in Figure 8. Three steps, corresponding to the first three steps, have been highlighted because they suffer from the early experiment deviation. In order to confirm that is the case, the range they covered was rerun as can be seen in the Figure. As ambient [CH₄] is around 2ppm, the high removal was promising.

The performance of the experimental setup has been investigated throughout the aforementioned experiments. Improved removal efficiency can be accomplished by increasing the power input or [Cl₂] for reaching an increase in Cl atoms. Longer residence times allow for more photodissociation of chlorine gas to occur and thereby increases the Cl atom concentration. The negative correlation for [CH₄] is understandable as RE% is a relative value. The absolute amount of removed methane scales with the [CH₄].

3.2 Model results

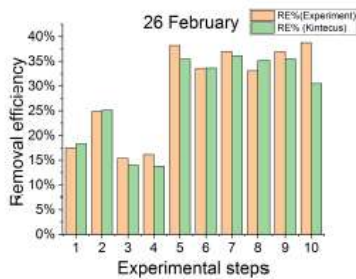


Figure 9. Removal efficiency for the steps of the 26 February as found experimentally (orange) and by model(green)

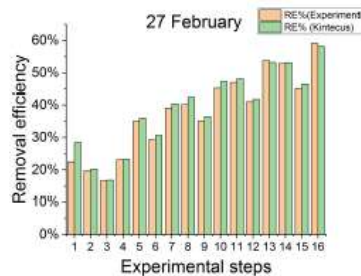


Figure 10. Removal efficiency for the steps of the 27 February as found experimentally (orange) and by model(green)

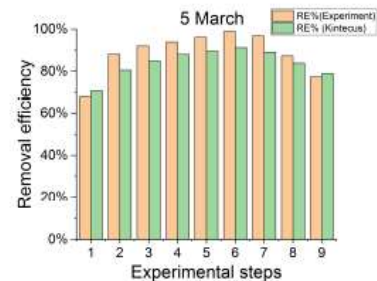


Figure 11. Removal efficiency for the steps of the 5 March as found experimentally (orange) and by model(green)

The efficiency constants a and b used in eq. 3 were fitted for the experimental data from steps 2 and 6-9 of the 26 February. In order to fit the sudden drop in the efficiency generated by overheating, two sets of a and b constants were generated to describe the effect in different power ranges. The J_{Cl_2} for the single tube single experiments are generated from the constants. The J_{Cl_2} dependence on the power input (W) for the single tube experiments of 26 February and 24 February is given by the equations D11 and D12. The equations incorporate a decrease in efficiency of the power input at higher levels due to overheating of the chamber as observed in Figure 5. The comparison between modeled and experimental efficiency is depicted in Figure 9. Multiple tubes experiment J_{Cl_2} values are generated in the same manner as aforementioned, and differs by using 9 March experiment to obtain kinetic J_{Cl_2} values (Figures D5-D6 and equation D13). In Figure 11 a comparison of experimental and kintecus model results are depicted for the 5 March. The optimization proceeded on the photochemical device the experiments during the experimental days result in that the 27 February and 3 March experiments can't be related to the J_{Cl_2} expressions aforementioned. The glue holding the circuit boards together is slightly removed after the 26 February and even further improvements are done after the 27 February. Following the 3 March the photochemical is optimized even further with additional improvements such as exchange of some of the LEDs and reconstruction of the photochemical device. Additional kinetic calculations are therefore used to estimate the J_{Cl_2} of those two experiments. The effectiveness obtained for the 27 February and 3 March is described in equations D14 and D15-D16, respectively. Figure 10 presents the comparison for 27 February. The model slightly underestimates the removal efficiency for most of the steps. This is most notably for the first two steps in Figure 9, which is caused by the early-experiments derivation. As visualized in Figure C6 the photochemical device was continued turned on during S6 -S8. In step eight the chamber was overheated and the effectiveness is decreased. This is also apparent in the comparison of kintecus simulated and experimental removal efficiencies regarding step eight. The overheating at high power inputs is eliminated with the improved photochemical device. This is also apparent when comparing the effectiveness, which is approximately 9 % for the multiple tubes, Figure D5, and approximately 0.6 % for the single tube, Figure D1, at the same power input at 15 W. Overall, the kintecus model follows the trend of the experimental results to a promising degree but likewise underestimated the removal efficiency. The model accounts poorly for the variations of initial methane concentrations in Figure D7. However, it reflects the trend to a small degree.

3.2.1 Parameters simulated and compared with experimental results

The experiment on the 9 March is representing the optimized experimental setup, and the fit found for the 9 March will be used as the basis for the final model. The final model will be used to run across the four different parameters and determine the performance in terms of removal efficiency, chlorine radical abundance, and the resulting abundance of $[CCl_2]$. As performed for the experiments, three of the parameters will be kept at a standard value, while the fourth parameter spans a range. The standard value and the range can be seen in Table 3.

Table 3. Parameter ranges

Parameter	Standard value	Ranges
Cl_2	50 ppm	20-100 ppm
CH_4	2.05 ppm	0.5- 5 ppm
Residence time	165 s	40-400 s
Power input	14.5 W	9-31 W
O_2	10%	
N_2	90%	

CCl_4 and Cl production

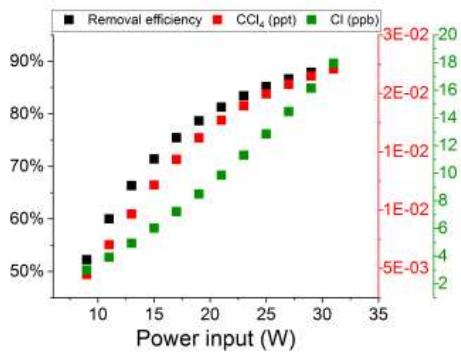


Figure 12. The J_{Cl_2} is varied and the remaining parameters are kept at the standard parameter presented in Table 3. In addition the Cl and CCl_4 production are noted. The Removal efficiency of methane depletion (Black), $[CCl_4]$ (Red) and $[Cl]$ (Green) is shown as a functions of the J_{Cl_2}

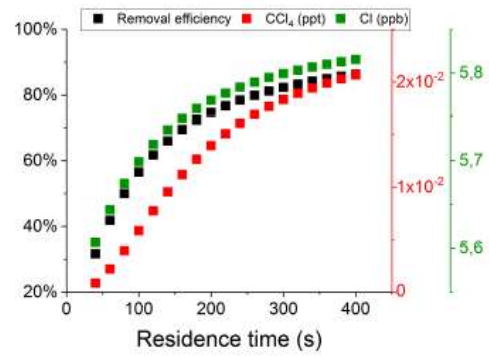


Figure 13. The residence time is varied and the remaining parameters are kept at the standard parameter presented in Table 3. In addition the Cl and CCl_4 production are noted. The Removal efficiency of methane depletion (Black), $[CCl_4]$ (Red) and $[Cl]$ (Green) is shown as a functions of the residence time

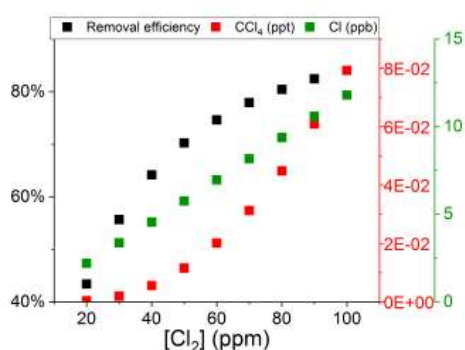


Figure 14. The $[Cl_2]$ is varied and the remaining parameters are kept at the standard parameter presented in Table 3. In addition the Cl and CCl_4 production are noted. The Removal efficiency of methane depletion (Black), $[CCl_4]$ (Red) and [Cl] (Green) is shown as a functions of the Cl_2 mixing ratio

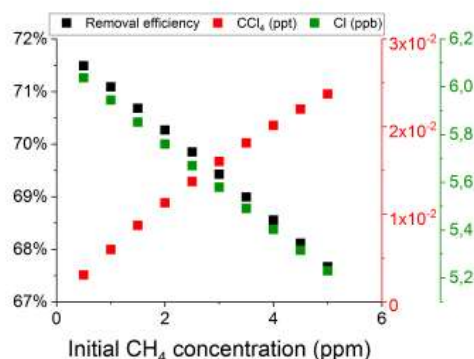


Figure 15. The initial $[CH_4]$ is varied and the remaining parameters are kept at the standard parameter presented in Table 3. In addition the Cl and CCl_4 production are noted. The Removal efficiency of methane depletion (Black), $[CCl_4]$ (Red) and [Cl] (Green) is shown as a functions of the $[CH_4]$.

The resulting removal efficiency as a function of each of the four parameters are depicted in Figures 12, 13, 14 and 15. The results are compared with the kintecus model with experimental results with varying parameters Power input (W), Residence time (s) and chlorine mixing ratio (ppm) in Figures 5, 6 and 7, respectively. An agreement in the observed response can be seen. However, the model is less sensitive to methane concentration and fails at recreating the magnitude of the experimental trends. The comparison of the model, Figure 13, with experimental results, Figure 8, clearly shows that the model RE% scales with approximately one-tenth of the trend observed in the experiment. While the reason for this is as of yet undetermined, we hypothesize that the used reaction rate for the methane oxidation is too slow. Tentative simulations of the system with an increased reaction rate for this reaction gave a better match in methane dependence between model and experiment. The necessary rate for the agreement was an order of magnitude higher than the value found in the literature. The setup was not designed for determining this reaction rate, therefore, the model will rely on the value found in the literature. The corresponding Cl_2 photo dissociation rates for the Power inputs in Figure 12 ranges from $4.04 \cdot 10^{-3}$ to $2.37 \cdot 10^{-2}$ which is a good agreement with previous J_{Cl_2} values found for a similar system. (Nilsson et al. (2009)) In addition to the removal efficiency, the [Cl] and $[CCl_4]$ are also depicted in the aforementioned Figures. The unwanted side-products of the experiment are the chlorinated methane compounds such as CH_3Cl and CCl_4 . These compounds can be toxic and have a much higher GWP than methane. Figure 14 clearly shows that an increase in Cl_2 concentrations enhances the $[CCl_4]$ production eight times more than increasing the other parameters in Figures 12, 13 and 15. Moreover, the [Cl] is highest when increasing the J_{Cl_2} . Therefore, if the chlorinated compounds should be avoided and a high RE% maintained, the photolysis rate must be enhanced to yield a higher methane depletion and a higher concentration of [Cl]. In the experimental setup CCl_4 removal is carried out on activated carbon. This is done on the basis of a study of Ryu and Choi (2004) proving that activated carbon fibers were an effective adsorbent for the

removal of toxic gases (such as CCl_4). Another study by Milchert et al. (2000) also verified the efficiency of CCl_4 adsorption in wastewater in an aqueous solution of activated carbon.

4 Conclusions

In the study presented we created a setup capable of continuously scrubbing air for methane. The concept builds on GPAO air pollution management and the effective recycling process called the HCl null cycle. Here the normal atmospheric oxidation pathway for methane has been enhanced by letting the oxidation be initiated by chlorine radicals rather than hydroxyl radicals. These were generated by photolyzing a chlorinated sample stream in a photochemical device. This device consisted of 420 LED's placed in a hexagon tube, illuminating a quartz tube connected to the sample stream. The performance of the setup was investigated by measurement of the resulting drop in $[\text{CH}_4]$ in relation to the four relevant variables; $[\text{CH}_4]$, $[\text{Cl}_2]$, luminescence and residence time within the photochemical device. The resulting trends observed experimentally were confirmed in a simple model, used to determine the photolysis rate and the production of the toxic side product CCl_4 . This was found to be produced in levels well below the guideline levels of the NIOSH, and is deemed non-problematic for the system. The highest removal levels achieved experimentally at ambient methane levels were above 98% which was maintained under stable condition. A level above 99.5% would be achievable by increasing the chlorine abundance. Replicating the design of the scrubbing setup would rely on a controllable supply of chlorine gas and a functional photochemical device. We advise using a high concentration chlorine source, as that would minimize the dilution of the sample stream. The resulting CCl_4 won't exceed the toxicity levels at ambient levels of methane, hence, the level of $[\text{Cl}_2]$ can be set higher than those used in the presented experiments to allow for shorter residence time with sufficient removal. Chlorine is highly corrosive in wet conditions we advise that a sample stream be dried prior to the introduction of chlorine. The corrosiveness of the chlorine and the hydrochloric acid resulting from the methane removal will also restrict the material choice in the sample stream between chlorine introduction and the instrument used for measurements. For that purpose an ascarite trap, commonly used for CO_2 removal, can be applied. Additionally acid-resistant tubes must be used. The design of a photochemical device can be accomplished by any light source with a peak center around 335nm. Based on the ease of arranging and acquiring LEDs, we will recommend their use, though if a higher intensity light-source is available this would allow for using a lower chlorine concentration. By copying this method we believe that users will be able to remove methane from a sample continuously, thus facilitating measurements by instruments that would otherwise be affected by it.

References

- Baulch, D., Duxbury, J., Grant, S., and Montague, D.: Evaluated kinetic data for high temperature reactions. Volume 4. Homogeneous gas phase reactions of halogen- and cyanide-containing species, Tech. rep., NATIONAL STANDARD REFERENCE DATA SYSTEM, 1981.
- Bonard, A., Daële, V., Delfau, J.-L., and Vovelle, C.: Kinetics of OH radical reactions with methane in the temperature range 295- 660 K and with dimethyl ether and methyl-tert-butyl ether in the temperature range 295- 618 K, *The Journal of Physical Chemistry A*, 106, 4384–4389, 2002.
- Bryukov, M. G., Slagle, I. R., and Knyazev, V. D.: Kinetics of reactions of Cl atoms with methane and chlorinated methanes, *The journal of physical chemistry A*, 106, 10 532–10 542, 2002.
- Burkholder, J., Sander, S., Abbatt, J., Barker, J., Huie, R., Kolb, C., Kurylo, M., Orkin, V., Wilmouth, D., and Wine, P.: Chemical kinetics and photochemical data for use in atmospheric studies: evaluation number 18, Tech. rep., Pasadena, CA: Jet Propulsion Laboratory, National Aeronautics and Space . . . , 2015.
- CULLIS, C. F. and WILLATT, B. M.: Oxidation of Methane over Supported Precious Metal Catalysts, *JOURNAL OF CATALYSIS*, 83, 267–285, [https://doi.org/10.1016/0021-9517\(83\)90054-4](https://doi.org/10.1016/0021-9517(83)90054-4), 1983.
- Harris, S. J., Liisberg, J., Xia, L., Wei, J., Zeyer, K., Yu, L., Barthel, M., Wolf, B., Kelly, B. F. J., Cendón, D. I., Blunier, T., Six, J., and Mohn, J.: N₂O isotopocule measurements using laser spectroscopy: analyzer characterization and intercomparison, *Atmospheric Measurement Techniques Discussions*, 2019, 1–84, <https://doi.org/10.5194/amt-2019-451>, <https://www.atmos-meas-tech-discuss.net/amt-2019-451/>, 2019.
- Hossaini, R., Chipperfield, M. P., Saiz-Lopez, A., Fernandez, R., Monks, S., Feng, W., Brauer, P., and Von Glasow, R.: A global model of tropospheric chlorine chemistry: Organic versus inorganic sources and impact on methane oxidation, *Journal of Geophysical Research: Atmospheres*, 121, 14–271, 2016.
- Ianni, J.: Kintecus, Windows version, 3, 2012.
- Ibraim, E., Wolf, B., Harris, E., Gasche, R., Wei, J., Yu, L., Kiese, R., Eggleston, S., Butterbach-Bahl, K., Zeeman, M., Tuzson, B., Emmenegger, L., Six, J., Henne, S., and Mohn, J.: Attribution of N₂O sources in a grassland soil with laser spectroscopy based isotopocule analysis, *Biogeosciences*, 16, 3247–3266, <https://doi.org/10.5194/bg-16-3247-2019>, <https://www.biogeosciences.net/16/3247/2019/>, 2019.
- Institute, T. C.: Other Hazards, <https://www.chlorineinstitute.org/stewardship/chlorine/other-hazards/>, 2020.
- Ivanov, A. V., Trakhtenberg, S., Bertram, A. K., Gershenson, Y. M., and Molina, M. J.: OH, HO₂, and ozone gaseous diffusion coefficients, *The Journal of Physical Chemistry A*, 111, 1632–1637, 2007.
- Johnson, M. S., Nilsson, E. J., Svensson, E. A., and Langer, S.: Gas-phase advanced oxidation for effective, efficient in situ control of pollution, *Environmental science & technology*, 48, 8768–8776, 2014.
- Judeikis, H. S. and Wun, M.: Measurement of chlorine atom diffusion, *The Journal of Chemical Physics*, 68, 4123–4127, 1978.
- Kaiser, E.: Pressure dependence of the rate constants for the reactions methyl+ oxygen and methyl+ nitric oxide from 3 to 104 torr, *The Journal of Physical Chemistry*, 97, 11 681–11 688, 1993.
- Milchert, E., Goc, W., and Pelech, R.: Adsorption of CCl₄ from aqueous solution on activated carbons, *Adsorption Science & Technology*, 18, 823–837, 2000.
- Moore, J. H., Davis, C. C., Coplan, M. A., and Greer, S. C.: *Building scientific apparatus*, Cambridge University Press, 2009.

- Müller, R., Sankaran, S., Drouin, N., Vaagaasar, A.-L., Bekker, M. C., and Jain, K.: A theory framework for balancing vertical and horizontal leadership in projects, *International Journal of Project Management*, 36, 83–94, 2018.
- Nilsson, E. J. K., Eskebjerg, C., and Johnson, M. S.: A photochemical reactor for studies of atmospheric chemistry, *Atmospheric Environment*, 43, 3029–3033, 2009.
- NIOSH: Carbon tetrachloride, <https://www.cdc.gov/niosh/npg/npgd0107.html>, 2020.
- Pletcher, D. and Walsh, F. C.: *Industrial electrochemistry*, Springer Science & Business Media, 2012.
- Rigby, M., Montzka, S. A., Prinn, R. G., White, J. W. C., Young, D., O'Doherty, S., Lunt, M. F., Ganesan, A. L., Manning, A. J., Simmonds, P. G., Salameh, P. K., Harth, C. M., Mühle, J., Weiss, R. F., Fraser, P. J., Steele, L. P., Krummel, P. B., McCulloch, A., and Park, S.: Role of atmospheric oxidation in recent methane growth, *Proceedings of the National Academy of Sciences*, 114, 5373–5377, <https://doi.org/10.1073/pnas.1616426114>, <https://www.pnas.org/content/114/21/5373>, 2017.
- Ryu, S. K. and Choi, S. R.: Activated carbon fibers for the removal of chemical warfare simulants, in: *Journal of the Ceramic Society of Japan, Supplement Journal of the Ceramic Society of Japan, Supplement 112-1, PacRim5 Special Issue*, pp. S1539–S1542, The Ceramic Society of Japan, 2004.
- Seinfeld, J. H. and Pandis, S. N.: *Atmospheric chemistry and physics: from air pollution to climate change*, John Wiley & Sons, 2016.
- Wolf, B., Merbold, L., Decock, C., Tuzson, B., Harris, E., Six, J., Emmenegger, L., and Mohn, J.: First on-line isotopic characterization of N₂O above intensively managed grassland, *Biogeosciences*, 12, 2517–2531, <https://doi.org/10.5194/bg-12-2517-2015>, <https://www.biogeosciences.net/12/2517/2015/>, 2015.

Appendix

1. CFA Dye 3

1.1 Thermal and gravitational fractionation calculation

$$\begin{aligned}\delta^{15}N_{obs} &= \delta T_{N_2} + \delta G_{N_2} \\ \delta^{40}Ar_{obs} &= \delta T_{Ar} + \delta G_{Ar} \\ \delta^{40}Ar_{obs} &= 0.65\delta T_{N_2} + 4 \cdot \delta G_{N_2} \\ \delta T_{N_2} &= \frac{\delta^{40}Ar_{obs} - 4 \cdot \delta G_{N_2}}{0.65} \\ \delta^{15}N_{obs} &= \frac{\delta^{40}Ar_{obs} - 4 \cdot \delta G_{N_2}}{0.65} + \delta G_{N_2} \\ \delta G_{N_2} \left(\frac{0.65 - 4}{0.65} \right) &= \delta^{15}N_{obs} - \frac{\delta^{40}Ar_{obs}}{0.65} \\ \delta G_{N_2} &= \frac{\delta^{40}Ar_{obs} - 0.65 \cdot \delta^{15}N_{obs}}{3.35} \\ \delta^{15}N_{obs} &= \delta T_{N_2} + \delta G_{N_2} \\ \delta T_{N_2} &= \delta^{15}N_{obs} - \delta G_{N_2} \\ \delta T_{N_2} &= \delta^{15}N_{obs} - \frac{(\delta^{40}Ar_{obs} - 0.65 \cdot \delta^{15}N_{obs})}{3.35} \\ \delta T_{N_2} &= \frac{4 * \delta^{15}N_{obs} - \delta^{40}Ar_{obs}}{3.35}\end{aligned}$$

1.2 Main matlab script

```
%%Combining with Isotope data - David Soestmeyer (20/03/2020)
clc;
clear all;
close all;

[File1,Path1] = uigetfile('*..*','Choose depth vs time file');
filename1 = strcat(Path1,File1);
Depth = readtable(filename1);
[File2,Path2] = uigetfile('*..*','Choose isotope file');
filename2 = strcat(Path2,File2);
Isotope = readtable(filename2,'ReadVariableNames',true);
filename = '1816_daily_air_error_pine_test1.txt';

%%
ratios = [0.740092659    0.323380425 0.832759842 0.072    -4.200
6.531    0.015 0.141    0.388]; % Here the daily ratio, delta value
and uncertainty for the lab air is plotted, in the order 15N, 36Ar,
Ar/N2
ratio29std=ratios(1);
```

```

ratio36std=ratios(2);
ratio40std=ratios(3);
delta29std=ratios(4);
delta36std=ratios(5);
delta40std=ratios(6);
e_std29 = ratios(7);
e_std36 = ratios(8);
e_std40 = ratios(9);

time = Isotope.time(50:end);
int_28 = Isotope.int_28;
int_29 = Isotope.int_29;
int_32 = Isotope.int_32;
int_36 = Isotope.int_36;
int_40 = Isotope.int_40;
int_44 = Isotope.int_44;
breaks = Depth.breaks;
newbag = Depth.newbag;

data28 = int_28(50:end) - mean(int_28(15:28));
data29 = int_29(50:end) - mean(int_29(15:28));
data32 = int_32(50:end) - mean(int_32(15:28));
data36 = int_36(50:end) - mean(int_36(15:28));
data40 = int_40(50:end) - mean(int_40(15:28));
data44 = int_44(50:end) - mean(int_44(15:28));
%%
% drift correction 4th only
Dr=-1;
dt=0.706279;
for i = 1:length(data40)
    data40(i)=data40(i)-1/(Dr*(time(i)-dt));
end

%
%%
Delta = 100; %Defines how much difference between datapoints you
need
%before defining actual data, instead of backgroundnoise only

% finding the indexes for at what points data shifts to and from
standard
in = [];
dy = [];
l=0;
for i = 2:length(data28)
    if abs(data28(i)-data28(i-1)) > Delta
        l=l+1;
        dy(l) = abs(data28(i)-data28(i-1)); % Getting the values too,
just in case
        in(l) = i; % Getting the indexes
    end
end

```

```

end
% Defining std and actual measurements

for i = 1:length(in)-1
ms2{i} = data28(in(i)+1:in(i+1));
end

ms28 = data28(in(1)+1:in(end));
ms29 = data29(in(1)+1:in(end));
ms36 = data36(in(1)+1:in(end));
ms40 = data40(in(1)+1:in(end));

std128 = data28(1:in(1));
std129 = data29(1:in(1));
std136 = data36(1:in(1));
std140 = data40(1:in(1));

std228 = data28(in(end):end);
std229 = data29(in(end):end);
std236 = data36(in(end):end);
std240 = data40(in(end) : end);

%% working std means

stdmean28 = (mean(std128) + mean (std228))/2;
stdmean40 = (mean(std140) + mean (std240))/2;

%% fitting for the std over time
fity28 = [mean(std128),mean(std228)];
fity29 = [mean(std129),mean(std229)];
fity36 = [mean(std136),mean(std236)];
fity40 = [mean(std140),mean(std240)];

fitx = [mean(linspace(1,in(1),in(1))),
mean(linspace(1,in(end),length(data28)))];

fit28 = fit(fitx',fity28','poly1'); % making a fit
fit29 = fit(fitx',fity29','poly1');
fit36 = fit(fitx',fity36','poly1');
fit40 = fit(fitx',fity40','poly1');

%%
precal_n15=(fity29(1)/fity28(1)/ratio29std-1)*1000;
postcal_n15=(fity29(2)/fity28(2)/ratio29std-1)*1000;

precal_ar36=(fity36(1)/fity40(1)/ratio36std-1)*1000;
postcal_ar36=(fity36(2)/fity40(2)/ratio36std-1)*1000;

precal_ar40=(fity40(1)/fity28(1)/ratio40std-1)*1000;
postcal_ar40=(fity40(2)/fity28(2)/ratio40std-1)*1000;

disp(precal_n15);
disp(postcal_n15);
disp(precal_ar36);
disp(postcal_ar36);
disp(precal_ar40);

```

```

disp(postcal_ar40);

% making a fit
%figure
%plot(fit1) % plotting to see it
a28 = fit28(1); % defining coefficients
b28 = fit28(2);

a29 = fit29(1);
b29 = fit29(2);

% a36 = fit36(1);
% b36 = fit36(2);
%
% a40 = fit40(1);
% b40 = fit40(2);
%
for m = 1:length(data28)

    data28(m) = data28(m)-(fit28(m)-fit28(mean(fitx)));
    data29(m) = data29(m)-(fit29(m)-fit29(mean(fitx)));
    % data36(m) = data36(m)-(fit36(m)-fit36(mean(fitx)));
    % data40(m) = data40(m)-(fit40(m)-fit40(mean(fitx)));
end
%%
D = Depth.mh_delay;
infmt = 'mm:ss.S';
mh_delay = duration(D, 'InputFormat', infmt);

%%
ms_delay = duration(00,02,18);

C_time11 = Depth.MHtime + ms_delay + mh_delay;
C_time22 = char(C_time11);
C_time111 = datetime(C_time22, 'InputFormat', 'HH:mm:ss');
C_time111.Format = 'HH:mm:ss.S';

for j = 1:length(C_time111)
    C_date111(j) = datetime(2019,10,31); %choose date of sample run!
end
C_date111 = C_date111';

CDT = C_date111 + timeofday(C_time111);
CDT.Format = 'HH:mm:ss.S';
CnewDT = dateshift(CDT, 'start', 'second', 'nearest');

ms_time = datetime(time, 'ConvertFrom', 'excel');
ms_time.Format = 'HH:mm:ss.S';
for i = 1:length(ms_time)
    ms_date(i) = datetime(2019,10,31); %choose date of sample run!
end

ms_date = ms_date';
IDT = ms_date + timeofday(ms_time);
IDT.Format = 'HH:mm:ss.S';

```

```

InewDT = dateshift(IDT, 'start', 'second', 'nearest');

%%
[LiA, LocB] = ismember(CnewDT, InewDT);

%%
depth = Depth.depthfinal;
methane = Depth.ch4final;
gaspercent = Depth.gascentmm;
timemh = Depth.MHtime;
timems = zeros(length(depth), 1);
iso_28 = zeros(length(depth), 1);
iso_29 = zeros(length(depth), 1);
iso_32 = zeros(length(depth), 1);
iso_36 = zeros(length(depth), 1);
iso_40 = zeros(length(depth), 1);
iso_44 = zeros(length(depth), 1);

for m = 1:length(depth)
    if LiA(m) > 0
        id(m) = LocB(m); %Finds index where Picarro time matches
        timems(m) = Isotope.time(id(m)); %Sets to value at that
index
        iso_28(m) = data28(id(m)); %Sets to value at that index
        iso_29(m) = data29(id(m));
        iso_32(m) = data32(id(m)); %Sets to value at that index
        iso_36(m) = data36(id(m));
        iso_40(m) = data40(id(m));
        iso_44(m) = data44(id(m));
    else
        timems(m) = timems(m-1);
        iso_28(m) = NaN; %Sets to NaN where times don't match
        iso_29(m) = NaN;
        iso_32(m) = NaN;
        iso_36(m) = NaN;
        iso_40(m) = NaN;
        iso_44(m) = NaN;
    end
end

%Removing data where depth is NaN (field end depth correction)
tfnan = isnan(depth);

for k = 1:length(depth)
    if tfnan(k) == 1
        timems(k) = timems(k-1);
        iso_28(k) = NaN; %Sets to NaN where times don't match
        iso_29(k) = NaN;
        iso_32(k) = NaN;
        iso_36(k) = NaN;
        iso_40(k) = NaN;
        iso_44(k) = NaN;
    end
end

%%

```

```

funccalc =
findRatioError(iso_28,iso_29,iso_36,iso_40,ratio29std,ratio36std,ra
tio40std,e_std29,e_std36,e_std40);

dms29 = funccalc(:,1); %corrected for pressure and chemical slope
dms36 = funccalc(:,2);
dms40 = funccalc(:,3);
e_dms29 = funccalc(:,4); %error of mass spec corrected values
e_dms36 = funccalc(:,5);
e_dms40 = funccalc(:,6);

delta29 = zeros(length(iso_28),1);
delta36 = zeros(length(iso_28),1);
delta40 = zeros(length(iso_28),1);

e_d29 = zeros(length(iso_28),1); % errors for the deltas
e_d36 = zeros(length(iso_28),1);
e_d40 = zeros(length(iso_28),1);

tfnan = isnan(iso_28);
for k = 1:length(iso_28)
    if tfnan(k) == 1
        delta29(k) = NaN;
        delta36(k) = NaN;
        delta40(k) = NaN;
        e_d29(k) = NaN;
        e_d36(k) = NaN;
        e_d40(k) = NaN;
    elseif tfnan(k) == 0
        delta29(k) = ((dms29(k)/1000+1)*(delta29std/1000+1)-1)*1000;
        delta40(k) = ((dms40(k)/1000+1)*(delta40std/1000+1)-1)*1000;
        delta36(k) = ((dms36(k)/1000+1)*(delta36std/1000+1)-1)*1000;

        e_d29(k) =
(((delta29std/1000+1)*e_dms29(k))^2+((dms29(k)/1000+1)*e_std29)^2)^0
.5;
        e_d36(k) =
(((delta36std/1000+1)*e_dms36(k))^2+((dms36(k)/1000+1)*e_std36)^2)^0
.5;
        e_d40(k) =
(((delta40std/1000+1)*e_dms40(k))^2+((dms40(k)/1000+1)*e_std40)^2)^0
.5;
    end
end
%%
gp=smooth(gaspercent,69);
e_gp = zeros(length(iso_28),1);
% E_gas= zeros(69,1);

for i = 69:(length(iso_28))
    E_gas = gaspercent(i-68:i);
    e_gp(i) = std(E_gas);
end

%%

```

```

funcalc =
setupcorrectionerror(delta29,delta36,delta40,gp,e_d29,e_d36,e_d40,e_
gp);

dsc29 = funcalc(:,1); %sample only pressure imbalance corrected
dsc36 = funcalc(:,2);
dsc40 = funcalc(:,3);

e_dsc29 = funcalc(:,4); %sample only pressure imbalance corrected
e_dsc36 = funcalc(:,5);
e_dsc40 = funcalc(:,6);

%%
IsoData =
table(depth,timemh,timems,methane,breaks,newbag,iso_28,iso_29,iso_32
,iso_36,iso_40,iso_44,dsc29,dsc36,dsc40,e_dsc29,e_dsc36,e_dsc40,gasp
ercent); % gascentmm);
writetable(IsoData,filename,'Delimiter',' '); %Saves as a text file

```

1.3 Matlab script for applying pressure imbalance and chemical slope corrections.

```
function ans
=findRatioNerror(data28,data29,data36,data40,ratio29std,ratio36std,r
atio40std,e_std29,e_std36,e_std40)

e_28 = 14.49; % uncertainty of the intensity as found on the of
31st 15:00-15:46
e_29 = 10.66; % uncertainty of the intensity as found on the of
31st 15:00-15:46
e_36 = 3.797; % uncertainty of the intensity as found on the of
31st 15:00-15:46
e_40 = 12.11; % uncertainty of the intensity as found on the of
31st 15:00-15:46

p29 = 1.046*10^-4; % constants for pressure imbalance correction
p36 = 6.76*10^-4;
p40 = 5.587E-04;

e_p29 = 2.07E-05; % errors for pressure imbalance correction
e_p36 = 1.55E-05;
e_p40 = 5.53E-05;

a = -1.78E-02; % constants for the chemical slope correction for
a function a*d^3+b*d^2+c*d
b = 9.59E-06;
%c = -0.016562565;

a_n15 = 4.97186E-05; % constants for the chemical slope
correction for a function a*d^3+b*d^2+c*d

e_a_n15= 3.03572E-06;

e_a = 4.5E-04; % error of the chemical slope constants
e_b = 1.4E-06;
%e_c = 0.000201539;

e_off28= e_28*2^0.5; % error of the offset
e_off40= e_40*2^0.5;

ratio29 = zeros(length(data28),1);
ratio36 = zeros(length(data28),1);
ratio40 = zeros(length(data28),1);

deltap29 = zeros(length(data28),1);
deltac29 = zeros(length(data28),1);
deltap36 = zeros(length(data28),1);
deltap40 = zeros(length(data28),1);
deltac36 = zeros(length(data28),1);

e_r29= zeros(length(data28),1); % error of the ratios
e_r36= zeros(length(data28),1);
e_r40= zeros(length(data28),1);

e_dp29 = zeros(length(data28),1); % error of delta p 29
```

```

e_dc29 = zeros(length(data28),1); % error of delta c 36
e_dp36 = zeros(length(data28),1); % error of delta p
e_dp40 = zeros(length(data28),1); % error of delta p
e_dc36 = zeros(length(data28),1); % error of delta c 36

%% defining ratio
tfnan = isnan(data28);
for k = 1:length(data28)
    if tfnan(k) == 1
        ratio29(k) = NaN;
        ratio36(k) = NaN;
        ratio40(k) = NaN;
        deltap29(k) = NaN;
        deltap36(k) = NaN;
        deltap40(k) = NaN;
        deltac36(k) = NaN;
        deltac29(k) = NaN;

        e_r29(k) = NaN;
        e_r36(k) = NaN;
        e_r40(k) = NaN;
        e_dp29(k) = NaN;
        e_dp36(k) = NaN;
        e_dp40(k) = NaN;
        e_dc36(k) = NaN;
        e_dc29(k) = NaN;

    elseif tfnan(k) == 0
        ratio29(k) = data29(k)./data28(k);
        ratio36(k) = data36(k)./data40(k);
        ratio40(k) = data40(k)./data28(k);

        e_r29(k) =
            ((1/data28(k)*e_29)^2+(data29(k)./data28(k)^2*e_28)^2)^0.5;
        e_r36(k) =
            ((1/data40(k)*e_36)^2+(data36(k)./data40(k)^2*e_40)^2)^0.5;
        e_r40(k) =
            ((1/data28(k)*e_40)^2+(data40(k)./data28(k)^2*e_28)^2)^0.5;

        deltap29(k) = ((ratio29(k)./ratio29std)-1)*1000-
            p29*(data28(k)-10500);
        deltap36(k) = ((ratio36(k)./ratio36std)-1)*1000-
            p36*(data40(k)-8900);
        deltap40(k) = ((ratio40(k)./ratio40std)-1)*1000-
            p40*(data40(k)-10500);
        deltac36(k) = deltap36(k)-(a*deltap40(k)+b*deltap40(k).^2);
        deltac29(k) = deltap29(k)-(a_n15*deltap40(k));

        e_dp29(k) =
            ((1/ratio29std*e_r29(k))^2+(ratio29(k)./ratio29std^2*e_std29')^2+(p2
            9*e_off28)^2+((data28(k)-10500)*e_p29)^2)^0.5;
        e_dp36(k) =
            ((1/ratio36std*e_r36(k))^2+(ratio36(k)./ratio36std^2*e_std36')^2+(p3
            6*e_off40)^2+((data40(k)-8900)*e_p36)^2)^0.5;

```

```

        e_dp40(k) =
        ((1/ratio40std*e_r40(k))^2+(ratio40(k)./ratio40std^2*e_std40')^2+(p4
0*e_off40)^2+((data40(k)-10500)*e_p40)^2)^0.5;
        e_dc29(k) =
        ((e_dp29(k))^2+(a_n15*e_dp40(k))^2+(deltap40(k)*e_a_n15)^2)^0.5;
        e_dc36(k) =
        ((e_dp36(k))^2+((a+2*b*deltap40(k))*e_dp40(k))^2+(deltap40(k)*e_a)^2
+(deltap40(k).^2*e_b)^2)^0.5;
    end
end

%% ans
ans(:,1) = deltac29;
ans(:,2) = deltac36;
ans(:,3) = deltap40;
ans(:,4) = e_dc29;
ans(:,5) = e_dc36;
ans(:,6) = e_dp40;
end

```

1.4 Matlab script for applying the solubility effect corrections.

```

function ans = setupcorrectionerror
(d29,d36,d40,gaspercent,e_29,e_36,e_40,e_gp)

sc29 = 5.846*10^-3;
sc36 = -0.2997;
sc40 = 27.337;

e_sc29 = 3.16*10^-3;
e_sc36 = 3.45*10^-2;
e_sc40 = 2.45;

%%
dc29 = zeros(length(d29),1); %+0.1  these are the values
we added from the difference between the oven valve and
the needlevalve
dc36 = zeros(length(d29),1);      %+5.96  I am of the
opinion they should not be subtracted from the values.
dc40 = zeros(length(d29),1);      %+3.8

e_dc29 = zeros(length(d29),1);
e_dc36 = zeros(length(d29),1);
e_dc40 = zeros(length(d29),1);

%%
tfnan = isnan(d29);

```

```

for k = 1:length(d29)
    if tfnan(k) == 1
        dc29(k) = NaN;
        dc36(k) = NaN;
        dc40(k) = NaN;
        e_dc29(k) = NaN;
        e_dc36(k) = NaN;
        e_dc40(k) = NaN;
    elseif tfnan(k) == 0
        dc29(k) = d29(k)-sc29*log(gaspercent(k)); %+0.1
these are the values we added from the difference between
the oven valve and the needlevalve
        dc36(k) = d36(k)-sc36*log(gaspercent(k));
%+5.96 I am of the opinion they should not be
substracted from the values.
        dc40(k) = d40(k)-sc40*log(gaspercent(k));
        e_dc29(k) =
(e_29(k)^2+(sc29/gaspercent(k)*e_gp(k))^2+(log(gaspercent
(k))*e_sc29)^2)^0.5;
        e_dc36(k) =
(e_36(k)^2+(sc36/gaspercent(k)*e_gp(k))^2+(log(gaspercent
(k))*e_sc36)^2)^0.5;
        e_dc40(k) =
(e_40(k)^2+(sc36/gaspercent(k)*e_gp(k))^2+(log(gaspercent
(k))*e_sc40)^2)^0.5; %
    end
end
%% ans
ans(:,1) = dc29;
ans(:,2) = dc36;
ans(:,3) = dc40;
ans(:,4) = e_dc29;
ans(:,5) = e_dc36;
ans(:,6) = e_dc40;
end

```

1.5 Pressure imbalance

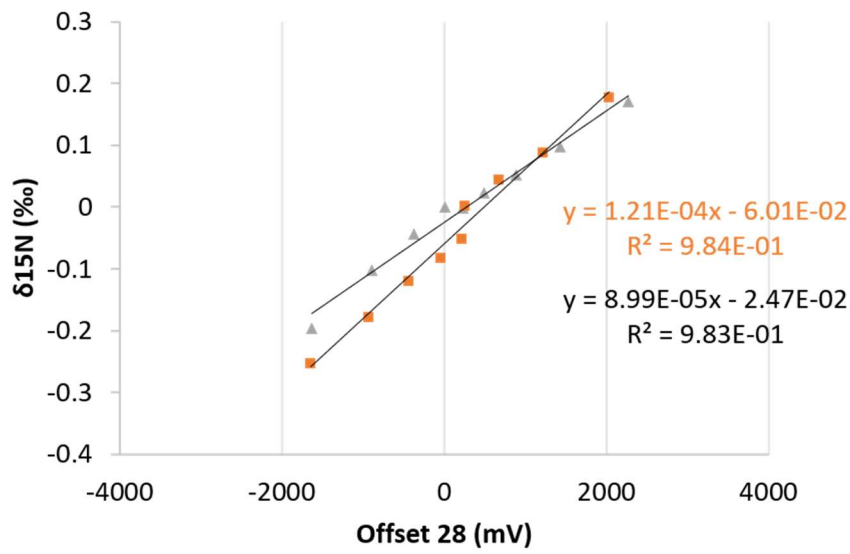


Figure 36: Pressure imbalance plot 15N. Resulting offset vs int28-10500mV.

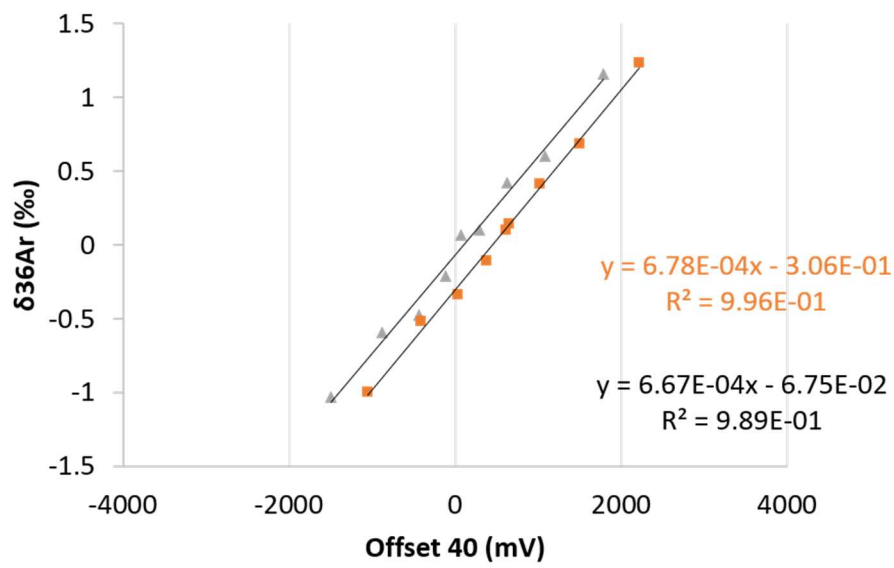


Figure 37: Pressure imbalance plot for 36Ar. Resulting offset vs int40-8900mV

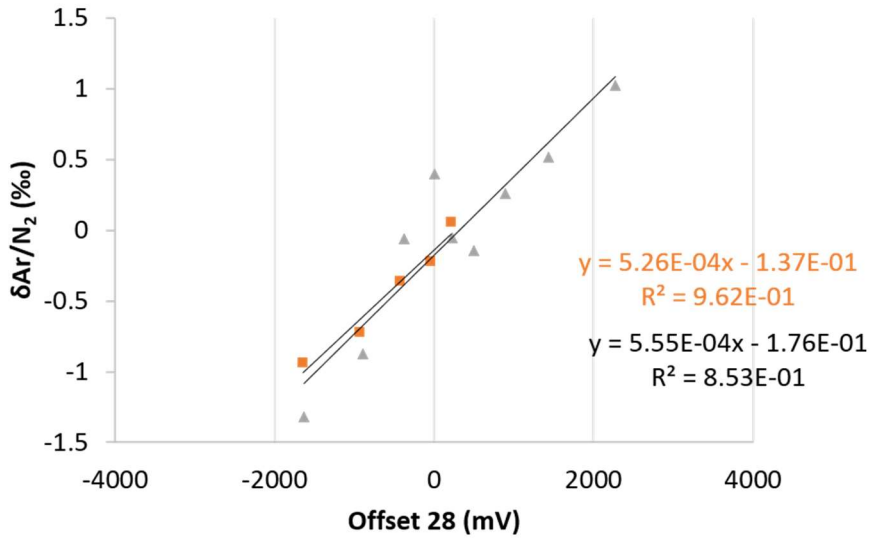


Figure 38: Pressure imbalance plot for $\delta Ar/N_2$ in ‰. Resulting offset vs int28-10500mV.

1.6 Chemical slope assessment data

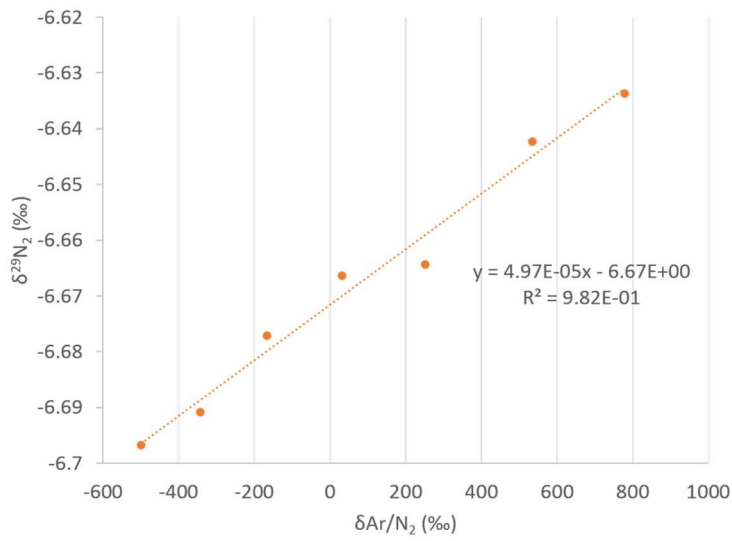


Figure 39: Chemical slope effect for $\delta^{29}N_2$ in ‰, plotted against $\delta Ar/N_2$ in ‰.

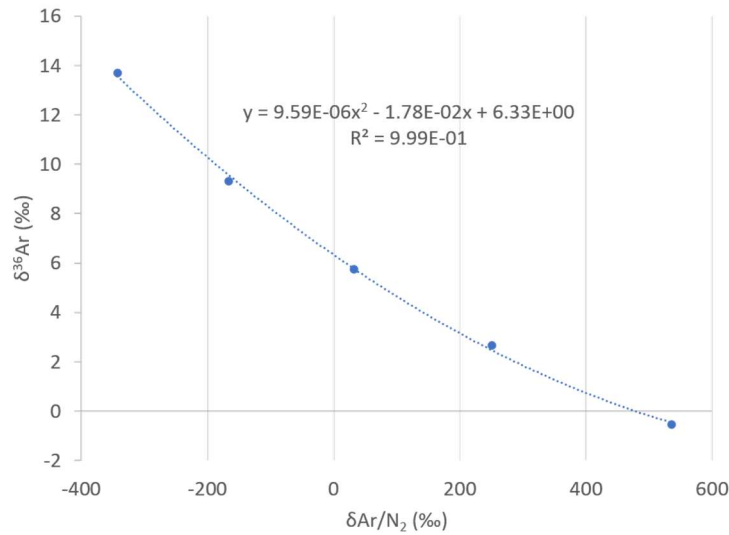


Figure 40: Chemical slope effect for $\delta^{36}\text{Ar}$ in ‰, plotted against $\delta\text{Ar}/\text{N}_2$ in ‰.

1.7 Dynamically mixed standard reconnected for full system effect determination.

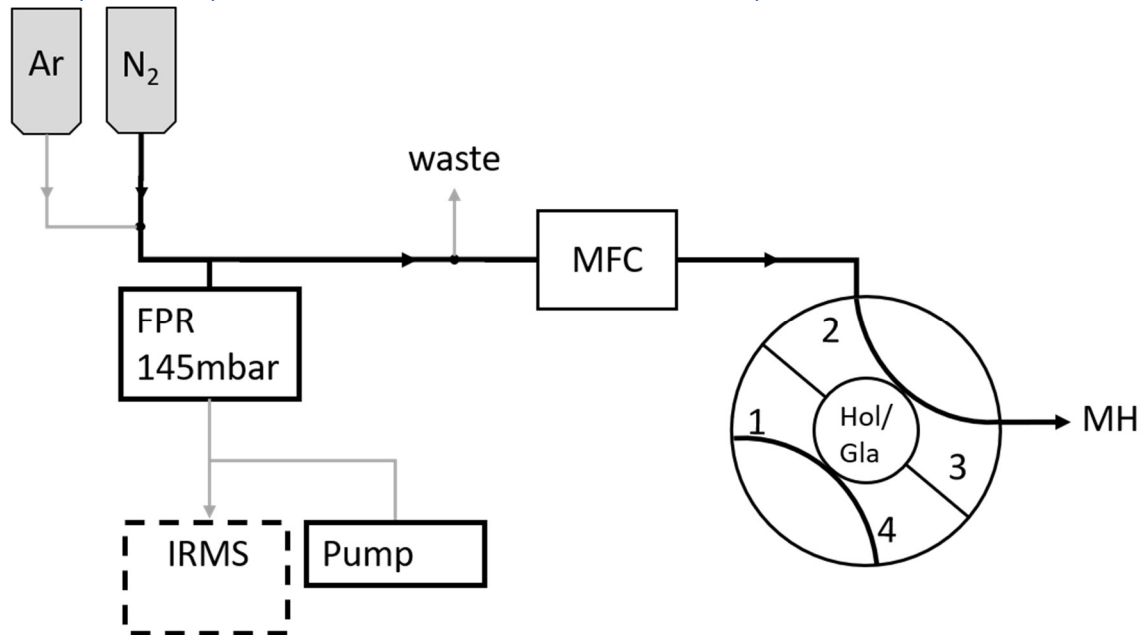


Figure 41: Cut out of the altered section for the solubility experiments setup. The line going to waste was a capillary offering enough resistance to create over pressure on the other side, driving the gas through the MFC. This over pressure created a bit of a problem, as the flow of argon was dependent on the pressure on the mixing side. Between each set-point at the MFC which would alter the resulting pressure, the argon pressure had to be reset to get the proper levels of the elemental ratio again. MH in this context refers to the full system, including the introduction of the gas into a liquid flow.

1.8 Error propagation for $\delta^{29}\text{N}_2$

$$\sigma(r_{29}) = \sqrt{\left(\frac{1}{int28} \cdot \sigma(int29)\right)^2 + \left(\frac{int29}{int28^2} \cdot \sigma(int28)\right)^2} \quad (1)$$

$$\sigma(\partial^{29}N_{P.cor}) = \sqrt{\left(\frac{1}{r_{29STD}} \cdot \sigma(r_{29})\right)^2 + \left(\frac{r_{29}}{r_{29STD}^2} \cdot \sigma(r_{29STD})\right)^2 + (P_{29} \cdot \sigma(int28))^2 + ((int28 - 10500mV) \cdot \sigma(P_{29}))^2} \quad (2)$$

$$\sigma(\partial^{29}N_{MS.cor}) = \sqrt{\sigma(\partial^{29}N_{P.cor})^2 + \left(\partial \frac{Ar}{N_{2MS.cor}} \cdot \sigma(a_{29})\right)^2 + \left(a_{29} \cdot \sigma\left(\partial \frac{Ar}{N_{2MS.cor}}\right)\right)^2} \quad (3)$$

$$\sigma(\partial^{29}N_{air.cor}) = \sqrt{\left((\partial^{29}N_{D.air} + 1) \cdot \sigma(\partial^{29}N_{MS.cor})\right)^2 + \left((\partial^{29}N_{MS.cor} + 1) \cdot \sigma(\partial^{29}N_{D.air})\right)^2} \quad (4)$$

$$\sigma(\partial^{29}N_{cor}) = \sqrt{\left(1 \cdot \sigma(\partial^{29}N_{air.cor})\right)^2 + \left(\frac{S_{29}}{G\%} \cdot \sigma(G\%)\right)^2 + \left(\ln(G\%) \cdot \sigma(S_{29})\right)^2} \quad (5)$$

$$\sigma(\partial^{29}N(x)_{smo}) = \sqrt{\sigma(\partial^{29}N(x)_{cor})^2 + \frac{1}{29} \cdot \sum_{i=x-1}^{x+14} (\partial^{29}N(i)_{cor} - \overline{\partial^{29}N_{cor}})^2} \quad (6)$$

1.9 Error propagation of $\delta^{40}\text{Ar}$

$$\sigma(r_{36}) = \sqrt{\left(\frac{1}{int40} \cdot \sigma(int36)\right)^2 + \left(\frac{int36}{int40^2} \cdot \sigma(int40)\right)^2} \quad (1)$$

$$\sigma(\partial^{36}Ar_{P.cor}) = \sqrt{\left(\frac{1}{r_{36STD}} \cdot \sigma(r_{36})\right)^2 + \left(\frac{r_{36}}{r_{36STD}^2} \cdot \sigma(r_{36STD})\right)^2 + (P_{36} \cdot \sigma(int40))^2 + ((int40 - 8900mV) \cdot \sigma(P_{36}))^2} \quad (2)$$

$$\sigma(\partial^{36}Ar_{MS.cor}) = \sqrt{\sigma(\partial^{36}Ar_{P.cor})^2 + \left((2b_{36} \cdot \delta 40 + a_{36}) \cdot \sigma(\partial^{40}Ar/N_{2MS.cor})\right)^2 + (\delta 40^2 \cdot \sigma(b_{36}))^2 + (\delta 40 \cdot \sigma(a_{36}))^2} \quad (3)$$

$$\sigma(\partial^{36}Ar_{air.cor}) = \sqrt{\left((\partial^{36}Ar_{D.air} + 1) \cdot \sigma(\partial^{36}Ar_{MS.cor})\right)^2 + \left((\partial^{36}Ar_{MS.cor} + 1) \cdot \sigma(\partial^{36}Ar_{D.air})\right)^2} \quad (4)$$

$$\sigma(\partial^{36}Ar_{cor}) = \sqrt{\left(1 \cdot \sigma(\partial^{36}Ar_{air.cor})\right)^2 + \left(\frac{S_{36}}{G\%} \cdot \sigma(G\%)\right)^2 + \left(\ln(G\%) \cdot \sigma(S_{36})\right)^2} \quad (5)$$

$$\sigma(\partial^{36}Ar(x)_{smooth}) = \sqrt{\sigma(\partial^{36}Ar(x)_{cor})^2 + \frac{1}{36} \cdot \sum_{i=x-1}^{x+14} (\partial^{36}Ar(i)_{cor} - \overline{\partial^{36}Ar_{cor}})^2} \quad (6)$$

$$\sigma(\partial^{40} Ar(x)_{smoot}) = \frac{\sigma(\partial^{36} Ar(x)_{smooth})}{(\partial^{36} Ar_{smooth} + 1)^2} \quad (7)$$

1.10 Error propagation for $\delta Ar/N_2$

$$\sigma(r_{Ar/N_2}) = \sqrt{\left(\frac{1}{int28} \cdot \sigma(int40)\right)^2 + \left(\frac{int40}{int28^2} \cdot \sigma(int28)\right)^2} \quad (1)$$

$$\sigma(\partial Ar/N_{2MS.cor}) = \sqrt{\left(\frac{1}{\frac{r_{Ar}}{N_2 STD}} \cdot \sigma(r_{Ar/N_2})\right)^2 + \left(\frac{\frac{r_{Ar}}{N_2}}{r^2 \frac{Ar}{N_2 STD}} \cdot \sigma\left(\frac{r_{Ar}}{N_2 STD}\right)\right)^2 + \left(\frac{P_{Ar}}{N_2} \cdot \sigma(int28)\right)^2 + \left((int28 - 10500mV) \cdot \sigma(P_{Ar/N_2})\right)^2} \quad (2)$$

$$\sigma(\partial Ar/N_{2air.cor}) = \sqrt{\left((\partial Ar/N_{2D.air} + 1) \cdot \sigma(\partial Ar/N_{2MS.cor})\right)^2 + \left((\partial Ar/N_{2MS.cor} + 1) \cdot \sigma(\partial Ar/N_{2D.air})\right)^2} \quad (3)$$

$$\sigma(\partial Ar/N_{2cor}) = \sqrt{\left(1 \cdot \sigma(\partial Ar/N_{2air.cor})\right)^2 + \left(\frac{S_{29}}{G\%} \cdot \sigma(G\%)\right)^2 + \left(\ln(G\%) \cdot \sigma(S_{29})\right)^2} \quad (4)$$

$$\sigma(\partial Ar/N_2(x)_{smoot}) = \sqrt{\sigma(\partial Ar/N_2(x)_{cor})^2 + \frac{1}{29} \cdot \sum_{i=x-1}^{x+14} (\partial Ar/N_2(i)_{cor} - \partial Ar/N_2_{cor})^2} \quad (5)$$

3. Chlorine induced methane oxidation

Appendix A: Preliminary experiments

A1 Electrochemical device setup A - Initial setup

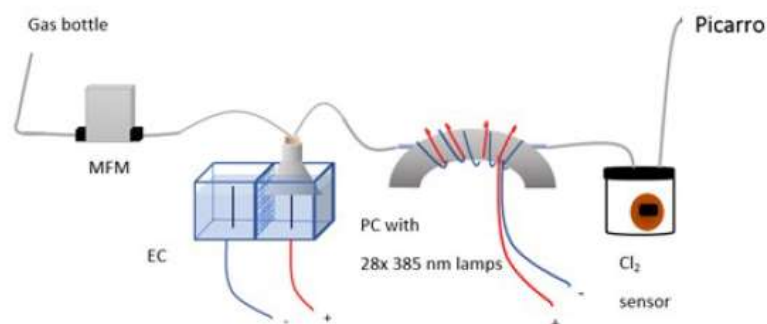
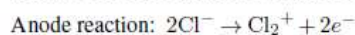
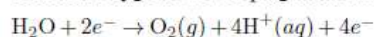


Figure A1. Experimental setup for Initial setup. Gas bottle: Ambient air sample, MFM: mass flow meter, EC: electrolytic device, PC: photochemical device.

The flow goes into the electrolytic device, which is built from a polycarbonate box. A Nafion membrane ,Chemours, Nafion N234, is installed to generate two cells with the same volume. Two holes were drilled at the bottom of the cell to install the electrode. The cell consists of two different solutions of NaCl in milli-Q water. The average concentration of NaCl is 1.3 M at the anodic site and 0.13 M at the cathodic site. The electrodes are carbon electrodes with a diameter of 2 mm and a length of 10 cm. The electrolysis is for the synthesis of Cl₂ in situ which is inspired by the chlor-alkali industry but is here on a smaller laboratory fit scale. The electric field applied to the system force the negative ions of the electrolyte to be attached to the positive electrode (anode) of the cell to which the electrons will be transferred. The positive ions will be attached to the negative electrode (cathode) of the EC from which they will receive the electrons by reduction.(Pletcher and Walsh (2012)9



The OH⁻ produced on the cathode side turns the solution basic, and on the anode side the solution is turned acidic. The presence of the membrane is essential due to its selectivity to cations. The membrane allows Na⁺ ions move from the anode to the cathode and form NaOH. If the membrane was not present the NaOH would encounter Cl₂ and form hypochlorite bleaches. Oxygen is developing in the anodic site as well;



The concentration of the two sides vary to prevent oxygen production.(Pletcher and Walsh (2012)).The following equilibrium is avoided by increasing the acidity of the solution and thereby shifting the equilibrium to the left side of the reaction equation and therefore avoiding the absorption of the chlorine into the water phase. This process is not instant, and the system, therefore, needs time to adjust.

$\text{Cl}_2(g) + \text{H}_2\text{O} \rightarrow \text{HCl}(aq) + \text{HOCl}(aq)$ The PC is made from PVC plastic. 30 holes were drilled into the chamber, two holes for the 4 mm in diameter and 20 cm in length quartz tube and 28 holes for the LED (385 nm), UV LED LAMP-VAOL-5EUV8T4, diodes. The holes were drilled in order to ensure most of the quartz tube is covered by the light. The LED diodes run in a parallel circuit with a forward voltage and forward current (Current move from positive to negative). The max current is 20 mA for each LED, and the max voltage is 3.6 V. The same voltage runs through the LED and the current is multiplied by the number of lamps which result in 0.480 A. The CRDS used in the experiments is Picarro G1301 with cavity pressure at 140 Torr, DAS temperature of 30.2 °C and cavity temperature of 45°C. The gas bottle used for all the Cl-initiated methane experiments has an ambient air combined with more stable concentrations of the investigated gases CH₄(1.98 ppm), CO₂ (376.1 ppm) and H₂O (1.17473% v). In the illustration it is followed by the mass flow meter (MFM), which has an average flow of around 9 ml/min, and the Picarro has an average suction of approximately 10 ml/min. The Cl₂ sensor used in all experiments is the PG610-CL2 model, Chlorine Cl₂ Gas Detector Gas Sound Light Vibration Alarm. The Cl₂ sensor is an electrochemical sensor, which targets the chlorine. Cl₂ interacts with an electrolyte causing electrochemical reactions producing a current. There is a correlation between the current and concentration of the target gas, chlorine, which is measured. The volume of the sensor is 141.12 ml (98mm x 60mm x 24mm). The sensor measures chlorine concentrations from 1-20 ppm. The sensor is placed in a 600 ml glass bottle. Three lines were marked on the funnel; lower and upper black lines describing the upper and lower limit of the water level. When the water level was lower than the lower line the Cl₂ will deposit at the surface, and when it was above the upper black line water will be sucked up into the gas stream and damage the system. In between these lines, a red line was marked, which indicates the desired water level for the optimal Cl₂ concentration. The laboratory tripod holding the funnel was marked as well. The flow from the MFM is called the Flow(in) and should on average be 9.7 ml/min and the flow from the Picarro is called the Flow(out) and should be 10.5 ml/min. For the optimal Cl₂ production the difference between the flows should be $0.8\text{ml}/\text{min} \pm 0.1\text{ml}/\text{min}$

The procedure for the system is as follows:

- Make two solutions, one for the anode side and one for the cathode side
- Let the system stabilize (Stable methane concentrations)
- Turn on the electrochemical device.
- Let the Cl₂ concentration stabilize
- Turn on the photochemical device
- Let the system stabilize to ensure a stable removal efficiency.
- Turn off the light.
- Let the system stabilize to the initial methane concentration before the light was on

A2 Electrochemical device setup B1 - Tenax tube experiments

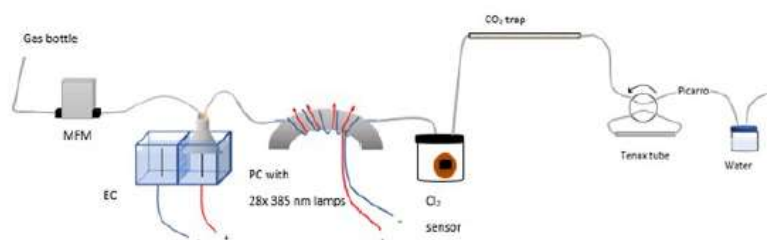


Figure A2. Experimental setup B1 for Tenax tube experiments. With inclusion of CO_2 trap and tenax trap for GC measurements. Gas bottle: Ambient air sample, MFM: mass flow meter, EC: electrochemical device, PC: photochemical device

The initial Picarro measurements are complimented with TD-GCMS measurements to investigate other compounds present in the system. A chemical trap is added to the system as well. The goal of the trap is to trap the CO_2 . The chemical trap consists of magnesium perchlorate to trap the water at the beginning and at the end. NaOH is placed in the middle to mineralize CO_2 and thereby trap it. The trap is also shown to be effective at trapping Cl_2 and H_2O . Before the flow reaches the Picarro it has to go through a Tenax tube. The gas stream usually goes directly into the Picarro, but by changing the flow direction, it will go through the tube first as seen in Figure A2. The procedure for the system is as follows:

- Make two solutions, one for the anode side and one for the cathode side
- Let the system stabilize (Stable methane concentrations)
- Turn on the electrochemical device.
- 10 min measurement with Tenax tube
- Let the Cl_2 concentration stabilize
- Turn on the photochemical device
- 10 min measurement (or multiple) with Tenax tube
- Let the system stabilize to ensure a stable removal efficiency.
- Turn off the light.
- Let the system stabilize to the initial methane concentration before the light was on

A3 Electrochemical device setup B2 - Tenax tube experiments

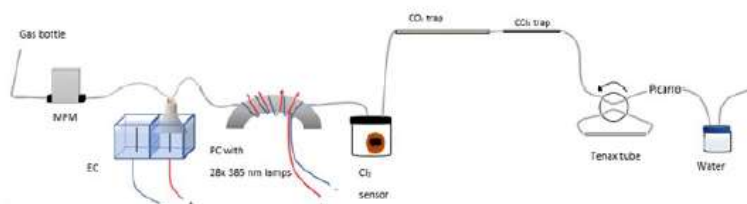


Figure A3. Experimental setup B2 for Initial setup, with inclusion of CO trap in the form of activated carbon. Gas bottle: Ambient air sample, MFM: mass flow meter, EC: electrolytic device, PC: photochemical device.

The setup follows the same procedure as the previous setup, but with the goal of trapping CCl_4 with the activated carbon trap. The goal of the experiment was also to maintain the same current at 0.05 A through the whole experiment, and the chlorine production is noted every 30 s until it reaches the fixed concentration of 20 ppm, then the light is turned on. The surface of the electrodes was scrubbed due to some salt formation on them. The same procedure described in “Electrochemical device setup B2 - Tenax tube experiments” is followed.

A4 Electrochemical device setup C1 - High pressure xenon lamp experiments

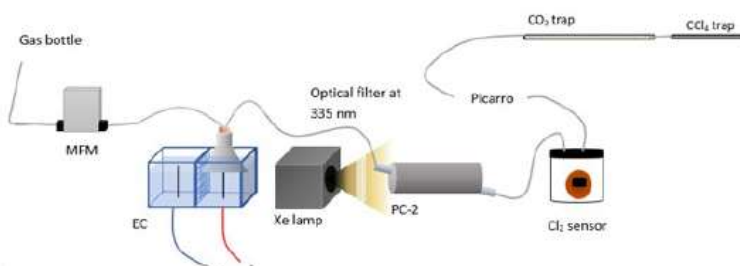


Figure A4. Experimental setup C1 for High pressure xenon lamp. Gas bottle: Ambient air sample, MFM: mass flow meter, EC: electrolytic device, PC2: second photochemical device.

A high-pressure Xenon lamp, ILC technology R100-IB, is utilized. The Xenon lamp lights up the new Photolyze Chamber (PC-2), where an 8 mm in diameter and 20 cm in length quartz tube is placed through the cylinder diagonally to ensure more of the quartz tube is getting hit by the light. The inner surface of the cylinder is covered with aluminum foil to reflect the light coming in. The Xenon lamp emits light in wavelengths from vacuum UV (200nm) to infrared (Moore et al. (2009), therefore an optical filter is needed to ensure that the wanted wavelength is emitted. The optical filter used is a 335 nm filter, and this is the cross section for chlorine dissociation which is eight times larger compared to 385 nm emitted by the LEDs. The outlet of

PC-2 the gas travels to the chlorine sensor chamber followed by the Picarro. Lastly at the Picarro outlet the two traps are used for trapping the gases tetrachloromethane, hydrochloric acid, chlorine gas, and carbon dioxide. The procedure for the system is as follows:

- Make two solutions, one for the anode side and one for the cathode side
- Let the system stabilize (Stable methane concentrations)
- Turn on the electrochemical device.
- Let the Cl_2 concentration stabilize
- Turn on the high pressure xenon lamp
- Let the system stabilize to ensure a stable removal efficiency.
- Turn off the lamp
- Let the system stabilize to the initial methane concentration before the lamp was on

A5 Electrochemical device setup C2 - High pressure xenon lamp experiments

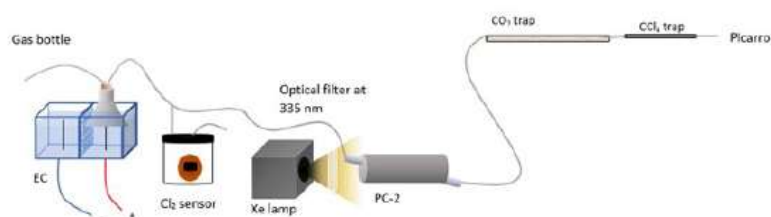


Figure A5. Experimental setup C2 for High pressure xenon lamp. The system is now run with over-pressure at the gas supply, venting by the Cl_2 sensor. Gas bottle: Ambient air sample, MFM: mass flow meter, EC: electrolytic device, PC2: second photochemical device.

The Cl_2 concentration is diluted to obtain the values above the fixed value of 20 ppm. Firstly, the metal tubes before the traps were replaced with a plastic tube, which does not react with HCl. As seen in figure the flow is not controlled by the MFM, because the experiment was executed with a flow of 100 ml/min (MFM does detect above 13.11 ml/min). At the EC outlet a tee is installed to divide the flow into two channels, one to the PC-2 and the other to the sensor chamber. The flow at the outlet of the sensor chamber is measured by ADM Flow Meter to ensure a flow of approximately 40-50 ml/min is coming through. The Inlet flow of the Picarro was unknown and therefore it was measured at the outlet of the Picarro to get an estimate of the flow. The same procedure described in “Electrochemical device setup C1 - High pressure xenon lamp experiments” is followed

Table A1. Table of the gas bottles used in the experiments

Bottle name	CH_4 (ppm)	Cl_2 (ppm)	Matrix composition	Flow range (ml/min)
A	0	100 ± 2.5	$>99\% N_2$	6-23
B	$2.003 \pm 5 \cdot 10^{-4}$	0	Atmospheric air	1-29
C	78 ± 2	0	$20.95\% O_2 + >79\% N_2$	0.3-1.2

Appendix B: Experimental setups

The experimental setup for the experiments conducted in this study is shown in these Figures;

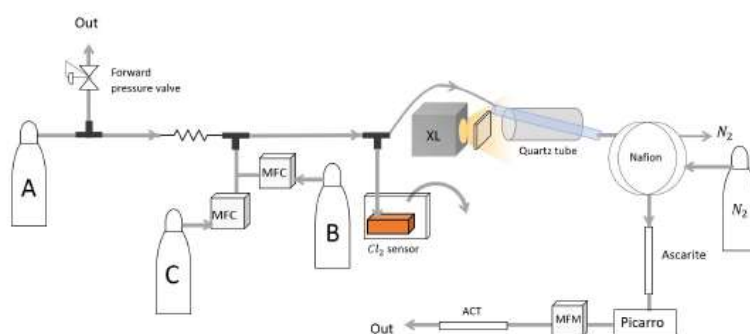


Figure B1. Repeated experiments using high pressure Xenon lamp with new setup. The experiment with this setup was conducted at the 18 February. XL: High pressure Xenon lamp. See Table A1 for gas bottle supply. ACT: Activated Carbon Trap. MFM: Mass Flow Meter. MFC: Mass Flow Controller.

The photochamber in "Repeated experiments using high-pressure Xenon lamp with new setup" uses a quartz tube with dimensions (20 cm in length, 1/2 inches (12.7 mm) in outer diameter) placed in the Xenon lamp (XL) photochemical device as described in "Electrochemical device setup C1-2 - High-pressure xenon lamp experiments" (Figure A4 and A5)

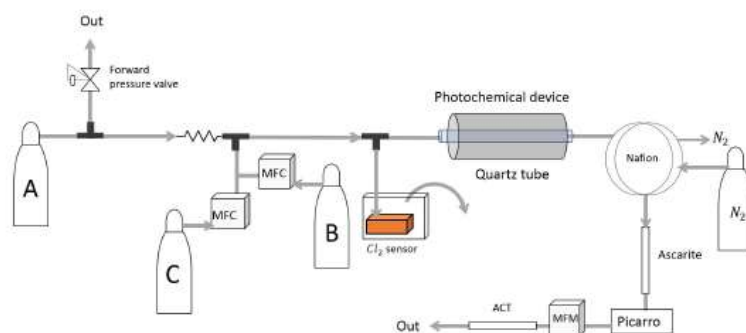


Figure B2. Hexagonal photochemical device experiments. The experiment with this setup was utilized on 24 part 1 February. See Table A1 for gas bottle supply. ACT: Activated Carbon Trap. MFM: Mass Flow Meter. MFC: Mass Flow Controller.

In addition to “Repeated experiments using high-pressure Xenon lamp with the setup” the high-pressure xenon lamp photochemical device is replaced with a photolysis chamber consisting of 420 LED at 365 nm (Figures B3, B2 and 1) peak wavelength connected by circuit boards in a hexagonal cylinder including the same quartz tube, see Figure 2. The LED diodes run in a parallel circuit with a forward voltage and forward current (from positive to negative). The max current is 13.2 mA for each LED, and the max voltage is 3.8 V. The same voltage runs through the LEDs, resulting in a total current across the system of 5.5 A.

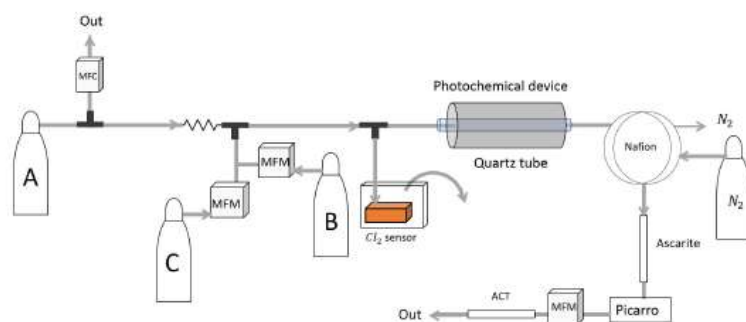


Figure B3. Hexagonal photochemical device experiments with MFC. The experiments with this setup was conducted on 24 part 2, 26 and 27 February. See Table A1 for gas bottle supply. ACT: Activated Carbon Trap. MFM: Mass Flow Meter. MFC: Mass Flow Controller.

The difference between the two similar setups “Hexagonal photochemical device with MFC and without MFC” is illustrated in Figures B2 and B3, respectively. The forward pressure valve is exchanged with a mass flow controller, as it was switching

between flows of several hundred ml/min and being closed. The periods where it was closed was limited, so the main concern was the high waste associated with several hundred ml/min lost to waste line. Installing the mass flow controller allowed for a smaller and more stable level of waste flow. The quartz tube of the previous experiments is substituted with seven smaller quartz tubes to yield a longer residence time in the photochemical device in the last experimental setup utilized

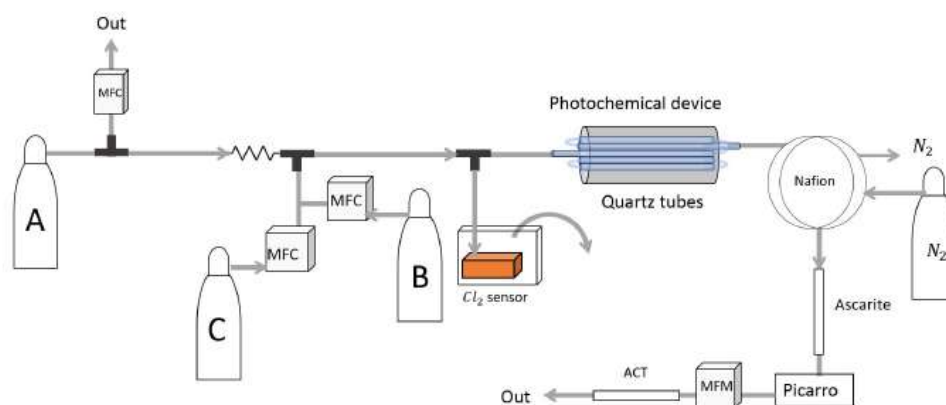


Figure B4. Experimental setup of Hexagonal photochemical device experiments with increased Residence Time. The experiments with this setup was conducted on 3, 4,5 and 9 March. See Table A1 for gas bottle supply. ACT: Activated Carbon Trap. MFM: Mass Flow Meter. MFC: Mass Flow Controller.

The new and optimized setup is seen in Figure B4. The seven quartz tubes are structured in a hexagonal shape for optimal packing and consist of five 8.33 mm in outer diameter with a 20 cm length, and two tubes with an outer diameter of 8.00mm and a length of 25 cm. The extra 5 cm of the two last tubes were outside the photolysis chamber for the purpose of connecting with the setup. The volume inside the photolysis chamber ended up at 42.8cm³ resulting in a 2.7 times increase in residence time in the photolysis chamber compared to the previous setup. The tubes were connected in series via Tygon tubes, Tygon R3603, of length 5cm. The insides of these tubes were coated with krytox,GPL-206 Grease Lubricant O-Rings SCUBA, in order to stop the consumption of Cl₂ that was observed for any soft tubing.

B1 Experimental procedure

- Tune the wanted flow of bottle C for methane and mix it with a flow from bottle B equal to the desired flow + the intended flow from bottle A.
- Let the system stabilize
- Add the desired flow of chlorine from bottle A, by adjusting the pressure at the bottle.

- Reduce the flow from bottle B by an equal amount to get the desired mixing ratio.
- Let the system stabilize and confirm that the resulting total flow fits with the expected. Make sure the chlorine value can be read on the chlorine sensor.
- When a stable methane level has been run for sufficient time, turn on the photochamber.
- Let the system stabilize to ensure a stable removal efficiency
- Turn off the light.
- Let the system stabilize to the initial methane concentration before the light was on

Appendix C: Settings and experimental results

C1 Experimental settings

Table C1. Experimental data for the 18, 24 and the 26 February. Columns: Experimental steps, [CH₄] in ppm, [Cl₂] in ppm, Residence time in seconds, Power in watts and the Resulting removal efficiency in % * : The power input of the xenon lamp was not varied nor determined

Experiment (#)	CH ₄ (ppm)	Cl ₂ (ppm)	Residence time (s)	Power (W)	Removal efficiency (%)
18-feb					
1	3.2729 ± 7E-04	16.7 ± 1.5	62.4 ± 1.6	*	0.01 ± 0.04
2	2.8327 ± 1.5E-03	25 ± 2	62.2 ± 1.6	*	6.40 ± 0.4
3	2.3769 ± 9E-04	50 ± 5	61.8 ± 1.6	*	27.29 ± 0.4
4	2.9367 ± 3E-03	92 ± 11	62.1 ± 1.6	*	52.69 ± 0.4
24-feb					
1	3.6391 ± 5E-03	16.7 ± 1.5	60.7 ± 1.6	17.43 ± 0.03	2.01 ± 0.5
2	3.6598 ± 1E-03	16.7 ± 1.5	60.9 ± 1.5	26.13 ± 0.04	6.52 ± 0.2
3	3.7069 ± 1.2E-03	16.7 ± 1.5	62.2 ± 1.6	9.91 ± 0.03	6.87 ± 0.2
4	3.7268 ± 6E-03	16.7 ± 1.5	62.4 ± 1.6	22.09 ± 0.04	10.96 ± 0.6
5	3.919 ± 1.5E-02	50 ± 5	61.0 ± 1.5	9.92 ± 0.03	23.91 ± 0.8
6	3.945 ± 1.4E-02	50 ± 5	61.4 ± 1.5	16.59 ± 0.03	32.69 ± 0.6
7	3.955 ± 2E-02	50 ± 5	129 ± 4	9.63 ± 0.03	44.51 ± 5.2
8	3.957 ± 6E-02	50 ± 5	41.4 ± 1.0	9.63 ± 0.03	18.90 ± 1.3
9	4.0301 ± 5E-03	50 ± 5	41.4 ± 1.0	17.30 ± 0.03	27.83 ± 1.0
10	3.986 ± 1.0E-02	50 ± 5	128 ± 4.7	17.30 ± 0.03	60.6 ± 8.7
26-feb					
1	3.5395 ± 5E-03	32 ± 3	62.5 ± 1.5	13.38 ± 0.03	17.55 ± 0.6
2	3.531 ± 1.5E-02	32 ± 3	85 ± 14	13.85 ± 0.03	24.82 ± 0.5
3	3.5570 ± 8E-03	32 ± 3	43.4 ± 1.1	13.73 ± 0.03	15.39 ± 0.3
4	3.5405 ± 9E-03	32 ± 3	43.0 ± 1.0	13.65 ± 0.03	16.18 ± 0.3
5	3.526 ± 4E-02	32 ± 3	135 ± 58	13.63 ± 0.03	38.19 ± 1.8
6	3.5261 ± 3E-03	32 ± 3	84 ± 2.6	17.65 ± 0.03	33.61 ± 0.9
7	3.564 ± 5E-02	32 ± 3	83 ± 2.2	22.05 ± 0.04	37.02 ± 1.3
8	3.567 ± 5E-02	32 ± 3	83 ± 2.2	28.22 ± 0.04	33.09 ± 1.5
9	3.5729 ± 3E-03	32 ± 3	83 ± 2.2	27.34 ± 0.04	34.72 ± 1.5
10	3.5447 ± 7E-03	32 ± 3	79 ± 2.1	33.10 ± 0.04	36.83 ± 1.4

Table C2. Experimental data for the 27 February and the 3 March. Columns: Experimental steps, [CH₄] in ppm, [Cl₂] in ppm, Residence time in seconds, Power in watts and the Resulting removal efficiency in %

(#)	CH ₄ (ppm)	Cl ₂ (ppm)	Residence time (s)	Power (W)	Removal efficiency (%)
27-feb					
1	3.3805 ± 6E-03	30 ± 3	62.7 ± 1.6	13.39 ± 0.03	22.46 ± 12
2	3.3984 ± 2E-03	20 ± 2	61.6 ± 1.7	13.36 ± 0.03	19.80 ± 1.9
3	3.3947 ± 3E-03	20 ± 2	61.4 ± 1.5	9.89 ± 0.03	16.65 ± 1.2
4	3.4014 ± 9E-04	20 ± 2	61.4 ± 1.5	17.50 ± 0.03	23.09 ± 1.9
5	3.3282 ± 5E-03	40 ± 4	61.0 ± 1.5	13.43 ± 0.03	34.99 ± 2.7
6	3.3309 ± 5E-03	40 ± 4	61.1 ± 1.6	9.92 ± 0.03	29.33 ± 1.6
7	3.3312 ± 4E-03	40 ± 4	61.0 ± 1.6	17.47 ± 0.03	38.99 ± 5.6
8	3.4096 ± 6E-03	50 ± 5	60.7 ± 1.5	13.43 ± 0.03	40.12 ± 5.2
9	3.4444 ± 3E-03	50 ± 5	60.6 ± 1.5	9.90 ± 0.03	35.05 ± 2.2
10	3.4377 ± 3E-03	50 ± 5	60.6 ± 1.5	17.49 ± 0.03	45.32 ± 3.7
11	3.3575 ± 5E-03	60 ± 6	60.4 ± 1.5	13.43 ± 0.03	47.06 ± 2.4
12	3.3800 ± 7E-03	60 ± 6	60.4 ± 1.5	9.90 ± 0.03	41.00 ± 1.9
13	3.3604 ± 3E-03	60 ± 6	60.3 ± 1.6	17.49 ± 0.03	53.80 ± 2.4
14	3.4122 ± 3E-03	70 ± 7	60.1 ± 1.6	13.43 ± 0.03	52.86 ± 2.5
15	3.4414 ± 1.5E-03	70 ± 7	60.0 ± 1.6	9.90 ± 0.03	45.12 ± 2.6
16	3.4566 ± 8E-03	70 ± 7	59.8 ± 1.6	17.49 ± 0.03	59.13 ± 2.0
03-mar					
1	3.5176 ± 6E-03	50 ± 5	162 ± 3.4	6.75 ± 0.02	27.99 ± 0.3
2	3.5475 ± 1.1E-03	50 ± 5	162 ± 3.4	9.74 ± 0.02	37.34 ± 0.3
3	3.5668 ± 1.8E-03	50 ± 5	161 ± 3.4	12.17 ± 0.03	46.83 ± 0.1
4	3.5920 ± 1.0E-03	50 ± 5	161 ± 3.4	14.63 ± 0.03	53.77 ± 0.1
5	3.6162 ± 1.9E-03	50 ± 5	161 ± 3.3	17.18 ± 0.03	55.24 ± 0.2
6	3.6425 ± 3E-03	50 ± 5	160 ± 3.4	19.73 ± 0.03	57.96 ± 0.3
7	3.6592 ± 1.2E-03	50 ± 5	160 ± 3.4	22.32 ± 0.03	59.22 ± 0.3

Table C3. Experimental data for the 4, 5 and the 9 March. Columns: Experimental steps, [CH₄] in ppm, [Cl₂] in ppm, Residence time in seconds, Power in watts and the Resulting removal efficiency in %. **: The [CH₄] values are calculated based on trend fitting

(#)	CH ₄ (ppm)	Cl ₂ (ppm)	Residence time (s)	Power (W)	Removal efficiency (%)
04-mar					
1	3.5594 ± 1.7E-03	50 ± 5	167 ± 3.5	14.46 ± 0.03	47.40 ± 1.2
2	3.2339 ± 1.3E-03	50 ± 5	168 ± 3.5	14.49 ± 0.03	54.73 ± 0.5
3	2.9339 ± 9E-04	50 ± 5	168 ± 3.5	14.56 ± 0.03	60.77 ± 0.5
4	2.684 ± 4E-02	50 ± 5	167 ± 3.6	14.60 ± 0.03	66.22 ± 0.6
5	2.2942 ± 3E-03	50 ± 5	164 ± 3.4	14.63 ± 0.03	69.64 ± 0.3
6	1.9817 ± 6E-04	50 ± 5	164 ± 3.5	14.46 ± 0.03	72.01 ± 0.4
7	1.6982 ± 7E-04	50 ± 5	166 ± 3.4	14.46 ± 0.03	74.06 ± 0.6
8	1.3899 ± 3E-04	50 ± 5	163 ± 3.5	14.46 ± 0.03	77.19 ± 0.7
9	3.8333 ± 7E-03	50 ± 5	162 ± 3.4	14.70 ± 0.03	60.32 ± 0.4
10	4.1285 ± 1.9E-03	50 ± 5	161 ± 3.4	14.63 ± 0.03	60.22 ± 0.2
11	3.5053 ± 1.7E-03	50 ± 5	161 ± 3.4	14.63 ± 0.03	64.01 ± 0.2
12	3.2045 ± 9E-04	50 ± 5	161 ± 3.4	14.63 ± 0.03	66.11 ± 0.3
05-mar					
1	1.9857 ± 8E-04	50 ± 5	164 ± 3.4	14.77 ± 0.03	67.89 ± 2.5
2	1.9872 ± 1.0E-03	50 ± 5	261 ± 5.9	14.77 ± 0.03	88.08 ± 1.3
3	1.9955 ± 1.0E-03	50 ± 5	348 ± 8.3	14.77 ± 0.03	92.0 ± 5.1
4	1.9995 ± 8E-04	50 ± 5	357 ± 8.9	17.36 ± 0.03	93.9 ± 5.0
5	2.0099 ± 8E-04	50 ± 5	342 ± 8.3	19.94 ± 0.03	96.1 ± 4.0
6 **	2.0021 ± 2E-03	50 ± 5	342 ± 8.2	22.80 ± 0.03	98.99 ± 0.1
7 **	2.0046 ± 3E-03	50 ± 5	265 ± 25	22.80 ± 0.03	96.74 ± 0.3
8 **	2.0061 ± 4E-03	50 ± 5	173 ± 20	22.80 ± 0.03	87.33 ± 0.1
9 **	2.0076 ± 6E-03	50 ± 5	128 ± 10	22.80 ± 0.03	77.30 ± 0.1
09-mar					
1	2.0471 ± 7E-04	50 ± 5	164 ± 3.4	7.92 ± 0.03	46.09 ± 1.8
2	2.0565 ± 9E-04	50 ± 5	164 ± 3.5	10.13 ± 0.03	56.59 ± 0.2
3	2.0586 ± 1.0E-03	50 ± 5	163 ± 3.5	12.54 ± 0.03	64.29 ± 0.1
4	2.0606 ± 1.1E-03	50 ± 5	163 ± 3.6	15.14 ± 0.03	70.31 ± 0.1
5	2.0627 ± 1.1E-03	50 ± 5	164 ± 3.6	17.71 ± 0.03	75.09 ± 0.1
6	2.0690 ± 1.4E-03	50 ± 5	162 ± 3.6	20.63 ± 0.03	80.28 ± 0.07
7	2.0710 ± 1.5E-03	50 ± 5	161 ± 3.5	23.63 ± 0.03	83.25 ± 0.04

C2 Experimental results

Numerous experiments have been prepared with the setups presented in the experimental section. In Table C1,C2 and C3 the four varying parameters; $[\text{CH}_4]_{\text{Initial}}$, $[\text{Cl}_2]$, residence time and power setting of the photo chemical-chamber are presented for each experiment alongside the resulting removal efficiency.

Repeated experiments using high-pressure Xenon lamp with new setup

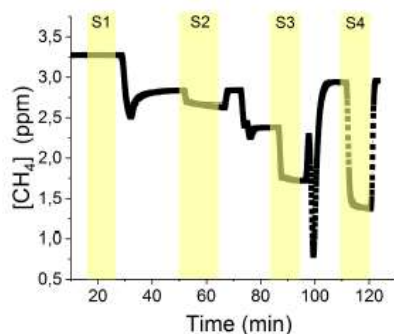


Figure C1. Experiment conducted on the 18 February. Each step has been highlighted. The CH_4 is seen as a function of time. The $[\text{Cl}_2]$ is varied.

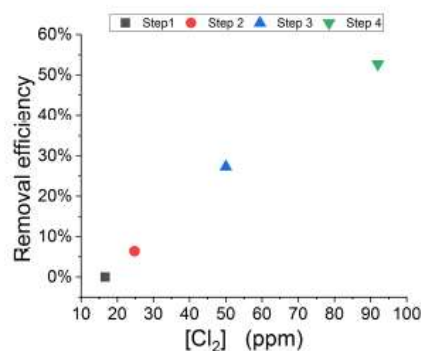


Figure C2. caption

The Xenon-lamp experiments shown in Figure C1 were performed to confirm that the Cl_2 added to the gas-mix could make it to the photolysis-chamber. The removal efficiency of methane was found as a result of varying the $[\text{Cl}_2]$ to 16.7, 25, 50, and 92 ppm as seen in Figure C2. Each concentration step was given 10 minutes to stabilize before the xenon-lamp was turned on for ten minutes. The xenon-lamp had been applied in the preliminary experiments where it had been shown to initiate methane oxidation. The gas provided to the system was a dynamic mix of flows from three different bottles (see table Gas bottles Table 2). Due to this, it was possible to vary the abundance of Cl while keeping the CH_4 constant. As can be seen in Figure C1 the changes in Cl_2 inadvertently also lead to changes in the abundance of CH_4 because the flow ratios chosen was based on the assumption that bottle C had a methane concentration of at a 100ppm CH_4 , whereas it had 78ppm as was later determined. From these experiments, it was confirmed that the level of Cl_2 could be controlled and that higher levels resulted in greater depletion of methane. It should also be noted that experiment one behaved differently from the main trend, which will also be seen in the later experiments. This is speculated to be due to the system needing longer flushing time than expected. This trend will be referred to in the later experiment as Early-experiment-deviation.

Hexagonal photochemical device experiments

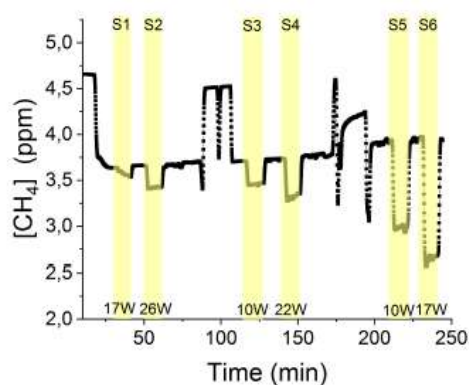


Figure C3. Experiment conducted on the 24 February. Each step has been highlighted. The CH_4 is seen as a function of time. The light intensity and $[\text{Cl}_2]$ are varied.

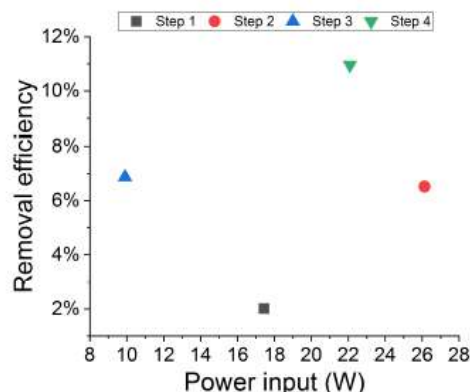


Figure C4. Removal efficiency as a function of power input for step 1-4 on the 24.

Throughout experimental steps, the power of the photochemical device was varied in step one to four presented in Figure C3. The aim was to determine the effect of varying light intensity. As can be seen in Figure C3, the unscrubbed methane concentration slowly increases during the experiment. This is speculated to be a result of flow from bottle A reducing over time resulting in a higher CH_4 and a lower Cl_2 level in the gas mix. This trend is seen varying degree in all experiments. Figure C4 shows the removal efficiency as a function of power input to the photochemical device for experiments one to four. The initial methane concentration is maintained at 3.68 ± 0.02 ppm. Step one and two are both examples of the Early-experiment-deviation. At the time of step three and four, sufficient flushing had taken place and the proper operational conditions were met. From their respective removal rate illustrates the effect of varying the power input for the photochemical device.

Table C4. 24 February experiments. The three experimental steps clearly shows an increasing removal efficiency as the power input and the Cl_2 mixing ratio are increased

Step (#)	CH_4 (ppm)	Cl_2 (ppm)	Residence time (s)	Power (W)	Removal efficiency (%)
3	$3.7069 \pm 1.1 \cdot 10^{-4}$	16.7 ± 1.5	62.2 ± 1.5	9.91 ± 0.03	6.87 ± 0.01
5	$3.919 \pm 1.4 \cdot 10^{-3}$	50 ± 5	61.0 ± 1.4	9.92 ± 0.03	23.91 ± 0.05
6	$3.945 \pm 1.3 \cdot 10^{-3}$	50 ± 5	61.4 ± 1.4	16.59 ± 0.03	32.69 ± 0.04

The chlorine concentration was increased from 16.7 to 50ppm for step 5 and up. The four relevant variables and resulting removal efficiency can be seen in Table C4. The $[\text{Cl}_2]$ was increased by a factor of 2.5 when comparing steps 3 and 5. The increase results in a 3.5 fold increase of RE%. Furthermore, the power input is increased when going from step 5 to 6, that

likewise lead to an increase in RE%. The comparison between these three steps, the positive relation for both chlorine concentration and power input on the RE% was confirmed.

Single tube Hexagonal photochemical device experiments

The experiments with this setup took place over three days (24, 26 and 27 February). The experiments will be referred to by the date they were performed.

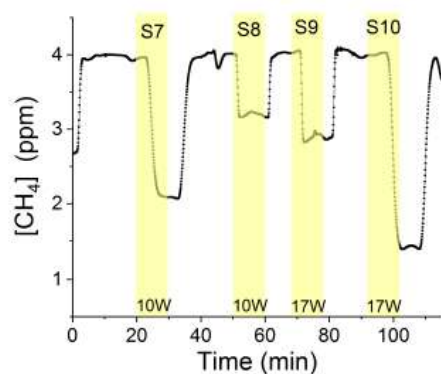


Figure C5. Experiment conducted on the 24 of February. Steps 7-10 highlighted. The CH_4 is seen as a function of time. The light intensity and residence time are varied.

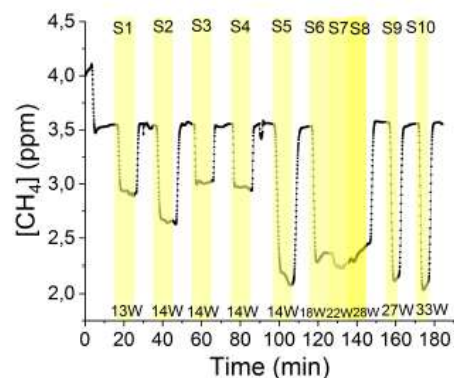


Figure C6. Experiment conducted on the 26 February. Steps 1-10 are highlighted. The CH_4 is seen as a function of time. The light intensity and residence time are varied.

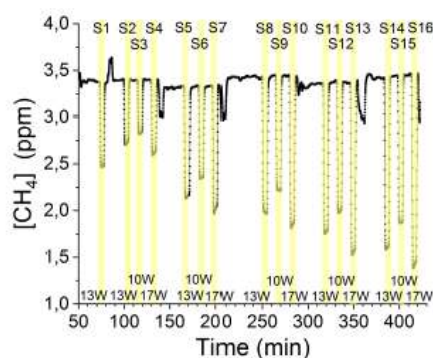


Figure C7. Experiment conducted on the 27 February. Steps 1-16 are highlighted. The CH_4 is seen as a function of time. The light intensity and $[\text{Cl}_2]$ are varied.

The 24 February experiment part II presented in Figure C5 were carried out with constant supply of $[Cl_2]$ at 50ppm and $[CH_4]$ at 3.981 ± 0.018 ppm. Step eight and nine had the same residence times, while step seven and ten have the same. The experiments vary in power input as seen in Table C5. Table C5 shows how the combination of increased residence time and power input yields a higher removal efficiency. In addition to the previous experiment, it is shown, as expected, that an increase in Cl_2 mixing ratio, longer residence time, and stronger power yield higher removal efficiencies for the system. The later experiments will tackle how greatly these parameters rely on each other.

Table C5. Experiment 7-10 for 24 February

Experiment (#)	CH_4 (ppm)	Cl_2 (ppm)	Residence time (s)	Power (W)	Removal efficiency (%)
8	$3.957 \pm 5 \cdot 10^{-3}$	50 ± 5	41.4 ± 1.0	9.63 ± 0.03	18.90 ± 0.11
9	$4.0301 \pm 5 \cdot 10^{-4}$	50 ± 5	41.4 ± 1.0	17.30 ± 0.03	27.83 ± 0.06
7	$3.955 \pm 2 \cdot 10^{-3}$	50 ± 5	129 ± 3	9.63 ± 0.03	44.51 ± 0.3
10	$3.986 \pm 9 \cdot 10^{-4}$	50 ± 5	128 ± 3	17.30 ± 0.03	60.6 ± 0.5

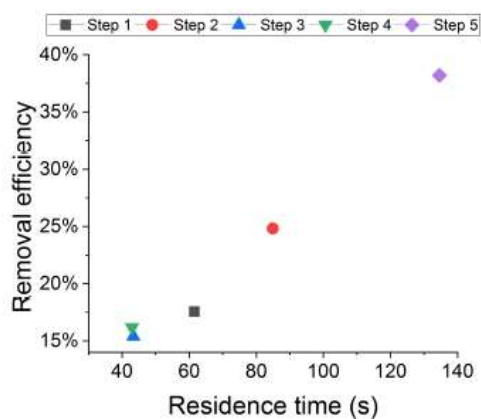


Figure C8. Experimental steps 1-5 on the 26 February : Residence time (min) in the photochemical device as a function of residence time in seconds

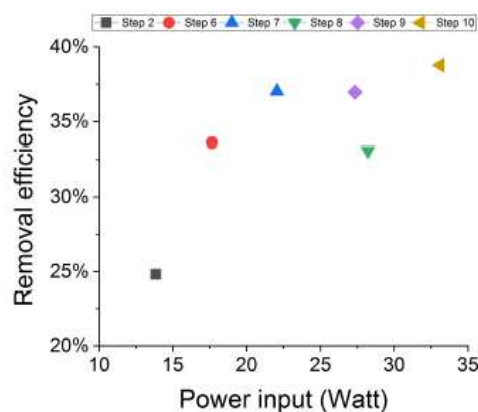


Figure C9. Experiment steps 2 and 6-10 for the 26 February : Removal efficiency as a function of power input in watt

The experiment of the 26 February was carried out with $[Cl_2]$ kept constant at 32ppm moreover the initial methane concentration was maintained at 3.547 ± 0.005 ppm. Similarly to the experiment on the 24 P2 February the residence time and power input where varied. Steps one to five are carried out with the same power input in the device but with varying residence times, see Figure C18 and C8. In Figure C18 the data for the 26 February exhibits a clear agreement between residence time and removal efficiency. The longer residence time within the photochamber results in greater removal efficiencies. The steps two

and six to ten are carried out with the same residence time but with varying power inputs, see Figure C17 and C9. The steps two, six, and seven in Figure C9 clearly shows the expected relation between increased power input and removal efficiency. The subsequent step see no significant increase in removal despite higher power input. The reason for this is thought to be that the system is saturated with Cl_2 and a higher power input will not make a difference, when all Cl_2 is already photolyzed. Another issue is problems with the photochemical device. Steps seven and eight experienced some difficulties with the power input, which may be the reason why they don't follow the trend. The circuit boards were held together by hot-glue, and when it was melting, it is believed that it created some resistance in the system. The photochemical device was then turned off to cold down, and steps nine and ten performed much better as seen in Figure C9.

The experimental steps of the 27 February, Figure C7, were held the same initial methane concentration at 3.39 ± 0.01 ppm and the same residence time at 60.82 ± 0.18 s. Throughout the experiments, three levels of power inputs for the photochemical device were tested against varied levels of Cl_2 mixing ratio spanning in the range 20-70ppm

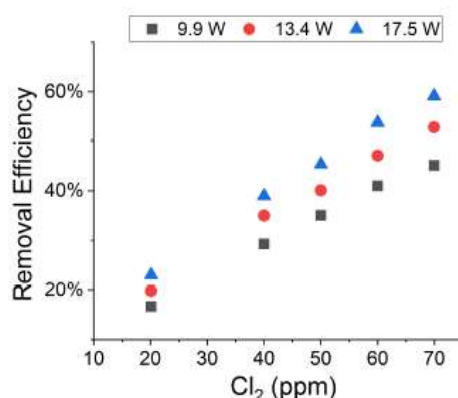


Figure C10. Resulting removal efficiency plotted against $[\text{Cl}_2]$ in ppm for experiment steps 2-16 for the 27 February. Three different power settings are used. 9.9W (black), 13.4W (red) and 17.5W (blue).

Figure C10 presents, looking at 20 ppm Cl_2 , that a greater power input yields higher RE%. However, the spacing between the point enhances as the Cl_2 mixing ratio is increased eg. comparing 20 ppm with 60 ppm Cl_2 mixing ratio. The increases spacing is due to at low Cl_2 mixing ratios the system becomes saturated and even if a greater amount of power is added it doesn't make a significant difference. However, at higher Cl_2 levels more Cl_2 is present and the system takes longer to become saturated.

Hexagonal photochemical device experiments with multiple tubes

The experiments with this setup have taken place over four days (3, 4, 5, and 9 March). The main difference compared to the previous setup was changing the volume within the photochemical device, by exchanging the single quartz tube, with 7 thinner tubes connected in series. The volume is increased from 15.7 ± 0.4 to 42.8 ± 0.9 ml. Longer residence time could then be achieved by in the same flow range.

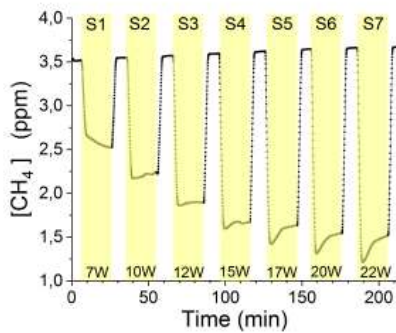


Figure C11. Experiment conducted on the 3 March. Steps 1-7 are highlighted. The CH_4 is seen as a function of time. The light intensity are varied.

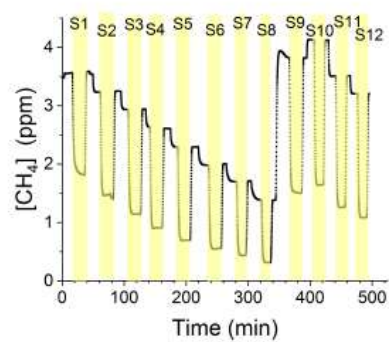


Figure C12. Experiment conducted on the 4 March. Steps 1-12 are highlighted. The CH_4 is seen as a function of time. The CH_4 level is varied, while the light intensity is kept the same.

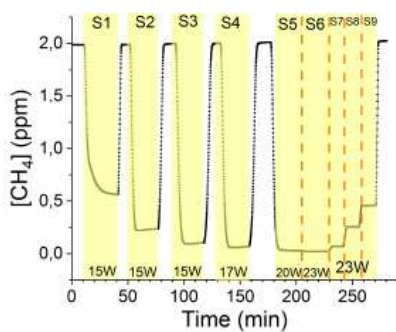


Figure C13. Experiment conducted on the 5 March. Steps 1-9 are highlighted. The CH_4 is seen as a function of time. The light intensity and residence time are varied.

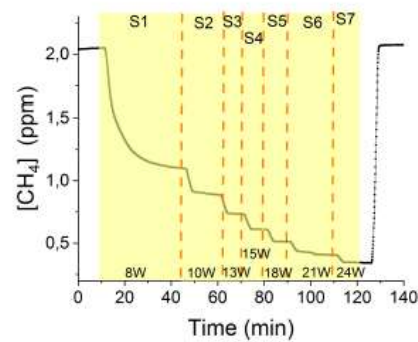


Figure C14. Experiment conducted on the 9 March. The CH_4 is seen as a function of time. Steps 1-7 are highlighted. The light intensity are varied. Prolonged and stable photolysis enabled due to cooling. Increasing levels of power input for the photochemical chamber defines the seven different steps

The experiments of the 3 March, Figure C11, were run at a constant level of $[\text{CH}_4]_{\text{initial}}$ at 3.593 ± 0.019 ppm and $[\text{Cl}_2]$ at 50 ± 5 ppm. At a flow kept at 15.5 ml/min the residence time in the photochamber was maintained at $161.06 \pm 3 \text{ s}$. Across the 3 March the step-wise changes were made for power input ranging from 6.75 - 22.92 W . The daily measurement is presented in Figure C11; where the removal for the steps, with the exception of the first step, is characterized by an initial removal efficiency but this efficiency drops during the first five minutes of illumination. We argue that the explanation for this is that

the LEDs start to heat up while being turned on, which would lower their effectiveness. Upon touching the LEDs following an experiment it was confirmed that considerable heat had been generated. Due to this effect, the declared average removed effect is calculated 2.5 min after initiation of photolysis till the light is turned off, as a semi-stable level is reached. The relationship found between removal and power input for the 3 March can be seen in Figure C17. The acquired removal efficiency of the 3 March is higher than for the 26 February, as expected with increased $[Cl_2]$ and the residence time for the 3 March. Therefore a comparison between the trend is more useful. Both the experiments follow a positive trend with power for the lower power inputs, but the removal efficiency flattens out at higher powers. For the two days, this happened at two different power inputs, which surprised us. The reason for this was found that the two days had investigated the same current range, but with different voltage, resulting in higher power input for the 26 February. Observing the removal along with the current, revealed that the flattening in efficiency happened at around 3.5A for both of them. This deviation from the initial positive trend is expected to be due to the overheating of the photochemical device at high currents. Based on this hypothesis the photochemical device went through a clean-up session where most of the silicone holding the six sides together was removed in favor of replacing it with the copper wires connecting the LED's.

The experiments of the 4 March were carried out with a step-wise change of $[CH_4]_{initial}$ in the range 1.39 to 4.13ppm, at constant residence time 164s, $[Cl_2]$ at 50ppm, and power input 14.6W. The daily result can be seen in Figure C12, where the improvement of silicone removal can be observed from stable levels of removal efficiency. As can be seen in Figure C15 decreasing the initial methane concentration yields, as expected, a greater removal efficiency.

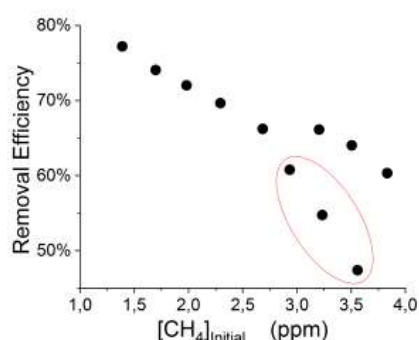


Figure C15. The removal efficiency is displayed as a function of the initial methane concentration with the remaining fixed parameters such as Cl_2 mixing ratio, residence time, and power input. The three encircled points in the Figure represent steps suffering from early-experiments-derivation.

The experiments of the 5 March were carried out with the constant $[CH_4]_{initial}$ at 2.000 ± 0.003 ppm and Cl_2 mixing ratio at 50 ± 5 ppm, but with mixed settings of residence time and power. The first three steps were done with constant power at 14.8W with residence times ranging form 164-350s. Then keeping residence time around 350s three steps of increasing power

were tested, ranging from 14.8-22.8W. In between step 4 and 5 a fan was installed, in order to see if cooling at the higher power settings could improve the efficiency. Because no drop in efficiency, as was seen at similar power levels on the 3 March, occurred at step 5, the power was increased for step 6 without turning off the lamp. As the removal remained stable across the 15 minutes, the light was left on, as the final 3 steps were tested. For these the power remained at 22.8W and stepped through reduced residence time from 342-130s. Usually, the photochemical device has shown some difficulties at working at higher power inputs, however, the results in Figure C16 present a great improvement due to the silicone removal and inclusion of cooling.

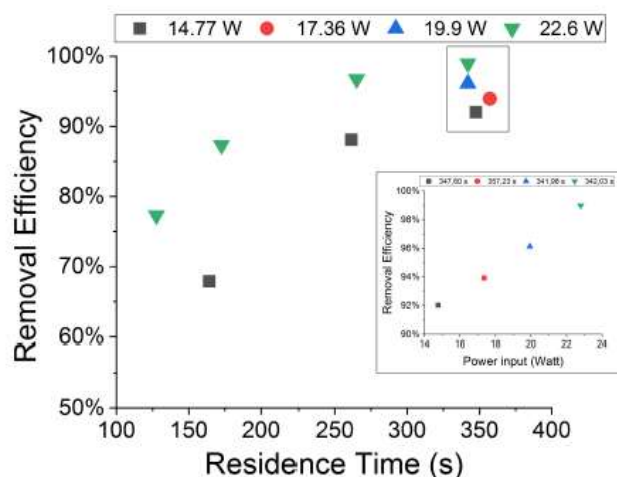


Figure C16. The resulting removal efficiencies of the 5 March plotted against residence time. An additional zoom inset Figure on the four points around 350s reveals the removal effect plotted against power.

The experiments of the 9 March were carried out with $[CH_4]_{initial}$ maintained around 2.01 ± 0.01 ppm, $[Cl_2]$ at 50 ppm and the residence time held at 163.1 ± 0.4 s. The only parameter varied was the power input to the photochemical device. Based on the improvement from cooling, the fan was also used for the experiment. After the initial stable level had been reached the light was turned on at 7.9W and was left on for the duration of the experiments with a step-wise increase in power after stable removal had been maintained for 5 min. The resulting methane can be seen in Figure C14. The $[CH_4]$ increases throughout the experiments due to the chlorine-pressure-decline. For the purpose of calculating removal efficiency, the expected $[CH_4]$ for each of the steps, was fitted from the initial $[CH_4]$ and the end $[CH_4]$; $CH_4 = 0.0002 \cdot t + 2.0461$. The relatively median values of initial methane and residence time were chosen in order to best resolve the effects of varying power input. As the removal effect approaches 100% asymptotically, the sensitivity to changes will be greater at lower removal values. The results presented for the 9 March in Figure C17 can be compared to the results from the 26 February and the 3 March and represents the improvements implemented to the system. Unlike for those two days, the trend of the 9 March is explained by one trend

asymptotically approaching 100% removal.

Comparison

The removal efficiencies as a function of power and residence time for various experiments is shown in Figures C17 and C18, respectively.

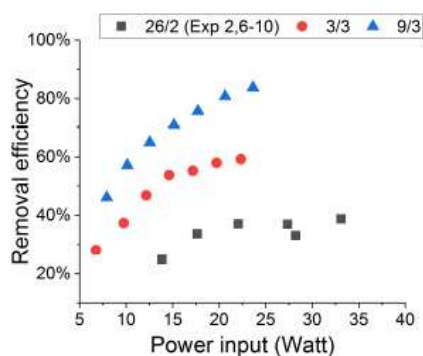


Figure C17. Removal efficiency of methane plotted against power input in W. The result from three experiments, 26 February (black), 3 March (red) and 9 March (blue) have different settings in residence time, $[CH_4]$ and $[Cl_2]$.

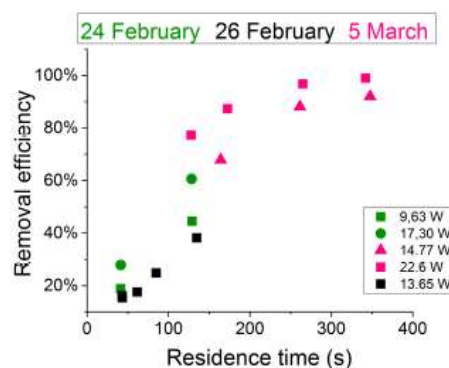


Figure C18. Removal efficiency of methane plotted against residence time in s. The result from three experiments, 24 February (green), 26 February (black) and 5 March (pink) have different settings in power input, $[CH_4]$ and $[Cl_2]$.

Figure C17 shows a comparison of three different days where the power input was varied. When comparing experiments of the 3 and 9 March the improvement of the photochamber is pretty clear. However, even if the residence time and Cl_2 are identical, the initial methane concentration of 3 March is 3.59 ppm compared to 9 March at 2.096 ppm. The 26 February alone shares some power input levels and is operated at the same initial methane level as the 3 March runs. The residence time and Cl_2 are lower and a lesser removal is accordingly expected. Hence, the main thing to observe is behavior at higher power inputs. The efficiency of the photochamber decreases as seen on the 3 March and 26 February. The improvements done on the photochamber and installation of a fan to cold the photochemical chamber have prolonged the lifetime of the chamber and improved efficiency. Figure C18 shows a comparison of three different days where the residence time was varied and in some cases the power input as well. The residence time is improved in the manner that the multiple tube setup made it possible to obtain higher residence time and more efficient use of the photochemical chamber. The experiments with a single tube can't exhibit long residence times. As seen in Figure C18 longer residence time greatly improves the removal efficiency and is, therefore, essential to further improve the setup.

C3 Error analysis

The uncertainty throughout this work has been either measured or assessed to the best of our conservative estimates. For methane measurements, both initial and final, the uncertainty was calculated as the standard error from the 5 min averages declared. The resulting uncertainty in the removal efficiency was found by error propagation of the two measured methane levels. The exception is the experiment sets for the 5 and 9 March, where different experiments were done without returning to standard conditions first. The initial CH₄ for each of those is therefore calculated based on the trend spanned between the beginning and end of experiments. The error for the experiments individually assigned initial CH₄ is, therefore, the error of the fit. For chlorine uncertainty, the estimate had to be assessed based on the variation inflow from the capillary relative to the total flow. The flow from the chlorine channel varied with 8.3% of set-point while flow from the methane channel was comparatively very stable with neglectable fluctuations. The flow uncertainty in combination with the unknown degree of loss of chlorine to the setup resulted in a high uncertainty of 10% of the declared values. The residence time was found from the variation in flow going through the Picarro, as it was measured by the mass flow meter and the uncertainty in the volume within the photochemical chamber which had an estimated uncertainty of 2%. The power uncertainty is calculated based on a 0.5% uncertainty in set-point for both the current and potential.

Appendix D: Kintecus Model

D1 Reactions and rate constants

Table D1. JPL: Burkholder et al. (2015). NIST: NIST Kinetics Database. A compilation of kinetics data on gas-phase reactions.

Reaction	Reaction Rate Coefficient	Reference
$\text{Cl}_2 \rightarrow 2 \text{Cl}$	X	
$\text{Cl} + \text{Cl} + \text{M} \rightarrow \text{Cl}_2 + \text{M}$	1.29E-32	Baulch et al. (1981)
$\text{O}_2 + \text{CH}_3 \rightarrow \text{CH}_3\text{O}_2$	1.34E-12	NIST
$\text{O}_2 + \text{CH}_3\text{O} \rightarrow \text{CH}_2\text{O} + \text{HO}_2$	9.60E-12	NIST
$\text{O}_2 + \text{HCO} \rightarrow \text{CO} + \text{HO}_2$	5.20E-12	NIST
$\text{O}_2 + \text{CH}_2\text{Cl} \rightarrow \text{CH}_2\text{ClO}_2$	2.91E-12	NIST
$\text{Cl} + \text{CH}_3\text{O} \rightarrow \text{CH}_2\text{O} + \text{HCl}$	1.91E-11	NIST
$\text{Cl} + \text{CH}_3\text{OH} \rightarrow \text{CH}_3\text{O} + \text{HCl}$	5.50E-11	JPL
$\text{Cl} + \text{CH}_2\text{O} \rightarrow \text{HCO} + \text{HCl}$	7.32E-11	JPL
$\text{Cl} + \text{Cl}_2\text{O} \rightarrow \text{Cl}_2 + \text{ClO}$	9.60E-11	JPL
$\text{Cl} + \text{CH}_3\text{Cl} \rightarrow \text{CH}_2\text{Cl} + \text{HCl}$	4.98E-13	JPL
$\text{Cl} + \text{CH}_2\text{Cl}_2 \rightarrow \text{CHCl}_2 + \text{HCl}$	3.57E-13	JPL
$\text{Cl} + \text{CCl}_3 \rightarrow \text{CCl}_4$	6.51E-11	NIST
$\text{Cl} + \text{CHCl}_3 \rightarrow \text{HCl} + \text{CCl}_3$	1.20E-13	JPL
$\text{Cl} + \text{CH}_3\text{O}_2 \rightarrow \text{CH}_3\text{O} + \text{ClO}$	1.60E-10	JPL
$\text{Cl} + \text{CH}_3\text{O}_2 \rightarrow \text{CH}_2\text{O}_2 + \text{HCl}$	1.60E-10	JPL
$\text{Cl} + \text{CH}_4 \rightarrow \text{CH}_3 + \text{HCl}$	1.07E-13	Bryukov et al. (2002)
$\text{Cl} + \text{CHClO} \rightarrow \text{HCl} + \text{Cl} + \text{CO}$	7.64E-13	NIST
$\text{Cl} + \text{H}_2\text{O}_2 \rightarrow \text{HCl} + \text{HO}_2$	4.10E-13	JPL
$\text{Cl} + \text{CH}_3 \rightarrow \text{CH}_3\text{Cl}$	1.61E-12	Kaiser (1993)
$\text{Cl}_2 + \text{CH}_2\text{Cl} \rightarrow \text{CH}_2\text{Cl}_2 + \text{Cl}$	2.54E-13	JPL
$\text{Cl}_2 + \text{CHCl}_2 \rightarrow \text{CHCl}_3 + \text{Cl}$	2.25E-14	NIST
$\text{Cl}_2 + \text{CH}_3 \rightarrow \text{CH}_3\text{Cl} + \text{Cl}$	1.55E-12	NIST
$\text{Cl}_2 + \text{HCO} \rightarrow \text{CHClO} + \text{Cl}$	5.59E-12	NIST
$\text{Cl}_2 + \text{OH} \rightarrow \text{HClO} + \text{Cl}$	6.42E-14	NIST
$\text{OH} + \text{CH}_4 \rightarrow \text{CH}_3 + \text{H}_2\text{O}$	6.30E-15	Bonard et al. (2002)
$\text{OH} + \text{CH}_3\text{OOH} \rightarrow \text{H}_2\text{O} + \text{CH}_3\text{O}_2$	7.40E-12	JPL
$\text{OH} + \text{CH}_3\text{OOH} \rightarrow \text{CH}_2\text{O} + \text{OH} + \text{H}_2\text{O}$	7.40E-12	JPL
$\text{OH} + \text{CH}_2\text{O} \rightarrow \text{HCO} + \text{H}_2\text{O}$	8.50E-12	JPL
$\text{OH} + \text{HCl} \rightarrow \text{Cl} + \text{H}_2\text{O}$	7.80E-13	JPL
$\text{OH} + \text{HClO} \rightarrow \text{ClO} + \text{H}_2\text{O}$	5.00E-13	NIST
$\text{OH} + \text{HO}_2 \rightarrow \text{H}_2\text{O} + \text{O}_2$	1.10E-10	NIST

Table D2. JPL: Burkholder et al. (2015). NIST: NIST Kinetics Database. A compilation of kinetics data on gas-phase reactions. Hossaini:Hossaini et al. (2016)

Reaction	Reaction Rate Coefficient	Reference
$\text{OH} + \text{CH}_3\text{Cl} \rightarrow \text{CH}_2\text{Cl} + \text{H}_2\text{O}$	3.50E-14	JPL
$\text{OH} + \text{CH}_2\text{Cl}_2 \rightarrow \text{CHCl}_2 + \text{H}_2\text{O}$	1.00E-13	JPL
$\text{OH} + \text{CHCl}_3 \rightarrow \text{CCl}_3 + \text{H}_2\text{O}$	1.00E-13	JPL
$\text{OH} + \text{CH}_3\text{O} \rightarrow \text{CH}_2\text{O} + \text{H}_2\text{O}$	3.01E-11	JPL
$\text{OH} + \text{CH}_3\text{OH} \rightarrow \text{CH}_3\text{O} + \text{H}_2\text{O}$	1.40E-13	NIST
$\text{OH} + \text{CH}_3 \rightarrow \text{CH}_3\text{OH}$	9.30E-11	NIST
$\text{OH} + \text{CH}_2\text{ClOOH} \rightarrow \text{CH}_2\text{ClO}_2 + \text{H}_2\text{O}$	3.60E-12	Hossaini
$\text{OH} + \text{CH}_2\text{ClOH} \rightarrow \text{CH}_3\text{O} + \text{HClO}$	4.54E-14	Hossaini
$\text{OH} + \text{H}_2\text{O}_2 \rightarrow \text{HO}_2 + \text{H}_2\text{O}$	1.80E-12	JPL
$\text{OH} + \text{CHClO} \rightarrow \text{Cl} + \text{CO} + \text{H}_2\text{O}$	3.20E-13	Hossaini
$\text{OH} + \text{ClO} \rightarrow \text{Cl} + \text{HO}_2$	1.80E-11	JPL
$\text{OH} + \text{ClO} \rightarrow \text{HCl} + \text{O}_2$	1.30E-12	JPL
$\text{HO}_2 + \text{CH}_3\text{O}_2 \rightarrow \text{CH}_3\text{OOH} + \text{O}_2$	5.12E-12	JPL
$\text{HO}_2 + \text{Cl} \rightarrow \text{HCl} + \text{O}_2$	3.50E-11	JPL
$\text{HO}_2 + \text{Cl} \rightarrow \text{ClO} + \text{OH}$	9.30E-12	JPL
$\text{HO}_2 + \text{ClO} \rightarrow \text{HClO} + \text{O}_2$	6.90E-12	JPL
$\text{HO}_2 + \text{CH}_3\text{O} \rightarrow \text{CH}_2\text{O} + \text{H}_2\text{O}_2$	5.00E-13	NIST
$\text{HO}_2 + \text{HO}_2 \rightarrow \text{H}_2\text{O}_2 + \text{O}_2$	1.60E-12	NIST
$\text{HO}_2 + \text{CH}_2\text{ClO}_2 \rightarrow \text{CH}_2\text{ClOOH} + \text{O}_2$	5.01E-12	Hossaini
$\text{HO}_2 + \text{CH}_2\text{ClO}_2 \rightarrow \text{CHClO} + \text{H}_2\text{O} + \text{O}_2$	5.01E-12	Hossaini
$\text{ClO} + \text{ClO} \rightarrow \text{O}_2 + \text{Cl}_2$	4.91E-15	JPL
$\text{ClO} + \text{ClO} \rightarrow 2\text{Cl} + \text{O}_2$	8.00E-15	JPL
$\text{ClO} + \text{Cl} \rightarrow \text{Cl}_2\text{O}$	1.56E-32	NIST
$\text{ClO} + \text{CH}_3\text{O}_2 \rightarrow \text{Cl} + \text{O}_2 + \text{CH}_3\text{O}$	2.40E-12	JPL
$\text{ClO} + \text{CH}_3 \rightarrow \text{CH}_3\text{OCl}$	5.69E-11	NIST
$\text{CH}_3\text{O}_2 + \text{CH}_3\text{O}_2 \rightarrow \text{CH}_3\text{O} + \text{CH}_3\text{O} + \text{O}_2$	3.50E-13	JPL
$\text{CH}_3\text{O}_2 + \text{CH}_3\text{O}_2 \rightarrow \text{CH}_3\text{OH} + \text{CH}_2\text{O} + \text{O}_2$	3.50E-13	JPL
$\text{CH}_3 + \text{CH}_3\text{O}_2 \rightarrow \text{CH}_3\text{O} + \text{CH}_3\text{O}$	4.50E-11	NIST
$\text{CH}_3\text{O} + \text{CH}_3\text{O} \rightarrow \text{CH}_2\text{O} + \text{CH}_3\text{OH}$	3.85E-11	NIST
$\text{CH}_2\text{ClO}_2 + \text{CH}_3\text{O}_2 \rightarrow \text{CH}_2\text{ClO} + \text{CH}_2\text{O} + \text{HO}_2$	2.50E-12	Hossaini
$\text{CH}_2\text{ClO}_2 + \text{CH}_3\text{O}_2 \rightarrow \text{CH}_2\text{ClOH} + \text{CH}_2\text{O} + \text{O}_2$	2.50E-12	Hossaini
$\text{CH}_2\text{ClO}_2 + \text{CH}_3\text{O}_2 \rightarrow \text{CHClO} + \text{CH}_3\text{OH} + \text{O}_2$	2.50E-12	Hossaini
$\text{CH}_2\text{ClO}_2 + \text{CH}_2\text{ClO}_2 \rightarrow \text{CH}_2\text{ClO} + \text{CH}_2\text{ClO} + \text{O}_2$	3.50E-12	Hossaini
$\text{CH}_2\text{Cl}_2 + \text{Cl} \rightarrow \text{CHCl}_2 + \text{HCl}$	3.57E-13	NIST
$\text{CHCl}_2 + \text{Cl}_2 \rightarrow \text{CHCl}_3 + \text{Cl}$	2.25E-14	NIST
$\text{CCl}_3 + \text{Cl} \rightarrow \text{CCl}_4$	6.51E-11	NIST
$\text{HCO} + \text{Cl}_2 \rightarrow \text{HC(O)Cl} + \text{Cl}$	5.59E-12	40 NIST
$\text{CH}_2\text{O}_2 \rightarrow \text{CO} + \text{H}_2\text{O}$	6.00E+04	NIST

By comparing the obtained J_{Cl_2} values and the associated power input efficiency of power conversion could be calculated.

D2 Kintecus generated J_{Cl_2} model

One of the parameters that need to be tunable in the model is the effect of varying power to the lamps. The way this could be incorporated into the model was by defining the photolysis rate, J_{Cl_2} , as a function of input power. To do this the J_{Cl_2} was fitted to reproduce the data collected on the 26 February and the 9 March, where power was the only variable adjusted in the system. The 26 February reflects the single tube system while the 9 March reflect the optimized multiple tubes setup. By comparing the obtained J_{Cl_2} values and the associated power input efficiency of power conversion could be calculated.

The J_{Cl_2} rate model

The photolysis rate J can be determined by equation D1.

$$J_{Cl_2} = \sigma(\lambda, T) \cdot \phi(\lambda, T) \cdot I(\lambda, W) \quad (D1)$$

Where $\sigma(\lambda, T)$ is the wavelength dependent cross section of Cl_2 with the unit $cm^2 \cdot molecule^{-1}$, $\phi(\lambda, T)$ the quantum yield for photolysis and it is determined to be 1 since no other reactions are present, and $I(\lambda, W)$ is the spectral actinic flux density in photons $s^{-1} \cdot cm^{-2}$. The cross-section of chlorine dissociation in the range 250-550nm is defined by D2.

$$\sigma(\lambda, T) = 10^{-20} \left(\tanh\left(\frac{402.7}{T}\right) \right)^{0.5} \cdot (27.3 \cdot e^{-99.0 \cdot (\tanh(\frac{402.7}{T})) \cdot (\ln(\frac{329.5}{\lambda}))^2} + 0.932 \cdot e^{-91.5 \cdot \tanh(\frac{402.7}{T}) \cdot (\ln(\frac{406.5}{\lambda}))^2}) \quad (D2)$$

T is the temperature and λ is the wavelength in nm. The actinic flux would be a function dependent on photochemical device, the power input, and the tube volume. The photochemical device in the setup uses 420 LED diodes that emit at a dominant wavelength of 365 nm. The photon output from the diodes was assumed to follow a normal distribution along wavelength. For this distribution, equation D3, we assumed a center value of 365nm with a spread of 10nm.

$$D(\lambda) = \frac{1}{(10nm \cdot (2\pi)^{0.5} \cdot e^{-0.5 \cdot (\frac{\lambda - 365nm}{10nm})^2})} \quad (D3)$$

The distribution function $D(\lambda)$ can then be used in combination with the crosssection to determine the scale factor J_{scale}

$$J_{scale}(\lambda, T) = \frac{l}{V} \cdot \int_{250nm}^{500nm} \frac{\lambda}{hc} \cdot \sigma(\lambda, T) \cdot D(\lambda) d\lambda \quad (D4)$$

The value of J_{scale} with unit $joule^{-1}$, could then be found from the overlap integral between the cross section $\sigma(\lambda, T)$ and the emitted photon distribution. l is the pathlength across the tube/tubes in cm, and V is the volume of the tube/tubes in ml. λ is the wavelength in nm, h is Planck's constant and c is the speed of light. Values for the constants a and b from eq. D5 are then fitted to match the photolysis rate in eq. D6 with the photolysis rate found from the Kintecus model.

$$P_{eff}(W) = (a \cdot W + b) \cdot W \quad (D5)$$

Where P_{eff} is the effective power and the constants a, with unit 1/W, and b, unitless, are setup dependent constants, that scales the effectivity of effective power output P_{eff} . From the effective power output the photolysis rate J_{Cl_2} could be calculated by

multiplying P_{eff} with J_{scale} .

$$J_{Cl_2}(W) = P_{eff}(W) \cdot J_{scale} \quad (D6)$$

D3 Additional kinetics added to the J_{Cl_2} model

In some experiments, the power input (watt) can't be linked to the obtained values from the kintecus model. Consequently, additional simple kinetic calculations are used to estimate the J_{Cl_2} . Four main reactions R11 -R14 are considered in the simple kinetic model



$$[k_{Cl+CH_4} = 1.07 \cdot 10^{-13} \cdot \frac{cm^3}{molecules \cdot s}]$$



$$[k_{self} = 1.24 \cdot 10^{-32} \cdot \frac{cm^6}{molecules^2 \cdot s} \cdot [M]]$$



$$(R15)$$

$[k_{wall} = 124.5s^{-1}$ or $48.9s^{-1}]$ The Cl radicals are consumed at a fast rate, therefore, steady state approximation for Cl has been assumed.

$$\frac{d[Cl]}{dt} = 2 \cdot J_{Cl_2}[Cl_2] - (2 \cdot k_{self} \cdot [Cl]^2 + k_{Cl+CH_4} \cdot [CH_4] \cdot [Cl] + k_{wall} \cdot [Cl]) = 0 \quad (D7)$$

The photolyze rate is thereby defined in equation D8

$$J_{Cl_2} = \frac{2 \cdot k_{self} \cdot [Cl]^2 + k_{Cl+CH_4}[CH_4][Cl] + k_{wall}[Cl]}{2 \cdot [Cl_2]} \quad (D8)$$

The photolysis rate is calculated from an estimated [Cl] concentration. This was achieved by assuming that the methane concentration would follow an exponential decay along time, equation D9. The necessary [Cl] to achieve a removal efficiency in t seconds is expressed in equation D10.

$$[CH_4]_t = [CH_4]_0 \cdot \exp(-k_{Cl+CH_4} \cdot [Cl] \cdot t) \quad (D9)$$

$[CH_4]_t$ is the methane concentration at time t, while $[CH_4]_0$ is the initial concentration.

$$[Cl] = \ln\left(\frac{1}{1-RE}\right) / (k_{Cl+CH_4} \cdot t) \quad (D10)$$

The values for J_{Cl_2} can then be generated by inserting the known experimental values of initial $[Cl_2]$, $[CH_4]$ and the estimated value of $[Cl]$ into eq. D8. The constants for a and b from eq. 3 can then be fitted to generate the J_{Cl_2} derived from kinetic calculations. The resulting Eff(W) is then used to generate J_{Cl_2} values applied in the Kintecus model.

Table D3. Radical Wall reaction parameters. *Diffusion coefficient is estimated from D_{HO-At} and D_{HO_2-He} , ** The Chapman and Cowling diffusion model was used to estimate the diffusion constant.

Setup	Reaction	Diffusion constant (cm^2/s)	Reference	Diffusion length (cm)	Wall-reaction rate (1/s)
Single tube	$Cl \rightarrow \frac{1}{2}Cl_2$	0.260	Judeikis and Wun (1978)	0.146	1.2E+02
Multiple tubes				0.091	4.8E+01
Single tube	$ClO \rightarrow \frac{1}{2}Cl_2 + \frac{1}{2}O_2$	0.184	Seinfeld and Pandis (2016)**	0.146	8.8E+01
Multiple tubes				0.091	3.4E+01
Single tube	$OH \rightarrow \frac{1}{2}H_2O + \frac{1}{4}O_2$	0.217	Ivanov et al. (2007)	0.146	1.0E+02
Multiple tubes				0.091	4.0E+01
Single tube	$HO_2 \rightarrow \frac{1}{2}H_2O + \frac{3}{4}O_2$	0.139	Ivanov et al. (2007)*	0.146	6.7E+01
Multiple tubes				0.091	2.6E+01

D4 Kintecus results

Single tube experiments

J_{Cl_2} values are generated on the basis of experimental data from 26 February experiments 2 and 6-9. The effectiveness of the power input is generated from the J_{Cl_2} model. A correlation between effectiveness(%) and experimental power input (watt) is obtained in Figure D1 as well as the correlation with the J_{Cl_2} (Kintecus) values in Figure D2 The J_{Cl_2} dependence on the power input(W) for the single tube experiments of 26 and 24 February is given by the equations D11 and D12. The equations incorporates a decrease in efficiency of the power input as higher levels due to overheating of the chamber as seen in Figure C17

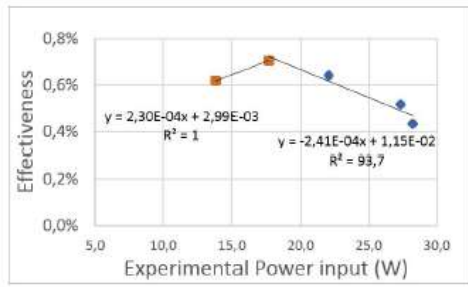


Figure D1. Effectiveness as a function of experimental power input for the 26 February. The correlation is used for calculating the effective power input for single tube experiments.

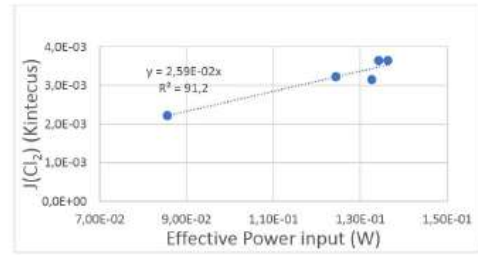


Figure D2. Kintecus obtained J_{Cl_2} as a function of the effective power input for the 26 February. The effective power input is calculated from Figure D1. The combination of the Figure with Figure D1 is used to calculate the J_{Cl_2} for single tube experiments by Eq. D11 - D12

$$J = 2.59 \cdot 10^{-2} \cdot (2.3 \cdot 10^{-4} \cdot W^2 + 2.99 \cdot 10^{-3} \cdot W) \text{ if Power} > 14.67W \quad (D11)$$

$$J = (2.59E \cdot 10^{-2} \cdot (-2.41 \cdot 10^{-4} \cdot W^2 + 1.15 \cdot 10^{-2} \cdot W) \text{ if Power} < 14.67W \quad (D12)$$

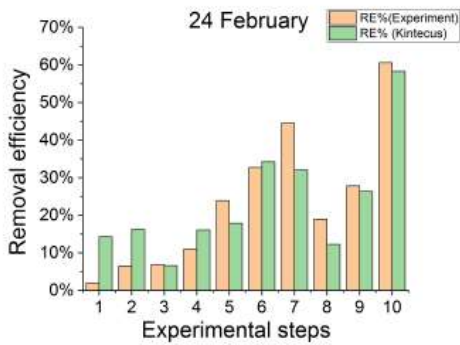


Figure D3. Removal efficiency for the steps of the 24 February as found experimentally (orange) and by model (green)

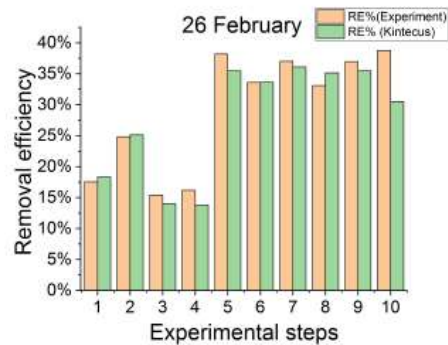


Figure D4. Removal efficiency for the steps of the 26 February as found experimentally (orange) and by model (green)

The comparison between modeled and experimental efficiency is seen in Figures D3 and D4. The J_{Cl_2} used for the two models are fitted to step 2, 6-9 of the 26 February, and got split up into two functions. For most of the steps the model

is underestimating the removal efficiency, most notably for the first two steps figure D3 caused by the early-experiments-derivation. . The kintecus model slightly underestimates the removal efficiency. From experiment six to eight the photochamber was continues turned on as visualized in Figure C6. In experiment eight the chamber was overheated an the effectiveness is decreased. This is also apparent in the comparison of kintecus simulated and experimental removal efficiencies at experiment eight.

Multiple tubes experiments

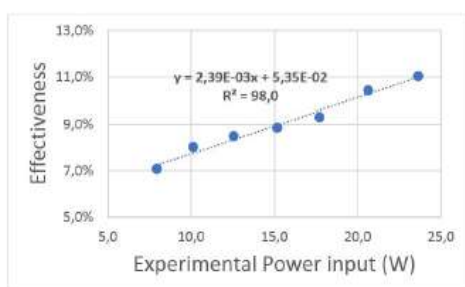


Figure D5. Effectiveness as a function of experimental power input for the 9 March. The correlation is used for calculating the effective power input for multiple tubes experiments.

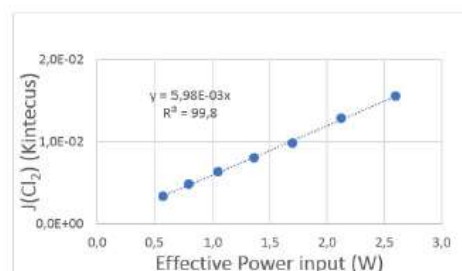


Figure D6. Kintecus obtained J_{Cl_2} as a function of the effective power input for the 9 March. The effective power input is calculated from Figure D5. The combination of the Figure with Figure D5 is used to calculate the J_{Cl_2} for Multiple tubes experiments by Eq. D13

The J_{Cl_2} rate is generated in the same manner for the experiments with multiple tubes. Here the 9 March experiments are used to obtain kintecus J_{Cl_2} -values. (Figures D5 and D6).

$$J = 5.98 \cdot 10^{-3} \cdot (2.39 \cdot 10^{-3} \cdot Power(W)^2 + 5.35E \cdot 10^{-2} \cdot Power(W)) \quad (D13)$$

The overheating at high power inputs is eliminated with the improved photochemical device. This is also apparent when comparing the effectiveness, which is approximately 9 % for the multiple tube, Figure D5, and approximately 0.6 % for the single tube, Figure D1 ,at the same power input at 15 W.

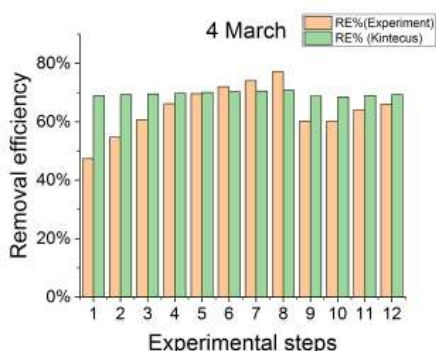


Figure D7. Removal efficiency for the steps of the 4 March as found experimentally (orange) and by model(green)

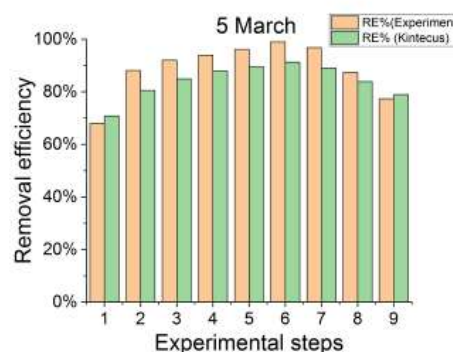


Figure D8. Removal efficiency for the steps of the 5 March as found experimentally (orange) and by model(green)

Figure D7 and D8 shows the comparison for 4 March and 5 March, respectively. The initial methane concentrations were varied in Figure D7. The kintecus model accounts poorly for the variations of initial methane concentrations. However, it still follows the trend to a small degree. The residence time in the photochamber was varied in Figure D8. The kintecus model follow the trend of the experimental results, but underestimated the removal efficiency.

27 February and 3 March

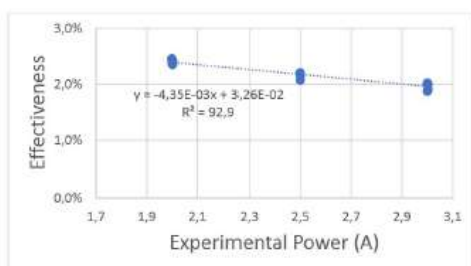


Figure D9. Removal efficiency for the steps of the 27 February as found experimentally (orange) and by model(green)

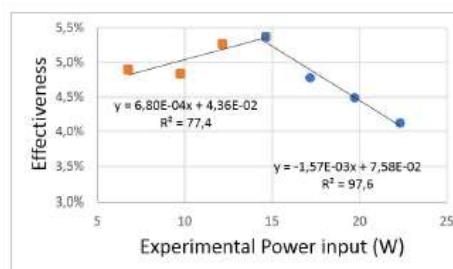


Figure D10. Removal efficiency for the steps of the 3 March as found experimentally (orange) and by model(green)

Some experiments can't be related to the relations presented for the single and multiple tube. This is due to the optimization done on the photochemical device. After the experiments on the 26 February the glue holding the circuit boards together is slightly removed. Therefore the 27 February experiments can't be related to the single tube J_{Cl_2} rates. After the 3 March the glue on the photochemical device is even further removed, and the chamber performs better. However, after the 3 March the photochemical is optimized even further with an additional improvements such as exchanged of some of the LEDs and reconstructed photochemical device. Therefore the 3 March experiments can't be related to the multiple tubes J_{Cl_2} . Additional

kinetic calculations is therefore used to estimate the J_{Cl_2} of these two experiments. The effectiveness for the 27 February is described shown in equation D14 and Figure D9

$$Effectivepower(W) = Power(W)(-4.35 \cdot 10^{-3} \cdot Power(Current) + 3.26 \cdot 10^{-2}) \quad (D14)$$

In the same manner the effectiveness of 3 March is shown in equations D15, D16 and Figure D10

$$EffectivePower(W) = Power(watt) \cdot (6.80 \cdot 10^{-4} \cdot Power(Watt) + 4.36 \cdot 10^{-2}) \text{ if } Power(W) > 14.31W \quad (D15)$$

$$EffectivePower(W) = Power(watt) \cdot (-1.57 \cdot 10^{-3} \cdot Power(Watt) + 7.58 \cdot 10^{-2}) \text{ if } Power(W) < 14.31W \quad (D16)$$

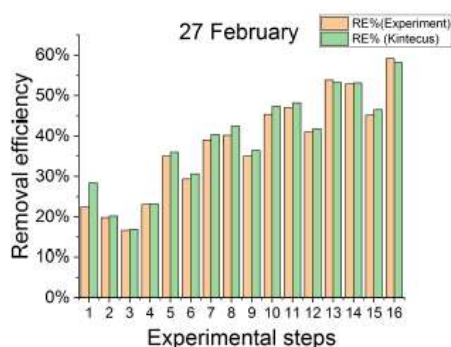


Figure D11. Removal efficiency for the steps of the 27 February as found experimentally (orange) and by model(green)

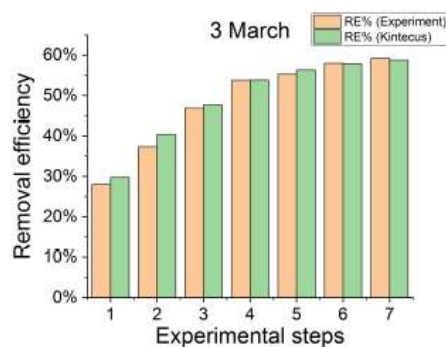


Figure D12. Removal efficiency for the steps of the 3 March as found experimentally (orange) and by model(green)

The kintecus model follows the experimental trend very accurately in Figure D9 and D12, and as expected the first experiments are overestimated.

Author contributions. TEXT

Matthew S. Johnson, Merve Polat and Jesper Baldtzer Liisberg conceived and planned the experiments. Merve Polat and Jesper Baldtzer Liisberg carried out the experiments. Merve Polat, Jepsen Naldtzer and Morten Krogsbøll planned and carried out the simulations. Merve Polat and Jesper Baldtzer Liisberg contributed to the interpretation of the results. Merve Polat and Jesper Baldtzer Liisberg wrote the manuscript in consultation with Thomas Blunier and Matthew S. Johnson.. All authors provided critical feedback and helped shape the research, analysis and manuscript.